

Doctoral Dissertation

博士論文

**Modeling and dynamic behavior analysis for energy
harvesting systems in rotational motion considering
effects of centrifugal force**

(遠心力を考慮した回転運動中のエネルギーハーベスティングシ
ステムのモデル化と動的挙動解析)

MEI Xutao

梅 旭濤

Contents

Abstract.....	5
1 Introduction	13
1.1 Background	14
1.2 Methods of Energy Harvesting	14
1.2.1 Electromagnetic Effect	14
1.2.2 Electrostatic Effect	15
1.2.3 Triboelectric Effect.....	15
1.2.4 Piezoelectric Effect.....	16
1.3 Energy Harvesting in Rotational Motion.....	19
1.3.1 Machine.....	19
1.3.2 Wind Turbine.....	20
1.3.3 Vehicle Wheel.....	21
1.4 Broadening Frequency Bandwidth	22
1.4.1 Multi-Frequency Harvester Array	22
1.4.2 Frequency-up Conversion	23
1.4.3 Nonlinearity.....	24
1.4.4 Self-tuning Harvester	26
1.5 Existing Issues and Challenges.....	27
1.6 Motivation and Objective	28
1.6.1 Motivation	28
1.6.2 Objective	28
1.7 Dissertation Overview	29
2. Modelling for Nonlinear Energy Harvester in Rotational Motion	33
2.1 Design and Operating Principle.....	33
2.2 Coordinate Transformation.....	34
2.3 Mathematical Modelling	36
2.3.1 Kinetic Energy Description	37
2.3.2 Potential Energy Description.....	39
2.3.3 Tip displacement Separation	41
2.3.4 Governing Equations Description	42
2.4 Calculation of Magnetic Force	44
2.4.1 Repulsive Configuration in Radial Direction	44
2.4.2 Attractive Configuration in Normal Direction.....	46
2.5 Theoretical Analyses	47
2.5.1 Influence of Coefficient K_c	49
2.5.2 Case Studies	50

2.6 Experimental Validation and Discussion	53
2.6.1 Experimental Validation	53
2.6.2 Results Discussion.....	59
2.7 Summary	59
3. Various Nonlinear Energy Harvesters in Rotational Motion	62
3.1 Bi-stable Energy Harvester in Rotational Motion	62
3.1.1 Bi-stable Energy Harvester.....	62
3.1.2 Bi-stable Energy Harvester in Rotational Motion	63
3.2 Symmetric Tri-stable Energy Harvester in Rotational Motion	64
3.2.1 Theoretical Model	66
3.2.2 Solutions for Asymmetric Oscillation	67
3.2.3 Solution for Symmetric Oscillation.....	71
3.3 Asymmetric Tri-stable Energy Harvester in Rotational Motion	73
3.4 Quad-stable Energy Harvester in Rotational Motion.....	74
3.4.1 Theoretical Model	76
3.4.2 Theoretical Solutions by Perturbation Method.....	77
3.4.3 Stability Analysis of Solutions	80
3.5 Parametric studies.....	80
3.6 Experimental Validation	83
3.6.1 Experimental Results.....	85
3.6.2 Centrifugal Stiffening Effect	92
3.6.3 Discussion	93
3.7 Summary	93
4. Self-tuning Harvester by Centrifugal Stiffening Effect	96
4.1 Principle of Passively Self-tuning Energy Harvester.....	97
4.2 Effect of System Parameters.....	98
4.2.1 Effect of Rotational Radius	98
4.2.2 Effect of Beam Length	99
4.2.3 Effect of Tip Mass	100
4.3 Experimental Validation	101
4.3.1 Experimental Setup	101
4.3.2 Experimental Results.....	103
4.4 Optimal Design for the Self-tuning Effect.....	108
4.5 Discussion	111
4.6 Summary	112
5. Low-frequency Energy Harvesting by Centrifugal Softening Effect	114
5.1 Operating Principle.....	114

5.2 Theoretical Modelling	115
5.2.1 Kinetic Energy Description	116
5.2.2 Potential Energy Description.....	117
5.2.3 Governing Equation	118
5.3 Theoretical Analyses	120
5.4 Experimental Validation	122
5.4.1 Experimental Setup	122
5.4.2 Experimental Results.....	124
5.5 Discussion	126
5.5.1 Further Improvement.....	126
5.5.2 Potential Application	127
5.6 Summary	128
6. Further Research and Discussion	130
6.1 Rotational Motion with Translational Motion	130
6.2 Theoretical Modelling with Translational Motion	131
6.3 Scenario for Experimental Validation.....	134
6.3.1 Real-vehicle Experimental Validation on Road.....	134
6.3.2 Circuit Management System for Energy harvester.....	135
6.3.3 Potential Application	135
6.4 Discussion	136
6.4.1 Optimal Design for Centrifugal Stiffening Effect	137
6.4.2 Optimal Design for Centrifugal Softening Effect.....	140
6.5 Summary	141
7 Summary and Conclusion	143
References	148

Abstract

Many wireless sensors are widely used to realize the convenient life and intelligent industry via Internet of Things (IoT). The traditional method for power supply is the chemical batteries, whose disadvantages are the limited lifespan, maintenance difficulties and pollution issues. Recently, the energy harvesting from the ambient energies has been considered as a promising way to provide sustainable power supply for these wireless sensors. Lastly, a self-powered wireless sensor can be achieved for structural health monitoring. According to previous studies of the piezoelectric energy harvesters (PEHs) in rotational motion, few of them considered the effect of rotational motion, namely the centrifugal force was neglected in their theoretical models, leading to their dynamic mechanism being not completely revealed. In order to solve these issues, the author mainly focus on modeling and dynamic behavior analysis for energy harvesting systems in rotational motion considering effects of centrifugal force.

Firstly, a nonlinear PEH in rotational motion is proposed, and related theoretical model is derived in a rotational coordinate system based on Lagrange equation and energy method. It can be noticed that the rotational coefficients, including the angular displacement, angular velocity and angular acceleration, are coupled in the proposed theoretical model. It also can be found that when the effect of rotational motion is considered, the $K_c \dot{\theta}^2$ term related to the rotational speed is added. The experimental results of a symmetric tri-stable PEH confirmed that the K_c coefficient has a great effect on predicting the energy harvesting performance, especially for the high rotational speeds at which the centrifugal stiffening effect occurs.

In this dissertation, the nonlinearities of different PEHs are caused by the magnetically coupled configuration. The dipole-dipole method is adopted to calculate the nonlinear magnetic forces of two configurations. Most importantly, for the PEHs in rotational motion, the periodic gravity component of tip mass can be an exciting force for the piezoelectric beam vibration. Based on that, the energy harvesting performance of various PEHs, including bi-stable, symmetric tri-stable, asymmetric tri-stable and quad-stable configurations, are theoretically and experimentally investigated. The experimental results demonstrate that the nonlinearity can broaden the effective frequency range via reducing the potential barriers, especially for the quad-stable PEH. An interesting phenomenon is that when the rotational speed reaches a certain value (440 rpm), the centrifugal stiffening effect will appear, reducing the energy harvesting performance.

Next, according to the centrifugal stiffening effect, a passively self-tuning effect is achieved for energy harvesting enhancement. As observed from the proposed theoretical model, as the

rotational speed increases, the corresponding axial tension due to the centrifugal force on the piezoelectric beam changes its resonance frequency. Thus, when the parameters of a PEH are in appropriate values, the resonance frequency is near or at the rotational speed in a wide frequency range. In the experiments, the bi-stable and tri-stable PEHs achieve the self-tuning effect in the ranges of 440 - 720 rpm and 990 - 1300 rpm, respectively, which are caused by the different rotational radiuses. Additionally, it is validated that a passively self-tuning method is effective way to widen the operation frequency bandwidth.

In order to further harvest low-frequency rotational energy (less than 120 rpm), an inverse PEH is installed in rotational motion, in which the centrifugal force is along with the inside of radial direction so that the centrifugal softening effect will be achieved. And the same nonlinear PEH is adopted for the experiments with forward and inverse configurations in rotational motion, which correspond to the centrifugal stiffening and softening effects respectively. The experimental results confirm that in low-frequency rotational motion, the inverse PEH is superior to the forward one, and the RMS voltage between 60 - 110 rpm can reach as high as 5 V, which is enough for powering a wireless sensor used for the structural health monitoring of the blade of a wind turbine.

This dissertation mainly focused on three keywords: rotational motion, centrifugal force and piezoelectric energy harvesting. All results demonstrate that the centrifugal force caused by the rotational motion has a great influence on the energy harvesting performance. Specifically, for the forward PEH, under high rotational speeds, the centrifugal force along with the outside of radial direction can lead to centrifugal stiffening effect, by which a passively self-tuning effect can be obtained to broaden the effective frequency range. For the inverse PEH, the centrifugal force along with the inside of radial direction can enhance the energy harvesting performance in low-frequency rotational motion via the centrifugal softening effect.

Nomenclature and Abbreviations

a_1	Amplitude of the steady-state displacement
\bar{A}	Complex conjugate A
A_b	Cross-sectional area of cantilever beam
A_p	Cross-sectional area of piezoelectric patch
b	Width of cantilever beam
b_p	Width of piezoelectric patch
B_r	Magnet's residual flux density
cc	Complex conjugate
C	Mechanical damping coefficient
C_p	Internal capacitance
d	Separation displacement between tip magnet and external magnet
d_{31}	Coupling coefficient
$D_n = \partial/\partial T_n$	Partial differential operator
$\hat{e}_x, \hat{e}_y, \hat{e}_z$	Unit vectors of X, Y, Z axis
EI, EI_1, EI_2	Bending rigidity of piezoelectric beam
EA	Axial rigidity of piezoelectric beam
E_b	Young's modulus of cantilever beam
E_p	Young's modulus of piezoelectric patch
F	Excitation force amplitude
F_c, f_r	Equivalent centrifugal force
F_e	Elastic force
F_m	Nonlinear magnetic force
F_r	Restoring force
$F(t), f(t)$	External excitation
g	Gravitational acceleration
h_1, h_2, h	Gap distance between magnets
i^*, j^*, k^*	Unit vectors of X^*, Y^*, Z^* axis

$I(t)$	Electric output charge of piezoelectric patch
J_A	Inertial moment of tip magnet
K_e	Equivalent stiffness of piezoelectric beam
K_c, K_{c1}, K_{c2}	Coefficient related to rotational motion
K_1	Linear coefficient
K_3, K_5, K_7	Nonlinear coefficient
l_c	Length scale
l_p	Length of piezoelectric patch
L	Length of cantilever beam
$\mathcal{L}(w, v)$	Lagrange function
m	Mass of piezoelectric beam per unit length
m_b	Mass of piezoelectric beam
M	Mass of tip magnet
M_e	Equivalent mass
M_j	Magnetization intensity
N_{eff}	Effective nonlinear coefficient
P_0	Position of infinitesimal segment
$P(t)$	Generalized force due to the non-conservative force
$q(t)$	Time-dependent generalized temporal coordinate
r	Rotational radius
r_A, r_B, r_C, r_D	Radius of magnets
\mathbf{r}_{jA}	Direction vector
R_l	Load resistance
t_b	Thickness of cantilever beam
t_p	Thickness of piezoelectric patch
T	Whole kinetic energy
$u(x, t)$	Axial deformation of piezoelectric beam at distance x

$u_a(L, t)$	Pure axial deformation of tip magnet
u_s	Non-zero stable equilibrium position
$u_\tau(\tau, \varepsilon)$	Displacement response around u_s
U	Whole potential energy
U_e	Elastic potential energy of piezoelectric beam
U_g	Gravitational potential energy
U_c	Centrifugal potential energy
U_{jA}	Potential energy between magnets
$v(t)$	Output voltage of piezoelectric patch
V_j	Volume of Magnets
$w(x, t)$	Transverse displacement of piezoelectric beam at distance x
$w(L, t)$	Transverse displacement of tip magnet
W_e	Internal electric energy
x_1, x_2, x_3, x_4, x_5	Stable and unstable equilibrium position
Δx	Deformation associated with the foreshortening quantity
$X^*Y^*Z^*$	Rotational coordinate system
XYZ	Newtonian coordinate system
$y(\tau, \varepsilon)$	Voltage response around u_s
α	Detuning parameter
β, η	Nondimensional nonlinear coefficient
γ	Nondimensional coefficient related to rotational motion
ε	Booking-keeping parameter
ε_0	Permittivity of free space
ε_{33}	Piezoelectric material permittivity
θ	Angular displacement
$\dot{\theta}$	Angular velocity
$\ddot{\theta}$	Angular acceleration
$\mathcal{G}_{p1}, \mathcal{G}_p$	Electromechanical coupling coefficient

ρ_b	Material density of cantilever beam
ρ_p	Material density of piezoelectric patch
μ_0	Magnetic permeability constant
$\boldsymbol{\mu}_j$	Magnetic moment vector
$\hat{\boldsymbol{\mu}}_A, \hat{\boldsymbol{\mu}}_j, \hat{\boldsymbol{r}}_{jA}$	unit vectors along $\boldsymbol{\mu}_A, \boldsymbol{\mu}_j, \boldsymbol{r}_{jA}$
δ	Rotational angle
ω	Nondimensional rotational angular velocity
ω_n	nominal short-circuit frequency
ω_1	Linearized oscillation frequency
ξ	Nondimensional damping ratio
ξ_e	Electric damping
ξ_{eff}	Effective damping
σ^2	Nondimensional electromechanical coupling coefficient
λ	Nondimensional internal capacitance
$\phi(x), \phi_1(x), \phi_2(x)$	Mode shape function
$\chi, \chi_1, \chi_2, \bar{\chi}$	Coefficient of angular acceleration
$\Gamma g, \bar{\Gamma} g, \Gamma_1 g, \Gamma_2 g$	Equivalent excitation from tip mass gravity
$\gamma_2, \gamma_3, \gamma_4, \gamma_5$	Nonlinear coefficient
$(\cdot)', (\cdot)''$	With respect to time

Acknowledgements

It is a great pleasure to express my great thanks to all who made contributions to my doctoral research work. I sincerely thank my supervisor, Professor Kimihiko Nakano, at The University of Tokyo, for his patient guidance, continuous support and enduring encouragement. He always gives professional advices on my research work through my doctoral period. His enthusiasm and attention to details will continue influence my research career in the future.

I great thank Professor Yoshihiro Suda, Professor Beomjoon Kim, Professor Yudai Yamasaki and Professor Yuji Yamakawa. As referees of my dissertation defence committee, all of their valuable comments and constructive suggestions helped me to complement my research and great improve my dissertation.

I also thank Dr. Shengxi Zhou, Professor of Northwestern Polytechnical University (China), for his supports in experiments and papers writing. He always gives me the quick response, valuable comments and suggestions. I convey my sincere thanks to Professor Zhichun Yang, he gives me important suggestions in the skills of paper writing and research point of energy harvesting.

I appreciate Dr. Tsutomu Kaizuka, the research assistant and Dr. Bo Yang the project researcher of K. Nakano Laboratory, they give me much advice about the purchase and use of experimental devices.

I would like to express my heartfelt gratitude to Ms. Atusko Hasegawa and Ms. Inosaka Ayako, for their help in my daily life in The University of Tokyo. I also thank to Dr. Zheng Wang, Mr. Ran Zhou, Mr. Wei Xue, Mr. Edric, and all the other members of K. Nakano Laboratory, for their kindness in discussion of my research work and daily life in Japan.

I am grateful to my beloved girlfriend, Chuchu Yang, as this work could not have been possible without her supports and encouragements. She makes my life so memorable, colourful and meaningful. She keeps inspiring me to be a better man. Additionally, I am deeply indebted to my family for their continuous support, concerns and encouragement.

Lastly, I am also thankful to MEXT Scholarship & China Scholarship Council, the work may have not been possible without the provided finical support.

January 26, 2020

Xutao MEI

Chapter 1

Introduction

1 Introduction

With the aim to realize the intelligent life via Internet of Things (IoT), many wireless sensors are widely used in industry, aerospace, environmental monitoring and other many fields [1,2]. Traditionally, the power supply is provided by the chemical batteries, but their disadvantages are the limited lifespan, maintenance difficulties and pollution issues, etc [3,4]. Thus, providing the sustainable power supply for these wireless sensors has becoming a key success factor of IoT. Recently, the energy harvesting from the ambient energies, such as the solar, wind and mechanical energy, has attracted widespread attentions and been considered as a promising way to provide the electric energy for these wireless sensors [5]. As observed from in Figure 1.1, a self-powered wireless sensor mainly includes a wireless sensor, an energy harvester and circuit management system (CMS). The CMS is used to manage the generated electric energy by energy harvester, providing the power source for the wireless sensor. The monitoring data of the structures, such as wind turbine, bridge, building, will be transmitted to the monitoring center to achieve real-time structural health monitoring. The schematic diagram of a self-powered wireless sensor for structural health monitoring is shown in Figure 1.1.

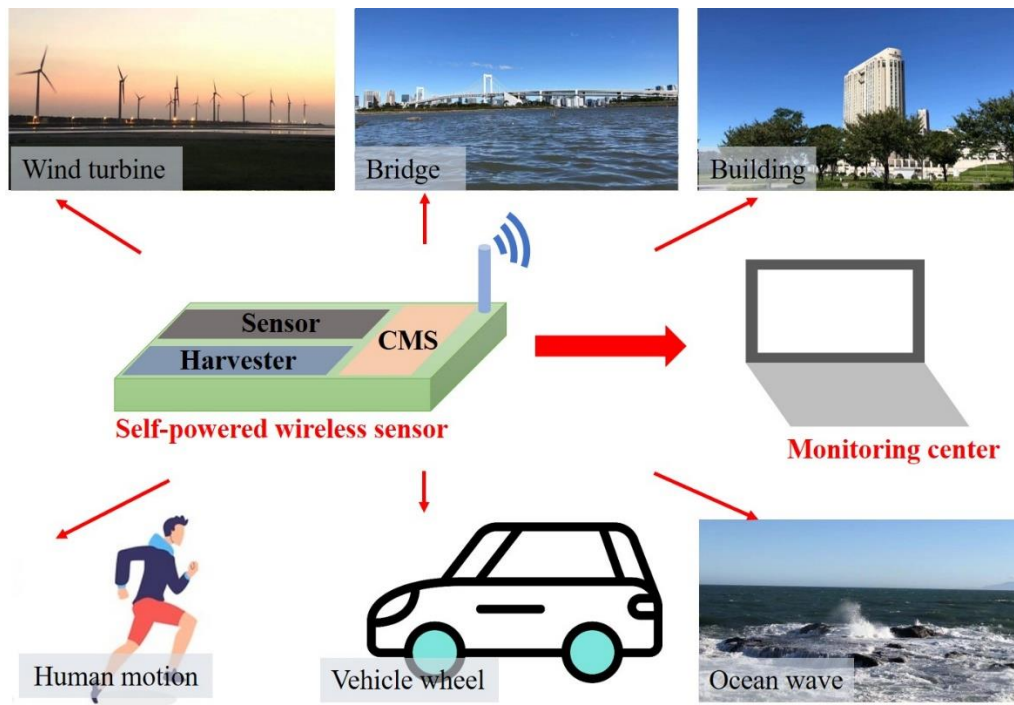


Figure 1.1 The schematic diagram of a self-powered wireless sensor for structural health monitoring, and the power source is provided by the energy harvesting form ambient energy.

1.1 Background

The rapid advancement in low-power integrated circuits, wireless communication and mobile electronics have greatly reduced the demands in power consumption requirements and promoted the possibility that the energy harvesting is a way to provide the sustainable power source for those wireless sensor sensors. As reported in 2018, the average power of a wireless sensor is 10 μW [6]. An excellent commercial example is from the Perpetuum Ltd., where the energy harvesting technology to power wireless sensors has been developed. Their wireless sensors provide real-time information that enables the rail industry to optimize railway operations such as in UK, Australian, USA, etc [7]. Wang *et al.* [8] explored an ultra-low-friction Triboelectric-Electromagnetic hybrid energy harvesting from the wind for a self-powered wind speed sensor, and the experimental results demonstrated that it can work as a self-powered wind speed sensor to detect wind speed as low as 3.5 m/s.

Some of recent research works have focused on the design of vibration energy harvester based on four major transduction mechanisms: electromagnetic [9,10,11], electrostatic [12,13,14] and triboelectric [15,16,17,18], piezoelectric [19,20,21,22,23,24,25,26] effects. Among these methods, the piezoelectric energy harvester (PEH) has been widely investigated due to the advantage of high density, simple structure and compact size [2, 4]. In the next subsection, the mechanism of four methods will be further presented.

1.2 Methods of Energy Harvesting

1.2.1 Electromagnetic Effect

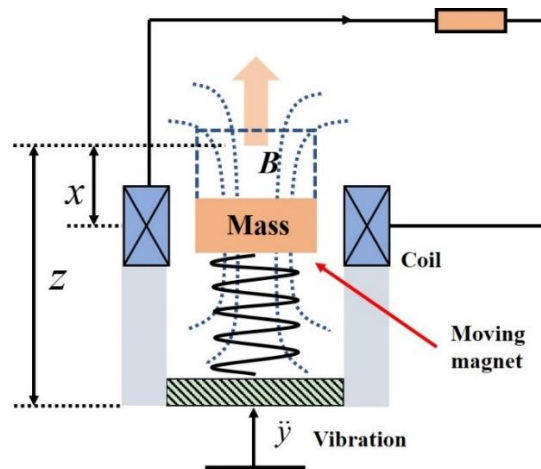


Figure 1.2 The schematic diagram of electromagnetic effect for vibration energy harvesting. [4]

Figure 1.2 shows the schematic diagram of electromagnetic effect for vibration energy harvesting. The vibration from ambient environment, such as the wind, ocean wave and road vibration, is regarded as the base excitation, which results in the relative movement between the magnet and the coils, according to Faraday's Law, the voltage can be induced in the coils.

$$\varepsilon_v = -\frac{d\phi B}{dt} \quad (1.1)$$

Where ε_v is the induced voltage and ϕB is the magnetic flux.

1.2.2 Electrostatic Effect

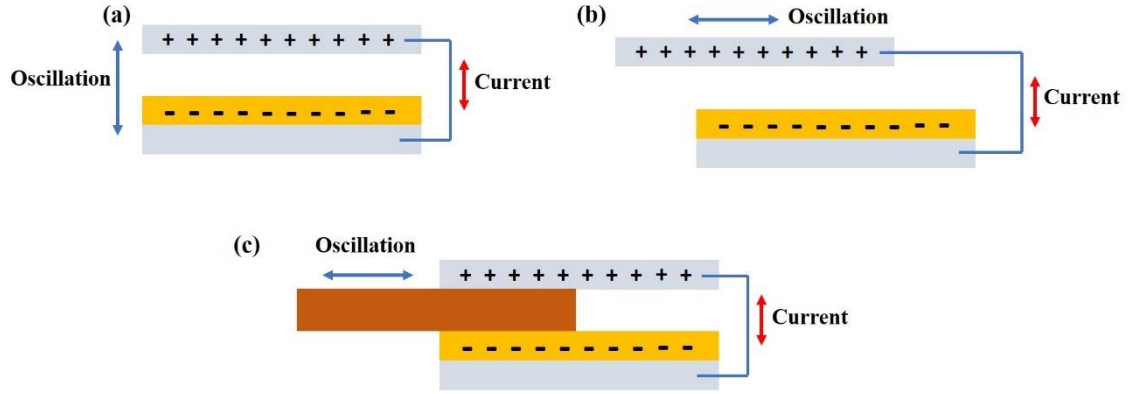


Figure 1.3 Principles of the electret energy harvester. [12]

Charges with opposite sign are induced on the counter-electrode by the electrostatic field of the electrets. Figure 1.3 illustrates the three various configuration of electret energy harvester. Figure 1.3(a) is a gap-closing electret energy harvester. Figure 1.3(b) represents an in-plane oscillation type. Figure 1.3(c) is an in-plane oscillation type with an insert inside the air gap.

1.2.3 Triboelectric Effect

The triboelectric effect, which was initially focused by the tribology study, is a type of contact electrification in which certain materials become electrically charged after contacting with another different material, then are separated [27]. In recent 10 years, its excellent performance and interesting phenomena have attracted widespread research interests, especially for Prof. Zhonglin Wang's Group [28,29]. According to the triboelectric effect, various triboelectric nanogenerators (TENGs) have been investigated. There are four working modes for TENGs, including the vertical contact mode, lateral sliding model, single electrode mode, and free-

standing triboelectric layer model as shown in Figure 1.4, respectively.

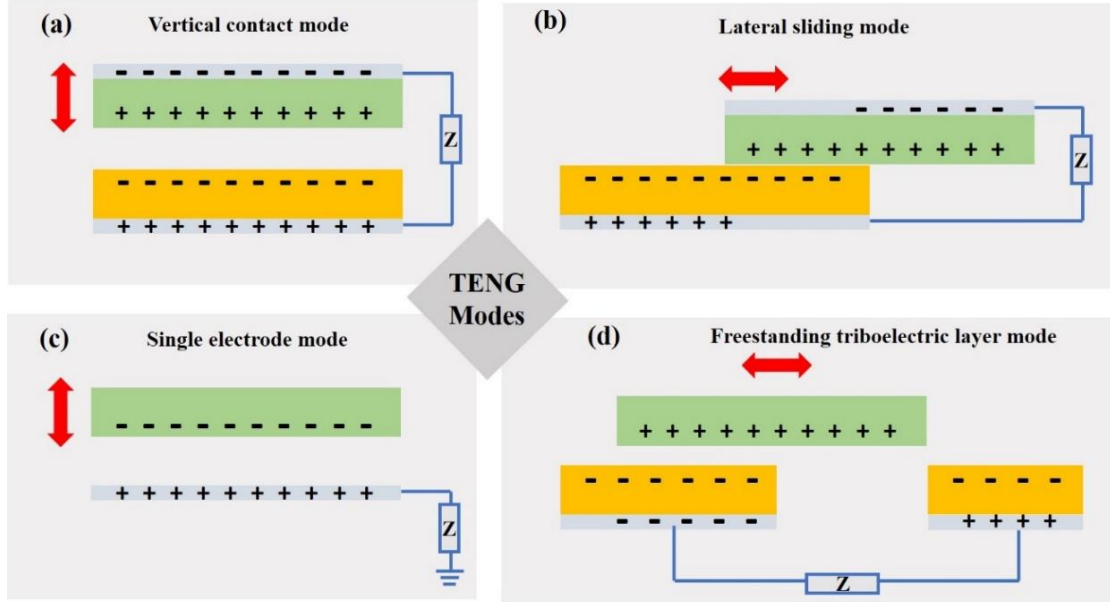


Figure 1.4 The four fundamental modes of TENGs: (a) vertical contact mode; (b) lateral sliding model; (c) single electrode model; (d) free-standing triboelectric layer mode. [30]

1.2.4 Piezoelectric Effect

Fundamentals of Piezoelectric Energy Harvesting

The direct piezoelectric effect is the basis for the piezoelectric energy harvesting. It is governed by the following constitutive equations (1.2), which connects the mechanical domain (stress T and strain S) with the electric domain (electric field E and charge density D):

$$\begin{bmatrix} S \\ D \end{bmatrix} = \begin{bmatrix} s^E & d^t \\ d & \varepsilon^T \end{bmatrix} \begin{bmatrix} T \\ E \end{bmatrix} \quad (1.2)$$

where s^E is the compliance under a constant electrical field, ε^T is the dielectric permittivity under a constant stress, d and d^t are the matrices for the direct and converse piezoelectric effect, where the superscript t is the transpose [1].

The direction of the applied stress can be either along the polar direction (3-direction) or at right angles to it (1-direction), resulting in two common piezoelectric energy harvesting configurations, 33-model and 31-model, as shown in Figure 1.5(a) and 1.5(b). For the 33-model, the compressive stress/strain is applied parallel to the 3-direction, while the generated voltage is along the same axis. For the 31-model, the stress/strain is applied perpendicular to the polar axis and the direction

of the generated voltage is at the right angle of the applied force. Note that the operation in 31-model results in the large strain in 1-direction, thus, it is widely adopted in vibration energy harvesting via the direct piezoelectric effect.

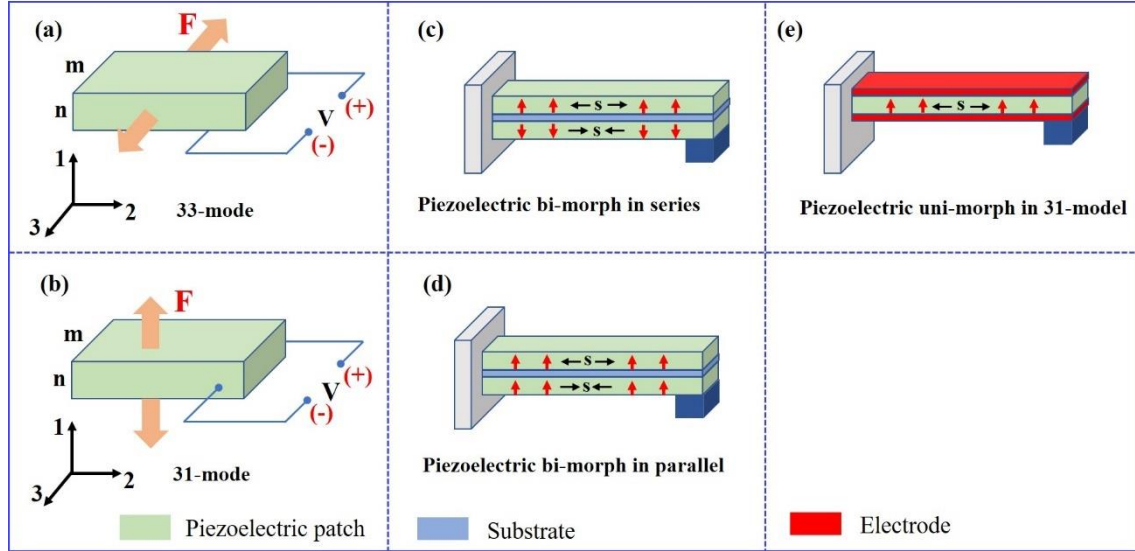


Figure 1.5 (a) and (b) Piezoelectric material used in 33-model and 31-model, respectively; (c) and (d) 31-model bi-morph cantilever in series and parallel connections respectively. (e) 31-model uni-morph cantilever configuration [2].

Bi-morph and uni-morph cantilever PEH

The cantilever-type is most common adopted configuration in piezoelectric energy harvesting, especially for the vibration energy harvesting due to the large mechanical strain can be produced in the fixed end of the cantilever beam. It is worth mentioning that the piezoelectric cantilever includes the bi-morph and uni-morph forms as shown in Figure 1.5(c) and 1.5(e), respectively. For the bi-morph configuration, top and bottom layers are poled either in the same direction or the opposite direction, which are termed as parallel or series poling, to induce accumulated current or voltage by each layer respectively, as shown in Figure 1.5(d) and 1.5(c). In all cases, the power conversion potential is the same. To further investigate the relationship or difference of two configurations, the analysis procedures are presented in subsection.

As illustrated in previous studies [31,32], the electromechanical equations are presented as follow:

$$\mathbf{M}\ddot{\mathbf{x}} + \mathbf{C}\dot{\mathbf{x}} + \mathbf{K}\mathbf{x} - \mathbf{\Theta}\mathbf{v} = \mathbf{F}(\mathbf{t}) \quad (1.3)$$

$$\mathbf{\Theta}^t \mathbf{x} + \mathbf{C}_p \mathbf{v} = -\mathbf{q} \quad (1.4)$$

where \mathbf{M} , \mathbf{C} , \mathbf{K} , $\mathbf{\Theta}$, $\mathbf{F}(t)$, \mathbf{C}_p and \mathbf{q} are the matrixes of mass, damping, stiffness, electromechanical coupling, excitation, capacitance and current, respectively. Eqs. (1.3) and (1.4) are known as the actuator and sensing equations, respectively. When the piezoelectric energy harvester consists of a single piezoelectric, Eq. (1.3) can reduce to a scalar equation. How, for the bi-morph configuration with two piezoelectric elements as shown in Figure 1.5(c) and 1.5 (d). Thus, the governing equations are rewritten as:

$$M\ddot{x} + C\dot{x} + Kx - (\theta_1 v_1 + \theta_2 v_2) = F(t) \quad (1.5)$$

$$\begin{Bmatrix} \theta_1 \\ \theta_2 \end{Bmatrix} x + \begin{bmatrix} C_{p1} & 0 \\ 0 & C_{p2} \end{bmatrix} \begin{Bmatrix} v_1 \\ v_2 \end{Bmatrix} = - \begin{Bmatrix} q_1 \\ q_2 \end{Bmatrix} \quad (1.6)$$

Thus, Eq. (1.6) also can be expressed as:

$$(\theta_1 + \theta_2)x + (C_{p1}v_1 + C_{p2}v_2) = -(q_1 + q_2) \quad (1.7)$$

The objective is to reduce Eq. (1.5) and (1.7) to equation with effective coefficient, and expressed as:

$$M\ddot{x} + C\dot{x} + Kx - \theta_e v = F(t) \quad (1.8)$$

$$\theta_e x + C_{pe} v = -q \quad (1.9)$$

where θ_e and C_{pe} are the equivalent electromechanical coupling and capacitance, respectively.

(1) For the uni-morph cantilever PEH, $\theta_e = \theta_1$ and $C_{pe} = C_{p1}$.

It should be noted that $\theta_1 = \theta \phi'(l_p) = E_p d_{31} b (h_s + h_p/2 + \tilde{h}) \phi'(l_p)$ and $C_{p1} = \epsilon_{33} b l_p / h_p$ are the electromechanical coupling and capacitance of a piezoelectric beam, respectively [33,34,35]. l_p is the active length of the piezoelectric material, which is assumed to start at the clamped end of the cantilever beam. h_s is the thickness of the beam, h_p is the thickness and b is the width of the piezoelectric patch. d_{31} is the piezoelectric constant. E_p is the Young's modulus of the piezoelectric material and \tilde{h} is the effective neutral axis as shown in Figure 1.6.

(2) For the series connection, $v_1 + v_2 = v$ and $q_1 = q_2 = q$, thus, $\theta_e = \theta_1$ and $C_{pe} = C_{p1}/2$.

(3) For the parallel connection, $v_1 = v_2 = v$ and $q_1 + q_2 = q$, thus, $\theta_e = \theta_1 + \theta_2$ and $C_{pe} = C_{p1} + C_{p2}$.

It is worth mentioning that these contents are the fundamental knowledge of piezoelectric energy

harvesting, and these are also the preparation for the research work in this dissertation. Thus, the piezoelectric effect is presented with more details.

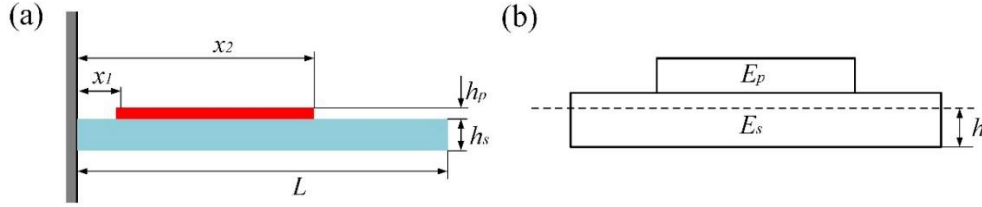


Figure 1.6 (a) Schematic of a simple uni-morph cantilever beam; (b) the neutral axis location [36].

1.3 Energy Harvesting in Rotational Motion

As investigated in recent research works [37,38,39,40,41,42], most of them are mainly focused on the rectilinear oscillation-based energy harvesting. But the rectilinear oscillation in ambient condition is low, variable and unpredictable especially in some situations the vibration sources are not sustainable. Different from those, the rotational motion is sustainable and widely existing in civil and industrial environments, such as the machine [43,44,45,46,47,48], wind turbine [49,50] and vehicle wheel [51,52,53]. Therefore, various energy harvesters have been explored in rotational motion, in which the advantages are summarized as follows: (1) the gravity component of the tip mass can be regarded as a periodic exciting force for the piezoelectric beam vibration; (2) the centrifugal force caused by the rotational motion is a promising way to achieve a self-tuning energy harvester for energy harvesting enhancement.

1.3.1 Machine

The rotational motion is widely existing in machine, and the features of those rotational machine are; (1) no base excitation; (2) some certain rotational speeds. Thus, for the energy harvesting from the machine, many studies focus on the energy harvesting performance under some constant rotational speeds.

Firstly, Khameneifar *et al.* [45,46] presented a linear PEH in rotational motion as Figure 1.7, whose gravity component can act as a source of the periodic exciting force. Zhang *et al.* [47] proposed a halbach electromagnetic energy harvester from bearing motion for power supply of wireless sensor, and the generated voltage of 2.79 - 4.59 V. However, the volume of this design is large, thus, the energy harvesting density is not acceptable. Guan *et al.* [48] proposed a rotational

PEH with a tip mass to reduce the effect of centrifugal force.

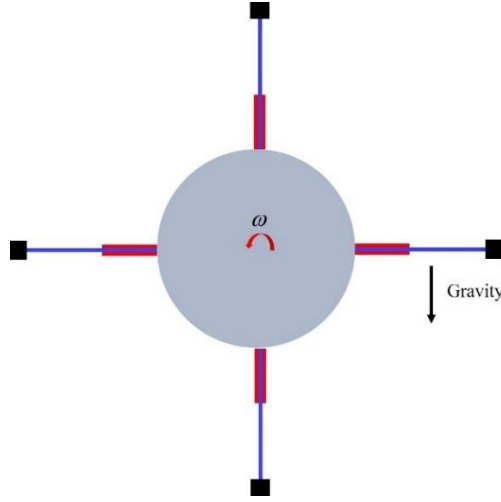


Figure 1.7 A linear PEH in rotating motion for energy harvesting. [45]

1.3.2 Wind Turbine

With the aim to develop a green future, wind power is one of the rapid growing renewable energy sources in the world. Ensuring the normal operation of wind turbines becomes a critical issue to input the sustainable wind power into the power grid. Therefore, in order to reduce the operation and maintenance cost, the remote structural health monitoring technique via wireless sensors has been explored by many researchers. Ensuring the normal operation of wind turbine becomes a critical issue to input the sustainable wind power in the power grid. The feature of energy harvesting in wind turbine is the low rotational speed (less than 120 rpm).

In recent years, energy harvesting from wind turbine has been widely explored and considered as a promising technology to achieve self-powered wireless sensors for the structural health monitoring. Febbo *et al.* [49] proposed a 2 degree of freedom (2DOF) cantilever beam-type energy harvester in rotational motion as shown in Figure 1.8, and experimentally verified the output power 26-105 μW in the proposed bandwidth (50-150 rpm). Nezami *et al.* [50] explored a disk-swing driven PEH for the potential application of wind turbine. In a normal operation of the wind turbine, when the rotational speed of the blade is slow, the orientation of the gravity-induced disk is toward the ground, but the orientation of the PEH is time-varying. The relative motion between them will enforce the PEH to generate the voltage. Thus, the rotational energy can be converted into vibration and electrical energy.

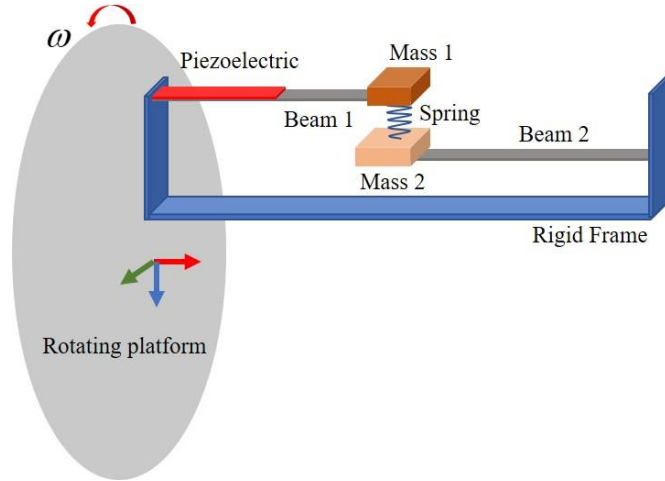


Figure 1.8 The schematic view of a nonlinear PEH in rotational motion. [49]

1.3.3 Vehicle Wheel

The automotive industry has a great interest in small-scale sensors for control and safety applications. Due to difficulties of wire connect in rotational wheels, the wireless sensors are adopted for Tire Pressure Monitoring System (TPMS). The traditional method of power supply is the embedded batteries, now various companies and researchers try to use energy harvesting method to replace the batteries for the power supply.

Sadeqi *et al.* [51] investigated a PEH embedded in a tire that uses a linear resonant structure to increase the operating frequency rang, as shown in Figure 1.9. Zhang *et al.* [52,53] explored a bi-stable PEH on the rim of a vehicle wheel, and they experimentally investigated the influence of rotational radius on the energy harvesting performance via real-vehicle tests.

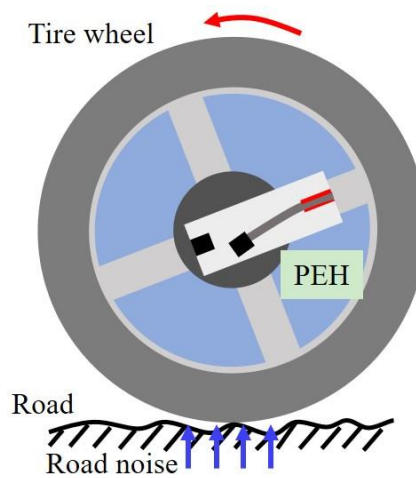


Figure 1.9 A tire-embedded PEH using a bi-stable PEH in the vehicle tire. [52]

1.4 Broadening Frequency Bandwidth

Although some PEHs for energy harvesting from rotational motion have been investigated, the low output power, low efficiency and poor environmental adaptability are the key issues that restrict its practical application. Initially, the linear PEHs, exploiting the resonance theory, usually lose their performance under realistic operational conditions in which the ambient vibrations are time-variable and broadband. In order to obtain high-efficiency broadband vibration energy harvesters, many researchers proposed broadband energy harvesting methods via multi-frequency harvester array [54,55,56], frequency-up conversion [57,58,59], nonlinearity [60,61,62,63,64,65] and self-tuning method [66,67,68].

1.4.1 Multi-Frequency Harvester Array

As for the multi-frequency harvester array, the response bandwidth is broadened by the array harvesters with different natural frequencies due to the various dimensions of components, such as the mass, the beam length. In ambient vibration with time-varying frequency, the array energy harvesters can keep some of the beams reach its natural frequency, resulting in a wide operation frequency range [54,55]. Similarly, a PEH, which consists of linear array harvesters connected by linear springs, was proposed by Zhou *et al.* [56] as shown in Figure 1.10, the geometrical relationship and the time-varying relative displacement between two adjacent harvesters could promote the energy harvesting performance.

This method has been validated to be an effective way for enhancing energy harvesting performance. However, the array harvesters, with various tip masses and beam length, leads to increasing the volume and mass of the whole energy harvester, thus, the power density is reduced to a low level. In some situations, the limitation of space or mass, this method is not appreciable.

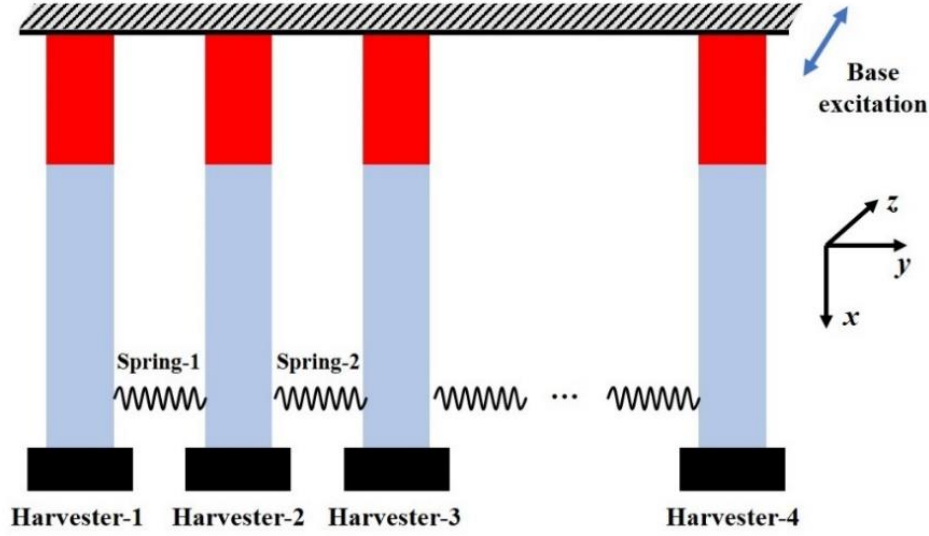


Figure 1.10 The structural diagram of the connected array harvesters. [56]

1.4.2 Frequency-up Conversion

Generally, the vibration or rotational motion in ambient is low in frequency, while most transducers requires high excitation for efficient operation. With the aim to achieve low-frequency energy from ambient energy, the excitation frequency can be increased by the frequency-up conversion method.

As for the energy harvesting in rotational motion, the plucking method including magnetic plucking and mechanical plucking has been proved to be effective in converting the low-frequency excitation of rotational motions to high frequency resonances of energy harvester. Zou *et al.* [58] proposed a magnetically coupled flextensional rotation energy harvester, as shown in Figure 1.11(a). Due to the rotational motion, a varying magnetic force is utilized to the flextensional transducer. In addition to this, Fang *et al.* [59] explored a rotational mechanical plucking energy harvesting as shown in Figure 1.11(b), in which the plucking force is transmitted on the piezoelectric beam via the plectrum of a rotating hub, thus achieving the frequency-up conversion.

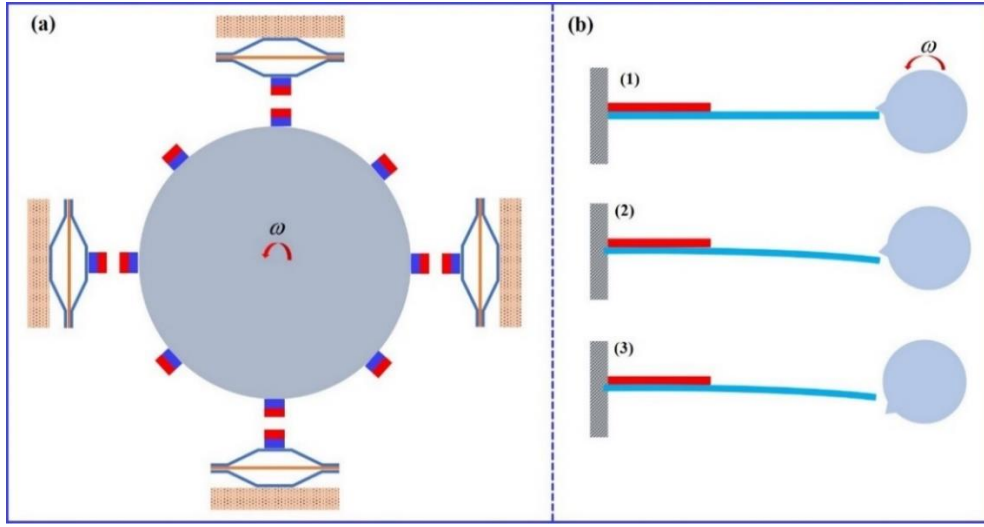


Figure 1.11 The schematic diagram of frequency-up conversion in rotational motion; (a) magnetic plucking [58]; (b) mechanical plucking [59].

1.4.3 Nonlinearity

As mentioned before, the task is to broaden the frequency bandwidth of energy harvesting. To this aim, the advantage of nonlinearity over linearity has been studied in Refs. [60,64,65]. A well-studied nonlinear energy harvester is shown in Figure 1.12, where the piezoelectric patches are attached at the fixed end of the cantilever beam and is connected to a resistive load. The electromechanical equations can be expressed as:

$$M\ddot{x}(t) + C\dot{x}(t) + F_r - \theta v(t) = -M\ddot{y}(t) \quad (1.10)$$

$$\theta\dot{x}(t) + C_p\dot{v}(t) + R_l^{-1}v(t) = 0 \quad (1.11)$$

where M is the equivalent mass, C is the mechanical damping coefficient, and F_r is the nonlinear restoring force.

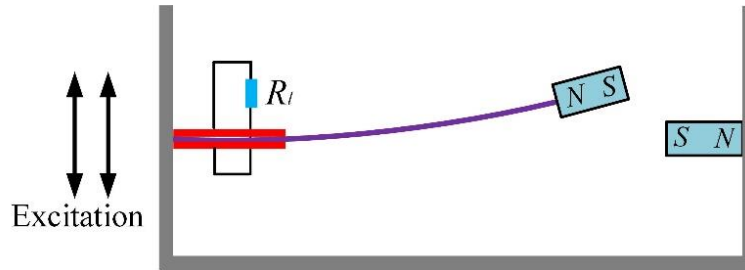


Figure 1.12 Nonlinear energy harvesting with bis-stable characteristics

The nonlinearity of a magnetically coupled can lead to mono-stable [69,70], bi-stable [71,72,73,74,75] and tri-stable [76,77,78,79,80,81] or multi-stable [82,83,84] characteristics, depending on the parameters of the system and the number of fixed external magnets. For the bi-stable PEH, it has the capability of inter-well oscillations from one potential well to another one, which results in high output power in low-frequency external excitations. Cottone *et al.* [71] explored a bi-stable PEH, and they numerically and experimentally demonstrated its advantages over the linear one under random excitations. Stanton *et al.* [72] presented the detailed derivation process of the theoretical model of a bi-stable PEH, and they numerically and experimentally validated the enhanced capabilities. Erturk *et al.* [73] and Litak *et al.* [74] investigated the performance of the bi-stable PEH, and they experimentally demonstrated the energy harvesting enhancement under harmonic and random excitations, respectively. Zheng *et al.* [75] investigated the stochastic resonance phenomenon in a bi-stable PEH, and they experimentally verified that the stochastic resonance was an effective way for enhancing energy harvesting performance. In case of tri-stable PEH, Zhou *et al.* [76] and Cao *et al.* [77] proposed a tri-stable PEH, and they experimentally validated its superior performance compared with the bi-stable PEH under the same excitation. Additionally, Zhu *et al.* [78] numerically and experimentally explored the effect of the potential well depth of the tri-stable PEH on energy harvesting performance with three categories, and their results demonstrated that the same potential barriers are better than other ones. To further improve the energy harvesting performance, Zhou *et al.* [82,83,84] focused on adding fixed external magnets to reduce the potential barriers, thus, the quad-stable characteristics were obtained. They experimentally verified the quad-stable PEH could realize the snap-through phenomena easier.

As for the nonlinear PEHs in rotational motion, the potential energy is time-varying in one cycle due to the gravity component of tip mass. Figure 1.13 illustrates the time-varying potential energy in rotational motion of a bi-stable PEH. Zhang *et al.* [52,53] explored a bi-stable PEH on the rim of a vehicle wheel, and they experimentally investigated the influence of rotational radius on the energy harvesting performance via real-vehicle tests. In addition to this, the stochastic resonance was explored to enhance the efficiency of energy harvesting in rotational motion. The experimental results indicated that the output power can be boosted to a higher level with mean power of 5.5 μW at the speed of 20 Km/h, due to the occurrence of stochastic resonance.

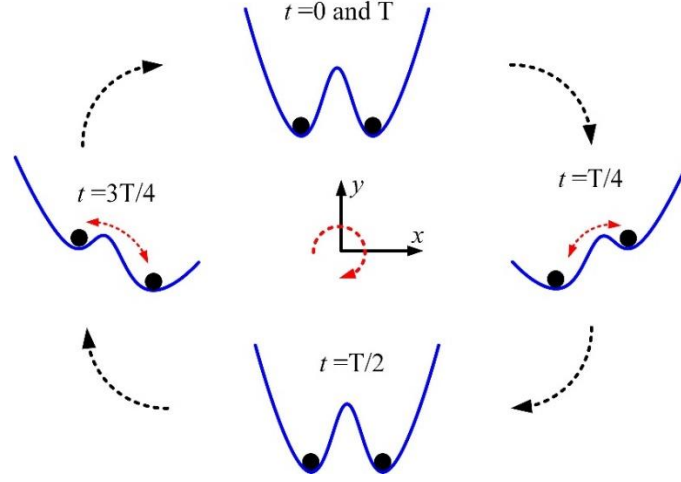


Figure 1.13 Time-varying potential energy in rotational motion in one cyclic variation; (1) Symmetric (2) asymmetric conditions.

Although the nonlinear piezoelectric energy harvesting via 31-model has been investigated in some studies, few of them considered the effect of rotational motion. As summarized by Ref. [3], the electromechanical coupling dynamics can be approximated as:

$$M\ddot{\delta} + C\dot{\delta} + K\delta - \Theta V = -Mg \cos(\omega t) \quad (1.12)$$

$$C_p \dot{V} + R_l^{-1} V + \Theta \dot{\delta} = 0 \quad (1.13)$$

where M , C and K are the equivalent mass, equivalent damping and equivalent stiffness, δ is the displacement of cantilever beam, Θ is the electromechanical coupling coefficient, C_p and R_l are the capacitance and load resistance. V is the generated voltage. ω is the rotational speed. And the gravity excitation is consistent with base excitation and excitation frequency is the rotational frequency. However, according to Eqs. (1.12) and (1.13), these governing equations are not suitable for the PEH in rotational motion, especially for high rotational speeds, because the centrifugal force, which has a great influence on the piezoelectric beam vibration, caused by the rotational motion is not considered. This issue will be solved and analyzed by this dissertation.

1.4.4 Self-tuning Harvester

According to the mass-spring-damper model, an obvious method for adjusting or tuning the resonance frequency of an energy harvester is to change the proof mass, structural dimensions or material properties, so that the equivalent mass [85,86,87] or equivalent stiffness [66,68,88,89,90,91] can be altered. Recently, both active and passive tuning methods have been

widely investigated. Although the active tuning method successfully broadens the frequency bandwidth of the PEHs, it requires the use of external power or manual shift, thereby it will reduce the real energy harvesting efficiency. Some examples of passive tuning method also have been explored. Kozinsky *et al.* [91] used the string models to alter the position of a free ball to change the resonance frequency. Gu *et al.* [66] reported a passive-tuned energy harvester that was radially oriented mounted at a distance r from the axis of beam. As the rotational speed varies, the corresponding tension due to the centrifugal force on the beam adjusts the resonance frequency of the beam so that the harvester always works at or near its resonance frequency. And their experimental results demonstrated the self-tuning performance of achieving 11 Hz bandwidth compared with the untuned PEH. The same author also presented an impact-based PEH that also works as a self-tuning advice with an optimized design. Later, Liu *et al.* [68] investigated a passive self-tuning energy harvester in rotational motion as shown in Figure 1.14, via the centrifugal force to increase the axial tension and decrease the length of the harvester, which results in the increase of resonance frequency simultaneously.

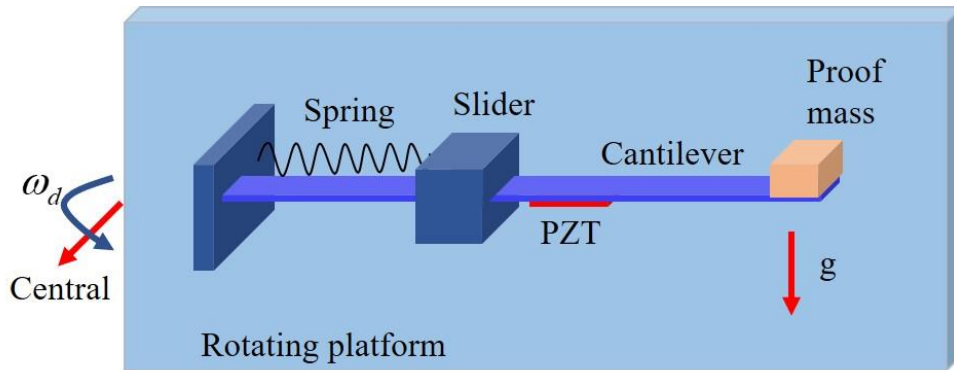


Figure 1.14 Schematic diagram of the self-tuning energy with length tuning. [68]

1.5 Existing Issues and Challenges

Although the energy harvesting in rotational motion has achieved great enhancements as summarized in above sections, some issues are still existing as follows:

- (1) Firstly, in previous studies of PEHs in rotational motion, the effect of rotational motion was not considered in their theoretical models, in other word, the effect of the centrifugal force was neglected. However, the centrifugal force has a great influence on energy harvesting performance of the PEHs in rotational motion, especially for high rotational speed.
- (2) Secondly, although in few studies [52,53,66] the centrifugal force has been considered in their

theoretical models, in order to calculate the transverse component of the centrifugal force, the lumped-parameter model and the small deformation assumption were utilized. However, for a nonlinear energy harvester, the tip mass may experience the large-amplitude inter-well oscillations.

(3) Thirdly, due to the difficulties of wire connections and sensors installations in rotational motion, most of previous studies [49,50] only measured the output voltage under low rotational speeds to verify their theoretical models. It results in some phenomena of the dynamic performance being missed.

(4) Lastly, among the proposed PEHs, few studies focus on the energy harvesting from low-frequency rotational motion.

Apart from the abovementioned issues, some challenges also exist. (1) The nonlinearity of PEHs is mainly caused by the magnetically coupled configurations, thus, how to precisely calculate the nonlinear magnetic force is also. (2) In the rotational motion, it is difficult to measure the tip displacement due to the foreshortening quantity caused by the bending of the cantilever beam, consequently the author decide to measure the dynamic response at one position of the piezoelectric beam to qualitatively validate the dynamic performance of a PEH.

1.6 Motivation and Objective

1.6.1 Motivation

In order to solve the above issues, the motivation of this dissertation is to build the methodology for the PEHs in rotational motion, in which the advantages of the centrifugal force and lower potential barriers of multi-stable system are combined for energy harvesting enhancement.

1.6.2 Objective

Additionally, the main objectives of this dissertation are highlighted as follows:

- (1) To establish a theoretical model for multi-stable PEHs in rotational motion, in which the rotational coefficients, including the angular displacement, angular velocity and angular acceleration, are coupled in their governing equations.
- (2) To explore the influence of potential barriers and centrifugal force acting on the tip mass on energy harvesting performance of a multi-stable PEH in rotational motion.
- (3) To design a self-tuning PEH the centrifugal stiffening effect to broaden effective frequency

range in rotational motion.

(4) To design a PEH utilizing the centrifugal softening effect to enhance energy harvesting performance.

1.7 Dissertation Overview

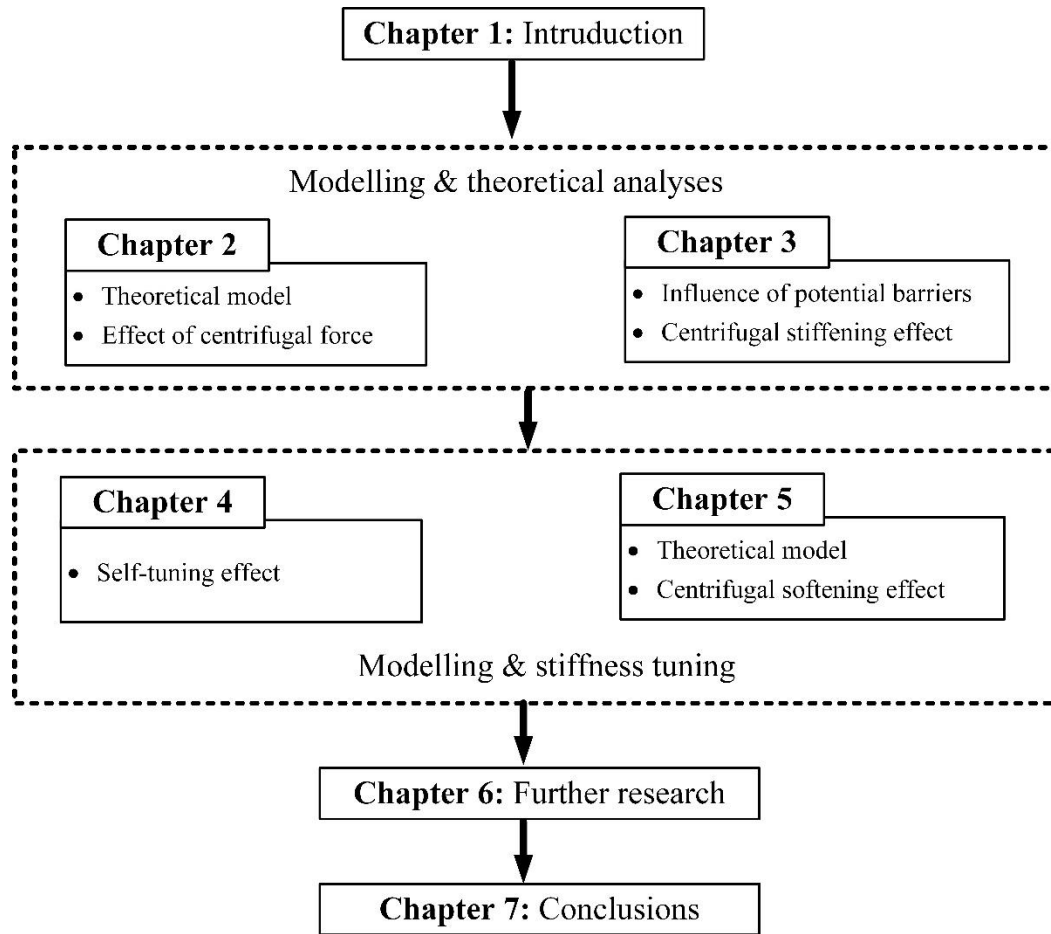


Figure 1.15 The structure of this doctoral dissertation.

In summary, the structure of this doctoral dissertation is shown in Figure 1.15. The details will be illustrated as follows:

In Chapter 1, the background of this research work, including the existing methods of the piezoelectric, electromagnetic, electrostatic and triboelectric effect for energy harvesting, are introduced by enumerating the progresses in recently studies. Meanwhile, Chapter 1 summarizes the methods of broadening frequency bandwidth, which includes the multi-frequency harvester

array, frequency-up conversion, nonlinearity and self-tuning methods. Next, the existing issues and challenges are summarized, and the motivation and objective of this dissertation are presented.

In Chapter 2, the theoretical model of a nonlinear PEH in rotational motion is derived in a rotational coordinate system. Additionally, the calculation of nonlinear magnetic force among the energy harvester is derived via the dipole-dipole method, which is also an important but challenging part for theoretical model. Furthermore, with the aim to validate the effect of rotational motion, the theoretical analyses between with and without consideration of rotational motion in theoretical models are conducted. The experimental results demonstrate that the centrifugal force related to the rotational motion has great effect on the energy harvesting especially for high rotational speed.

In Chapter 3, based on the proposed theoretical model, in order to investigate the influence of the potential barriers on the energy harvesting performance, the bi-stable, symmetrical and asymmetrical tri-stable, and quad-stable PEHs are presented. Theoretically and experimentally validations are carried out to test their dynamic performance under various constant rotational speeds. Most importantly, one interesting phenomenon is that at high rotational speeds (more than 440 rpm), all the proposed energy harvesters experience the centrifugal stiffening effect, namely, the centrifugal force acting on the tip mass reduces the dynamic performance of piezoelectric beam, which results in low output voltages with the increase of rotational speed. However, the centrifugal stiffening effect provides a feasibility for achieving a self-tuning energy harvester, and the further details will be discussed in next chapter.

In Chapter 4, according to the centrifugal stiffening effect, it is found that the resonance frequency of the energy harvester is increasing with the increase of rotational speed. To utilize this phenomenon, the principle of passively self-tuning energy harvester is theoretically analysed. Then the effect of system parameters, including the rotational radius r , beam length L and tip mass M_e , on achieving a self-tuning harvester is analysed. The bi-stable and tri-stable self-tuning energy harvesters have been validated in experiments with different rotational radiuses, respectively. Lastly, the parameter optimization is conducted to broaden the perfect match region of self-tuning effect, which provides the theoretical guidance for the further design of self-tuning energy harvester.

In Chapter 5, as mentioned in above chapters, the performance of all proposed energy harvesters is still not desirable under low-frequency rotational motion, such as the wind turbine. To overcome this challenge, inspired by the centrifugal stiffening effect, utilizing the centrifugal softening effect by inversely installing a PEH in rotational motion can be a promising way to achieve low-frequency energy harvesting. Firstly, the related theoretical model is derived also in a rotational

coordinate system, then theoretical analyses and experimental validations are conducted to verify the advantage of centrifugal softening effect.

In Chapter 6, the further research and discussion are presented. The centrifugal stiffening and softening effects of different nonlinear energy harvesters are theoretically and experimentally in above chapters. Additionally, one of the potential applications is the TPMS of a vehicle (centrifugal stiffening effect) or the wind turbine (centrifugal softening effect). As for the energy harvester installed in a vehicle wheel, the translation motion (running motion) and rotational motion should be considered in the theoretical model. Thus, the further research works, including the modelling and real-vehicle test, will be conducted in future research. After that, in order to achieve a self-powered sensor by combining the proposed nonlinear PEH and a wireless sensor used for structural health monitoring, the rectifier circuit for the proposed nonlinear energy harvester in rotational motion will be designed. In addition to this, the discussion of optimal design for the centrifugal stiffening effect and softening effect are discussed for the further research.

In Chapter 7, the conclusions and significances of this dissertation are summarized and presented.

Chapter 2

Methodology for Energy Harvesting in Rotational motion

2. Modelling for Nonlinear Energy Harvester in Rotational Motion

As summarized in Chapter 1, few of previous studies considered the effect of rotational motion in their theoretical models. Namely, the centrifugal force, which has a great influence on the dynamic performance of a piezoelectric energy harvester (PEH) especially for high rotational speed, was neglected. To fill these gaps, the new theoretical model considering the effect of rotational motion will be derived in a rotational coordinate system. It should be noted that Chapter 2 is also the theoretical foundation of the whole doctoral dissertation.

2.1 Design and Operating Principle

The schematic configuration of the proposed nonlinear PEH in rotational environment, which is composed of a cantilever beam with a tip mass (magnet A) and some external fixed magnets on the frame, is shown in Figure 2.1. The cantilever beam is mounted on a rotating hub. Two uni-morph piezoelectric patches are installed at its fixed end of the cantilever beam. Note that whole of them are called the piezoelectric beam in this doctoral dissertation. In practical operation, the nonlinear PEH will be mounted on a vertical plate structure, such as the vehicle wheel, machine and wind turbine, as shown in Figure 2. 1(b). When it rotates in the vertical plate, the gravity component of the tip mass can produce a periodic exciting force for the piezoelectric beam vibration. Based on the direct piezoelectric effect of 31- mode [92,93], vibration energy can be converted into electric energy to provide the power supply for the wireless sensors.

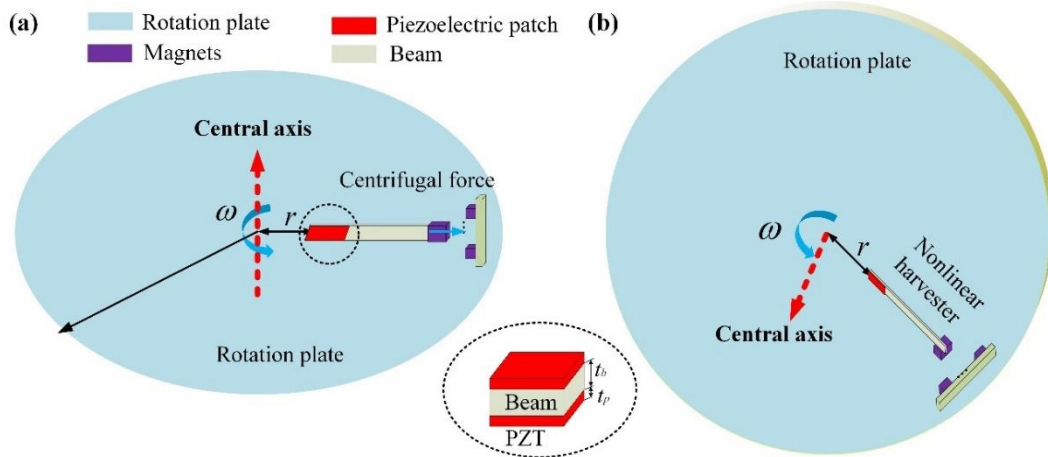


Figure. 2.1 (a) The schematic view of the nonlinear energy harvester in rotational motion; (b) the schematic diagram of the nonlinear energy harvester installed on a vertical rotation wheel.

Figure 2.2(a) represents the schematic diagram of the nonlinear PEH in rotational motion with the base excitation. Both the excitation and the rotational motion can enforce the piezoelectric beam vibration. In Figure 2.2 (b), r denotes the rotational radius. d is the separation between the surface of the tip magnet and that of the external magnets. It is worth mentioning that the tip mass is a permanent magnet which is oriented with opposite polarity to the external ones. Depending on the number of magnets and configuration parameters of the PEH, the mono-stable, bi-stable, tri-stable or multi-stable characteristics will exhibit. In summary, the nonlinear magnetic force resulting in different potential functions can lead to complexed dynamic performance.

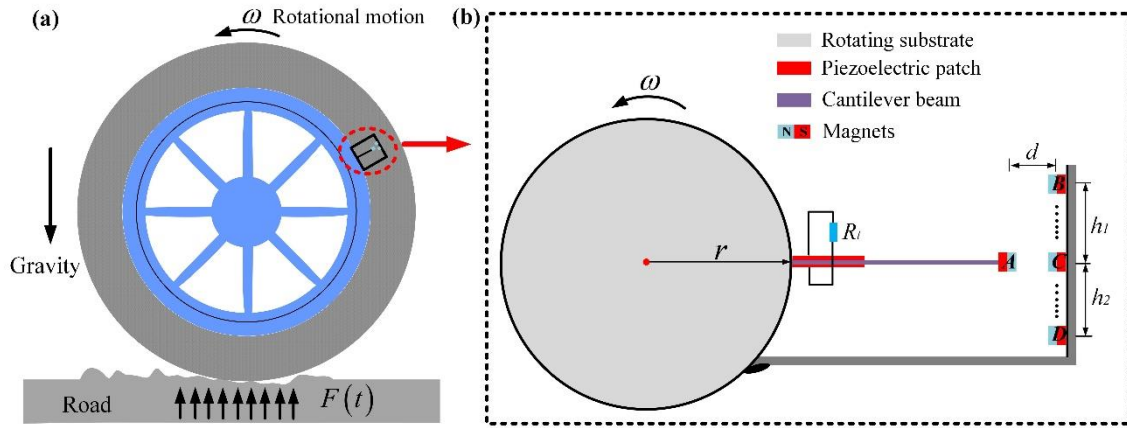


Figure 2.2 (a) The harvester installed in rotational motion with base excitation; (b) the schematic diagram of the nonlinear piezoelectric energy in rotational motion.

2.2 Coordinate Transformation

With the aim to the derive related theoretical mode in rotational coordinate system, the relationship between the rotational and fixed coordinate systems is investigated firstly. And their schematic diagrams are shown in Figure 2.3.

As observed from Figure 2.3(a), it is the view from positive direction of Z axis. XYZ is the inertial coordinate system with the unit vectors i , j and k in X , Y and Z axis, respectively. The $X^*Y^*Z^*$ is the rotational coordinate system with its central axis at angular velocity $\omega = \dot{\theta}k$, including the unit vectors i^* , j^* and k^* in X^* , Y^* and Z^* axis, respectively.

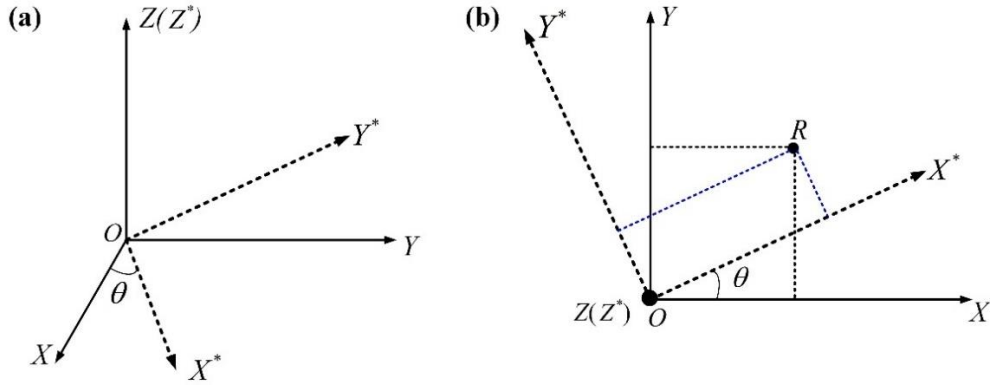


Figure 2.3 The relationship between XYZ and $X^*Y^*Z^*$ coordinate systems; (a) the three-dimensional schematic diagram; (b) the XOY plate and X^*OY^* .

Arbitrary point in the vertical plane can be expressed by two coordinate systems:

$$\mathbf{R} = x\mathbf{i} + y\mathbf{j} + z\mathbf{k} = x^*\mathbf{i}^* + y^*\mathbf{j}^* + z^*\mathbf{k}^* \quad (2.1)$$

Therefore, the relationship between unit vectors in two coordinate systems can be written as:

$$\mathbf{i}^* = \cos\theta\mathbf{i} + \sin\theta\mathbf{j} \quad (2.2a)$$

$$\mathbf{j}^* = -\sin\theta\mathbf{i} + \cos\theta\mathbf{j} \quad (2.2b)$$

$$\mathbf{k}^* = \mathbf{k} \quad (2.2c)$$

The differential of position vector \mathbf{R} with respect to time, namely the velocity of position, can be derived from Eq. (2.1) and expressed as:

$$\frac{d\mathbf{R}}{dt} = \frac{dx}{dt}\mathbf{i} + \frac{dy}{dt}\mathbf{j} + \frac{dz}{dt}\mathbf{k} = \frac{dx^*}{dt}\mathbf{i}^* + \frac{dy^*}{dt}\mathbf{j}^* + \frac{dz^*}{dt}\mathbf{k}^* + x^*\frac{d\mathbf{i}^*}{dt} + y^*\frac{d\mathbf{j}^*}{dt} + z^*\frac{d\mathbf{k}^*}{dt} \quad (2.3)$$

Note that $\left(\frac{d\mathbf{R}}{dt}\right)_I$ and $\left(\frac{d\mathbf{R}}{dt}\right)_R$ are the time differentiation in an inertial and rotational coordinate

systems, respectively. Thus, the time differentiation in the inertial coordinate system XYZ can be defined as:

$$\left(\frac{d\mathbf{R}}{dt}\right)_I = \frac{dx}{dt}\mathbf{i} + \frac{dy}{dt}\mathbf{j} + \frac{dz}{dt}\mathbf{k} \quad (2.4)$$

Additionally, if we view in the rotational coordinate system $X^*Y^*Z^*$, the time differentiation in it can be also defined as:

$$\left(\frac{d\mathbf{R}}{dt}\right)_R = \frac{dx^*}{dt}\mathbf{i}^* + \frac{dy^*}{dt}\mathbf{j}^* + \frac{dz^*}{dt}\mathbf{k}^* \quad (2.5)$$

Based on Eq. (2.2), the time differentiation of unit vectors in the rotational coordinate system can be written in inertial coordinate system as:

$$\left(\frac{d\mathbf{i}^*}{dt}\right)_I = \frac{d}{dt}(\cos\theta\mathbf{i} + \sin\theta\mathbf{j}) = -\dot{\theta}\sin\theta\mathbf{i} + \dot{\theta}\cos\theta\mathbf{j} = \dot{\theta}\mathbf{j}^* = \dot{\theta}\mathbf{k}^* \times \mathbf{i}^* \quad (2.6)$$

$$\left(\frac{d\mathbf{j}^*}{dt}\right)_I = \frac{d}{dt}(-\sin\theta\mathbf{i} + \cos\theta\mathbf{j}) = -(\dot{\theta}\cos\theta\mathbf{i} + \dot{\theta}\sin\theta\mathbf{j}) = -\dot{\theta}\mathbf{i}^* = \dot{\theta}\mathbf{k}^* \times \mathbf{j}^* \quad (2.7)$$

Lastly, according to Eqs. (2.4)- (2.7), Eq. (2.2) can be expressed in the inertial coordinate system:

$$\left(\frac{d\mathbf{R}}{dt}\right)_I = \left(\frac{d\mathbf{R}}{dt}\right)_R + \dot{\theta}(x^*\mathbf{j}^* - y^*\mathbf{i}^*) = \left(\frac{d\mathbf{R}}{dt}\right)_R + \dot{\theta}\mathbf{k}^* \times \mathbf{R} \quad (2.8)$$

2.3 Mathematical Modelling

For the theoretical model of the PEH, Erturk and Inman [33] presented a comprehensive review of different theoretical models and the related ensuing issues. Various theoretical models, including the distributed and lumped parameter models, have been explored by the previous studies in Refs. [48,66,69,]. However, for the harvesters in rotational motion, most researchers adopted the theoretical models of the PEH in the rectilinear motion. Additionally, most of them in experiments only measured the output voltage to verify their theoretical models, but they did not measure the dynamic performance of the harvesters. Thus, an accurate theoretical model should be derived for the harvester in rotational motion, and corresponding experiments should be conducted to validate the theoretical model via measuring the dynamic performance and output voltage.

Based on the foundations in section 2.2, next the theoretical model of the nonlinear PEH, which is related to the mechanical deformation and the rotational motion, will be derived. Figure 2.4 is the schematic diagram of the nonlinear PEH in rotational motion. XYZ is a fixed coordinate system, and the $X^*Y^*Z^*$ is a rotational coordinate system, namely, both of them are defined as the inertial frame and the reference frame, respectively. Note that Z axis, forming the rotational axis of the hub pointing out of the vertical plane, is parallel to Z^* axis all the times. This study mainly focuses on the deformation of the piezoelectric beam in the transverse direction, which is always changing due to the rotational motion as shown in Figure 2.4. Thus, the theoretical model should be established in the rotational coordinate system $X^*Y^*Z^*$. R is assumed to be the position P_0 of an infinitesimal segment on the beam in the rotational coordinate system.

$\theta = \int_0^t \omega dt$, defined as the angle subtended by X axis and X^* axis as shown in Figure 2.4, is

the angular displacement of the hub. Furthermore, L is the length of the cantilever beam. $w(x,t)$ and $u(x,t)$ are the transverse displacement and axial deformation associated with the distance x the time t of the piezoelectric beam.

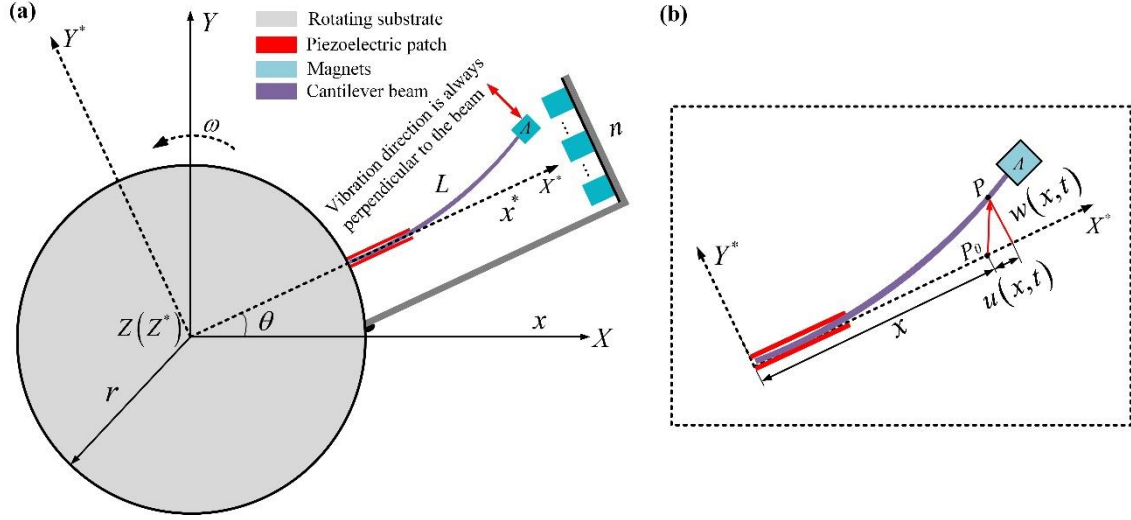


Figure 2.4 (a) The schematic diagram of the nonlinear PEH in a rotational coordinate system; (b) the piezoelectric beam description of deformation.

2.3.1 Kinetic Energy Description

The following relationship can be obtained based on the geometrical relations shown in Figure 2.4:

$$\mathbf{R} = [x + r + u_a(x,t) + \Delta x] \mathbf{i}^* + w(x,t) \mathbf{j}^* \quad (2.9)$$

where \mathbf{i}^* , \mathbf{j}^* and \mathbf{k}^* are the unit vectors of the rotational coordinate system along X^* , Y^* and Z^* axis, respectively. $(\bullet)'$ refers to $\partial/\partial x$. $u_a(x,t)$ represents the pure axial deformation.

Δx , represented as [94] $\Delta x = -\frac{1}{2} \int_0^x [w'(x,t)]^2 dx$, is the deformation associated with the foreshortening quantity due to the pure transverse deformation $w(x,t)$. In order to simplify the analyses, $u(x,t) = u_a(x,t) - \frac{1}{2} \int_0^x [w'(x,t)]^2 dx$ is defined in subsequent derivations.

Therefore, ignoring the high order small quantities, the velocity of an infinitesimal segment of the harvester can be written as [45,46,49]:

$$\dot{\mathbf{R}} = \left(\frac{d\mathbf{R}}{dt} \right)_R + \dot{\theta} \mathbf{k}^* \times \mathbf{R} = -w(x,t) \dot{\theta} \mathbf{i}^* + \left[\dot{w}(x,t) + (x+r+u(x,t)) \dot{\theta} \right] \mathbf{j}^* \quad (2.10)$$

where the overdot denotes the derivative with respect to time. Thus, the whole kinetic energy of the harvester can be expressed as:

$$T = \frac{1}{2} m \int_0^L \dot{R}_1^2 dx + \frac{1}{2} M \dot{R}_A^2 + \frac{1}{2} J_A \dot{w}'(L,t)^2 \quad (2.11)$$

where m is the mass of piezoelectric beam per unit length, and M is the mass of tip magnet. J_A is the inertia moment of the tip mass.

$$m = \begin{cases} m_1 = \rho_b A_b + 2\rho_p A_p, & 0 \leq x < l_p \\ m_2 = \rho_b A_b, & l_p \leq x \leq L \end{cases} \quad (2.12)$$

where A_b and ρ_b are the cross-sectional area and the material density of the cantilever beam, respectively. l_p , A_p and ρ_p are the length, the cross-sectional area and the material density of piezoelectric patches, respectively.

Therefore, the velocity of the piezoelectric beam and the tip mass can be respectively expressed as:

$$\dot{R}_1^2 = \dot{\theta}^2 w^2(x,t) + \left[\dot{w}(x,t) + (x+r+u(x,t)) \dot{\theta} \right]^2 \quad (2.13a)$$

$$\dot{R}_A^2 = \dot{\theta}^2 w^2(L,t) + \left[\dot{w}(L,t) + (L+r+u(L,t)) \dot{\theta} \right]^2 \quad (2.13b)$$

For the tip mass, $x=L$, thus, the tip displacement and axial deformation are represented as $w(L,t)$ and $u(L,t)$, respectively. Substituting Eqs. (2.12) - (2.13b) into Eq. (2.11), the whole kinetic energy of the harvester can be rewritten as:

$$T = \frac{1}{2} m \int_0^L \left\{ \dot{\theta}^2 w^2(x,t) + \left[\dot{w}(x,t) + (x+r+u(x,t)) \dot{\theta} \right]^2 \right\} dx + \frac{1}{2} J_A \dot{w}'(L,t)^2 + \frac{1}{2} M \left\{ \dot{\theta}^2 w^2(L,t) + \left[\dot{w}(L,t) + (L+r+u(L,t)) \dot{\theta} \right]^2 \right\} \quad (2.14)$$

Note that the theoretical model of the proposed tri-stable PEH in rotational motion are derived based on the following assumptions. Firstly, the piezoelectric beam has a slender shape so that the shear and rotary inertia effect are neglected [96,97]. Secondly, as pointed out in Refs. [45,46,49,97,98,99], the bending motion of the piezoelectric beam, under not high rotational motion, will not induce a significant axial motion, thus, for simplicity the axial motion will be neglected in the kinetic energy description. However, it will be considered in the potential energy caused by the centrifugal force.

2.3.2 Potential Energy Description

For a PEH, the potential energy is the sum of the elastic energy U_e of the piezoelectric beam, the gravitational potential energy U_g , the centrifugal potential energy U_c and the magnetic potential energy U_m . Therefore, it can be written as:

$$U = U_e + U_g + U_c + U_m \quad (2.15)$$

According to the Euler-Bernoulli beam theory, the potential energy of the piezoelectric beam due to the bending and axial deformation is given by [95,96,97]:

$$U_e = \frac{1}{2} \int_0^L EI [w''(x,t)]^2 dx + \frac{1}{2} \int_0^L EA [u_a''(x,t)]^2 dx \quad (2.16)$$

where $()''$ refers to $\partial/\partial x^2$, and g is the gravitational acceleration (9.8 m.s^{-2}). EI and EA are the bending and axial rigidity of the piezoelectric beam, respectively, and they are expressed by [56]:

$$EI = \begin{cases} EI_1 = \frac{1}{12} E_b b t_b^3 + 2E_p b_p \left(\frac{t_p^3}{3} + \frac{t_p^2 t_b}{2} + \frac{t_p t_b^2}{4} \right), & 0 \leq x < l_p \\ EI_2 = \frac{1}{12} E_b b t_b^3, & l_p \leq x \leq L \end{cases} \quad (2.17)$$

$$EA = \begin{cases} EA_1 = E_b b t_b + 2E_p b_p t_p, & 0 \leq x < l_p \\ EA_2 = E_b b t_b, & l_p \leq x \leq L \end{cases} \quad (2.18)$$

where E_b and E_p are the Young's modulus, b and b_p are the width, t_b and t_p are the thickness of the cantilever beam and the piezoelectric patches, respectively.

The gravitational potential energy of the nonlinear PEH is given by [96,98,99]:

$$U_g = mg \int_0^L [(x+r) \sin \theta + w(x,t) \cos \theta] dx + Mg [(L+r) \sin \theta + w(L,t) \cos \theta] \quad (2.19)$$

The potential energy in the magnetic configuration is expressed as:

$$U_m = \oint F_m dx \quad (2.20)$$

Firstly, the potential energy caused by the centrifugal force is expressed as:

$$U_c = \int_0^L f_c(x,t)(ds - dx) \quad (2.21)$$

where $f_c(x,t)$ is an axial force arising from the centrifugal effect and Eq. (2.21) represents the

work done by this force. s is the arc length along the deformed center-line of the beam. Considering the equilibrium of the differential element shown in Figure 2.4, we can conclude that $\Delta P = m\Delta x(r+x)\dot{\theta}^2$, thus, Eq. (2.21) can be rewritten as:

$$f_c(x,t) = \int_x^L m(r+x)\dot{\theta}^2 dx + M(r+L)\dot{\theta}^2 \quad (2.22)$$

For a piezoelectric beam with a tip mass, Eq. (2.22) can be reduced to

$$f_c(x,t) = \frac{1}{2}m(L^2 - x^2)\dot{\theta}^2 + mr(L-x)\dot{\theta}^2 + M(r+L)\dot{\theta}^2 \quad (2.23)$$

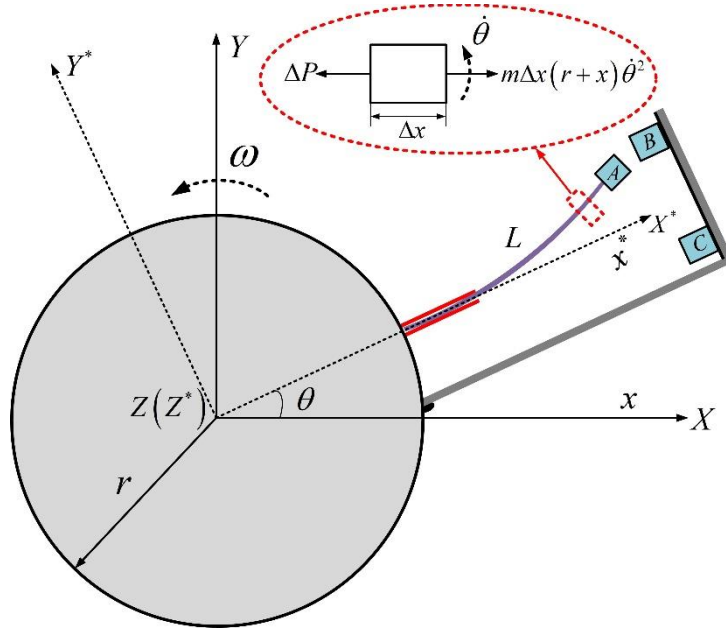


Figure 2.5 A differential beam element of the piezoelectrical beam in rotational motion.

According to the geometrical relations as shown in Figure 2.5, the relationship can be concluded as $ds - dx = \sqrt{(dx)^2 + [w'(x,t)dx]^2}$. Based on the binomial theorem, it can be approximated by

$ds - dx = \frac{1}{2}[w'(x,t)]^2 dx$, therefore, Eq. (2.21) can be rewritten as:

$$U_c = \frac{1}{2} \int_0^L \left[\frac{1}{2}m(L^2 - x^2)\dot{\theta}^2 + mr(L-x)\dot{\theta}^2 + M(r+L)\dot{\theta}^2 \right] [w'(x,t)]^2 dx \quad (2.24)$$

The internal electric energy in the piezoelectric patch is calculated as follows:

$$W_e = \int_0^{l_p} \mathcal{G}_{p_1} v(t) w''(x,t) dx + \frac{1}{2} C_p v(t)^2 \quad (2.25)$$

where $v(t)$ is the generated voltage across the electric load. As presented in Ref. [34], \mathcal{G}_{p1} is the electromechanical coupling coefficient. C_p is the internal capacitance of the piezoelectric patches, and ε_{31} is the piezoelectric material permittivity.

2.3.3 Tip displacement Separation

For the vibration response, according to the Galerkin's concept, the transverse displacement $w(x, t)$ can be written as:

$$w(x, t) = \sum_{i=1}^n \phi_i(x) q_i(t) \quad (2.26)$$

where $q_i(t)$ is a time-dependent generalized temporal coordinate, and $\phi_i(x)$ is the first order mode shape function of the piezoelectric beam. In this doctoral dissertation, assuming the mass of the tip magnet A is larger than that of the piezoelectric beam, thus, the single-mode approximation of the piezoelectric beam deformation is enough [49]. Taking into consideration of the geometric change caused by two piezoelectric patches, the orthogonal basis function $\phi(x)$ should be expressed by:

$$\phi(x) = \begin{cases} \phi_1(x), & 0 \leq x < l_p \\ \phi_2(x), & l_p \leq x \leq L \end{cases} \quad (2.27)$$

For brevity, the solutions for the two-beam section $\phi(x)$, which should satisfy the corresponding compatibility and the boundary conditions. Due the installation of piezoelectric patches, we can assume the shape model $\phi(x)$ of the harvester as two different parts $\phi_1(x)$ and $\phi_2(x)$ respectively, as follows [56,49]:

$$\phi_1(x) = A_1 \sin \beta_1 x_1 + B_1 \cos \beta_1 x_1 + C_1 \sinh \beta_1 x_1 + D_1 \cosh \beta_1 x_1 \quad \text{for } 0 \leq x_1 < l_p \quad (2.28)$$

$$\phi_2(x) = A_2 \sin \beta_2 x_2 + B_2 \cos \beta_2 x_2 + C_2 \sinh \beta_2 x_2 + D_2 \cosh \beta_2 x_2 \quad \text{for } l_p \leq x_2 \leq L \quad (2.29)$$

where A_i , B_i , C_i and D_i ($i=1,2$) are constants to be determined, as follows:

$$\omega_n = \beta_1^2 \sqrt{\frac{EI_1}{m_1}} = \beta_2^2 \sqrt{\frac{EI_2}{m_2}} \quad (2.30)$$

Assuming the piezoelectric beam of the proposed PEH to meet Euler-Bernoulli beam assumption, the corresponding continuous condition of the displacement, the rotation angle, the bending

moment and the shear force are defined as [100]:

$$\phi_1(0)=0 \quad (2.31a)$$

$$\phi_1'(0)=0 \quad (2.31b)$$

$$\phi_1(l_p)=\phi_2(l_p) \quad (2.31c)$$

$$\phi_1'(l_p)=\phi_2'(l_p) \quad (2.31d)$$

$$EI_1\phi_1''(l_p)=EI_2\phi_2''(l_p) \quad (2.31e)$$

$$EI_1\phi_1'''(l_p)=EI_2\phi_2'''(l_p) \quad (2.31f)$$

The boundary condition of the tip mass [49,101,102,103]:

$$EI_2\phi_2''(L)=\omega_n^2 ML_A\phi_2(L)+\omega_n^2 (ML_A^2 + I_t)\phi_2'(L)-ML_A\ddot{\theta} \quad (2.32a)$$

$$EI_2\phi_2'''(L)=-\omega_n^2 M\phi_2(L)-\omega_n^2 ML_A\phi_2'(L)+ML_A\ddot{\theta} \quad (2.32b)$$

2.3.4 Governing Equations Description

Based on the kinetic energy and potential energy, the Lagrange function of the harvester can be defined as:

$$\mathcal{L}(w,v)=T-U+W_e \quad (2.33)$$

In the next subsection, this function will be used to obtain electromechanical equations of the PEH in rotational motion. Regardless of the mechanical losses, the virtual work done by the non-conservative forces, including the dissipation of the damping force and the electrical load resistance, can be written as:

$$\delta W = -\int_0^L c\dot{w}(x,t)\delta w(x,t)dx - Q(t)\delta v(t) \quad (2.34)$$

According to the extended Hamilton principle, the electromechanical equations are written as:

$$\frac{d}{dt}\left(\frac{\partial \mathcal{L}}{\partial \dot{q}}\right) - \frac{\partial \mathcal{L}}{\partial q} = P(t) \quad (2.35a)$$

$$\frac{d}{dt}\left(\frac{\partial \mathcal{L}}{\partial \dot{\lambda}}\right) - \frac{\partial \mathcal{L}}{\partial \lambda} = I(t) \quad (2.35b)$$

where $P(t) = -C\dot{q}(t)$ is the generalized force due to the non-conservative force acting on the

piezoelectric beam. $I(t)$ is the electric output charge of the piezoelectric patches ($\dot{\lambda}=v(t)$) and $I(t)=-v(t)/R_l$, where R_l is the load resistance.

Finally, by utilizing the Lagrange function, the electromechanical equations of the proposed harvester can be expressed as:

$$M_e \ddot{q}(t) + C \dot{q}(t) + (K_e + K_c \dot{\theta}^2) q(t) + \chi \ddot{\theta} - \mathcal{G}_p v(t) + F_m = [-\Gamma g + F(t)] \cos \theta \quad (2.36a)$$

$$C_p \dot{v}(t) + R_l^{-1} v(t) + \mathcal{G}_p \dot{q}(t) = 0 \quad (2.36b)$$

where M_e is the equivalent mass. C is the mechanical damping coefficient. K_e is the equivalent stiffness of the piezoelectric beam. Additionally, θ , $\dot{\theta}$ and $\ddot{\theta}$ are the angular displacement, angular velocity and angular acceleration of the rotational motion, respectively. K_c , which represents the coefficient of equivalent centrifugal force, is the coefficient of the coupling term $\dot{\theta}^2 q(t)$. χ is the coefficient of the angular acceleration. Γg is the equivalent excitation from the gravity of the tip mass due to the rotational motion. Furthermore, $F(t)$ refers to the external excitation, such as the road-wheel interaction of the vehicle tire application. F_m is the nonlinear magnetic force along the transverse direction of the piezoelectric beam. The details of above coefficients are given as follows:

$$M_e = m \int_0^L \phi(x)^2 dx + M \phi(L)^2 + \frac{1}{2} J_A \phi'(x)^2 \Big|_{x=L} \quad (2.37a)$$

$$K_e = EI \int_0^L \phi''(x)^2 dx \quad (2.37b)$$

$$K_c = m \left(r \int_0^L (L-x) \phi'(x)^2 dx + \frac{1}{2} \int_0^L (L^2 - x^2) \phi'(x)^2 dx - \int_0^L \phi(x)^2 dx \right) + M \left[(L+r) \int_0^L \phi'(x)^2 dx - \phi(L)^2 \right] \quad (2.37c)$$

$$\chi = M (L+r) \phi(L) + m \int_0^L \phi(x) (x+r) dx \quad (2.37d)$$

$$\mathcal{G}_p = \mathcal{G}_{p1} \int_0^{l_p} \phi''(x) dx \quad (2.37e)$$

$$\Gamma = M \phi(L) + m \int_0^L \phi(x) dx \quad (2.37f)$$

$$C = c \int_0^L \phi(x) dx \quad (2.37g)$$

Most importantly, from the right side of Eq. (2.36a), it is obvious that the component gravity of tip mass will produce a periodic exciting force for the piezoelectric beam vibration due to the rotational motion. Additionally, an interesting observation from Eq. (2.36a) is that the term $K_c \dot{\theta}^2$

varies with the rotational speed. It also can be validated that it is non-negative, which implies that the rotational motion will stiffen the piezoelectric beam of a PEH. It is worth mentioning that the proposed theoretical model of Eqs. (2.36a) and (2.36b) are suitable for the linear and nonlinear PEHs in rotational motion. For the linear PEH, the magnetically coupled term $F_m = 0$ in Eq. (2.36a). While for the nonlinear one, the term F_m is the nonlinear force. The further details will be introduced in the Chapter 3 and Chapter 4.

2.4 Calculation of Magnetic Force

In the study of the magnetically coupled nonlinear PEHs, it is important but challenging to precisely calculate the nonlinear magnetic force, which is directly related to the dynamic response of the harvester under exactions. In this section, the modelling of calculating magnetic force will be conducted. Note that with the aim to calculate the nonlinear magnetic force, the permanent magnets can be regarded as dipole-dipole [104,105,106].

2.4.1 Repulsive Configuration in Radial Direction

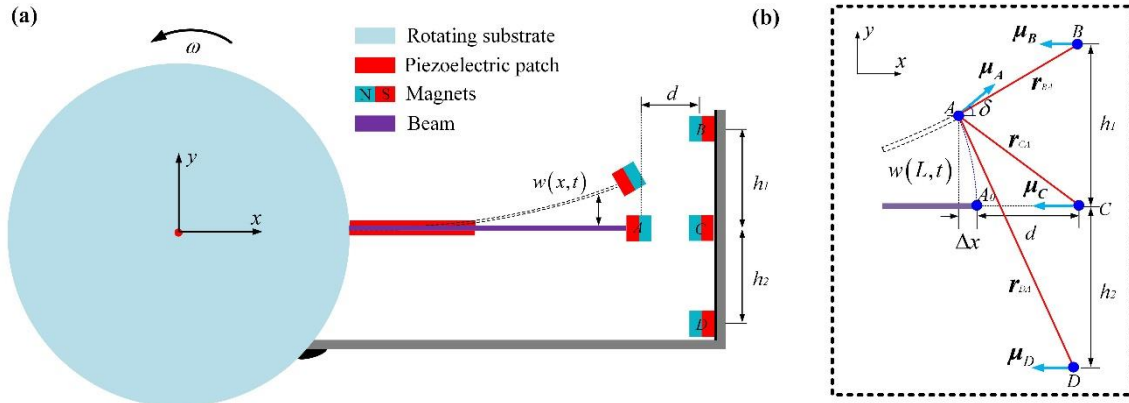


Figure 2.6 (a) The schematic diagram of the repulsive configuration in radial direction; (b) the schematic diagram of dipole-dipole methods.

Figure 2.6 shows the repulsive configuration in radial direction (A, B, C and D) with the associated geometric parameters. The nonlinear magnetic force, generated by the three external magnets (B, C and D) upon on the tip magnet A, can be calculated from the magnetic potential energy and the corresponding expression is expressed as:

$$U_m = \sum U_{jA} = U_{BA} + U_{CA} + U_{DA} \quad (j = B, C, D) \quad (2.38)$$

where U_{BA} , U_{CA} and U_{DA} refer to the potential energy between the external magnets (B, C and D) and the tip magnet A, respectively, and can be expressed as:

$$U_{jA} = \frac{\mu_0}{4\pi} \nabla \left(\frac{\boldsymbol{\mu}_j \cdot \mathbf{r}_{jA}}{\|\mathbf{r}_{jA}\|_2^3} \right) \boldsymbol{\mu}_A = \frac{\mu_0}{4\pi} \left(\frac{\boldsymbol{\mu}_j}{\|\mathbf{r}_{jA}\|_2^3} - (\boldsymbol{\mu}_j \cdot \mathbf{r}_{jA}) \frac{3\mathbf{r}_{jA}}{\|\mathbf{r}_{jA}\|_2^5} \right) \boldsymbol{\mu}_A \quad (j = B, C, D) \quad (2.39)$$

where $\|\cdot\|_2$ and ∇ represent the Euclidean norm and vector gradient operator, respectively. μ_0 is the magnetic permeability constant. $\boldsymbol{\mu}_j$ ($j = B, C, D$) denotes the magnetic moment vectors of magnets. \mathbf{r}_{jA} is the direction vector directed from the magnetic moment source (B or C or D) to tip magnet A. According to the geometrical relations as shown in Figure 2.6(b), \mathbf{r}_{jA} can be written as:

$$\mathbf{r}_{jA} = -d_i \hat{\mathbf{e}}_x + s_i \hat{\mathbf{e}}_y \quad (2.40)$$

where $\hat{\mathbf{e}}_x$ and $\hat{\mathbf{e}}_y$ are the unit vectors along X axis and Y axis, respectively. As illustrated in Figure 2.6(b), the horizontal distance between the tip magnet A and external magnets (B, C and D) are $d = [d_1 \ d_2 \ d_3]$, and related vertical distances are $s = [s_1 \ s_2 \ s_3]$, which are expressed as follows:

$$d = [d + \Delta x + (t_A + t_B) \quad d + \Delta x + (t_A + t_C) \quad d + \Delta x + (t_A + t_D)] \quad (2.41)$$

$$s = [w(L, t) - h_1 \quad w(L, t) \quad w(L, t) + h_2] \quad (2.42)$$

where t_A is the thickness of magnet A, t_j ($j = B$ or C or D) is the thickness of external magnets. h_1 and h_2 are the gap distance between the center of magnets C and B, and that of magnets C and D when the tip displacement is zero, respectively. d is the separation between external magnets to tip mass magnet A as $w(L, t) = 0$, as shown in Figure 2.6. Since the piezoelectric beam is slender enough and can be presumed inextensional in axial direction, Δx is the deformation associated with the foreshortening quantity due to the tip displacement, which has been presented in section 2.1. Moreover, according to the deformation theory, the rotational angle δ of the piezoelectric beam can be calculated as:

$$\delta = \arctan [w'(x, t)]|_{x=L} \quad (2.43)$$

Thus, the magnetic moment vector $\boldsymbol{\mu}_A$, $\boldsymbol{\mu}_B$, $\boldsymbol{\mu}_C$ and $\boldsymbol{\mu}_D$ can be respectively expressed as:

$$\boldsymbol{\mu}_A = M_A V_A \cos \delta \hat{\mathbf{e}}_x + M_A V_A \sin \delta \hat{\mathbf{e}}_y \quad (2.44a)$$

$$\boldsymbol{\mu}_B = -M_B V_B \hat{\mathbf{e}}_x \quad (2.44b)$$

$$\boldsymbol{\mu}_C = -M_C V_C \hat{\mathbf{e}}_x \quad (2.44c)$$

$$\boldsymbol{\mu}_D = -M_D V_D \hat{\mathbf{e}}_x \quad (2.44d)$$

where M_j ($M_j = B_r / \mu_0$) and V_j ($j=A, B, C$ and D) denote the magnetization intensity and the volume of magnets, respectively. B_r is the residual flux density of magnets. Thus, the potential energy between the external magnets and the tip magnet A can be calculated by substituting Eqs. (2.39) - (2.44d) into Eq. (2.38).

$$U_m = \frac{\mu_0 M_A V_A M_j V_j}{4\pi (d_i^2 + s_i^2)^{5/2}} \cdot \left[(d_i^2 - 2s_i^2) \cos \delta - 3d_i s_i \sin \delta \right] \quad (j = B, C, D \quad i = 1, 2, 3) \quad (2.45)$$

The magnetic force can be obtained by taking the derivative of Eq. (2.45) with respect to \mathbf{r}_{jA} :

$$F = -\nabla U_m = \frac{3\mu_0 M_A V_A M_j V_j}{4\pi \|\mathbf{r}_{jA}\|_2^4} \left[\hat{\mathbf{r}}_{jA} (\hat{\boldsymbol{\mu}}_A \cdot \hat{\boldsymbol{\mu}}_j) + \hat{\boldsymbol{\mu}}_j (\hat{\boldsymbol{\mu}}_A \cdot \hat{\mathbf{r}}_{jA}) + \hat{\boldsymbol{\mu}}_A (\hat{\boldsymbol{\mu}}_j \cdot \hat{\mathbf{r}}_{jA}) - 5\hat{\mathbf{r}}_{jA} (\hat{\boldsymbol{\mu}}_A \cdot \hat{\mathbf{r}}_{jA}) (\hat{\boldsymbol{\mu}}_j \cdot \hat{\mathbf{r}}_{jA}) \right] \quad (2.46)$$

where $\hat{\boldsymbol{\mu}}_A$, $\hat{\boldsymbol{\mu}}_j$ and $\hat{\mathbf{r}}_{jA}$ are the unit vectors along $\boldsymbol{\mu}_A$, $\boldsymbol{\mu}_j$ and \mathbf{r}_{jA} , respectively. Based on Eq. (2.46), the nonlinear magnetic force in the y -direction of this configuration can be calculated as:

$$F_m = \frac{3\mu_0 M_A V_A M_j V_j}{4\pi (d_i^2 + s_i^2)^{7/2}} \left[(d_i \sin \delta - s_i \cos \delta) (d_i^2 + s_i^2) + 5d_i s_i (d_i \cos \delta - s_i \sin \delta) \right] \quad (2.47)$$

2.4.2 Attractive Configuration in Normal Direction

Similarly, the nonlinear magnetic force of attractive configuration in normal direction also can be derived according to the dipole-dipole method, which is the same as in section 2.3.1. Note that the important differences will be illustrated in the next parts.

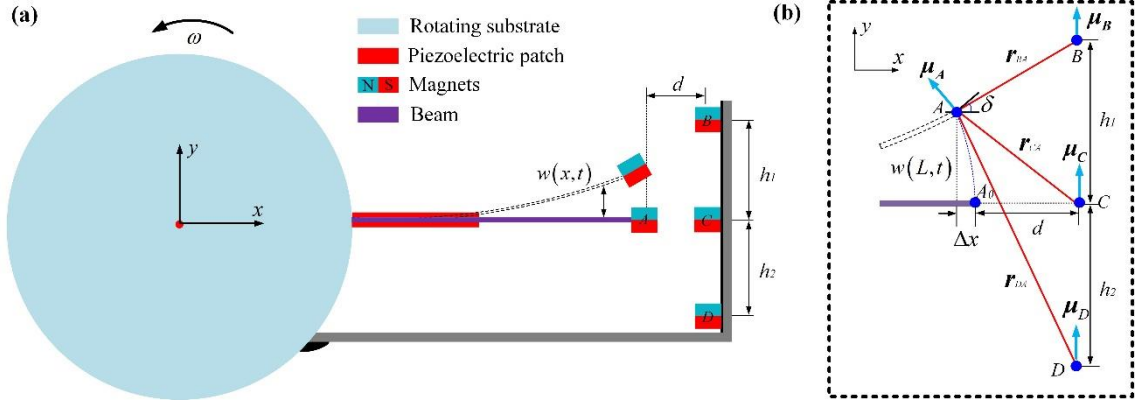


Figure 2.7 (a) The schematic diagram of the attractive configuration in normal direction; (b) the schematic diagram of dipole-dipole methods.

As illustrated in Figure 2.7(b), the horizontal distance between the tip magnet A and fixed magnets (B, C and D) are $d = [d_1 \ d_2 \ d_3]$, and related vertical distances are $s = [s_1 \ s_2 \ s_3]$ respectively. As follows:

$$d = [d + \Delta x + (r_A + r_B) \quad d + \Delta x + (r_A + r_C) \quad d + \Delta x + (r_A + r_D)] \quad (2.48)$$

$$s = [w(L, t) - h_1 \quad w(L, t) \quad w(L, t) + h_2] \quad (2.49)$$

Thus, the magnetic moment vector μ_A , μ_B , μ_C and μ_D can be respectively expressed as:

$$\mu_A = -M_A V_A \sin \delta \hat{e}_x + M_A V_A \cos \delta \hat{e}_y \quad (2.50a)$$

$$\mu_B = M_B V_B \hat{e}_y \quad (2.50b)$$

$$\mu_C = M_C V_C \hat{e}_y \quad (2.50c)$$

$$\mu_D = M_D V_D \hat{e}_y \quad (2.50d)$$

According to Eq. (2.46), the nonlinear magnetic force in the y -direction of the attractive configuration in normal direction also can be calculated as:

$$F_m = \frac{3\mu_0 M_A V_A M_j V_j}{4\pi (d_i^2 + s_i^2)^{7/2}} [(3s_i \cos \delta + d_i \sin \delta)(d_i^2 + s_i^2) - 5s_i^2 (d_i \sin \delta + s_i \cos \delta)] \quad (2.51)$$

2.5 Theoretical Analyses

Firstly, we mainly focused on the performance of the nonlinear PEHs in rotational motion under various constant rotational speeds without the base excitation. Namely, $\ddot{\theta}=0$ and $F(t)=0$ in

Eq. (2.36a). Therefore, Eqs. (2.36a) and (2.36b) can be rewritten as:

$$M_e \ddot{q}(t) + C\dot{q}(t) + (K_e + K_c \dot{\theta}^2)q(t) - \mathcal{G}_p v(t) + F_m = -\Gamma g \cos \theta \quad (2.52a)$$

$$C_p \dot{v}(t) + R_l^{-1}v(t) + \mathcal{G}_p \dot{q}(t) = 0 \quad (2.52b)$$

Next, with the aim to validate the importance of rotational motion in the proposed theoretical model, the comparison between two models, with and without the consideration of rotational motion, are conducted via the numerical simulations. Additionally, the case studies also have been performed to validate the theoretical predictions including the dynamic performance and output voltage. It is worth mentioning that all numerical analyses and case studies are conducted by MATLAB software. Defining the space vector of Eqs. (2.52a) and (2.52b) as:

$$\begin{bmatrix} y_1 & y_2 & y_3 \end{bmatrix}^T = \begin{bmatrix} q(t) & \dot{q}(t) & v(t) \end{bmatrix}^T \quad (2.53)$$

Thus, the governing Eqs. (2.52a) and (2.52b) of the nonlinear PEH in rotational motion can be rewritten as:

$$\dot{y}_1 = y_2 \quad (2.54a)$$

$$\dot{y}_2 = -\frac{1}{M_e} \left[Cy_2 + (K_e + K_c \dot{\theta}^2) y_1 + F_m + \chi \ddot{\theta} - \mathcal{G}_p y_3 + \Gamma g \cos \theta \right] \quad (2.54b)$$

$$\dot{y}_3 = -\frac{1}{C_p} \left(\frac{1}{R_l} y_3 + \mathcal{G}_p y_2 \right) \quad (2.54c)$$

Note that a symmetrical tri-stable PEH is adopted in Chapter 3 for numerical analyses and experimental validations. And all parameters adopted in the numerical simulations are the same as those of the experiments. The parameters are listed in Table 2.1.

Table 2.1 Parameter used in the numerical simulations

Parameter	Value	Unit
M_e	0.0096	Kg
C	0.005	N.s/m
K_e	16.4	N /m
K_c	0.0071	
\mathcal{G}_p	1.387e-4	
Γ	0.0094	
C_p	2.3e-7	
R_l	1000000	Ω

2.5.1 Influence of Coefficient K_c

For a nonlinear PEH in rotational motion, the higher-order nonlinearities of magnetic force lead to more complex dynamic responses. From the mechanical Eq. (2.52a), we can notice that the rotational coefficients, including the angular displacement θ , angular velocity $\dot{\theta}$ and angular acceleration $\ddot{\theta}$, are coupled in the proposed theoretical model. Firstly we investigate the influence of K_c coefficient on the prediction of dynamic performance. Based on the electromechanical Eqs. (2.52a) and (2.52b), the bifurcation diagrams, of the dynamic performance of the tri-stable PEH under various constant rotational speeds, are presented. Figure 2.8(a) and 2.8(b) show the results of bifurcation diagram via the theoretical models with and without the consideration of rotational motion, respectively. Namely, when the rotational motion is considered in the theoretical model, K_c coefficient is existing in Eq. (2.52a), otherwise, $K_c = 0$.

As shown in Figures 2.8(a) and 2.8(b), both of them are divided into three regions: Region I, Region II and Region III, respectively. In Region I, the rotational speed ranges from 5 to 240 rpm, and it is obvious that the dynamic performances of the tri-stable PEH are almost the same. Additionally, under this rotational speed in Region I, the proposed tri-stable PEH performs chaotic oscillations. However, when the rotational speed is increased to Region II, the prediction results of the displacement responses are totally different. Specifically, the inter-well and chaotic oscillations are respectively found in Figures 2.8(a) and 2.8(b). Furthermore, as the rotational speed is increased to Region III, the predicted displacement response by Model 1 in Figure 2.8(a) decreases dramatically instead of the intra-well oscillation around the middle stable equilibrium position, which means the corresponding output voltage decreases simultaneously. On the contrary, the predicted dynamic response by Model 2 in Figure 2.8(b) also experiences the chaotic oscillations. With the increasing of rotational speed, the tri-stable PEH will hold the same state.

Based on the above theoretical analyses, It can be concluded that under the lower rotational speed (in Region I), the predicted dynamic responses based on two Models are almost the same, however, when the rotational speed reaches a certain value (Region II and Region III), they are totally different. In order to verify the proposed theoretical model, more case studies will be carried out to make a comparison between Model 1 and Model 2.

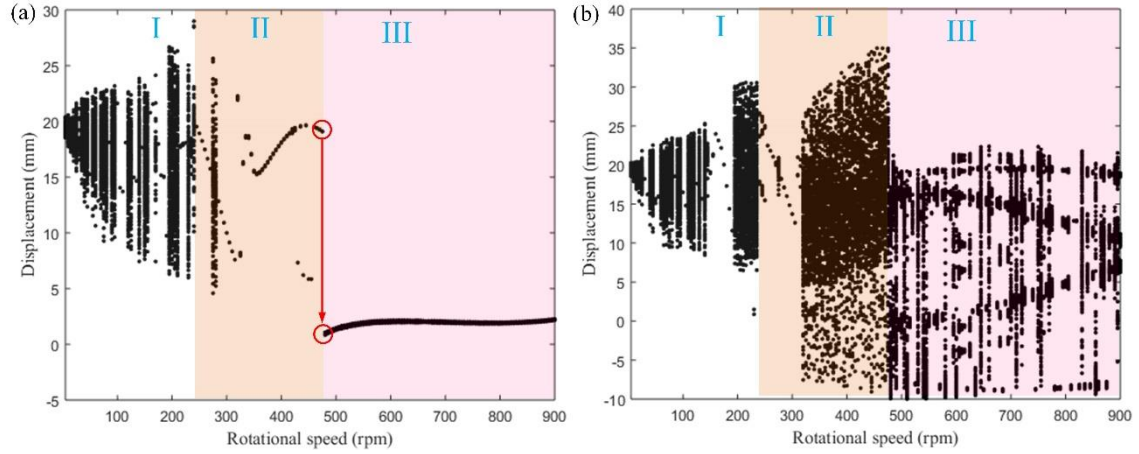


Figure 2.8 Bifurcation diagrams for a tri-stable PEH versus various rotational speeds by the theoretical models with and without the consideration of rotational motion, namely, (a) K_c coefficient is existing (Model 1), and (b) $K_c = 0$ (Model 2).

2.5.2 Case Studies

This section focuses on analyzing the performance of the tri-stable PEH based on the above two Models, namely, Model 1 considers the effect of the rotational motion in theoretical model (K_c is existing), and Model 2 does not consider that in theoretical model ($K_c = 0$). Thus, several case studies, including the rotational speed in Region I (120 rpm and 240 rpm), Region II (420 rpm) and Region III (720 rpm), are investigated to reveal the influence of K_c coefficient on the predicted dynamic performance, and the numerical results are shown in Figures 2.9-2.12, respectively. Note that the Figures (a) and (b) of each figure are the results based on Model 1 (Proposed theoretical model), and Figure (c) and (d) are the results based on Model 2. (Previous theoretical model)

Figure 2.9 illustrates the numerical results of the displacement response, the phase portraits and the related Poincare map of the tri-stable PEH at rotational speed 120 rpm (Region I). As observed from Figure 2.9, the predicted dynamic performance based on the two theoretical models are almost the same. From the Poincare maps in Figure 2.9(b) and Figure 2.9(d), both them experience chaotic oscillations at this rotational speed, which are agreed with the results in Figure 2.8. When the rotational speed is further increased to 240 rpm (Region I), the numerical results are shown in Figure 2.10. It can be found that when the rotational speed is increased to 240 rpm, from the Poincare map of Figures 2.10(b) and 2.10(d), the tri-stable PEH performs the quasi-oscillation, which also validates the predictions of the bifurcation diagram in Figure 2.8. For the tri-stable

PEH at a lower rotational speed, K_c has not a great effect on the dynamic performance of the tri-stable PEH.

In order to further investigate the influence of K_c coefficient at a higher rotational speed, the rotational speed 420 rpm in Region II is selected for the numerical simulation. The numerical results are shown in Figure 2.11, it is obviously noticed that the dynamic performance of the tri-stable PEH performs the inter-well oscillation. For the output voltage, when the effect of rotational motion in the theoretical model is considered, it can be found that the maximum displacement is 20 mm as shown in Figure 2.11(b). However, if we conduct the numerical simulations via the theoretical model without the consideration of rotational motion, the maximum displacement is 50 mm as shown in Figure 2.11(d). According to the numerical results at the rotational speed 420 rpm in Region II, it is clearly noticed that K_c coefficient has a great influence on the dynamic performance of the tri-stable PEH.

As the rotational speed is further increased to Region III, from the bifurcation diagrams as shown in Figures 2.8(a) and 2.8(b), it can be found that that the dynamic performances are different. Thus, the rotational speed 720 rpm is chosen for the numerical simulation, and related results are shown in Figure 2.12. As observed from Figures 2.12(a) and 2.12(b), the dynamic performance of the tri-stable PEH will be deduced, and the maximum displacement is 6 mm. However, if the effect of rotational motion is not considered in the theoretical model, as the numerical results shown in Figures 2.12(c) and 2.12(d), the dynamic performance of the tri-stable PEH will keep the quasi-oscillation state, and the maximum displacement is 20 mm.

In summary, the rotational speeds in Region I (120 rpm and 240 rpm), Region II (420 rpm) and Region III (720 rpm) are chosen for numerical simulations via Model 1 and Model 2. The numerical analyses indicate that under lower rotational speeds in Region I, the displacement response of the tri-stable PEH predicted by two Models are almost the same. However, when the rotational speed is increased to Region II and Region III, they are totally different. Thus, the experimental investigations will be carried out to validate the proposed theoretical model in the next section.

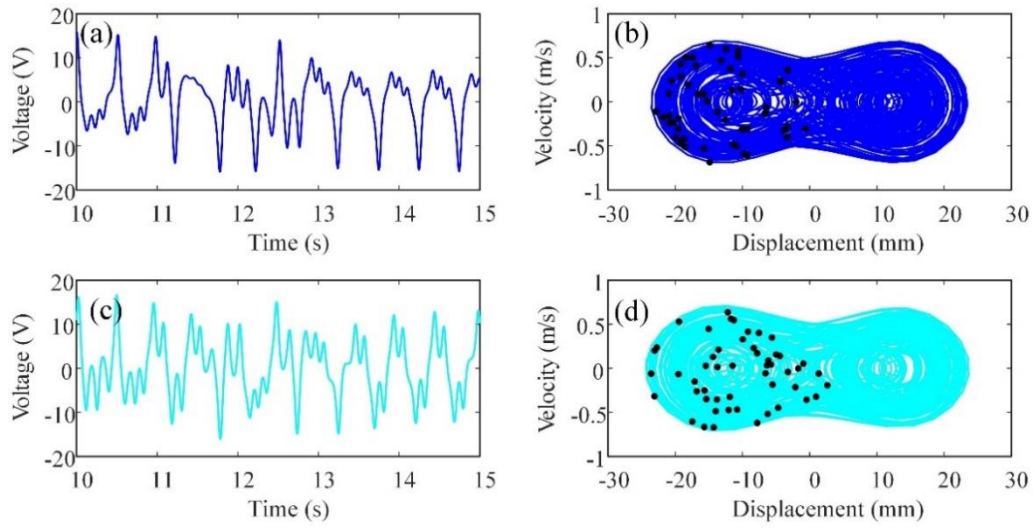


Figure 2.9 The numerical results of the tri-stable PEH at the rotational speed 120 rpm: (a) and (b) are based on the proposed theoretical model; (c) and (d) are based on the theoretical model without the consideration of rotational motion.

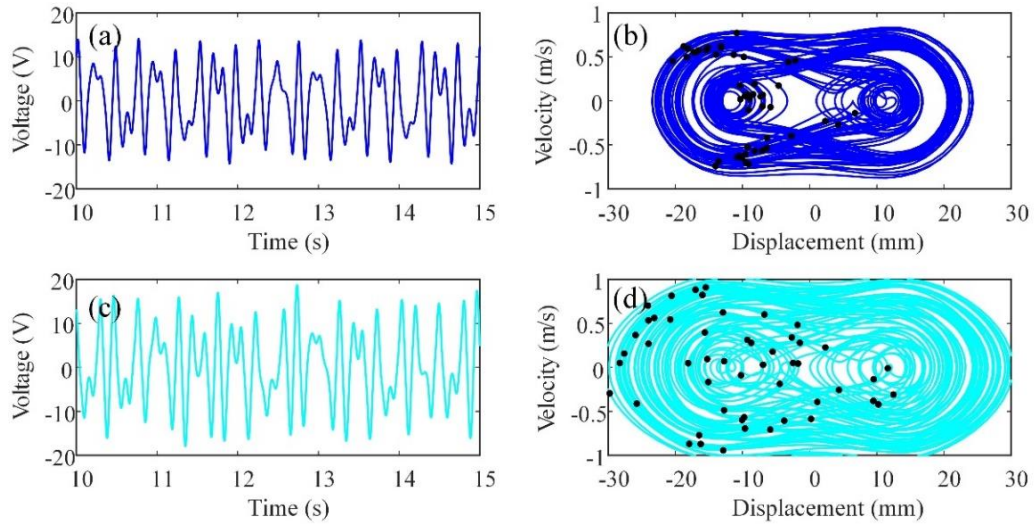


Figure 2.10 The numerical results of the tri-stable PEH at the rotational speed 240 rpm: (a) and (b) are based on the proposed theoretical model; (c) and (d) are based on the theoretical model without the consideration of rotational motion.

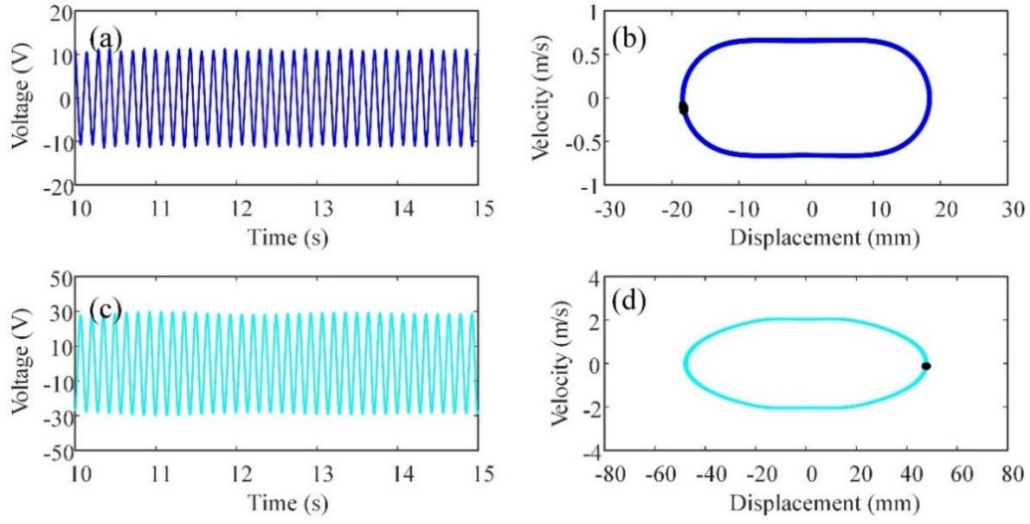


Figure 2.11 The numerical results of the tri-stable PEH at the rotational speed 420 rpm: (a) and (b) are based on the proposed theoretical model; (c) and (d) are based on the theoretical model without the consideration of rotational motion.

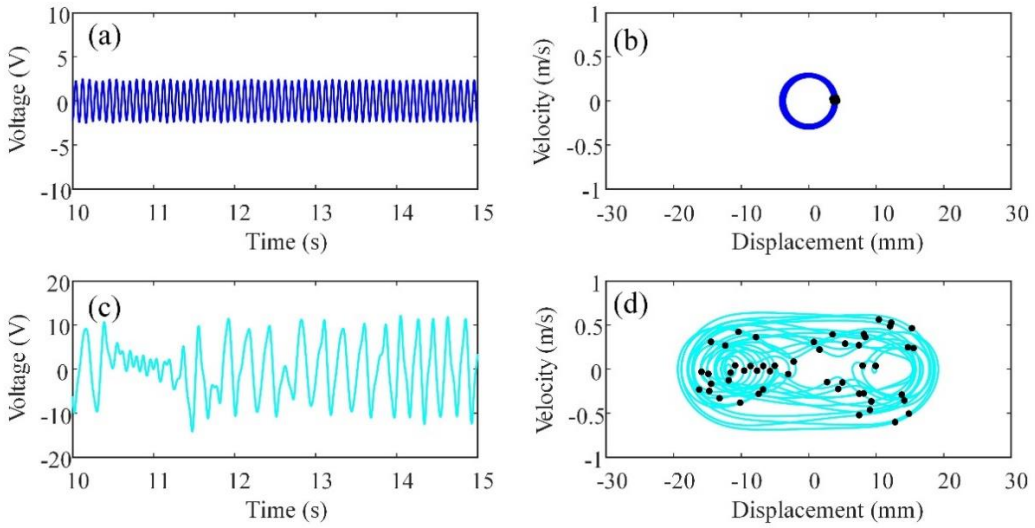


Figure 2.12 The numerical results of the tri-stable PEH at the rotational speed 720 rpm: (a) and (b) are based on the proposed theoretical model; (c) and (d) are based on the theoretical model without the consideration of rotational motion.

2.6 Experimental Validation and Discussion

2.6.1 Experimental Validation

In this section, some experiments are conducted to validate the proposed theoretical model and

the theoretical analyses in section 2.5. The energy harvesting performance of the tri-stable PEH is investigated based on the experimental setup as shown in Figure 2.13 (a), in which a servo motor (SGM7J, YASKAWA) controlled by a matching servo actuator (SGD7S, YASKAWA) is used to provide the rotational motion for the rotation plate. The parameters of rotational motion can be set via the software SigmaWin+ (Version 7.0, YASKAWA) on the computer, then the signal is input into the motor actuator to control the servo motor. The energy harvesters and associated laser sensors (HG-C1100, Panasonic) are fixed on the rotation plate as shown in Figure 2.13(a). The electrical slip ring (SENRING, CHINA), including one stator and one rotor, is mounted on the rotation axis to address the issue of wire connection in rotational motion. Additionally, a digital oscilloscope (DSOX3014T, KEYSIGHT) is used to monitor and measure the output voltage and the displacement of the PEHs. The sample frequency in these experiments is 500 sample per second.

As shown in Figure 2.13(b), the tri-stable PEH consists of a cantilever beam with a tip magnet and two external magnets, and two piezoelectric patches are symmetrically attached at the fixed end of the beam. Note that all the magnets are NdFeB cylinder magnets, whose grade is 1.2 T. The tip mass is consisting of one magnet $D12 \times 1.7 \text{ mm}^3$ (D is the diameter) and two magnets $D12 \times 2.7 \text{ mm}^3$. To create the tri-stable configuration, two external magnets with the dimension of $D12 \times 1.7 \text{ mm}^3$ are fixed on the frame. Additionally, the substrate layer of a tri-stable PEH is made of stainless steel with the dimension of $95 \times 12 \times 0.2 \text{ mm}^3$. Each piezoelectric patch (K2512U1, THRIVE, JAPAN) has the dimensions of $25 \times 12 \times 0.13 \text{ mm}^3$. It should be emphasized that the tri-stable PEH is operated in 31 mode with the parallel connection between the two piezoelectric patches. The parameters of tri-stable PEH in experiment are $h_1=20 \text{ mm}$, $h_2=20 \text{ mm}$ and $d=15 \text{ mm}$. In this situation, the piezoelectric beam has three stable equilibrium positions as shown in Figure 2.13(c). The parameters of the system are listed in Table 2.2.

Based on the abovementioned experimental setup, we choose two group experimental results, including Region II (300 rpm and 420 rpm), and Region III (560 rpm), to validate the theoretical model. Due to the difficulty of measuring the tip displacement, which will lead to the foreshortening quantity Δx caused by the bending of the cantilever beam. Therefore, the displacement of the tri-stable PEH in experiments is measured by the laser sensor at the distance of 54 mm from the fixed end of the piezoelectric beam. This is the same as the Refs. [73,74,107], according to the measured displacement data at one position of the piezoelectric beam to compare with the numerical displacement, and qualitatively verify the proposed theoretical model.

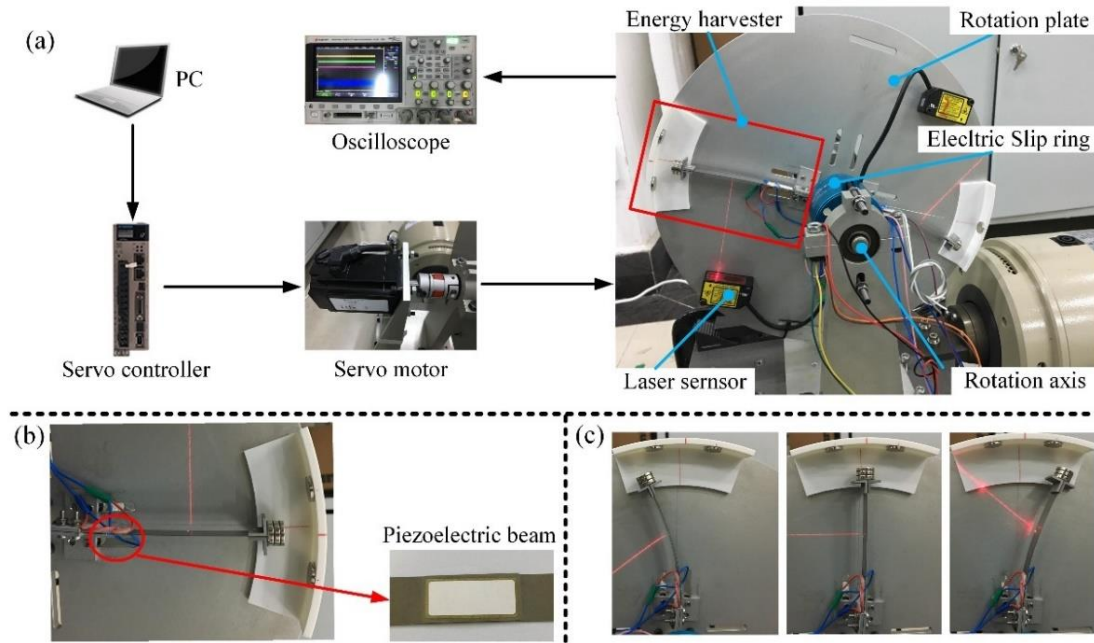


Table 2.2. The parameters used in the experimental validation

Parameters	Symbol	Value
Cantilever beam		
Length \times Width \times Thickness	$L \times b \times t_b$	$95 \times 12 \times 0.20 \text{ mm}^3$
Young's modulus	E_b	210 Gpa
Density	ρ_b	7765 Kg/m ³
Damping ratio	C	0.005
Radius of the hub	r	42 mm
Piezoelectric patch		
Length \times Width \times Thickness	$l_p \times b_p \times t_p$	$25 \times 12 \times 0.13 \text{ mm}^3$
Young's modulus	E_p	66 Gpa
Density	ρ_p	7800 Kg/ m ³
Coupling coefficient	d_{31}	$-320 \times 10^{-12} \text{ C/N}$
Permittivity constant	ϵ_{33}	$4000 \epsilon_0$
Permittivity of free space	ϵ_0	$8.854 \times 10^{-12} \text{ F/m}$
Permanent magnets		
Density	$\rho_A \quad \rho_B \quad \rho_C$	7500 Kg/ m ³
Magnet's residual flux density	B_r	1.2 T
Permeability of free space	μ_0	$4\pi \times 10^{-7}$
Load resistance	R_l	1 M Ω

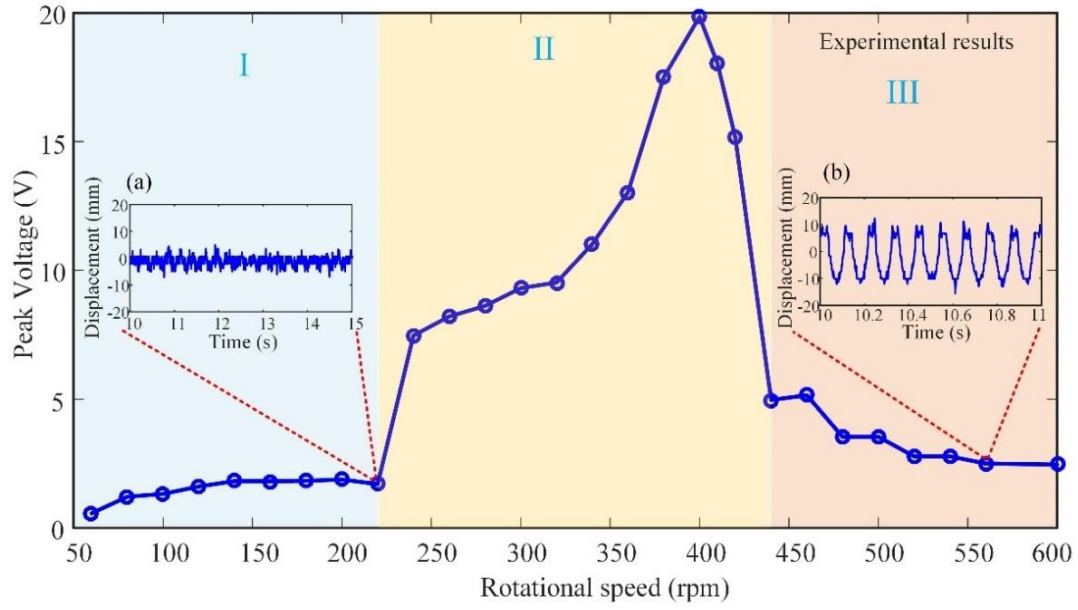


Figure 2.14 Experimental peak voltage for varied rotational speed from 60 – 600 rpm; Region I is related to the intra-well oscillation, Region II corresponds to the inter-well oscillation, Region III is related to the intra-well oscillation due to the centrifugal stiffening effect.

Figure 2.14 depicts the rotational speed sweeping experimental ranging from 60 rpm (1Hz) to 600 rpm (10Hz) by increasing per 20 rpm. From 60 - 220 rpm, the output voltage of the tri-stable PEH is nearly 2 V, and the tri-stable PEH experiences the intra-well oscillation, as the measured displacement shown in Figure 2.14(a). When the rotational speed is increased to 240 rpm, the peak voltage increases remarkably due to the high-energy inter-well oscillations. As the rotational speed is 240 - 420 rpm, the output voltage is high, which corresponds to the inter-well oscillation in Region II, and this is also the desirable frequency range for energy harvesting. However, when the rotational speed is becoming 440 rpm, the output voltage decreases significantly due to the centrifugal stiffening effect of the tri-stable PEH. Namely, when the rotational speed reaches a certain value, the centrifugal force acting on the tip mass of harvester will reduce the vibration of piezoelectric beam, as the measured displacement shown in Figure 2.14(b), which results in undesirable energy harvesting performance. Note that the centrifugal stiffening effect can be explained by the term $K_c \dot{\theta}^2$ in Eq. (2.36a) of the proposed theoretical model. Based on the experimental results, three regions are divided. Region I is related to the intra-well oscillation, which is not desirable for energy harvesting. Region II corresponds to the inter-well oscillation, which is suitable for energy harvesting. And in Region III, the proposed tri-stable PEH will experience the intra-well oscillation around the middle stable equilibrium position due to centrifugal stiffening effect. All in all, the experimental results in Figure 2.14 qualitatively verify

the proposed theoretical model.

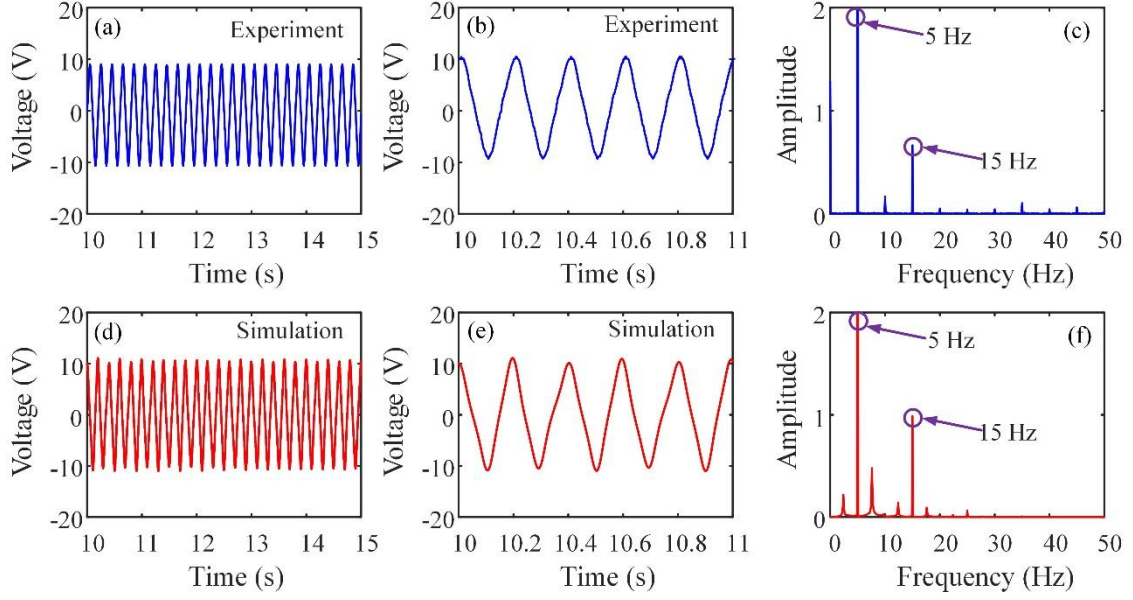


Figure 2.15 Experimental (blue line) and numerical (red line) results of the tri-stable PEH versus time under 300 rpm; (a) and (d) are respectively measured and numerical voltages versus time, (b) and (e) are the corresponding zoomed-in versions, (c) and (f) are corresponding power spectrum.

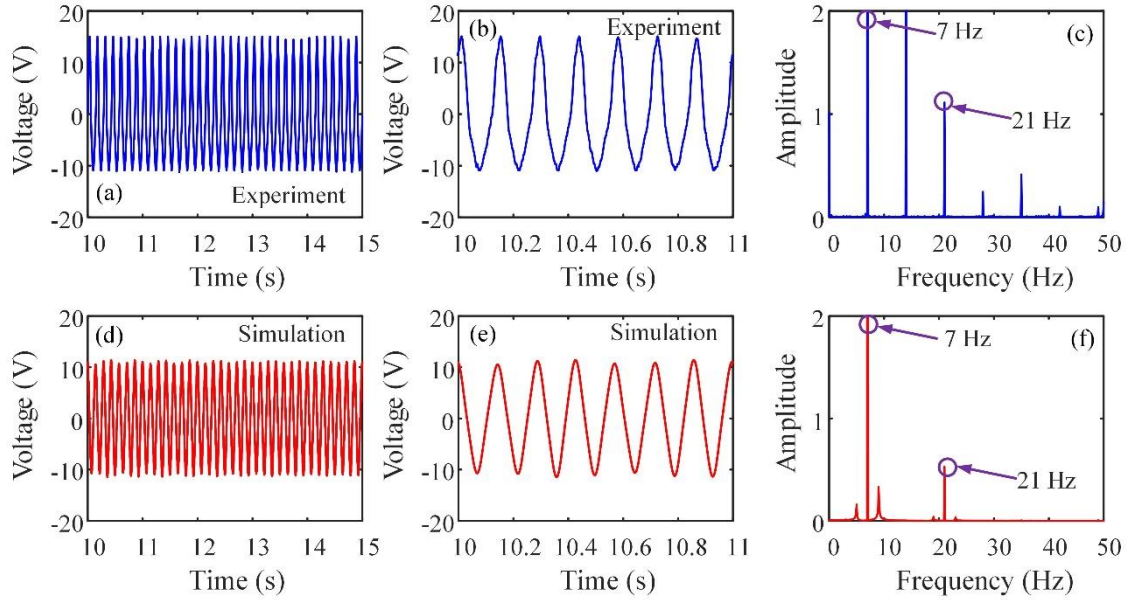


Figure 2.16 Experimental (blue line) and numerical (red line) results of the tri-stable PEH versus time under 420 rpm; (a) and (d) are respectively measured and numerical voltages versus time, (b) and (e) are the corresponding zoomed-in versions, (c) and (f) are corresponding power spectrum.

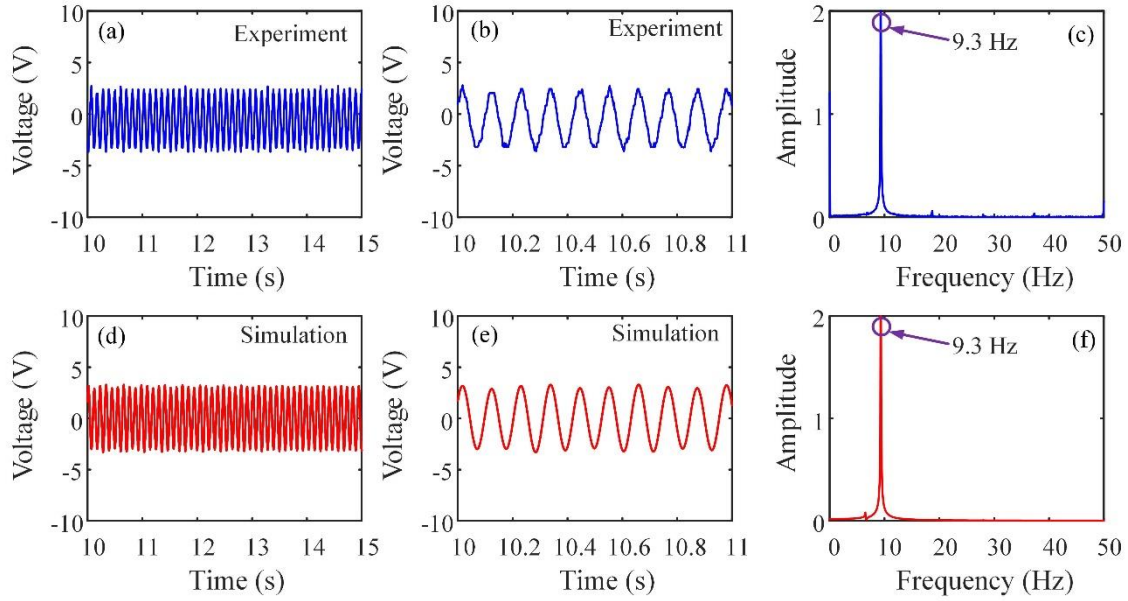


Figure 2.17 Experimental (blue line) and numerical (red line) results of the tri-stable PEH versus time under 560 rpm; (a) and (d) are respectively measured and numerical voltage versus time, (b) and (e) are the corresponding zoomed-in versions, (c) and (f) are corresponding power spectrum.

To further investigate the dynamic characteristic of the proposed tri-stable PEH, the experimental and numerical results, including the rotational speed of 300 rpm, 420 rpm and 560 rpm, are shown in Figure 2.15, Figure 2.16 and Figure 2.17, respectively. Fast Fourier Transform (FFT) has been used to obtain the frequency response.

Figure 2.15 shows the experimental and numerical output voltage of the tri-stable PEH in the time domain under 300 rpm (5 Hz), at which the tri-stable PEH experiences the inter-well oscillations, and the peak output voltage reaches 10 V. Furthermore, from the power spectrum in Figure 2.15(c), one frequency component of the output put voltage is equal to the rotational frequency, and the super-harmonic components are also existing. When the rotational speed is further increased to 420 rpm (7Hz), as shown in Figure 2.16, it is clearly noticed that the tri-stable PEH performs the large-amplitude inter-well oscillation. It can be found that the corresponding output voltage is nearly 18 V, thus, it is suitable for energy harvesting. As the rotational speed is increased to 560 rpm, from Figure 2.17, the results demonstrate that the dynamic performance of the tri-stable PEH decreases dramatically, and consequently leads to lower output voltage. Furthermore, it is experimentally demonstrated that at high rotational speeds, the coefficient K_c has a great effect on the performance of the tri-stable PEH. Thus, the effect of rotational motion should be considered in the theoretical model. Additionally, the experimental results match well with the

numerical results based on the proposed theoretical model. Those analyses verify the proposed theoretical model.

2.6.2 Results Discussion

In this section, we validate the proposed theoretical model by experimental investigation. Additionally, the comparison of numerical simulations between the two theoretical model verify that the K_c coefficient has a great effect on the dynamic performance of a PEH especially under high rotational speed, and can also explain the centrifugal stiffening effect.

In our experiments, due to the difficulty of measuring the tip displacement, we just make a comparison of output voltage between the numerical and experimental results. Furthermore, one thing should be noted is that the tri-stable PEH is the nonlinear system which is very sensitive to the nonlinear force. However, the nonlinear in this dissertation is calculated by the dipole-dipole method, in addition to this, in our experiments, the external magnetic with thickness of 1.7 mm and diameter of 12 mm. Thus, the calculation of nonlinear magnetic force is not precisely, consequently the numerical results cannot match well with the experimental results in Region I, in which the comparison is not presented.

2.7 Summary

In Chapter 2, the theoretical model, of a nonlinear PEH in rotational motion, has been derived by modelling in a rotational coordinate system. Furthermore, the nonlinear magnetic force of different configurations is calculated based on the dipole-dipole method. Next, the theoretical analyses and numerical simulations are performed to validate the proposed theoretical model under various constant rotational speeds. Furthermore, the influence of the K_c coefficient is explored, and experimental results quantitatively validate the theoretical model. The following conclusions can be obtained:

- (1) Based on Lagrange equation, the theoretical model of a PEH in a rotational coordinate system is derived.
- (2) The difference between the theoretical model with or without the consideration of effect of rotational motion is the existence of K_c coefficient. In a lower rotational speed, K_c has little influence. However, in a higher rotational speed, K_c has a great effect on the dynamic performance of a tri-stable PEH. Thus, the future optimization design should pay attention on K_c

coefficient.

(3) The experimental validations verify the proposed theoretical model and demonstrate the centrifugal stiffness effect at high rotational speeds due to the centrifugal force acting on the tip mass of nonlinear PEH.

In summary, Chapter 2 presents a novel theoretical model considering the centrifugal force. It also has been theoretically and experimentally validated by a symmetrical tri-stable PEH in rotational motion. In order to reveal the dynamic performance of different nonlinear PEHs in rotational motion, the further research will be investigated in Chapter 3.

Chapter 3

Nonlinear Energy Harvesters in Rotational Motion

3. Various Nonlinear Energy Harvesters in Rotational Motion

In order to obtain high-efficiency energy harvesters, many efforts have been made to enhance the energy harvesting performance in broadening operating bandwidth, improving output voltage and lowering the input excitation level. The nonlinearity is one of the methods for broadening operation frequency bandwidth. As presented in Refs. [32,33,37,40], the nonlinearities are mainly caused by the magnetic force or pre-load-beam configuration which can lead to different shapes of their potential functions, such as mono-stable, bi-stable, tri-stable, and quad-stable characteristics, etc. Some many research works about the bi-stability, tri- stability and even multi- stability can be found in Refs. [73,76,83], few of them are applied in the rotational motion. Furthermore, most researchers only measure the output voltage in some certain rotational speed range, which leads to the dynamic response of the PEH being not revealed. With the aim to reveal the dynamic mechanism of different nonlinear PEHs in rotational motion, theoretical analyses and experimental validations will be conducted in Chapter 3.

In Chapter 3, the bi-stable, symmetric and asymmetric tri-stable, and quad-stable PEHs are theoretically and experimentally investigated. Additionally, the centrifugal stiffening effect predicted by the proposed theoretical model has been verified in experiments.

3.1 Bi-stable Energy Harvester in Rotational Motion

3.1.1 Bi-stable Energy Harvester

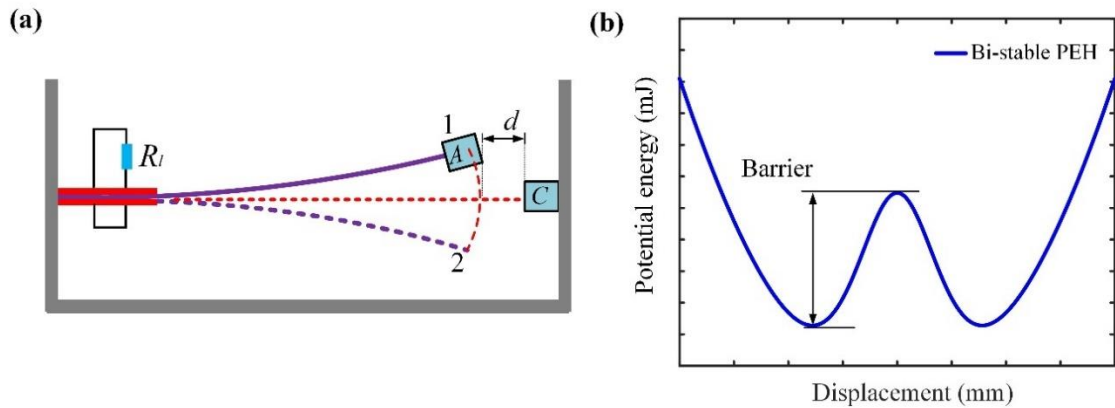


Figure 3.1 (a) The schematic diagram of a bi-stable PEH; (b) the related potential energy.

The schematic diagram and related potential energy of a bi-stable PEH is shown in Figure 3.1. As illustrated in Figure 3.1, the bi-stable PEH consists of a cantilever beam, partially covered by two uni-morph piezoelectric patches, with a tip magnet A and external magnet C. Adjusting the gap distance d , the bi-stable PEH will hold two stable equilibrium positions when the elastic force of piezoelectric beam is balanced by the magnetic force. The related potential energy is shown in Figure 3.1(b), we can notice two stable positions and one unstable position respectively, and the potential barrier is the energy which should be conquered from one stable position to another one. In previous studies [72,73,74], the governing equations of a bi-stable PEH under harmonic excitation (rectilinear motion) can be obtained as:

$$M_e \ddot{x}(t) + C \dot{x}(t) + K_1 x(t) + K_3 x(t)^3 - \mathcal{G}_p v(t) = F \sin(\omega t + \phi_0) \quad (3.1a)$$

$$C_p \dot{v}(t) + R_l^{-1} v(t) + \mathcal{G}_p \dot{x}(t) = 0 \quad (3.1b)$$

where $x(t)$ is the relative displacement, M_e is the equivalent mass, K_1 and K_3 are the linear and cubic coefficients of the restoring force, respectively. \mathcal{G}_p is the electromechanical coupling coefficient. C_p is the internal capacitance of the piezoelectric patches. $F \sin(\omega t + \phi_0)$ is the harmonic excitation, F is the amplitude of harmonic force, ω is the angular velocity, ϕ_0 is the initial phase angle between the excitation and the response. R_l is the resistance of electric load.

3.1.2 Bi-stable Energy Harvester in Rotational Motion

When the bi-stable PEH is applied in rotational motion, the potential energy function is time-varying due to the change of gravity component in one period of rotational motion. As observed from Figure 3.2, if the potential barrier of the bi-stable PEH is low enough, the periodic gravity component of the tip mass can be an exciting force to across the potential barriers, thus, the inter-well oscillations can be obtained even without the base excitation.

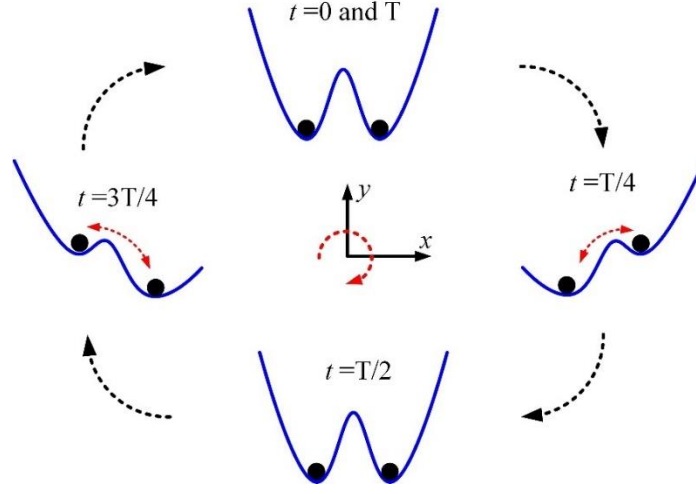


Figure 3.2 The time-varying potential well function of bi-stable PEH in one period of rotational motion.

As the bi-stable PEH in rotational motion, the term F_m in Eq. (2.36a) is the nonlinear magnetic force. Thus, the equivalent restoring force F_r , including the elastic force of piezoelectric beam and magnetic force, can be expressed and rewritten as:

$$F_r = K_e q(t) + F_m = K_1 q(t) + K_3 q(t)^3 \quad (3.2)$$

Thus, based on the proposed theoretical model, the governing equations of bi-stable PEH in rotational motion can be expressed as:

$$M_e \ddot{q}(t) + C \dot{q}(t) + (K_1 + K_c \dot{\theta}^2) q(t) + K_3 q(t)^3 + \chi \ddot{\theta} - \mathcal{G}_p v(t) = [-\Gamma g + F(t)] \cos \theta \quad (3.3a)$$

$$C_p \dot{v}(t) + R_l^{-1} v(t) + \mathcal{G}_p \dot{q}(t) = 0 \quad (3.3b)$$

As observed from Eq. (3.3a), we can notice two interesting phenomena: (1) In rotational motion the centrifugal force acting on the tip mass, which is $K_c \dot{\theta}^2 q(t)$ term, has an effect on the energy harvesting performance. (2) The gravity component of tip mass due to rotational motion, which corresponds to $-\Gamma g \cos \theta$ term, can be regarded as a periodic exciting force for the piezoelectric beam vibration. Additionally, the existence of periodic force due to rotational motion makes it possible to achieve the stochastic resonance, the further details can refer to Ref. [53].

3.2 Symmetric Tri-stable Energy Harvester in Rotational Motion

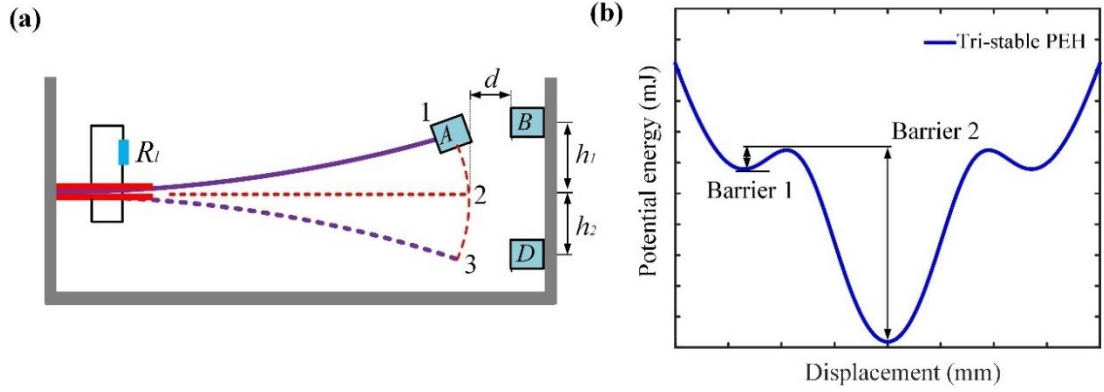


Figure 3.3 (a) The schematic diagram of a tri-stable PEH; (b) the related potential energy of a tri-stable PEH.

Different from the bi-stable PEH, there are two magnets in a tri-stable PEH as shown in Figure 3.3(a). Adjusting the parameters d , h_1 and h_2 , the tri-stable PEH with three equilibrium positions (position 1, 2 and 3 as shown in Figure 3.3) can be obtained. The advantages of tri-stable PEH have been theoretically and experimentally demonstrated in Refs. [76,78,79]. Similarly, when it is applied in rotational motion, the related time-varying potential well function is shown in Figure 3.4.

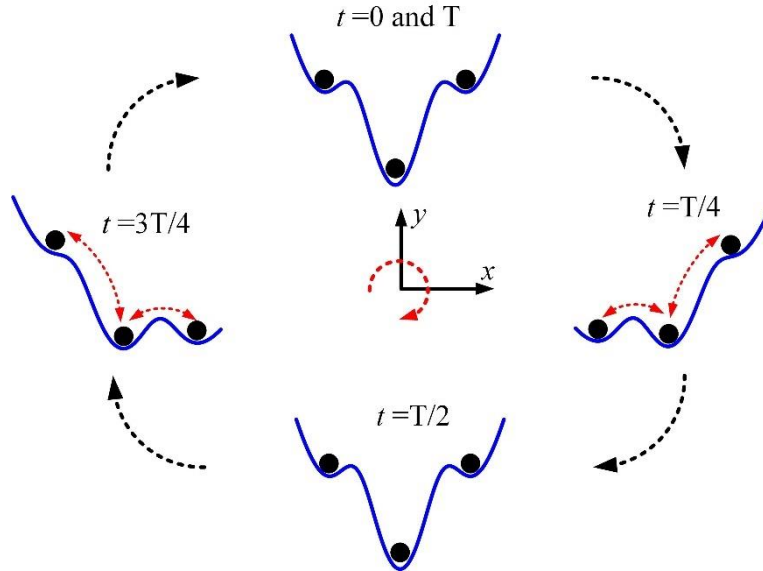


Figure 3.4 The time-varying potential well function of tri-stable PEH in one period of rotational motion.

When h_1 is equal to h_2 , the stable positions 1 and 3 are symmetric about the stable position 2.

Thus, the equivalent restoring force can be rewritten as:

$$F_r = K_e q(t) + F_m = K_1 q(t) + K_3 q(t)^3 + K_5 q(t)^5 \quad (3.4)$$

3.2.1 Theoretical Model

Similarly, based on the proposed theoretical model, the governing equations of tri-stable PEH in rotational motion can be expressed as:

$$M_e \ddot{q}(t) + C \dot{q}(t) + (K_1 + K_c \dot{\theta}^2) q(t) + K_3 q(t)^3 + K_5 q(t)^5 + \chi \ddot{\theta} - \mathcal{G}_p v(t) = [-\Gamma g + F(t)] \cos \theta \quad (3.5a)$$

$$C_p \dot{v}(t) + R_l^{-1} v(t) + \mathcal{G}_p \dot{q}(t) = 0 \quad (3.5b)$$

For simplicity, the electromechanical equations of the tri-stable PEH can be rewritten as non-dimensional equations by introducing the following dimensionless quantities:

$$u(\tau) = \frac{q(t)}{l_c}; \quad \tau = t \omega_n; \quad y(\tau) = \frac{C_p}{\mathcal{G}_p l_c} v(t) \quad (3.6)$$

where l_c is a length scale for nondimensionalizing the displacement, and $\omega_n = \sqrt{K_1/M_e}$ is the nominal short-circuit frequency. Based on Eqs. (3.5a) and (3.5b), the following non-dimensional equations can be derived:

$$\ddot{u}(\tau) + 2\xi \dot{u}(\tau) + (1 + \gamma \omega^2) u(\tau) + \beta u(\tau)^3 + \eta u(\tau)^5 + \bar{\chi} \ddot{\theta} - \sigma^2 y(\tau) = [\bar{\Gamma} g + f(t)] \cos \omega \tau \quad (3.7a)$$

$$\dot{y}(\tau) + \lambda y(\tau) + \dot{u}(\tau) = 0 \quad (3.7b)$$

where the variables are defined as follows:

$$\begin{aligned} \xi &= \frac{C}{2\sqrt{M_e K_1}}; & \sigma^2 &= \frac{\mathcal{G}_p^2}{C_p K_1}; & \gamma &= \frac{K_c}{M_e}; & \omega &= \frac{\dot{\theta}}{\omega_n}; & \beta &= \frac{K_3}{K_1} l_c^2; \\ \eta &= \frac{K_5}{K_1} l_c^4; & \lambda &= \frac{1}{\omega_n C_p R_l}; & \bar{\chi} &= \frac{\chi}{M_e}; & \bar{\Gamma} &= -\frac{\Gamma}{M_e}; & f(t) &= \frac{F(t)}{M_e}. \end{aligned}$$

Chapter 3 mainly focused on the performance of nonlinear PEH in rotational motion under various constant rotational speed, without the external base excitation. Thus, in Eq. (3.7a) $\ddot{\theta} = 0$ and $f(t) = 0$. Additionally, it should be noted that the term $\bar{\Gamma} g$ caused by its gravity is considered as the exciting force F , namely, $F = \bar{\Gamma} g$. Therefore, Eqs. (3.7a) and (3.7b) can be rewritten and

expressed as:

$$\ddot{u}(\tau) + 2\xi\dot{u}(\tau) + (1 + \gamma\omega^2)u(\tau) + \beta u(\tau)^3 + \eta u(\tau)^5 - \sigma^2 y(\tau) = F \cos \omega\tau \quad (3.8a)$$

$$\dot{y}(\tau) + \lambda y(\tau) + \dot{u}(\tau) = 0 \quad (3.8b)$$

Furthermore, most nonlinear systems will finally enter into the steady-state vibration state lastly. Currently, the harmonic balance method [108,109,110] and the perturbation method [111,112,113,114] are mainly utilized to solve the electromechanical equations, and theoretically predict their responses. In order to get the theoretical solutions around the non-zero and zero stable equilibrium positions of the symmetric tri-stable PEH in rotational motion, the detailed derivation process via the perturbation method will be presented in next sections.

3.2.2 Solutions for Asymmetric Oscillation

In this part, we will investigate the global inter-well oscillation or the local intra-well oscillation around non-zero stable equilibrium position u_s . For this purpose, the oscillation around the stable nodes by introducing $u_\tau = u(\tau) - u_s$ is used to expand Eqs. (3.8a) and (3.8b) into quantic terms.

As follows:

$$\ddot{u}_\tau + 2\xi\dot{u}_\tau + (\omega_1 + \gamma\omega^2)u_\tau + \gamma_2 u_\tau^2 + \gamma_3 u_\tau^3 + \gamma_4 u_\tau^4 + \gamma_5 u_\tau^5 - \sigma^2 y_\tau = F \cos \omega\tau \quad (3.9a)$$

$$\dot{y}_\tau + \lambda y_\tau + \dot{u}_\tau = 0 \quad (3.9b)$$

where $\omega_1 = \sqrt{1 + 3\beta u_s^2 + 5\eta u_s^4}$ represents the linearized oscillation frequency within a single outer potential well. $\gamma_2 = 3\beta u_s + 10\eta u_s^3$, $\gamma_3 = \beta + 10\eta u_s^2$, $\gamma_4 = 5\eta u_s$ and $\gamma_5 = \eta$ are the nonlinear coefficients, respectively. Moreover, it should be noted that the expanded Eq. (3.9a), including the quadratic and quartic terms, can trap the asymmetric characteristics of the response around one of the outer potential wells. Furthermore, the time dependence is expanded into multiple time scales in the following form:

$$T_n = \varepsilon^n \tau \quad (3.10)$$

where ε is a book-keeping parameter.

Based on the definition of the time scales, the derivatives with respect to time can be written as

$$\frac{d}{d\tau} = D_0 + \varepsilon D_1 + \varepsilon^2 D_2 + O(\varepsilon^3) \quad (3.11)$$

$$\frac{d^2}{d\tau^2} = D_0^2 + 2\varepsilon D_0 D_1 + \varepsilon^2 (D_1^2 + 2D_0 D_2) + O(\varepsilon^3) \quad (3.12)$$

where $D_n = \partial/\partial T_n$ is the partial differential operator. Moreover, the theoretical solutions of the displacement response u_τ and voltage response y in Eqs. (3.9a) and (3.9b) can be written as the second-order expansion:

$$u_\tau(\tau, \varepsilon) = u_0 + \varepsilon u_1 + \varepsilon^2 u_2 + O(\varepsilon^2) \quad (3.13)$$

$$y(\tau, \varepsilon) = y_0 + \varepsilon y_1 + \varepsilon^2 y_2 + O(\varepsilon^2) \quad (3.14)$$

The parameters in Eqs. (3.9a) and (3.9b) are scaled, and we let the effect of the viscous damping at the same order of the perturbation problem as the nonlinear coefficients, electromechanical coupling and equivalent exciting force. As follows:

$$\xi = \varepsilon^2 \xi, \quad \gamma_2 = \varepsilon \gamma_2, \quad \gamma_3 = \varepsilon^2 \gamma_3, \quad \gamma_4 = \varepsilon^2 \gamma_4, \quad \gamma_5 = \varepsilon^2 \gamma_5, \quad \sigma^2 = \varepsilon^2 \sigma^2, \quad F = \varepsilon^2 F \quad (3.15)$$

Additionally, in order to describe the closeness of the rotational frequency ω to the resonance frequency ω_1 of one outer potential well, the detuning parameter α is defined as:

$$\omega = \Omega_1 + \varepsilon^2 \alpha \quad (3.16)$$

It should be noted that $\Omega_1 = \omega_1 \sqrt{1 + \gamma}$ is defined. Next, substituting Eqs. (3.11) - (3.16) into Eqs. (3.9a) and (3.9b), and equating the terms with the identical powers of ε , then we can obtain a set of equations, as follows:

$$\varepsilon^0: D_0^2 u_0 + \Omega_1^2 u_0 = 0 \quad (3.17a)$$

$$D_0 y_0 + \lambda y_0 + D_0 u_0 = 0 \quad (3.17b)$$

$$\varepsilon^1: D_0^2 u_1 + \Omega_1^2 u_1 = -2D_0 D_1 u_0 - \gamma_2 u_0^2 \quad (3.18a)$$

$$D_0 y_1 + \lambda y_1 = -D_0 u_1 - D_1 u_0 - D_1 y_0 \quad (3.18b)$$

$$\varepsilon^2: D_0^2 u_2 + \Omega_1^2 u_2 = -2D_0 D_1 u_1 - D_1^2 u_0 - 2D_0 D_2 u_0 - 2\xi D_0 u_0 - 2\gamma \alpha \Omega_1 u_0 - 2\gamma_2 u_0 u_1 - \gamma_3 u_0^3 - \gamma_4 u_0^4 - \gamma_5 u_0^5 + \sigma^2 y_0 + F_0 \cos \omega \tau \quad (3.19a)$$

$$D_0 y_2 + \lambda y_2 = -D_1 y_1 - D_2 y_0 - D_0 u_2 - D_1 u_1 - D_2 u_0 \quad (3.19b)$$

To get the solutions of the zero-order perturbation problem, Eqs. (3.17a) and (3.17b) can be solved:

$$u_0 = A(T_2) e^{i\Omega_1 T_0} + cc \quad (3.20a)$$

$$y_0 = X_0 A(T_2) e^{i\Omega_1 T_0} + cc \quad (3.20b)$$

where cc is the complex conjugate (the same in the following parts), and $X_0 = -(\Omega_1^2 + i\lambda\Omega_1)/(\lambda^2 + \Omega_1^2)$. A is a complex valued function of the slow time scale $A = A(T_2)$ that is determined by imposing the solvability condition at second order. Based on these results, the solutions of the first-order term in Eqs. (3.18a) and (3.18b) can be solved as the following form:

$$u_1 = \frac{\gamma_2}{\Omega_1^2} \left[\frac{1}{3} A^2 e^{2i\Omega_1 T_0} - 2A\bar{A} \right] + cc \quad (3.21a)$$

$$y_1 = X_1 \frac{\gamma_2}{3\Omega_1^2} A^2 e^{2i\Omega_1 T_0} + cc \quad (3.21b)$$

where \bar{A} denotes the complex conjugate of A , and $X_1 = -(4\Omega_1^2 + 2i\lambda\Omega_1)/(\lambda^2 + 4\Omega_1^2)$. Next, substituting Eqs. (3.20a), (3.20b) and (3.21a) into Eq. (3.19a), then eliminating the secular terms to obtain the following nonlinear first-order differential equation for the unknown A :

$$-2i\Omega_1 D_2 A - 2i\xi\Omega_1 A + \left[\frac{10\gamma_2^2}{3\Omega_1^2} - 3\gamma_3 \right] A^2 \bar{A} - 10\gamma_5 A^3 \bar{A}^2 + \sigma^2 X_0 A + \frac{F}{2} e^{i\alpha T_2} = 0 \quad (3.22)$$

Since $A = A(T_2)$, to solve the corresponding solvability condition of Eq. (3.22), the polar forms are assumed as the following form:

$$A(T_2) = \frac{1}{2} a(T_2) e^{i\psi(T_2)}, \quad \bar{A}(T_2) = \frac{1}{2} a(T_2) e^{-i\psi(T_2)} \quad (3.23)$$

where a and ψ are real functions of the slow time scale T_2 . Next, substituting Eq. (3.23) into Eq. (3.22), the real part and the imaginary part will be respectively obtained, as follows:

$$D_2 a = -(\xi + \xi_e) a + \frac{F}{2\Omega_1} \sin \phi \quad (3.24a)$$

$$a D_2 \phi = (\alpha - \gamma_s) a - N_{eff} a^3 - \frac{5\gamma_5}{16\Omega_1} a^5 + \frac{F}{2\Omega_1} \cos \phi \quad (3.24b)$$

where $\phi = \alpha T_2 - \psi$ is defined. $\xi_e = \sigma^2 \lambda / 2(\lambda^2 + \Omega_1^2)$ is the electric damping,

$\gamma_s = \sigma^2 \Omega_1 / 2(\lambda^2 + \Omega_1^2)$ is the linear shift in the natural frequency of the harvester due to the

electric coupling, and $N_{eff} = \frac{1}{\Omega_1} \left[\frac{3}{8} \gamma_3 - \frac{5\gamma_2^2}{12\Omega_1^2} \right]$ represents the effective nonlinear coefficient.

For the nonlinear vibration of the harvester, we will focus on the steady-state response. All the time derivatives of Eqs. (3.24a) and (3.24b) are assumed to be zero, therefore, the nonlinear

frequency-response function of the steady-state displacement can be obtained.

$$\xi_{eff}^2 a_1^2 + \left[(\alpha - \gamma_s) a_1 - N_{eff} a_1^3 - \frac{5\gamma_5}{16\Omega_1} a_1^5 \right]^2 = \frac{F^2}{4\Omega_1^2} \quad (3.25)$$

where $\xi_{eff} = \xi + \xi_e$ is the effective damping and a_1 denotes the amplitude of the steady-state displacement. According to Eq. (3.25), we can analytically solve the steady-state amplitude for the given excitation force amplitude F . The steady-state solutions of the tip displacement $u_\tau(\tau)$ and output voltage $y(\tau)$ can be written in the following forms:

$$u_\tau(\tau) = \frac{1}{\Omega_1^2} \left(-\frac{\gamma_2}{2} a_1^2 - \frac{3\gamma_4}{8} a_1^4 \right) + a_1 \cos(\omega\tau - \phi_0) + \frac{\gamma_2 a_1^2 + \gamma_4 a_1^4}{6\Omega_1^2} \cos(2\omega\tau - 2\phi_0) \quad (3.26a)$$

$$y(\tau) = \frac{\Omega_1}{\sqrt{\lambda^2 + \Omega_1^2}} a_1 \sin(\omega\tau - \phi_0 - \psi_1) + \frac{\gamma_2 a_1^2 + \gamma_4 a_1^4}{3\Omega_1 \sqrt{\lambda^2 + 4\Omega_1^2}} \sin(2\omega\tau - 2\phi_0 - \psi_2) \quad (3.26b)$$

$$\text{where } \phi_0 = \tan^{-1} \left(\frac{\xi_{eff}}{\Lambda a_1^2 + (\gamma_s - \alpha)} \right), \quad \Lambda = N_{eff} + \frac{5\gamma_5 a_1^2}{16\Omega_1}, \quad \psi_n = \tan^{-1} \left(\frac{n\Omega_1}{\lambda} \right).$$

Stability analysis of solutions for asymmetric oscillation

To demonstrate the stability of the steady-state solution for the asymmetric oscillation, the perturbation terms could be introduced as [115]:

$$a = a_1 + a_0 \quad (3.27a)$$

$$\phi = \phi_1 + \phi_0 \quad (3.27b)$$

where a_1 and ϕ_1 are governed by Eqs. (3.24a) and (3.24b) under the steady-state, respectively. a_0 and ϕ_0 are the perturbation terms, respectively.

Substituting Eqs. (3.27a) and (3.27b) into Eqs. (3.24a) and (3.24b), whose linearization modulation at a_0 and ϕ_0 can be obtained via neglect the nonlinear terms, and expressed as follows:

$$D_2 a_0(T_2) = -(\xi + \xi_e) a_0 + \frac{F}{2\Omega_1} \cos \phi_1 \cdot \phi_0 \quad (3.28a)$$

$$a_1 D_2 \phi_0(T_2) = \left[(\alpha - \gamma_s) - 3N_{eff} a_1^2 - \frac{25\gamma_5}{16\Omega_1} a_1^4 \right] a_0 + \frac{F}{2\Omega_1} \sin \phi_1 \cdot \phi_0 \quad (3.28b)$$

Based on the Routh-hurwitz criterion [116], the steady-state solutions of Eqs. (3.28a) and (3.28b)

are asymptotically stable when the following two equations are satisfied. Thus, the stability condition can be obtained and expressed by the following equations:

$$I_1 + I_4 < 0 \quad (3.29a)$$

$$I_1 I_4 - I_2 I_3 > 0 \quad (3.29b)$$

$$\text{Where } I_1 = -(\xi + \xi_e), \quad I_2 = \frac{F}{2\Omega_1} \cos \phi_1, \quad I_3 = \frac{\alpha - \gamma_s}{a_1} - 3N_{eff} a_1 - \frac{25\gamma_1}{16\Omega_1} a_1^3 \quad \text{and} \quad I_4 = \frac{F}{2a_1\Omega_1} \sin \phi_1$$

3.2.3 Solution for Symmetric Oscillation

In this part, the global inter-well oscillation or the local intra-well oscillation around zero stable equilibria will be investigated, namely, $u_s = 0$. To this end, we express the nearness of the rotational frequency ω from the resonance frequency ω_2 within the middle potential well using a detuning parameter α_2 , as follows:

$$\omega^2 = \omega_2^2 + \varepsilon \alpha_2 \quad (3.30)$$

The parameters in Eqs. (3.8a) and (3.8b) are also scaled, and we let the effect of the viscous damping at the same order of the perturbation problem as the nonlinear coefficients, electromechanical coupling and the equivalent exciting force. The terms are shown as:

$$\xi = \varepsilon \xi, \quad \beta = \varepsilon \beta, \quad \eta = \varepsilon \eta, \quad \sigma^2 = \varepsilon \sigma^2, \quad F = \varepsilon F \quad (3.31)$$

It should be noted that $\Omega_2 = \omega \sqrt{1 + \gamma}$ is defined, thus, substituting Eqs. (3.30) and (3.31) into Eqs. (3.8a) and (3.8b), then we obtain:

$$\ddot{u} + 2\varepsilon \xi \dot{u} + (\Omega_2^2 - \varepsilon \alpha_2) u_\tau + \varepsilon \beta u^3 + \varepsilon \eta u^5 - \varepsilon \sigma^2 y = \varepsilon F \cos \omega \tau \quad (3.32a)$$

$$\dot{y} + \lambda y + \dot{u} = 0 \quad (3.32b)$$

Then equating the terms with the identical powers in ε , then we obtain a set of equations as follows:

$$\varepsilon^0: D_0^2 u_0 + \Omega_2^2 u_0 = 0 \quad (3.33a)$$

$$D_0 y_0 + \lambda y_0 + D_0 u_0 = 0 \quad (3.33b)$$

$$\varepsilon^1: D_0^2 u_1 + \Omega_2^2 u_1 = -2D_0 D_1 u_0 - 2\xi D_0 u_0 - \beta u_0^3 - \eta u_0^5 + \alpha_2 u_0 + \sigma^2 y_0 + F \cos \omega \tau \quad (3.34a)$$

$$D_0 y_1 + \lambda y_1 = -D_1 y_0 - D_0 u_1 - D_1 u_0 \quad (3.34b)$$

For the solutions of the zero-order perturbation problem, Eqs. (3.34a) and (3.34b) can be solved,

as follows:

$$u_o = A(T_1)e^{i\Omega_2 T_0} + cc \quad (3.35a)$$

$$y_o = X_0 A(T_1)e^{i\Omega_2 T_0} + cc \quad (3.35b)$$

where $X_0 = -(\Omega_2^2 + i\lambda\Omega_2)/(\lambda^2 + \Omega_2^2)$. Similarly, the nonlinear frequency-response equation of the steady-state displacement can also be obtained, as follows:

$$(2\Omega_2 \xi_{eff} a_2)^2 + \left[(\alpha_2 - \gamma_s) a_2 - \frac{3\beta}{4} a_2^3 - \frac{5\eta}{8} a_2^5 \right]^2 = F^2 \quad (3.36)$$

where $\xi_{eff} = \xi + \xi_e$ is the effective damping. $\xi_e = \sigma^2 \lambda / 2 (\lambda^2 + \Omega_2^2)$ is the electric damping.

$\gamma_s = \sigma^2 \Omega_2^2 / (\lambda^2 + \Omega_2^2)$ is the linear shift in the natural frequency of the harvester due to the electrical coupling. Eliminating secular terms from Eq. (3.36), we can obtain:

$$D_0^2 u_1 + \Omega_2^2 u_1 = -\left(\frac{\beta a_2^3}{8} + \frac{5\eta a_2^5}{32} \right) e^{i3(\Omega_2 T_0 + \psi_0)} - \frac{\eta a_2^5}{32} e^{i5(\Omega_2 T_0 + \psi_0)} + cc \quad (3.37)$$

The particular solution of Eq. (3.37) can be obtained:

$$u_1 = \left(\frac{\beta a_2^3}{64\Omega_2^2} + \frac{5\eta a_2^5}{256\Omega_2^2} \right) e^{i3(\Omega_2 T_0 + \psi_0)} + \frac{\eta a_2^5}{768\Omega_2^2} e^{i5(\Omega_2 T_0 + \psi_0)} + cc \quad (3.38a)$$

$$y_1 = X_1 \left(\frac{\beta a_2^3}{64\Omega_2^2} + \frac{5\eta a_2^5}{256\Omega_2^2} \right) e^{i3(\Omega_2 T_0 + \psi_0)} + X_2 \frac{\eta a_2^5}{768\Omega_2^2} e^{i5(\Omega_2 T_0 + \psi_0)} + cc \quad (3.38b)$$

where $X_1 = -(9\Omega_1^2 + 3i\lambda\Omega_2)/(\lambda^2 + 9\Omega_2^2)$ and $X_2 = -(25\Omega_1^2 + 5i\lambda\Omega_2)/(\lambda^2 + 25\Omega_2^2)$.

Similarly, the steady-state solutions of the tip displacement and the output voltage can be written in the following forms:

$$u(\tau) = a_2 \cos(\Omega_2 \tau + \psi_0) + \left(\frac{\beta a_2^3}{32\Omega_2^2} + \frac{5\eta a_2^5}{128\Omega_2^2} \right) \cos(3\Omega_2 \tau + 3\psi_0) + \frac{\eta a_2^5}{384\Omega_2^2} \cos(5\Omega_2 \tau + 5\psi_0) \quad (3.39a)$$

$$y(\tau) = \frac{\Omega_2}{\sqrt{\lambda^2 + \Omega_2^2}} a_2 \sin(\Omega_2 \tau + \psi_0 - \Phi_1) + \frac{3a_2^3}{32\Omega_2 \sqrt{\lambda^2 + 9\Omega_2^2}} \left(\beta + \frac{5\eta a_2^2}{4} \right) \sin(3\Omega_2 \tau + 3\psi_0 - \Phi_3) \\ + \frac{5\eta a_2^5}{384\Omega_2 \sqrt{\lambda^2 + 25\Omega_2^2}} \sin(5\Omega_2 \tau + 5\psi_0 - \Phi_5) \quad (3.39b)$$

Where $\psi_0 = \tan^{-1} \left(\frac{16\xi_{eff}\Omega_2}{8(\gamma_s - \alpha_2) + 6\beta a_2^2 + 5\eta a_2^4} \right)$, $\Phi_n = \tan^{-1} \left(\frac{n\Omega_2}{\lambda} \right)$.

3.3 Asymmetric Tri-stable Energy Harvester in Rotational Motion

As mentioned in section 3.3, when h_1 is equal to h_2 , the stable positions 1 and 3 are symmetric about the stable position 2. In some situations, as shown in Figure 3.4, the potential barriers of symmetric tri-stable PEH is still high for inter-well oscillation. Thus, the asymmetric tri-stable PEH is proposed to reduce the potential barrier as h_1 is not equal to h_2 . Thus, the equivalent restoring force F_r can be rewritten as:

$$F_r = K_e q(t) + F_m = K_1 q(t) + K_2 q(t)^2 + K_3 q(t)^3 + K_4 q(t)^4 + K_5 q(t)^5 \quad (3.40)$$

where K_1 is the linear coefficient, and K_2 , K_3 , K_4 and K_5 represent the nonlinear coefficient, respectively. The related potential energy function can be expressed as:

$$U = \frac{1}{2} K_1 q(t)^2 + \frac{1}{3} K_2 q(t)^3 + \frac{1}{4} K_3 q(t)^4 + \frac{1}{5} K_4 q(t)^5 + \frac{1}{6} K_5 q(t)^6 \quad (3.41)$$

Furthermore, the potential energy curves of asymmetric ($h_1 = 20$ mm and $h_2 = 10$ mm) and symmetric ($h_1 = 20$ mm and $h_2 = 20$ mm) tri-stable PEH are shown in Figure 3.5. It can be found that the bilateral potential barriers of symmetric tri-stable PEH are the same. However, the Barrier 1 and Barrier 2 of the asymmetric tri-stable PEH are different, which means that the asymmetric tri-stable PEH can overcome the lower potential Barrier 1 to achieve inter-well oscillation between two adjacent potential wells in low-frequency rotational motion. When the rotational speed reaches the threshold value for crossing the higher Barrier 2, the high-energy inter-well oscillation can be induced, resulting in the high-energy output voltage.

Additionally, the governing equation of the asymmetric tri-stable PEH can be rewritten as:

$$M_e \ddot{q}(t) + C \dot{q}(t) + K_c \theta^2 q(t) + F_r + \chi \ddot{\theta} - \mathcal{G}_p v(t) = [-\Gamma g + F(t)] \cos \theta \quad (3.42a)$$

$$C_p \dot{v}(t) + R_l^{-1} v(t) + \mathcal{G}_p \dot{q}(t) = 0 \quad (3.42b)$$

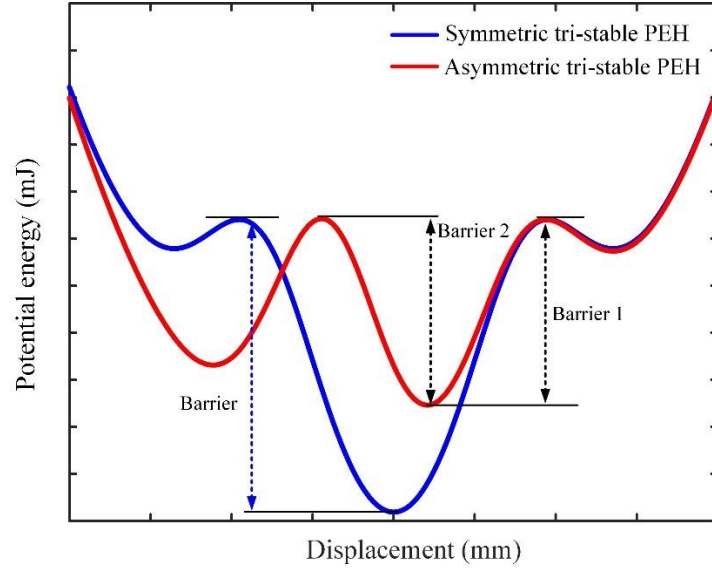


Figure 3.5 The potential energy curves of an asymmetric tri-stable (red line) and symmetric tri-stable (blue line) PEH.

3.4 Quad-stable Energy Harvester in Rotational Motion

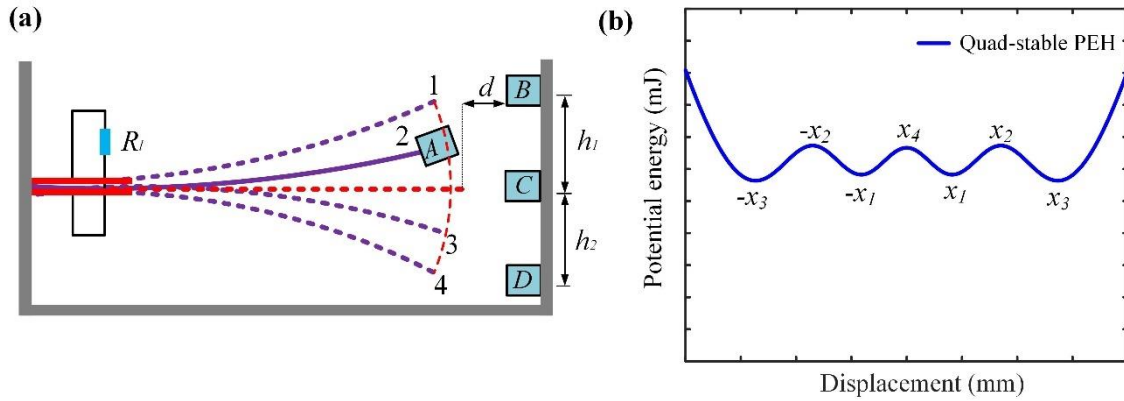


Figure 3.6 (a) The schematic diagram of a quad-stable PEH; (b) the related potential energy of a quad-stable PEH.

Based on the foundation of the tri-stable PEH, one magnet is added to further reduce the potential barrier. Thus, the quad-stable PEH can be achieved with with four equilibrium positions as shown in Figure 3.6(a). Adjusting the parameters d , h_1 and h_2 , the quad-stable PEH can be obtained. The corresponding potential energy curves of quad-stable PEH is shown in Figure 3.6(b), respectively. When h_1 is equal to h_2 , the potential wells are symmetric about the middle

unstable position. Where $x = \pm x_1$ and $x = \pm x_3$ are the two inner and two outer stable equilibrium positions, respectively. $x_4 = 0$ represents the middle unstable equilibrium position, and $x = \pm x_2$ are the two outer unstable equilibrium positions. From Figure 3.6(b), the potential barriers of the quad-stable PEH is lower than those of the bi-stable and tri-stable ones, which means that even in low-level excitation the quad-stable PEH can achieve the inter-well oscillation among two potential wells easier compared with the others.

Similarly, when it is applied in rotational motion, the related time-varying potential well function is shown in Figure 3.7, from which we can notice that in rotational motion, the periodic gravity component can let the quad-stable PEH across the potential barrier easier to achieve inter-well oscillation among potential wells, which leads to the high output voltage.

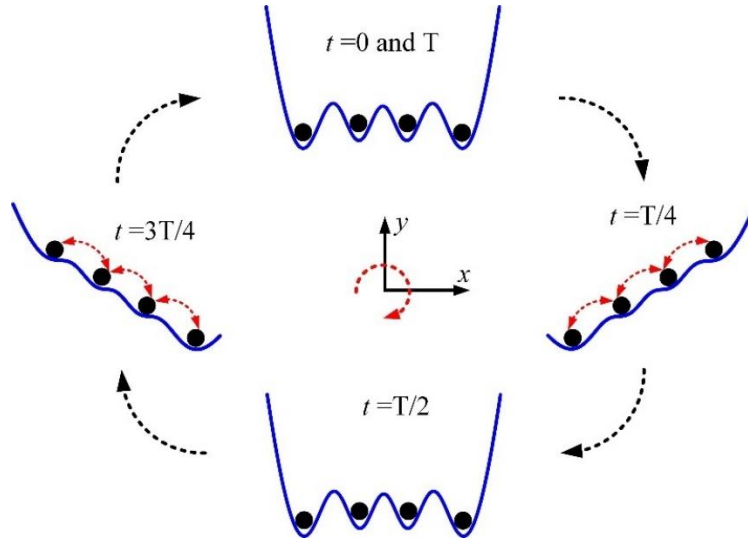


Figure 3.7 The time-varying potential well function of a quad-stable PEH in one period of rotational motion.

Furthermore, the equivalent restoring force F_r can be expanded into 7th polynomial due to four stable and three unstable equilibrium positions as shown in Figure 3.6(b).

$$F_r = K_e q(t) + F_m = K_1 q(t) + K_3 q(t)^3 + K_5 q(t)^5 + K_7 q(t)^7 \quad (3.43)$$

where K_1 is the linear coefficient, and K_3 , K_5 and K_7 represent nonlinear coefficients of the restoring force respectively. Thus, Eq. (3.43) can be rewritten as an expression comprising of all equilibrium positions

$$F_r = K_7 (x^2 - x_1^2)(x^2 - x_2^2)(x^2 - x_3^2)(x - x_4) \quad (3.44)$$

Thus, the relationship between the coefficients and equilibrium positions, can be expressed as:

$$K_5 = -K_7 (x_1^2 + x_2^2 + x_3^2) \quad (3.45a)$$

$$K_3 = K_7 (x_1^2 x_2^2 + x_1^2 x_3^2 + x_2^2 x_3^2) \quad (3.45b)$$

$$K_1 = -K_7 x_1^2 x_2^2 x_3^2 \quad (3.45c)$$

The related potential energy function of the quad-stable PEH can be written as:

$$U = \frac{1}{2} K_1 q(t)^2 + \frac{1}{4} K_3 q(t)^4 + \frac{1}{6} K_5 q(t)^6 + \frac{1}{8} K_7 q(t)^8 \quad (3.46)$$

3.4.1 Theoretical Model

Similarly, based on the proposed theoretical model, the governing equations of quad-stable PEH in rotational motion can be expressed as:

$$M_e \ddot{q}(t) + C \dot{q}(t) + K_c \theta^2 q(t) + F_r + \chi \ddot{\theta} - \mathcal{G}_p v(t) = [-\Gamma g + F(t)] \cos \theta \quad (3.47a)$$

$$C_p \dot{v}(t) + R_l^{-1} v(t) + \mathcal{G}_p \dot{q}(t) = 0 \quad (3.47b)$$

For simplicity, we also firstly consider the quad-stable PEH under constant rotational speed and no external excitation. Thus, the electromechanical Eqs. (3.47a) and (3.47b) can be rewritten as non-dimensional equations by introducing the following dimensionless quantities:

$$u(\tau) = \frac{q(t)}{l_c}; \quad \tau = t\omega_n; \quad y(\tau) = \frac{C_p}{\mathcal{G}_p l_c} v(t) \quad (3.48)$$

where l_c is the length scale for nondimensionalizing the displacement, and $\omega_n = \sqrt{K_l/M_e}$ is the nominal short-circuit frequency. Thus, the following non-dimensional equations can be derived:

$$\ddot{u}(\tau) + 2\xi \dot{u}(\tau) + (1 + \gamma \omega^2) u(\tau) + k_3 u^3(\tau) + k_5 u^5(\tau) + k_7 u^7(\tau) - \sigma^2 y(\tau) = F \cos(\omega \tau) \quad (3.49a)$$

$$\dot{y}(\tau) + \lambda y(\tau) + \dot{u}(\tau) = 0 \quad (3.49b)$$

where other variables are as follows:

$$\begin{aligned} \xi &= \frac{C}{2\sqrt{M_e K_1}}; & \sigma^2 &= \frac{\mathcal{G}_p^2}{C_p K_1}; & \gamma &= \frac{K_c}{M_e}; & \omega &= \frac{\dot{\theta}}{\omega_n}; & k_3 &= \frac{K_3}{K_1} l_c^2 \\ k_5 &= \frac{K_5}{K_1} l_c^4; & k_7 &= \frac{K_7}{K_1} l_c^6; & \lambda &= \frac{1}{C_p R_l \omega_n}; & F &= -\frac{\Gamma g}{M_e}. \end{aligned}$$

3.4.2 Theoretical Solutions by Perturbation Method

Similarly, in order to get the theoretical solutions of the proposed mathematical model around the stable equilibrium positions of the quad-stable PEH in rotational motion, the detailed derivation process will be presented. In this paper, we mainly concern the global inter-well oscillation around the stable equilibria. Thus, according to the methods of multiple scales, the approximate analytical solution of Eqs. (3.49a) and (3.49b) are obtained in the following parts. Firstly, the time dependence is expanded into multiple time scales in the form:

$$T_n = \varepsilon^n \tau \quad (3.50)$$

where ε is a book-keeping parameter. Moreover, T_0 represents the fast time scale, and T_n ($n=1, 2, \dots$) are slow time scales. Based on the definition of the time scales, the derivatives with respect to time can be written as

$$\frac{d}{d\tau} = D_0 + \varepsilon D_1 + \varepsilon^2 D_2 + O(\varepsilon^3) \quad (3.51a)$$

$$\frac{d^2}{d\tau^2} = D_0^2 + 2\varepsilon D_0 D_1 + \varepsilon^2 (D_1^2 + 2D_0 D_2) + O(\varepsilon^3) \quad (3.51b)$$

where $D_n = \partial/\partial T_n$ is the symbol of the partial differential operator. Moreover, the solutions of the displacement response $u(\tau, \varepsilon)$ and the voltage response $y(\tau, \varepsilon)$ in Eqs. (3.49a) and (3.49b) can be written as the second-order expansion:

$$u(\tau, \varepsilon) = u_0 + \varepsilon u_1 + \varepsilon^2 u_2 + O(\varepsilon^3) \quad (3.52a)$$

$$y(\tau, \varepsilon) = y_0 + \varepsilon y_1 + \varepsilon^2 y_2 + O(\varepsilon^3) \quad (3.52b)$$

Additionally, the parameters in Eqs. (3.49a) and (3.49b) are also scaled, and we define the effect of the mechanical damping at the same order of the perturbation problem as the nonlinear coefficients, electromechanical coupling and excitation force.

$$\xi = \varepsilon \xi, \quad k_3 = \varepsilon k_3, \quad k_5 = \varepsilon k_5, \quad k_7 = \varepsilon k_7, \quad \sigma^2 = \varepsilon \sigma^2, \quad F = \varepsilon F \quad (3.53)$$

Next, we express the nearness of the rotational frequency ω from the resonance frequency ω_2 within the potential well via a detuning parameter α_2

$$\omega^2 = \omega_2^2 + \varepsilon \alpha_2 \quad (3.54)$$

In this section, it should be noted that $\Omega_2 = \omega \sqrt{1 + \gamma}$ is defined, thus, substituting the Eqs. (3.53) and (3.54) into Eqs. (3.49a) and (3.49b), then we can get

$$\ddot{u} + 2\varepsilon\xi\dot{u} + \left[\Omega_2^2 - \varepsilon\alpha_2\right]u + \varepsilon k_3 u^3 + \varepsilon k_5 u^5 + \varepsilon k_7 u^7 - \varepsilon\sigma^2 y = \varepsilon F \cos \omega\tau \quad (3.55a)$$

$$\dot{y} + \lambda y + \dot{u} = 0 \quad (3.55b)$$

Next, substituting the Eqs. (3.50) - (3.54) into the governing equations Eqs. (3.55a) and (3.55b), and equating the terms with the identical powers in ε , then we obtain a set of equations as follows:

$$\varepsilon^0: D_0^2 u_0 + \Omega_2^2 u_0 = 0 \quad (3.56a)$$

$$D_0 y_0 + \lambda y_0 + D_0 u_0 = 0 \quad (3.56b)$$

$$\varepsilon^1: D_0^2 u_1 + \Omega_2^2 u_1 = -2D_0 D_1 u_0 - 2\xi D_0 u_0 - k_3 u_0^3 - k_5 u_0^5 - k_7 u_0^7 + \alpha_2 u_0 + \sigma^2 y_0 + F \cos \omega\tau \quad (3.57a)$$

$$D_0 y_1 + \lambda y_1 = -D_1 y_0 - D_0 u_1 - D_1 u_0 \quad (3.57b)$$

The solutions of the zero-order perturbation problem, Eqs. (3.56a) and (3.56b) can be solved

$$u_0 = A(T_1) e^{i\Omega_2 T_0} + cc \quad (3.58a)$$

$$y_0 = X_0 A(T_1) e^{i\Omega_2 T_0} + cc \quad (3.58b)$$

where cc is the complex conjugate (same in the following part), and $X_0 = -(\Omega_2^2 + i\lambda\Omega_2)/(\lambda^2 + \Omega_2^2)$. It should be noted that $A(T_1)$ is the complex-valued function without relationship to the time T_0 . Next, substituting the Eqs. (3.58a) and (3.58b) into Eq. (3.57a), then eliminating the secular terms to obtain the following nonlinear first-order differential equation for the unknown A :

$$-2i\Omega_2 D_1 A - 2i\xi\Omega_2 A - 3k_3 A^2 \bar{A} - 10k_5 A^3 \bar{A}^2 - 35k_7 A^4 \bar{A}^3 + \sigma^2 X_0 A + \alpha_2 A + \frac{F}{2} = 0 \quad (3.59)$$

where \bar{A} denotes the complex conjugate of A , and $A = A(T_1)$. To obtain the solution of Eq. (3.59), the polar forms are assumed as following forms:

$$A(T_1) = \frac{1}{2} a(T_1) e^{i\psi(T_1)}, \quad \bar{A}(T_1) = \frac{1}{2} a(T_1) e^{-i\psi(T_1)} \quad (3.60)$$

Next, substitute the Eq. (3.60) into Eq. (3.59), then the real part and the imaginary part will be respectively obtained, as follows:

$$D_1 a = -(\xi + \xi_e) a - \frac{F}{2\Omega_2} \sin \psi \quad (3.61a)$$

$$a D_1 \psi = \frac{1}{2\Omega_2} \left[\frac{3}{4} k_3 a^3 + \frac{5}{8} k_5 a^5 + \frac{35}{64} k_7 a^7 + (\gamma_s - \alpha_2) a \right] - \frac{F \cos \psi}{2\Omega_2} \quad (3.61b)$$

where $\xi_e = \sigma^2 \lambda / 2 (\lambda^2 + \Omega_2^2)$ is the electric damping, $\gamma_s = \sigma^2 \Omega_2 / 2 (\lambda^2 + \Omega_2^2)$ is the linear shift in the natural frequency of the harvester due to the electric coupling. As for the nonlinear vibration of the harvester, we will focus on the state of steady-state response. All time derivatives of the Eqs. (3.61a) and (3.61b) are assumed to be zero, therefore, the nonlinear frequency-response function of the steady-state displacement can be obtained

$$(2\Omega_2 \xi_{eff} a_0)^2 + \left[(\gamma_s - \alpha_2) a_0 + \frac{3k_3}{4} a_0^3 + \frac{5k_5}{8} a_0^5 + \frac{35k_7}{64} a_0^7 \right] = F^2 \quad (3.62)$$

Where $\xi_{eff} = \xi + \xi_e$ is the effective damping and a_0 denotes the amplitude of the steady-state displacement. According to Eq. (3.62), we can solve analytically for the steady-state amplitude for the given excitation force amplitude F . Next, eliminating secular terms from Eq. (3.57a), we can obtain

$$D_0^2 u_1 + \Omega_2^2 u_1 = - \left(\frac{k_3 a_0^3}{8} + \frac{5k_5 a_0^5}{32} + \frac{35k_7 a_0^7}{128} \right) e^{i3(\Omega_2 T_0 + \psi_0)} - \left(\frac{k_5 a_0^5}{32} + \frac{7k_7 a_0^7}{128} \right) e^{i5(\Omega_2 T_0 + \psi_0)} + cc \quad (3.63)$$

Next, the particular solution of Eq. (3.63) can be obtained

$$u_1 = \left(\frac{k_3 a_0^3}{64\Omega_2^2} + \frac{5k_5 a_0^5}{256\Omega_2^2} + \frac{21k_7 a_0^7}{1024\Omega_2^2} \right) e^{i3(\Omega_2 T_0 + \psi_0)} + \left(\frac{k_5 a_0^5}{768\Omega_2^2} + \frac{7k_7 a_0^7}{3072\Omega_2^2} \right) e^{i5(\Omega_2 T_0 + \psi_0)} + cc \quad (3.64a)$$

$$y_1 = X_1 \left(\frac{k_3 a_0^3}{64\Omega_2^2} + \frac{5k_5 a_0^5}{256\Omega_2^2} + \frac{21k_7 a_0^7}{1024\Omega_2^2} \right) e^{i3(\Omega_2 T_0 + \psi_0)} + X_2 \left(\frac{k_5 a_0^5}{768\Omega_2^2} + \frac{7k_7 a_0^7}{3072\Omega_2^2} \right) e^{i5(\Omega_2 T_0 + \psi_0)} + cc \quad (3.64b)$$

where $X_1 = -(9\Omega_2^2 + 3i\lambda\Omega_2) / (\lambda^2 + 9\Omega_2^2)$, and $X_2 = -(25\Omega_2^2 + 5i\lambda\Omega_2) / (\lambda^2 + 25\Omega_2^2)$.

Similarly, the steady-state solutions of the tip displacement $u(\tau, \varepsilon)$ and the output voltage $y(\tau, \varepsilon)$ can be written in the following forms:

$$u(\tau) = a_0 \cos(\Omega_2 \tau + \psi_0) + \frac{a_0^3}{32\Omega_2^2} \left(k_3 + \frac{5k_5 a_0^2}{4} + \frac{21k_7 a_0^4}{16} \right) \cos(3\Omega_2 \tau + 3\psi_0) + \frac{a_0^5}{384\Omega_2^2} \left(k_5 + \frac{7k_7 a_0^2}{4} \right) \cos(5\Omega_2 \tau + 5\psi_0) \quad (3.65a)$$

$$y(\tau) = \frac{\Omega_2 a_0}{\sqrt{\lambda^2 + \Omega_2^2}} \sin(\Omega_2 \tau + \psi_0 - \Phi_1) + \frac{3a_0^3}{32\Omega_2 \sqrt{\lambda^2 + 9\Omega_2^2}} \left(k_3 + \frac{5k_5 a_0^2}{4} + \frac{21k_7 a_0^4}{16} \right) \sin(3\Omega_2 \tau + 3\psi_0 - \Phi_3) + \frac{5a_0^5}{384\Omega_2 \sqrt{\lambda^2 + 25\Omega_2^2}} \left(k_5 + \frac{7k_7 a_0^2}{4} \right) \sin(5\Omega_2 \tau + 5\psi_0 - \Phi_5) \quad (3.65b)$$

Where $\psi_0 = \tan^{-1} \left(\frac{128\xi_{eff}\Omega_2}{64(\gamma_s - \alpha) + 48k_3a_0^2 + 40k_5a_0^4 + 35k_7a_0^6} \right)$, $\Phi_n = \tan^{-1} \left(\frac{n\Omega_2}{\lambda} \right)$.

3.4.3 Stability Analysis of Solutions

To demonstrate the stability of the steady-state solution for asymmetric oscillation, the perturbation terms could be introduced as:

$$a = a_1 + a_0 \quad (3.66)$$

$$\phi = \phi_1 + \phi_0 \quad (3.67)$$

Where a_1 and ϕ_1 are governed by the Eqs. (3.61a) and (3.61b) under the steady-state cases. a_0 and ϕ_0 are the perturbation terms.

Substituting Eqs. (3.66) and (3.67) into Eqs. (3.61a) and (3.61b), whose the linearization modulation at a_0 and ϕ_0 can be obtained via neglect the nonlinear terms, and expressed as follows:

$$D_2a_0(T_2) = -(\xi + \xi_e)a_0 + \frac{F}{2\Omega_1} \cos \phi_1 \cdot \phi_0 \quad (3.68a)$$

$$a_1D_2\phi_0(T_2) = \left[(\alpha - \gamma_s) - 3N_{eff}a_1^2 - \frac{25\gamma_5}{16\Omega_1}a_1^4 \right] a_0 + \frac{F}{2\Omega_1} \sin \phi_1 \cdot \phi_0 \quad (3.68b)$$

Based on the Routh-hurwitz criterion [116], the steady-state solutions of the Eqs. (3.68a) and (3.68b) are asymptotically stable when the following two inequations are satisfied. Thus, the stability condition can be obtained and expressed by the following inequations:

$$I_1 + I_4 < 0 \quad (3.69a)$$

$$I_1I_4 - I_2I_3 < 0 \quad (3.69b)$$

where $I_1 = -(\xi + \xi_e)$, $I_2 = \frac{F}{2\Omega_1} \cos \phi_1$, $I_3 = \frac{\alpha - \gamma_s}{a_1} - 3N_{eff}a_1^2 - \frac{25\gamma_5}{16\Omega_1}a_1^4$ and $I_4 = \frac{F}{2a_1\Omega_1} \sin \phi_1$

3.5 Parametric studies

In section 2.4.1, the nonlinear magnetic force and magnetic potential energy of a quad-stable PEH is derived and calculated. It should be noted that for the bi-stable PEH, there is only one external magnet C. For the tri-stable PEH, there are two external magnets (B and D). For the quad-stable

PEH, there are three external magnets (B, C and D). Thus, Eq. (2.47), the calculation model of the quad-stable, is also suitable for the bi-stable and tri-stable PEHs.

In order to investigate the influence of the nonlinear magnetic force on the energy harvesting performance of PEHs in rotational motion, the related potential energies and restoring forces of the bi-stable, tri-stable and quad-stable PEHs are shown in Figure 3.8, Figure 3.9 and Figure 3.10, respectively. Note that all the numerical results are calculated by MATLAB software, and the material properties and dimensions of these PEHs are listed in Table 3.1 and Table 3.2, which are also the same to those in experiments.

Table 3.1 Parameters of the piezoelectric beam

Parameters	Symbol	Value
Cantilever beam		
Length \times Width \times Thickness	$L \times b \times t_b$	$95 \times 12 \times 0.20 \text{ mm}^3$
Young's modulus	E_b	210 Gpa
Density	ρ_b	7765 Kg/m ³
Piezoelectric patch		
Length \times Width \times Thickness	$l_p \times b_p \times t_p$	$25 \times 12 \times 0.13 \text{ mm}^3$
Young's modulus	E_p	66 Gpa
Density	ρ_p	7800 Kg/ m ³
Coupling coefficient	d_{31}	$-320 \times 10^{-12} \text{ C/N}$
Permittivity constant	ϵ_{33}	$4000 \epsilon_0$
Permittivity of free space	ϵ_0	$8.854 \times 10^{-12} \text{ F/m}$

Table 3.2 Parameters of Bi-stable, tri-stable and quad-stable PEHs

Parameters	Symbol	Value
Permanent magnets		
Density	$\rho_A \quad \rho_B \quad \rho_C \quad \rho_D$	7500 Kg/ m ³
Magnet's residual flux density	B_r	1.2 T
Permeability of free space	μ_0	$4\pi \times 10^{-7}$
Magnet A	$D \times t_A$	D12 \times 7.1 mm ³
Magnet B	$D \times t_B$	D12 \times 1.7 mm ³
Magnet C	$D \times t_C$	D12 \times 1.7 mm ³
Magnet D	$D \times t_D$	D12 \times 1.7 mm ³

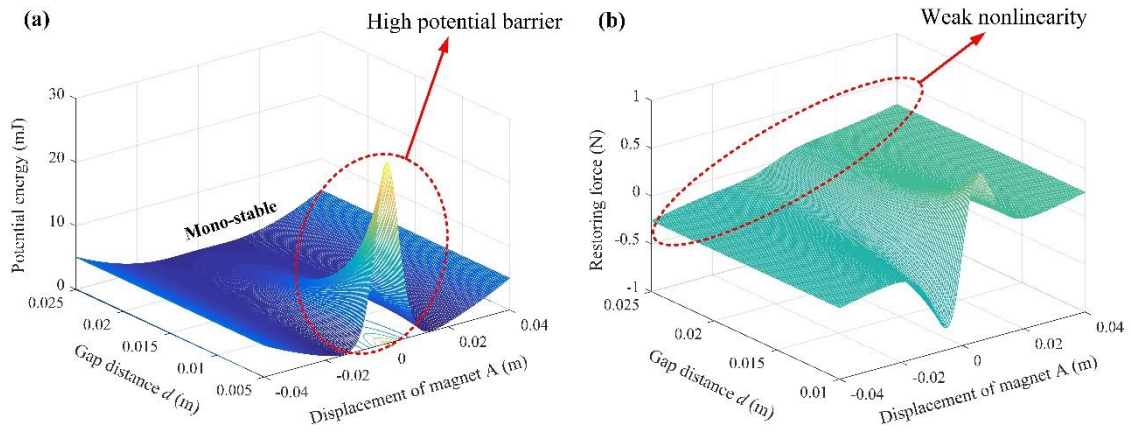


Figure 3.8 The bi-stable PEH: (a) The potential energy; (b) the magnetic force in transverse direction.

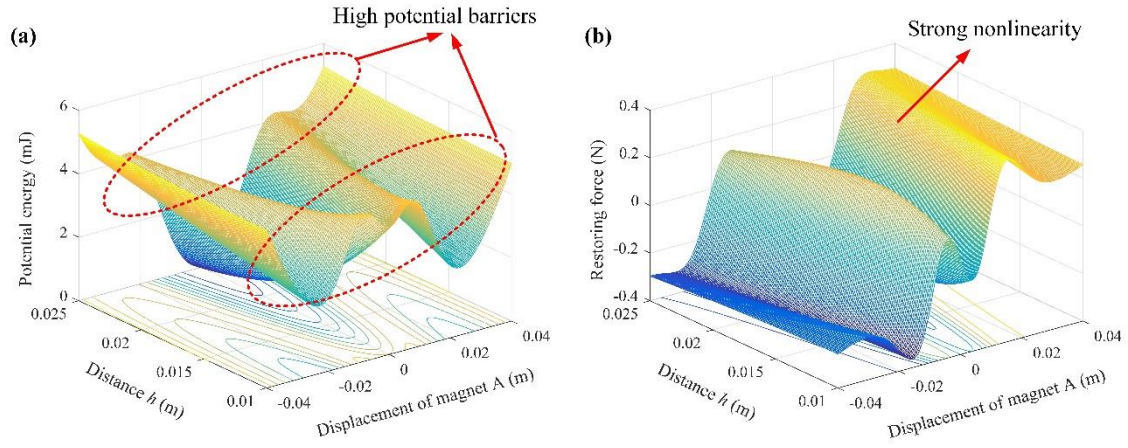


Figure 3.9 The tri-stable PEH: (a) The potential energy; (b) the magnetic force in transverse direction, when gap distance $d = 15$ mm.

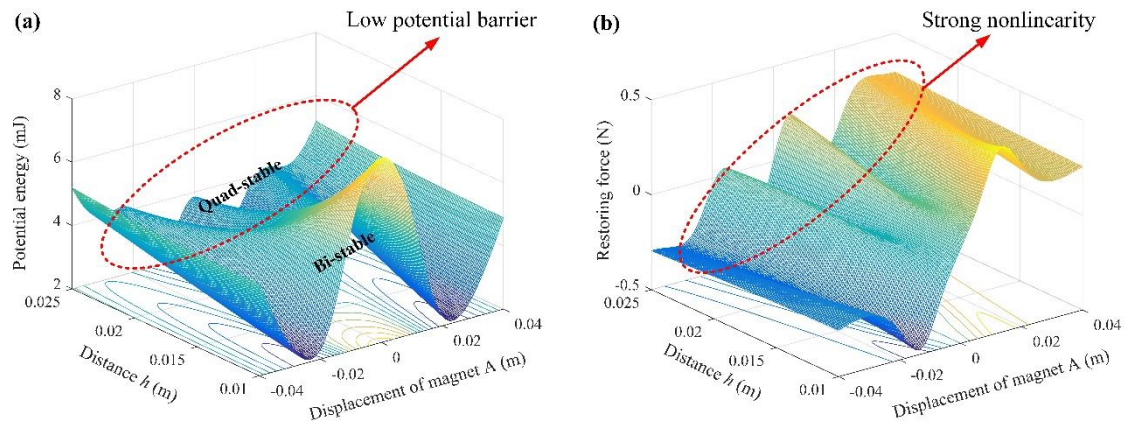


Figure 3.10 The quad-stable PEH: (a) The potential energy; (b) the magnetic force in transverse direction, when gap distance $d = 15$ mm

As observed from Figure 3.8(a), it can be noticed that with the increase of the gap distance d , the potential barrier of bi-stable PEH gradually decrease, and it will become a mono-stable PEH. When the gap distance is set as 5 mm to 10 mm, the corresponding potential barrier is so high that it is difficult to achieve the snap-through oscillation which is beneficial for high output voltage. The equivalent restoring force, including the nonlinear magnetic force in the transverse direction and the elastic force of the piezoelectric beam, is shown in Figure 3.8(b). With the increase of the gap distance, the nonlinear characteristic of the system is gradually weakening.

Figure 3.9(a) illustrates the potential energy of the tri-stable PEH. For the symmetric tri-stable PEH, $h = h_1 = h_2$ (as shown in Figure 3.9(b)). When the distance h is from 10 mm to 16 mm, the potential barrier between the outer and middle potential wells is high. In this situation, it is easy to obtain the snap-through oscillation (inter-well motion) from the middle potential well to the outer one. However, it is difficult for the snap-through oscillation from the outer potential well to the middle one, even from one outer potential well to another outer one. Along with the increase of the distance h , the outer potential well is becoming shallow and the middle potential well is simultaneously becoming deep. Thus, the potential barriers are large, leading the large-amplitude inter-well oscillation to be hard achieved. From Figure 3.9(b), it can be observed that the equivalent restoring force is becoming large with the increase of distance h , and the whole system shows strong nonlinear characteristics.

In order to further reduce the potential barriers, one more external magnet C is added between the magnets B and D to realize the quad-stable configuration. The corresponding potential energy is shown in Figure 3.10(a). When the distance h is from 10 mm to 15 mm, the system is the bi-stable PEH. With the increase of the distance h , the system is becoming the quad-stable PEH with low potential barriers. Combined with the equivalent restoring force as shown in Figure 3.10(b), it can be found that the quad-stable PEH has strong nonlinearity.

3.6 Experimental Validation

In above sections, the bi-stable, asymmetric tri-stable, symmetric tri-stable and quad-stable PEHs are theoretically analysed. With the aim to validate their performance under various constant rotational speeds. The related experiments are conducted by the experimental setup as shown in Figure 3.11, which is same as that in Chapter 2. The different PEHs are installed on the rotation plate to validate their energy harvesting performance.

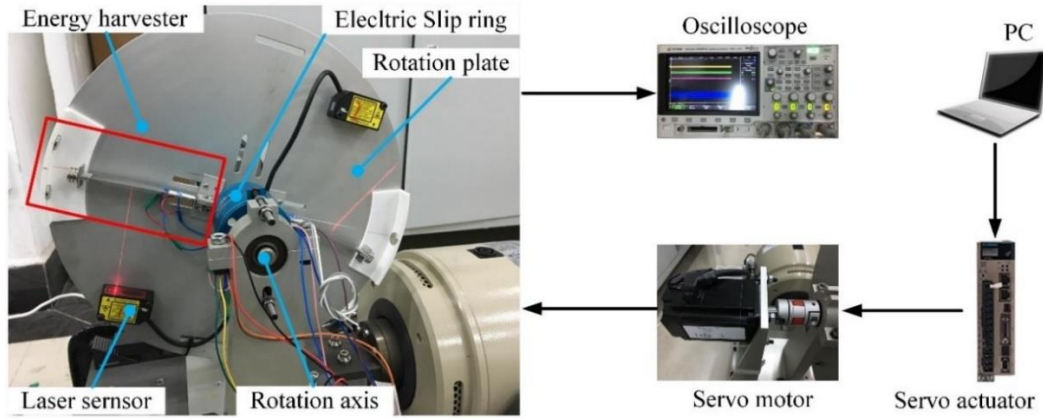


Figure 3.11 The experiment setup for experiments of nonlinear PEHs in rotational motion.

Furthermore, the bi-stable, asymmetric tri-stable, symmetric tri-stable and quad-stable PEH are adopted in the experiments to make comparison of their energy harvesting performance and output voltage. The substrate layer, with the dimension of $95 \times 12 \times 0.2 \text{ mm}^3$, is the stainless steel. Two piezoelectric patches (K2512U1, THRIVE, JAPAN), with the dimension of $25 \times 12 \times 0.13 \text{ mm}^3$, are parallelly connected and glued at the fixed end of the substrate. Additionally, note that all the magnets adopted in different nonlinear PEHs are NdFeB cylinder magnets, whose grade is 1.2 T. All tip magnets, which are consisting of one magnet $D12 \times 1.7 \text{ mm}^3$ (D is the diameter) and two magnets $D12 \times 2.7 \text{ mm}^3$, have the same dimension. For the bi-stable PEH, there is one external magnet as shown in Figure 3.12(a), and $d=15 \text{ mm}$. There are two external magnets for the symmetric and asymmetric tri-stable PEHs, respectively. For the symmetric tri-stable PEH as shown in Figure 3.12(b), the corresponding parameters are $h_1=20 \text{ mm}$, $h_2=20 \text{ mm}$ and $d=15 \text{ mm}$. For the asymmetric tri-stable one as shown in Figure 3.12(c), $h_1=20 \text{ mm}$, $h_2=10 \text{ mm}$ and $d=15 \text{ mm}$. For the quad-stable PEH as shown in Figure 3.12(d), the related parameters are $h_1=20 \text{ mm}$, $h_2=20 \text{ mm}$ and $d=15 \text{ mm}$. Additionally, the other parameters adopted in the experiments are listed in Table 3.1 and Table 3.2.

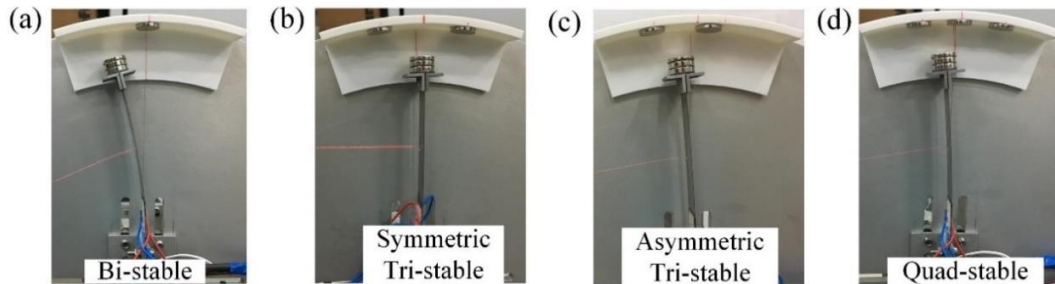


Figure 3.12 (a) The bi-stable PEH; (b) the symmetric tri-stable PEH; (c) the asymmetric tri-stable PEH; (d) the quad-stable.

3.6.1 Experimental Results

Figure 3.13 depicts the rotational speed sweeping experiments, ranging from 60 rpm (1 Hz) to 960 rpm (16 Hz) by increasing 20 rpm, bi-stable (black line), symmetric tri-stable (blue line), asymmetric tri-stable (cyan line) and quad-stable (red line). According to the energy harvesting performance, three regions, including Region I (60 - 240 rpm), Region II (240 - 440 rpm) and Region III (440 - 960 rpm), are divided. As observed from Figure 3.13, in Region II, the RMS voltages of these PEHs are more than 6 V, especially reaches almost 14 V around 380 rpm, due to their inter-well oscillations. In Region III, when the rotational speed is becoming 440 rpm, the RMS voltages decrease significantly due to the centrifugal stiffening effect of PEHs. Namely, the centrifugal force, which is related to the square of rotational speed, acting on the tip mass (magnet A) will reduce the vibration in transverse direction of piezoelectric beam. Note that the centrifugal stiffening effect can be explained by the term $K_c \dot{\theta}^2$ in the proposed theoretical model of Eq. (2.36a). Additionally, the great differences of dynamic performance among these PEHs are in Region I. Specifically, for the bi-stable and symmetric tri-stable (STri-stable), the RMS voltages of both are almost 1V, because they experience the intra-well oscillations rather than the inter-well oscillations. However, for asymmetric tri-stable PEH (ATri-stable), as the rotational speed is 100 rpm, it experiences the inter-well oscillations rather than the intra-well oscillations due to the lower potential barrier 1 and barrier 2 as shown in Figure 3.5. For the quad-stable PEH, from the rotational speed 60 rpm, it experiences the inter-well oscillation because of the lower potential barriers as shown in Figure 3.6. Furthermore, the corresponding RMS powers of these PEHs are illustrated in Figure 3.14. It should be noted that for the quad-stable PEH, the RMS power is more than 30 uW (60 – 420 rpm), which is enough for powering the sensor node used for structural health monitoring. It provides the foundation for potential application.

In order to further show the dynamic performance and output voltage of the nonlinear PEHs under various constant rotational speeds in Region I, Region II and Region III. Experimental results, including Region I (60 rpm and 180 rpm), Region II (240 rpm, 300 rpm and 410 rpm) and Region III (440 rpm, 520 rpm, 720 rpm and 900 rpm), are selected. The related experimental results are illustrated from Figure 3.15 to Figure 3.23. Note that black line, blue line, cyan line and red line are the experimental results of bi-stable, STri-stable, ATri-stable and quad-stable PEHs, respectively. Additionally, in all these Figures, the first column is measured displacement, and the second column is the measured output voltage, and the last column is the spectrum based on the Fast Fourier Transform (FFT).

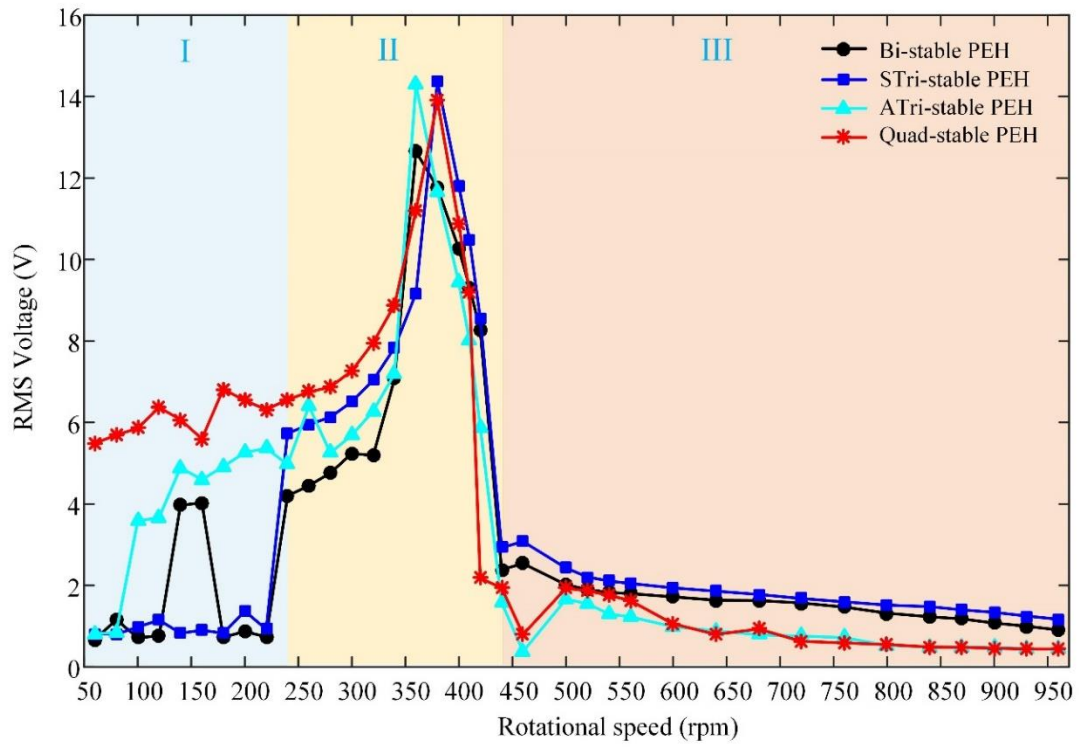


Figure 3.13 The experimental RMS voltage for various rotational speed from 60 - 1060 rpm; bi-stable (black line); STri-stable (blue line), ATri-stable (cyan line) and quad-stable (red line) PEHs, respectively.

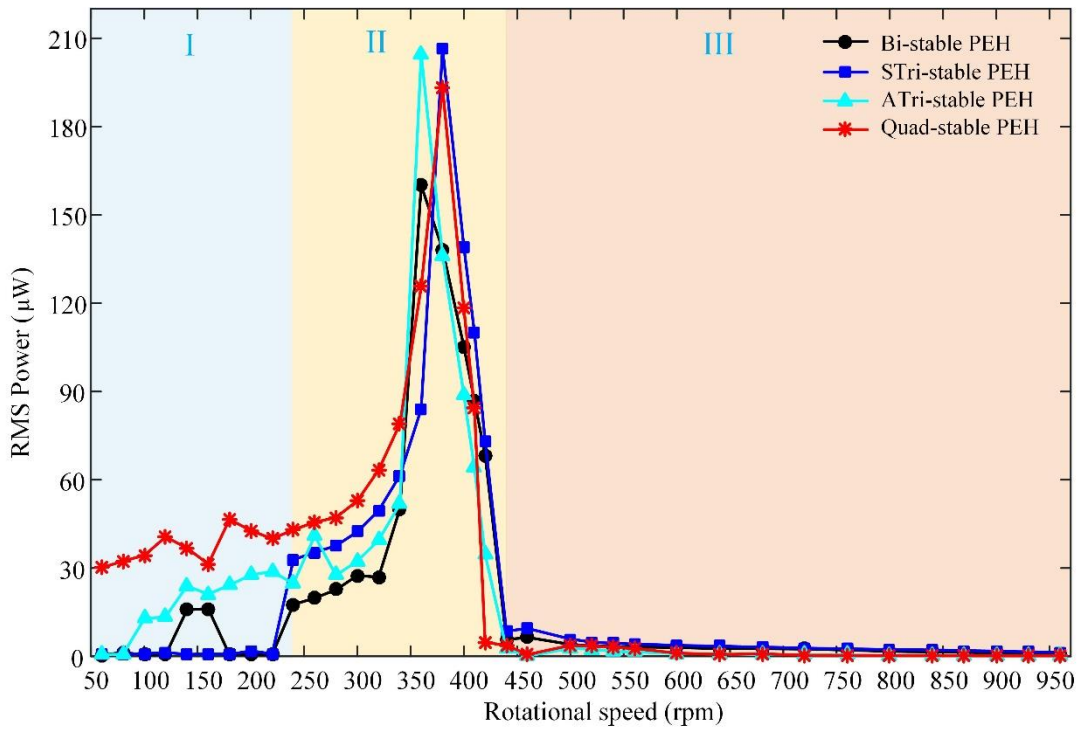


Figure 3.14 The experimental RMS power for various rotational speed from 60 - 1060 rpm bi-stable (black line); STri-stable (blue line), ATri-stable (cyan line) and quad-stable (red line) PEHs, respectively.

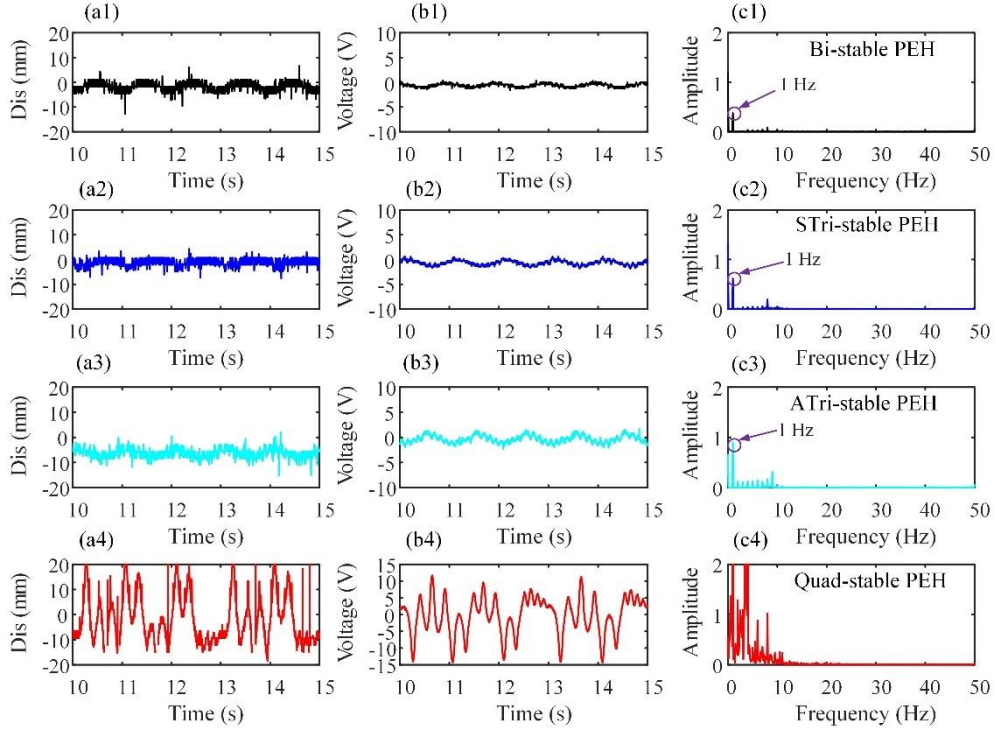


Figure 3.15 The experimental results of bi-stable (black line), STri-stable (blue line), ATri-stable (cyan line) and quad-stable (red line) PEHs under rotational speed 100 rpm, respectively.

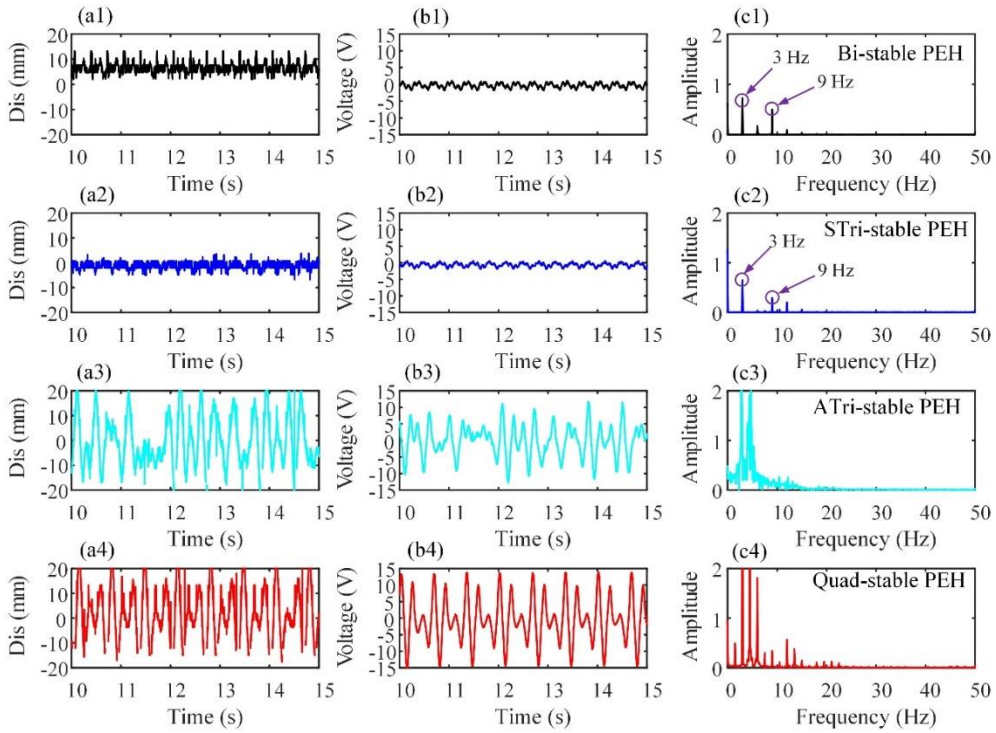


Figure 3.16 The experimental results of bi-stable (black line), STri-stable (blue line), ATri-stable (cyan line) and quad-stable (red line) PEHs under rotational speed 180 rpm, respectively.

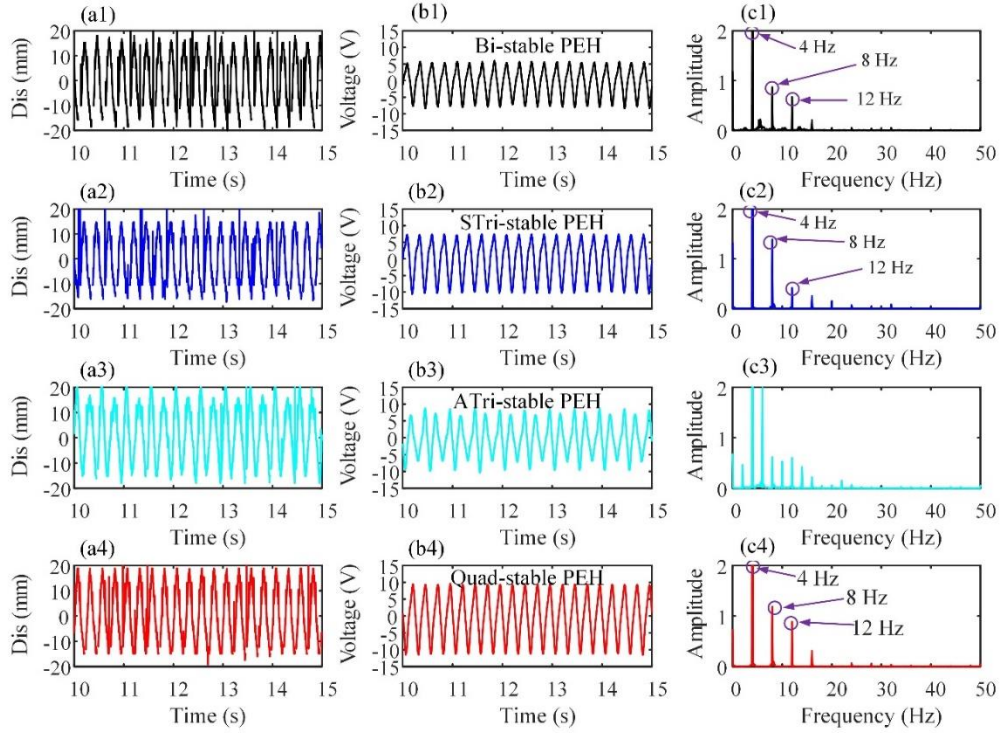


Figure 3.17 The experimental results of bi-stable (black line), STri-stable (blue line), ATri-stable (cyan line) and quad-stable (red line) PEHs under rotational speed 240 rpm, respectively.

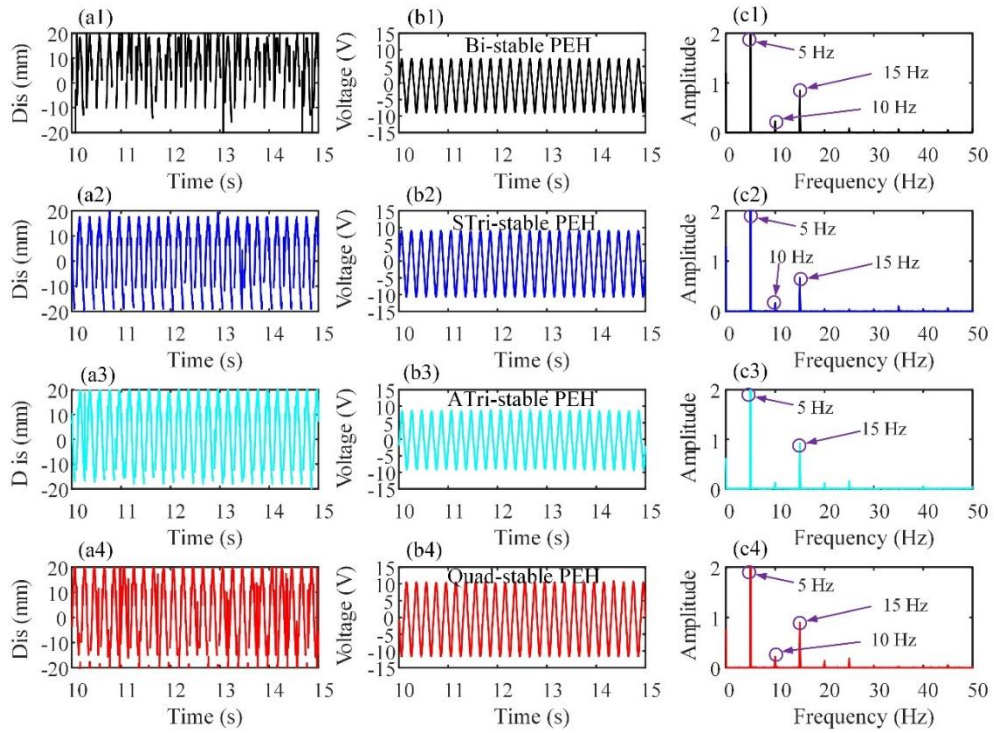


Figure 3.18 The experimental results of bi-stable (black line), STri-stable (blue line), ATri-stable (cyan line) and quad-stable (red line) PEHs under rotational speed 300 rpm, respectively.

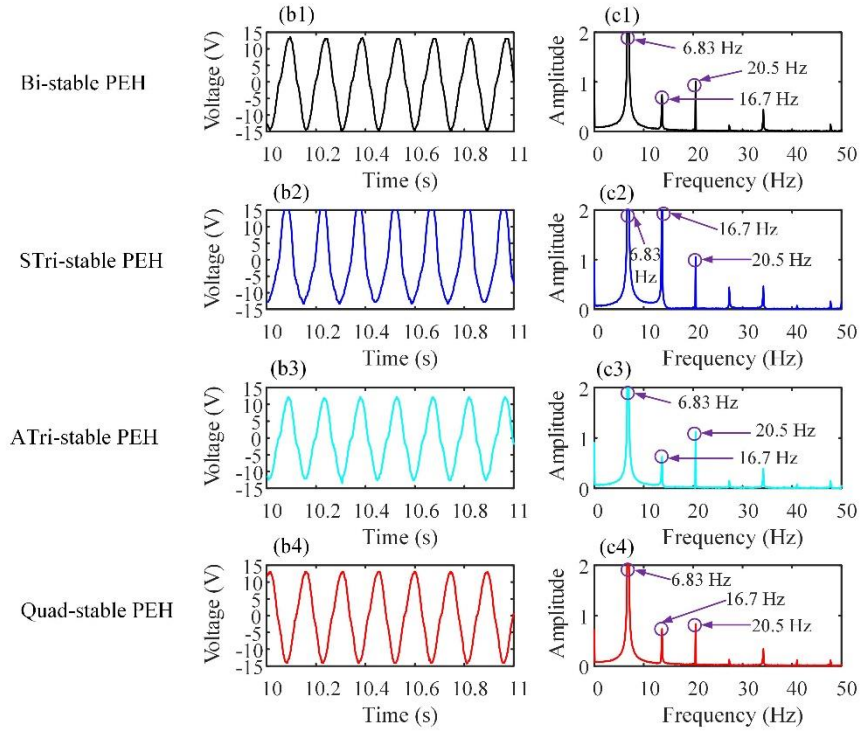


Figure 3.19 The experimental results of bi-stable (black line), STri-stable (blue line), ATri-stable (cyan line) and quad-stable (red line) PEHs under rotational speed 410 rpm, respectively.

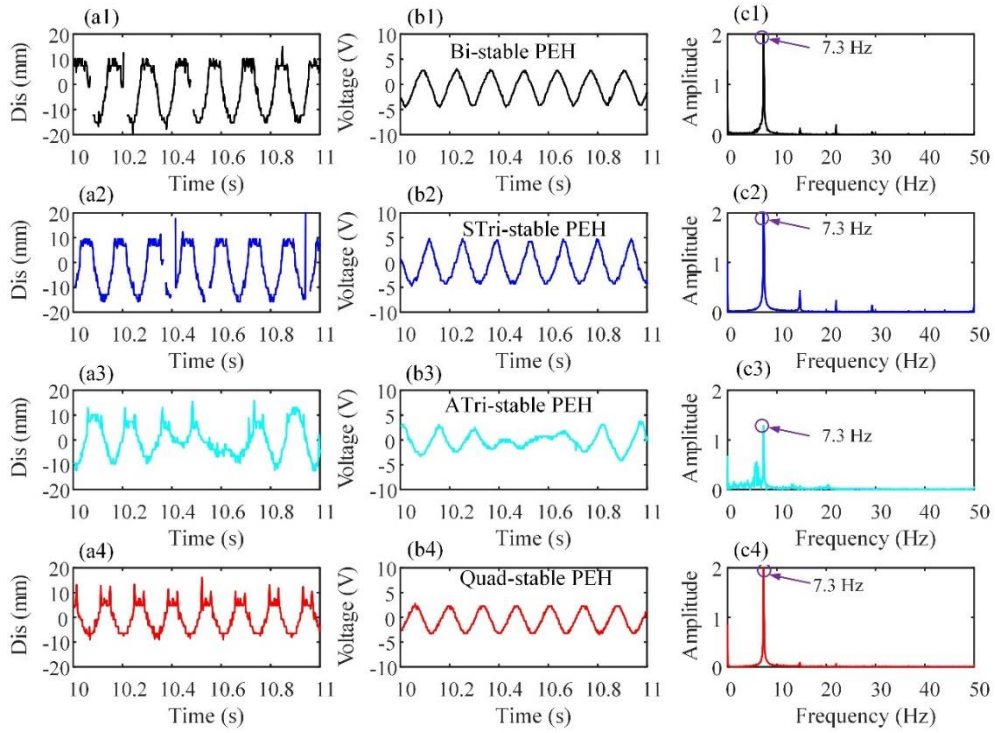


Figure 3.20 The experimental results of bi-stable (black line), STri-stable (blue line), ATri-stable (cyan line) and quad-stable (red line) PEHs under rotational speed 440 rpm, respectively.

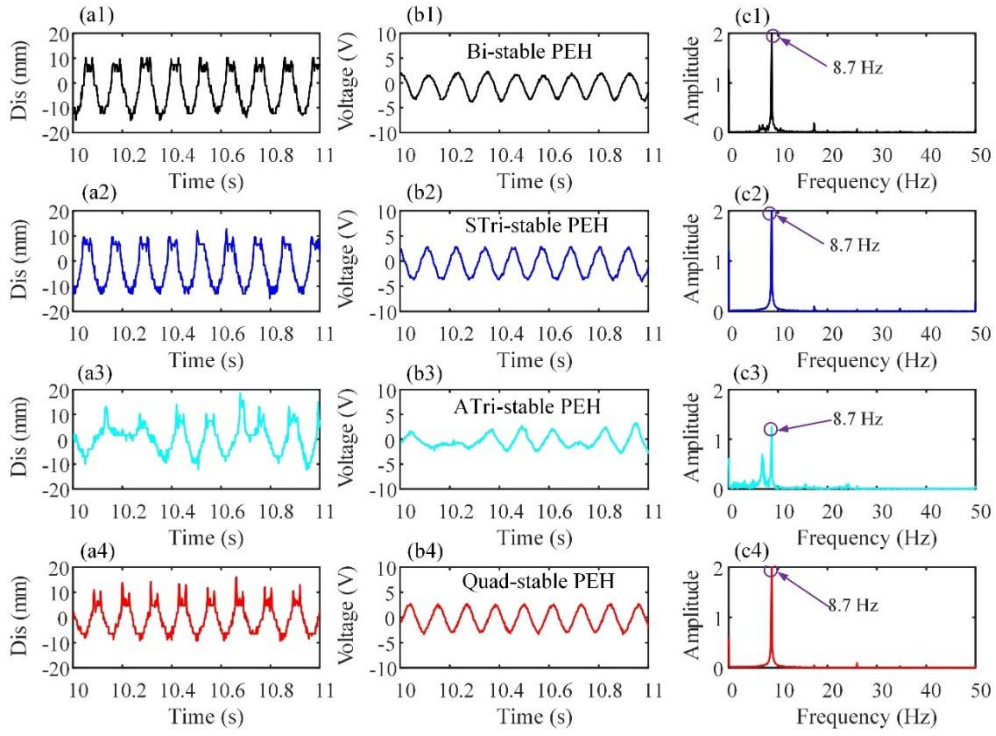


Figure 3.21 The experimental results of bi-stable (black line), STri-stable (blue line), ATri-stable (cyan line) and quad-stable (red line) PEHs under rotational speed 520 rpm, respectively.

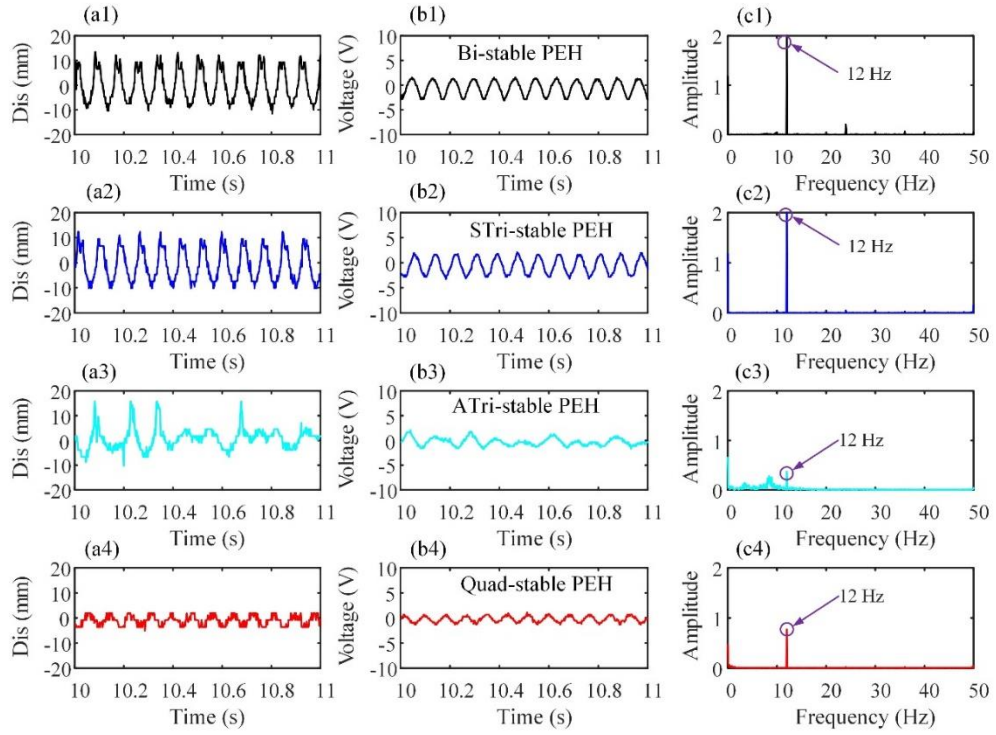


Figure 3.22 The experimental results of bi-stable (black line), STri-stable (blue line), ATri-stable (cyan line) and quad-stable (red line) PEHs under rotational speed 720 rpm, respectively.

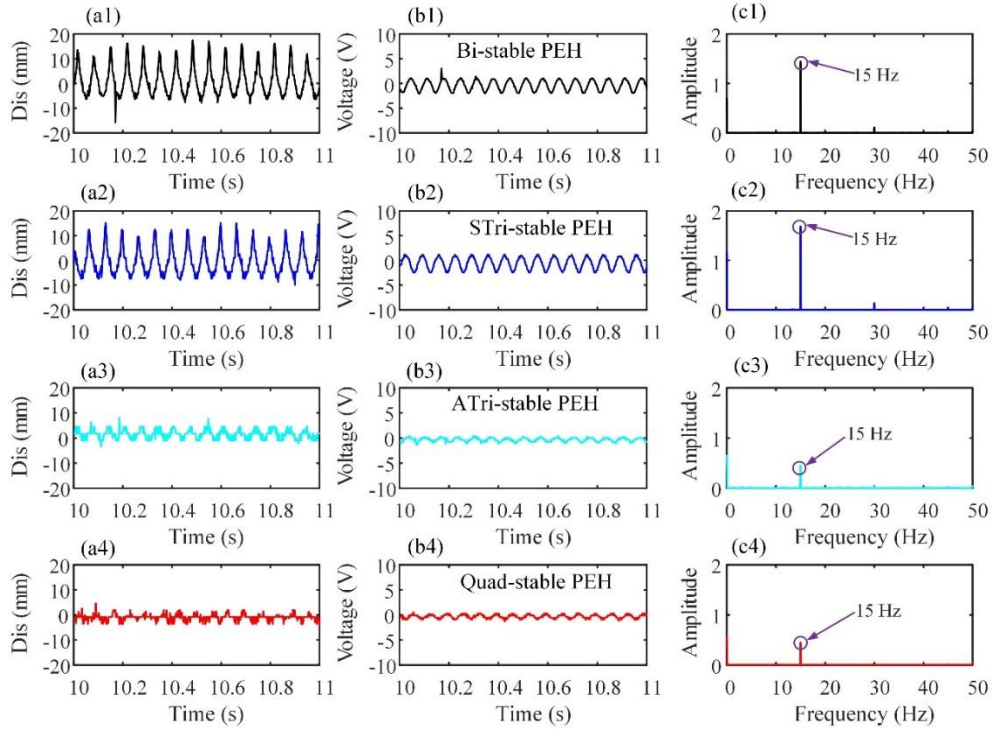


Figure 3.23 The experimental results of bi-stable (black line), STri-stable (blue line), ATri-stable (cyan line) and quad-stable (red line) PEHs under rotational speed 900 rpm, respectively.

Figure 3.15 shows the experimental results of bi-stable, ATri-stable, STri-stable and quad-stable PEHs under rotational speed 60 rpm. As shown in first column of Figure 3.15, the bi-stable, STri-stable and ATri-stable PEHs experience the intra-well oscillations around one of their stable positions, respectively, resulting in the low output voltage. However, the quad-stable PEH undergo the chaotic oscillation due to its lower potential barrier, and it produces the high output voltage. As the rotational speed is increased into 180 rpm, the experimental results of these PEHs are illustrated in Figure 3.15. From their dynamic performance as shown in first column, the difference between the rotational speed 60 rpm and 180 rpm is that the ATri-stable PEH goes through the chaotic oscillation. Additionally, from the spectrum in third column, the three times super-harmonic frequency components are existing in the intra-well oscillation which is theoretically validated in their theoretical solutions.

When the rotational speed is becoming into 240 rpm (Region II), the experimental results of these PEHs are presented in Figure 3.17. All bi-stable, STri-stable, ATri-stable and quad-stable PEHs experience the inter-well motion among their stable positions, respectively. And the corresponding RMS voltages are as high as 10 V. Furthermore, from the spectrum in third column, we can notice that the super-harmonic frequency components are also appearing. As the rotational

speed is 300 rpm as shown in Figure 3.18 or 410 rpm as shown in Figure 3.19, all these PEHs undergo the inter-well oscillation. In these situations, the super-harmonic frequency components can also be noticed in spectrums.

Furthermore, when the rotational speed is increased into 440 rpm (Region III), the dynamic performance of these PEHs are decreased significantly, consequently, their output voltages simultaneously decrease as shown in Figure 3.20. As the rotational speed is further increased, such as the experimental results of 520 rpm, 720 rpm and 900 rpm as shown in Figure 3.21, Figure 3.22 and Figure 3.23, respectively. With the increase of rotational speed, the equivalent centrifugal force is increasing at the same time, thus, the dynamic performance of these PEHs gradually decrease and enter into the intra-well oscillation around the position $w(L,t)=0$. This phenomenon is the centrifugal stiffening effect, which is caused by the centrifugal force acting on the tip mass (magnet A) to reduce the energy harvesting performance of PEHs. Additionally, from their spectrums, the frequency component is equal to the rotational frequency, which means the super-harmonic resonance is not triggered under these rotational speeds.

3.6.2 Centrifugal Stiffening Effect

From the experimental results of bi-stable, symmetric tri-stable, asymmetric tri-stable and quad-stable PEHs, we can notice that when the rotational speed reaches a certain value (440 rpm), their dynamic performance will decrease significantly. Namely, these PEHs experience the intra-well oscillations around the position $w(L,t)=0$, corresponding to the low output voltages. The reason for this interesting phenomenon is that when the rotational speed is increased, the tip mass (magnet A) of the PEHs in rotational motion will produce a non-negligible centrifugal force, which restrains the vibration of piezoelectric beam in transverse direction. Thus, the centrifugal stiffening effect occurs, it can be explained by the term $K_c \dot{\theta}^2$ in the proposed theoretical model. Although the centrifugal stiffening effect reduces the energy harvesting performance under high rotational speeds, the equivalent stiffness of piezoelectric beam is increasing with the increase of rotational speed.

Based on this phenomenon, a self-tuning PEH can be achieved in rotational motion, further details will be illustrated in Chapter 4.

3.6.3 Discussion

While all the PEHs are the nonlinear systems, they are sensitive to the nonlinear magnetic force. Thus, it is essential to calculate the nonlinear magnetic force F_m to predict their dynamic performance and energy harvesting performance. As shown in experiments, the thickness of tip mass (magnet A) is 7.1 mm, and that of external magnets (B or C or D) is 1.7 mm, while their diameter is 12 mm. Due to these reasons, according the dipole-dipole method, it is difficult to calculated the magnetic force precisely. Additionally, this issue is also the challenge for magnetically coupled nonlinear PEH. Additionally, the experimental results have been validated that the multi-stability characteristic is an effective way to reduce the potential barrier of PEHs so that the periodic gravity component can across them to achieve inter-well oscillations. Thus, in the further research, the parameters of PEH should be optimised to broaden the energy harvesting frequency range.

In this Chapter, the bi-stable, ATri-stable, STri-stable and quad-stable PEHS are experimentally validated under rotational speed of 60 - 960 rpm. The quad-stable PEH shows excellent energy harvesting performance, especially for the rotational speed of 60 - 440 rpm, corresponding to the RMS power more than 30 μW . Thus, the quad-stable PEH with lower potential barriers is suitable for the energy harvesting from rotational motion.

3.7 Summary

In Chapter 3, we theoretically analysed the bi-stable, symmetric tri-stable, asymmetric tri-stable and quad-stable PEHs in rotational motion under various constant rotational speeds. The difference among these PEHs is the nonlinearity caused by the external magnets. Next, the perturbation method is used to solve their theoretical models of bi-stable, symmetric tri-stable and quad-stable PEHs in rotational motion, respectively. Lastly, the corresponding experiments are conducted to present the dynamic performances and output voltages under various constant rotational speeds. The following conclusions can be obtained:

- (1) The nonlinear PEH is an effective way for energy harvesting from rotational motion. The nonlinearity and lower potential barriers can broaden the effective frequency range.
- (2) When the rotational speed reaches certain values, all these PEHs will experience the intra-well motion around the position $w(L, t) = 0$. And this phenomenon is called centrifugal stiffening effect due to the centrifugal force acting on the tip mass of the PEH.
- (3) Adjusting the parameters, including the number of external magnets or configuration

dimension, of system, the different stable PEHs can be achieved. In the rotational motion, the time-varying potential well is beneficial for energy harvesting, especially for the quad-stable PEH.

Chapter 4

Self-tuning Harvester by Centrifugal Stiffening Effect

4. Self-tuning Harvester by Centrifugal Stiffening Effect

In Chapter 3, the centrifugal stiffening effect has been theoretically predicted and experimentally validated by different PEHs. According to the centrifugal stiffening effect, it is found that with the increase of rotational speed, the corresponding tension due to the centrifugal force on the beam increases the resonance frequency of the piezoelectric beam simultaneously. One idea is to design the parameters of a PEH in appropriate values so that the PEH can work at or near its resonance frequency at a wide frequency range. In chapter 4, the self-tuning harvester by the centrifugal stiffening effect will be conducted.

Firstly, it should be noted that according to the direction of centrifugal force, the PEH in rotational motion can be categorized into the forward PEH and inverse PEH as shown in Figure 4.1(a) and 4.1(b) respectively. When a PEH is installed in rotational motion, the centrifugal force acting on the tip mass is always along the outer of radial direction as shown in Figure 4.1. Due to the different configurations (forward PEH and inverse PEH) resulting from installation position, the centrifugal force can lead to the centrifugal stiffening effect and centrifugal softening effect respectively.

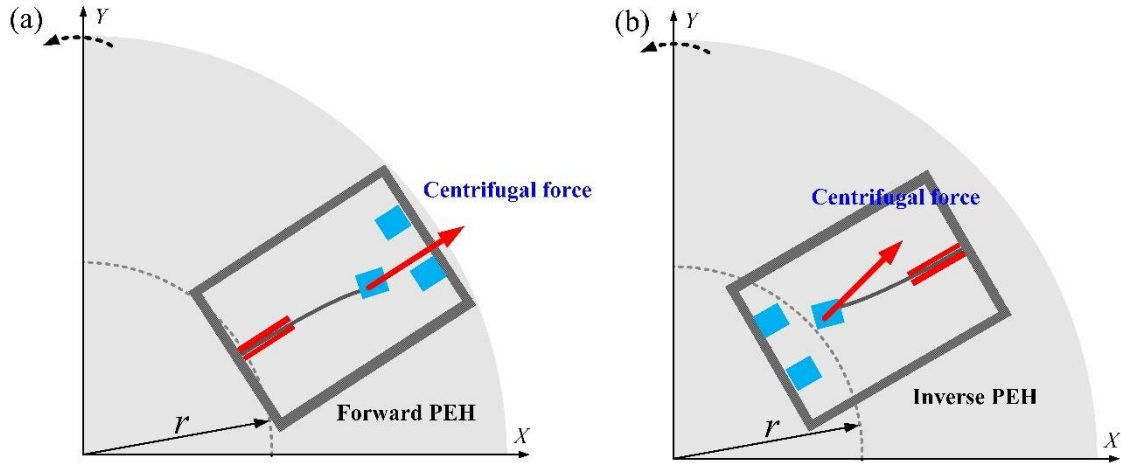


Figure 4.1 The PEH in rotational motion: (a) Forward PEH in rotational motion; (b) Inverse PEH in rotational motion.

4.1 Principle of Passively Self-tuning Energy Harvester

As illustrated in Chapter 2, the theoretical model of a nonlinear PEH in rotational motion has been derived via the distribute-parameter model as following Eqs. (4.1) and (4.2):

$$M_e \ddot{q}(t) + C \dot{q}(t) + (K_e + K_c \dot{\theta}^2) q(t) + \chi \ddot{\theta} - \mathcal{G}_p v(t) + F_m = -\Gamma g \cos \theta \quad (4.1)$$

$$C_p \dot{v}(t) + R_l^{-1} v(t) + \mathcal{G}_p \dot{q}(t) = 0 \quad (4.2)$$

Next, we mainly analyze the principle of self-tuning effect utilizing the centrifugal stiffen caused by the rotational motion. In previous study [66], the self-tuning linear PEH was investigated and the passive self-tuning phenomenon was validated in their experiments. In order to calculate the component of centrifugal force in transverse direction, the deformation was assumed as a small deformation to establish the geometrical relationship. In this situation that the PEH is linear system with small deformation, this assumption is reasonable. However, for the nonlinear PEHs, sometimes they undergo the inter-well oscillation with the large-amplitude deformation. Thus, with the aim to solve the issue, firstly we obtain the K_c coefficient, including the rotational radius r , the tip mass M , the length L and the mass m_b of piezoelectric beam, to calculate the equivalent centrifugal force F_c . It is related to the rotational speed $\dot{\theta}$ and can be expressed as:

$$F_c = K_c \dot{\theta}^2 \cdot q(t) \quad (4.3)$$

Simplified as a mass-spring-damper system, the equivalent resonance frequency of the piezoelectric beam with a tip mass can be described as $\omega_n = \sqrt{K_e/M_e}$. However, for a PEH in rotational motion, the term $K_e + K_c \dot{\theta}^2$ in Eq. (4.1) shows that the centrifugal stiffening effect changes the stiffness and the resonance frequency of the beam, and it can be calculated as:

$$\omega_n = \sqrt{\frac{K_e + K_c \dot{\theta}^2}{M_e}} \quad (4.4)$$

where the K_c coefficient is calculated:

$$K_c = m_b \left(0.06 + 0.37 \frac{r}{L} \right) + M \left(0.23 + 1.23 \frac{r}{L} \right) \quad (4.5)$$

where m_b is the mass of the piezoelectric beam. As the rotational speed $\dot{\theta}$ increases, the resonance frequency of the piezoelectric beam will also be increased. The schematic diagram of a self-tuning nonlinear energy harvester is shown in Figure 4.2. Figure 4.2(a) shows the relationship between the rotational frequency and resonance frequency. Figure 4.2(b) is the local

amplification of Figure 4.2(a), it is found that when the parameters of the harvesters are in appropriate values that are listed in Table 4.1, the rotational frequency can approximately track the equivalent resonance frequency over a wide frequency range.

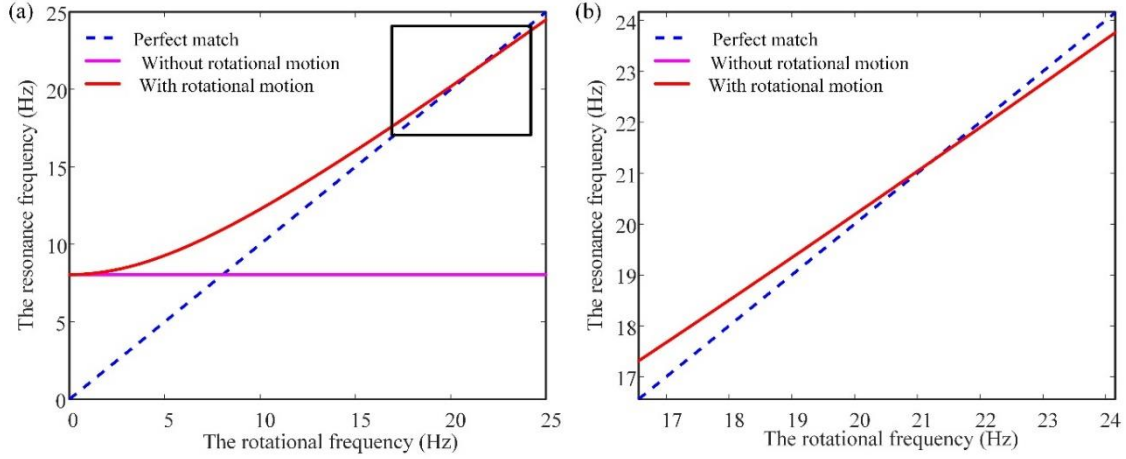


Figure 4.2 (a) The relationship between the rotational frequency and the equivalent resonance frequency of the nonlinear harvester; (b) the local amplification of Figure 4.2(a).

Table 4.1. The parameters value adopted in Figure 4.2

Symbol	r (mm)	L (mm)	b (mm)	t_b (mm)	M (g)	m_b (g)
Value	40	80	12	0.20	7.5	1.8

4.2 Effect of System Parameters

4.2.1 Effect of Rotational Radius

From Eq. (4.5), we can notice that the rotational radius r has an influence on the coefficient K_c which leads to the change of the equivalent resonance frequency. Thus, the effect of rotational radius will be analyzed. Figure 4.3 illustrates the simulated frequency of a PEH versus the rotational frequency for different rotational radiuses (30 mm, 35 mm, 40 mm, 45 mm and 50 mm) while $L = 80$ mm and $M = 7.5$ g. From Figure 4.3(a) and 4.3(b), we can find several apparent trends. Firstly, with the increasing of rotational radius r at 30 mm, 35 mm and 40 mm, the resonance frequency can match well with the driving frequency (rotational frequency) in some regions. However, when the rotational radius is more than 45 mm or 50mm, both of them cannot be matched at the frequency range of 0 - 25 Hz (0 -1500 rpm). Thus, the self-tuning effect cannot

be obtained in this range. Secondly, for each rotational radius, there is a specific frequency where the resonance frequency of the harvester matches perfectly the rotational frequency as shown in Figure 4.3(b), which is the local amplification of Figure 4.3(a). The perfect match occurs at 15 Hz for $r = 30$ mm, 17.5 Hz for $r = 35$ mm and 21.5 Hz for $r = 40$ mm, respectively. In general, increasing the rotational radius r will lead to quick increasing of the resonance frequency, which may not obtain the perfect match in the rotational frequency range as shown in Figure 4.3(b), such as $r = 45$ mm or $r = 50$ mm. Furthermore, once a nonlinear PEH in rotational motion has been designed, the only parameter that can be changed is the rotational radius r by adjusting the installation position. Therefore, adjusting the rotational radius can achieve self-tuning harvester in the rotational frequency range.

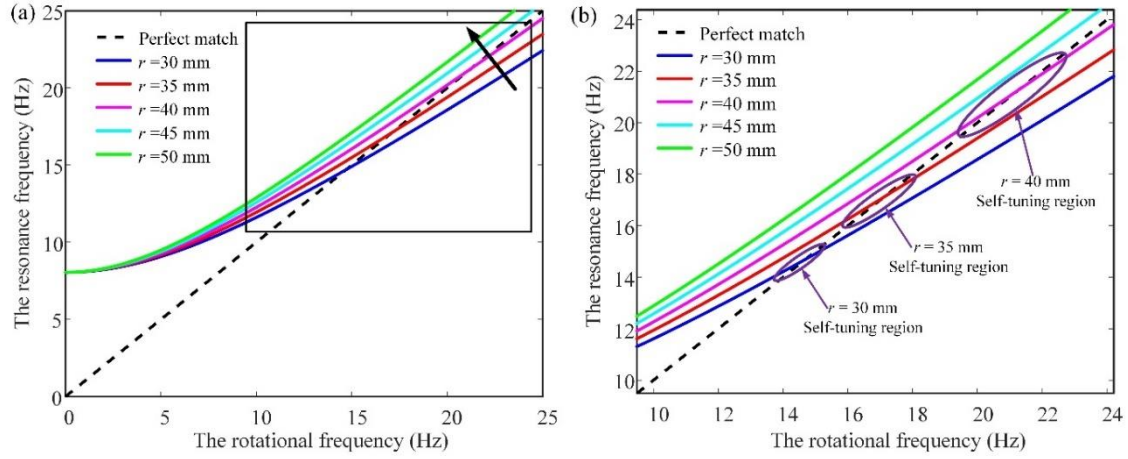


Figure 4.3 (a) Calculated resonance frequency versus rotational frequency for different rotational radii, $r = 30$ mm, $r = 35$ mm, $r = 40$ mm, $r = 45$ mm and $r = 50$ mm, respectively when $L = 80$ mm and $M = 7.5$ g; (b) the local amplification of Figure 4.3(a).

4.2.2 Effect of Beam Length

The relationship between the resonance frequency and rotational frequency with the variation of length L is shown in Figure 4.4. The length L of the piezoelectric beam varies from 75 mm to 95 mm while keeping $r = 40$ mm and $M = 7.5$ g. It should be noted that it changes the mass m_b and the equivalent mass M_e simultaneously. In order to show further details, the local amplification of Figure 4.4(a) is presented in Figure 4.4(b), in which the results demonstrate that the increase of length L will decrease the perfect match frequency. Furthermore, as shown in Figure 4.4(b), the perfect match occurs at 12.4 Hz for $L = 95$ mm, 14.5 Hz for $L = 90$ mm, 17.3 Hz for $L = 85$

mm and 21.1 Hz for $L = 80$ mm, respectively. Another interesting phenomenon is that when the length L is less than 80 mm, the self-tuning range is wider. In general, in some situations where the rotational radius is constant due to the limitation of installation space, we can change the length of the piezoelectric beam to obtain the self-tuning nonlinear PEH in a range of the rotational frequency.

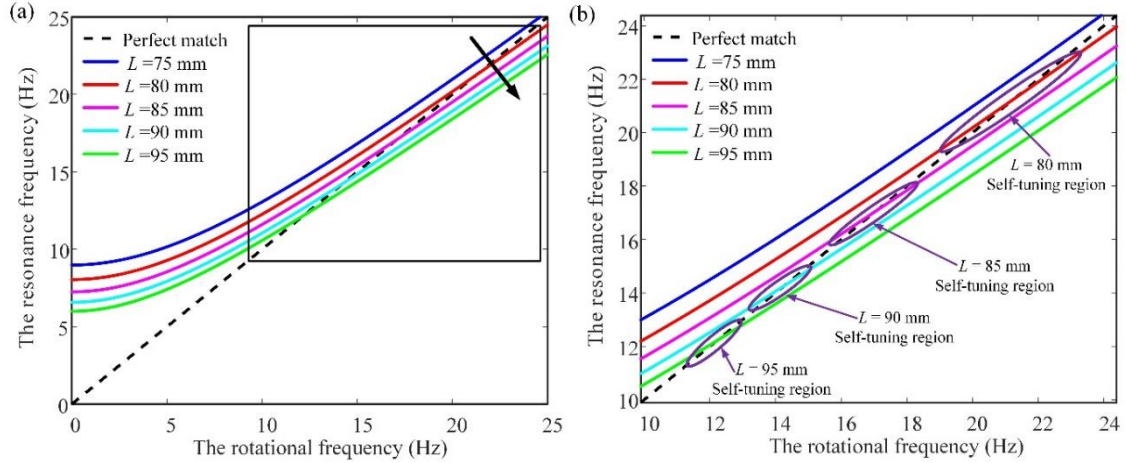


Figure 4.4 (a) Calculated resonance frequency versus rotational frequency for different lengths of the piezoelectric beam, $L = 75$ mm, $L = 80$ mm, $L = 85$ mm, $L = 90$ mm and $L = 95$ mm, respectively when $r = 40$ mm and $M = 7.5$ g; (b) the local amplification of Figure 4.4(a).

4.2.3 Effect of Tip Mass

The relationship between the resonance frequency and rotational frequency with the variation of tip mass M is shown in Figure 4.5. The tip mass varies from 7.3 g to 8.1 g while keeping $r = 40$ mm and $L = 80$ mm. It should be noted that the variation of tip mass M will lead to the variation of the equivalent mass M_e and the equivalent stiffness K_e as shown in Eq. (4.5). From Figure 4.5(a) and 4.5(b), we can see that the resonance frequency is sensitive to the tip mass M . The local amplification of Figure 4.5(a) is shown in Figure 4.5(b), which demonstrates that the increase of the tip mass M will decrease the perfect match frequency (the resonance frequency is equal to rotational frequency). Additionally, as shown in Figure 4.5(b), the perfect match occurs at 22.9 Hz for $M = 7.3$ g, 21.0 Hz for $M = 7.5$ g, 19.2 Hz for $M = 7.7$ g, 17.9 Hz for $M = 7.9$ g and 16.6 Hz for $M = 8.1$ g, respectively. The results demonstrate that a change of the tip mass has a great effect on the perfect match frequency. Thus, in some situations, if the rotational radius r and the length L of piezoelectric beam are both limited, changing the tip mass is a good way to achieve a

self-tuning nonlinear PEH.

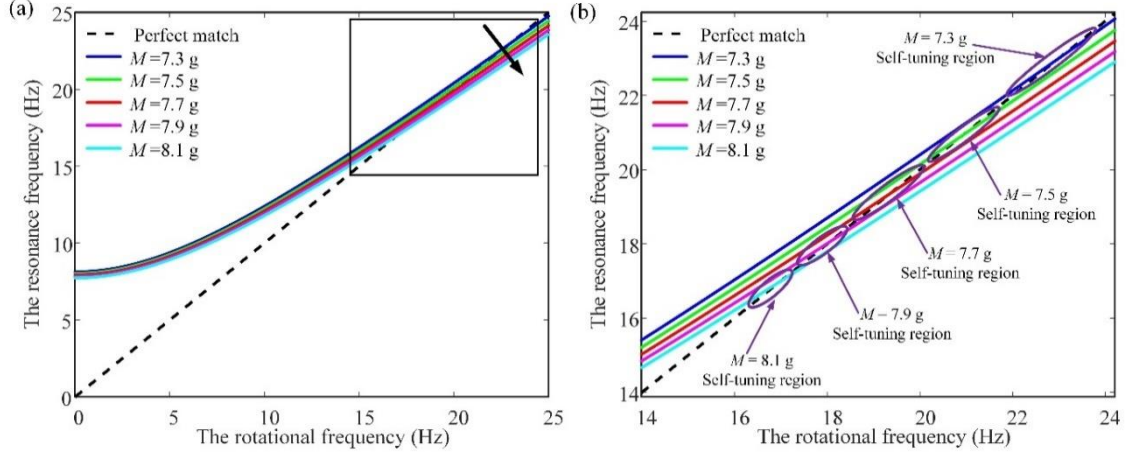


Figure 4.5 (a) Calculated resonance frequency versus the rotational frequency for different tip masses, $M=7.3$ g, $M=7.5$ g, $M=7.7$ g, $M=7.9$ g, $M=8.1$ g, respectively when $r=40$ mm and $L=80$ mm; (b) the local amplification of Figure 4.5(a).

4.3 Experimental Validation

The aim of this section is to investigate the self-tuning phenomenon of the nonlinear PEHs in rotational motion, the corresponding experiments are carried out under various constant rotational speeds. Figure 4.6 shows the layout of the experimental setup, which is the same as that in Chapter 2. It should be noted that the sampling frequency is 750 Hz.

4.3.1 Experimental Setup

As for the components of the PEHs, the cantilever beam is made of stainless steel with the dimension of $80 \times 12 \times 0.2$ mm³, and the piezoelectric patch (K2512U1, Thrive, JAPAN) has the dimension of $25 \times 12 \times 0.13$ mm³. Note that the magnetization direction of the harvester is along with the normal direction of the rotation plate. All the magnets in the experiments are NdFeB cylinder magnets, whose grade is 1.2 T. In order to explore the energy harvesting performance of different PEHs in rotational motion, the tri-stable and bi-stable PEHs are adopted for making a comparison in experiments. The tip mass of both have the same dimension, which is consisting of two magnets $D12 \times 1.7$ mm³ (D is the diameter) and two magnets $D12 \times 2.7$ mm³. For the bi-stable PEH, one external magnet ($D12 \times 2.7$ mm³) is utilized, and two stable equilibrium positions can be obtained as shown in Figure 4.6(b). While for the tri-stable PEH, two external magnets

D12×2.7 mm³ are adopted, and three stable equilibrium positions can be achieved as shown in Figure 4.6(c). It should be noted that the laser sensor measures the displacement at the distance of $x = 49$ mm from the end of the piezoelectric beam (but not the tip displacement), which is the same as the Refs. [73,74,107]. The parameters in the experiments are listed in Table 4.2.

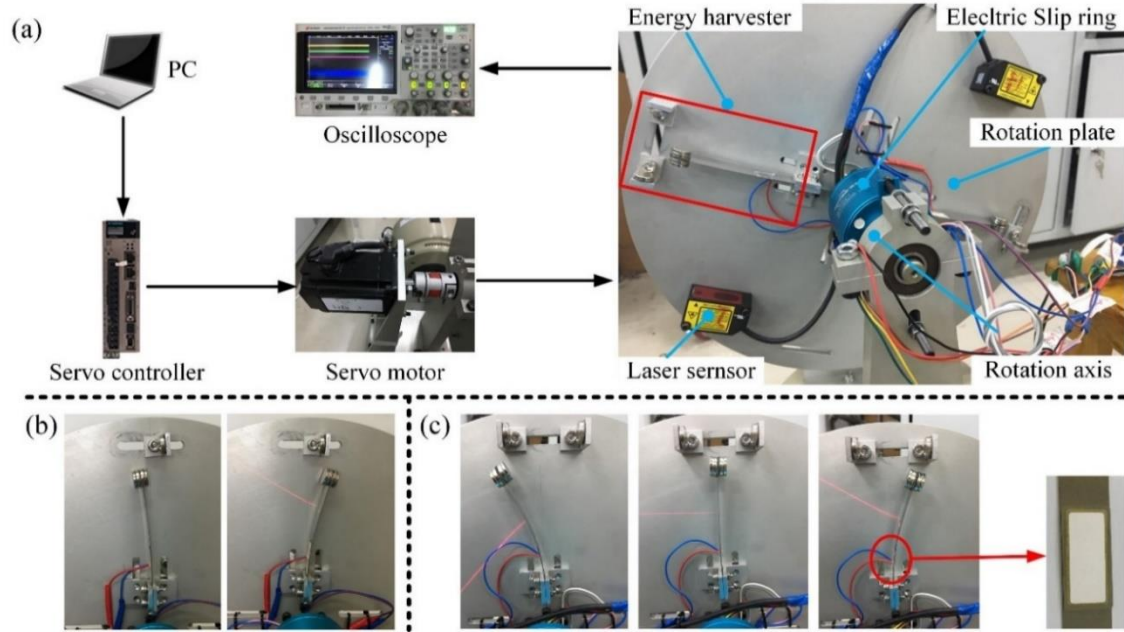


Figure 4.6 (a) Experimental setup; (b) two stable equilibrium positions of the bi-stable PEH; (c) three stable equilibrium positions of the tri-stable PEH.

Table 4.2. The parameters in the experiment

Parameters	Symbol	Value
Cantilever beam		
Length \times Width \times Thickness	$L \times b \times t_b$	$80 \times 12 \times 0.20 \text{ mm}^3$
Young's modulus	E_b	210 Gpa
Density	ρ_b	7765 Kg/m^3
Damping ratio	C	0.005
Piezoelectric patch		
Length \times Width \times Thickness	$l_p \times b_p \times t_p$	$25 \times 12 \times 0.13 \text{ mm}^3$
Young's modulus	E_p	66 Gpa
Density	ρ_p	7800 Kg/ m^3
Coupling coefficient	d_{31}	$-320 \times 10^{-12} \text{ C/N}$
Permittivity constant	ϵ_{33}	$4000 \epsilon_0$
Permittivity of free space	ϵ_0	$8.854 \times 10^{-12} \text{ F/m}$
Permanent magnets		
Density	$\rho_A \quad \rho_B \quad \rho_C$	7500 Kg/ m^3
Magnet's residual flux density	B_r	1.2 T
Magnetic permeability constant	μ_0	$4\pi \times 10^{-7}$
Load resistance	R_l	1 $\text{M}\Omega$

4.3.2 Experimental Results

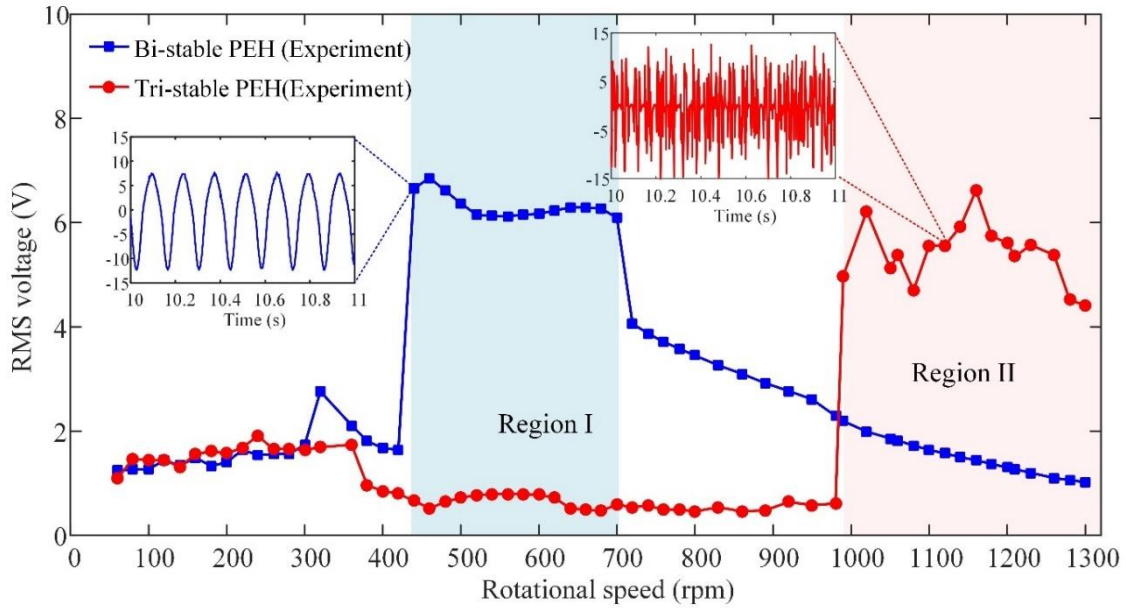


Figure 4.7 The RMS voltage of the bi-stable PEH (blue line) and the tri-stable PEH (red line) for varied rotational speed from 60-1300 rpm in experiments.

Figure 4.7 illustrates the RMS voltage of the bi-stable and tri-stable PEHs from the rotational speed range of 60 - 1300 rpm in experiments, respectively. From 60 to 300 rpm, the RMS voltage of the tri-stable PEH is little higher than that the bi-stable one. From 300 to 360 rpm, the RMS voltage of the bi-stable PEH is over that of the tri-stable PEH. However, from 360 to 440 rpm, the RMS voltage of them shows a downtrend due to the centrifugal force acting on the tip mass of both harvesters. An interesting phenomenon is that a dramatic increase of the RMS voltage occurs for the bi-stable PEH, and then maintain this high output voltage state from 440 to 700 rpm. At the rotational speed of 720 rpm, the output voltage of the bi-stable PEH decreases suddenly, then from 720 to 1300 rpm, the RMS voltage decreases gradually. While for the tri-stable PEH, from 440 to 980 rpm, the RMS voltage always maintains the value around 1.5 V, which corresponds to the intra-well oscillation around the middle stable position. However, at the rotational speed of 980 rpm, the RMS voltage of tri-stable PEH dramatically increases, then this phenomenon maintains until the rotational speed reaches 1300 rpm. As shown in Figure 4.7, the bi-stable PEH has achieved the self-tuning effect in region I, while for the tri-stable PEH, the effect achieves in region II.

From Eq. (4.3), we can know that the equivalent centrifugal force acting on the tip mass of a PEH is related to the square of rotational speed. It means that the centrifugal force increases quickly especially for high rotational speeds. As mentioned that the centrifugal force can also change the resonance frequency of the harvesters. In order to investigate the effect of centrifugal force on the energy harvesting performance, more details of dynamic performance under various rotational speeds will be presented in next parts. Note that the experimental results, including the measured displacement, output voltage and power spectrum, of bi-stable PEH are shown by blue line, and these of tri-stable PEH are shown by red line.

The experimental results, obtained from the rotational speed of 140 rpm, are shown in Figure 4.8. The bi-stable PEH experiences the intra-well oscillation around one stable position, however, the tri-stable PEH appears the inter-well oscillation in two adjacent potential wells due to the lower potential barrier. It leads to a higher output voltage than that of the bi-stable PEH. When the rotational speed is 240 rpm, the experimental results are illustrated in Figure 4.9. The inter-well oscillation cannot be triggered for the bi-stable PEH, instead of intra-well oscillation. However, the tri-stable PEH achieves a large-amplitude inter-well oscillation, which corresponds to the higher output voltage.

When the rotational speed is increased to 430 rpm, the experimental results are shown in Figure 4.10. The dynamic performance is the intra-well oscillation for the bi-stable PEH, however, the tri-stable PEH undergoes the inter-well oscillation. As observed from Figure 4.7, when the

rotational speed is higher than 430 rpm in region I, the centrifugal force acting on the tip mass influences the energy harvesting performance. Thus, the rotational speed 520 rpm is selected for the analyses as shown in Figure 4.11. The bi-stable PEH achieves the larger-amplitude inter-well oscillation, which leads to the high-energy output voltage. This phenomenon is caused by the self-tuning effect due to the centrifugal force for the bi-stable PEH. On the contrary, the centrifugal force has a negative influence on the energy harvesting performance of the tri-stable PEH, namely, it decreases the deformation of piezoelectric beam, and leads to the intra-well oscillation around the middle stable position as shown in Figure 4.11(b).

Figure 4.12 shows the experimental results of the bi-stable and tri-stable PEHs at rotational speed 950 rpm. As observed from Figure 4.12(a), the bi-stable PEH turns into intra-well oscillation, but the deformation of piezoelectric beam is larger than that of the tri-stable PEH. For the tri-stable PEH as shown in Figure 4.12(b), it also experiences the intra-well oscillation around the middle stable position, thus, the corresponding voltage is low. However, when the rotational speed is changed into 990 rpm in region II, the tri-stable will achieve the self-tuning effect. Therefore, the experimental results of rotational speed 1300 rpm are presented in Figure 4.13. It is clearly found that the tri-stable PEH obtains the large-amplitude inter-well oscillation due to the self-tuning effect, while the bi-stable one still experiences the intra-well oscillation because the centrifugal force decreases the deformation of piezoelectric beam.

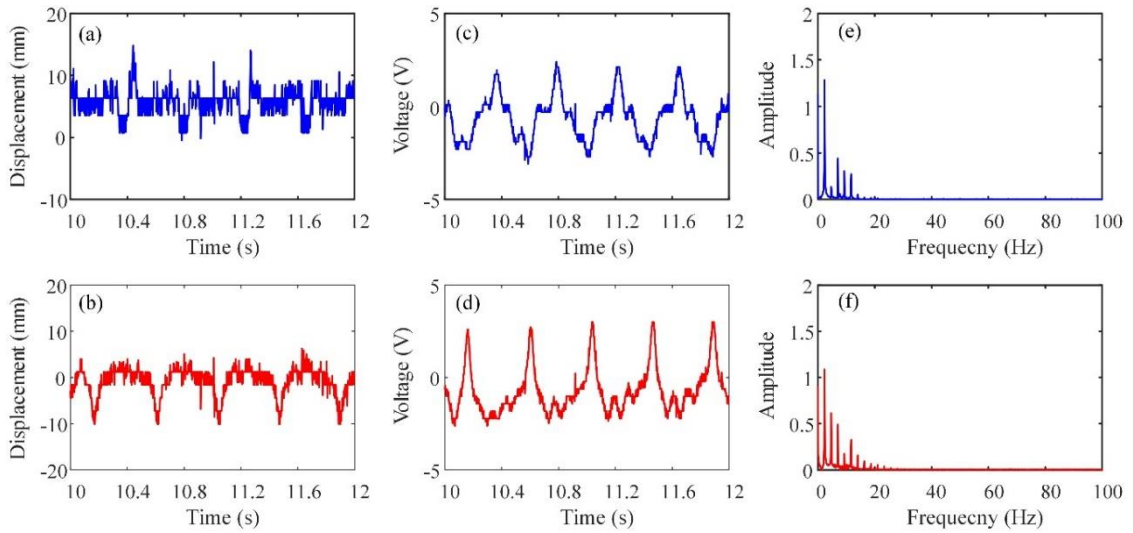


Figure 4.8 Measured displacement, output voltage and power spectrum of the bi-stable PEH (blue) and the tri-stable PEH (red) at the rotational speed of 140 rpm.

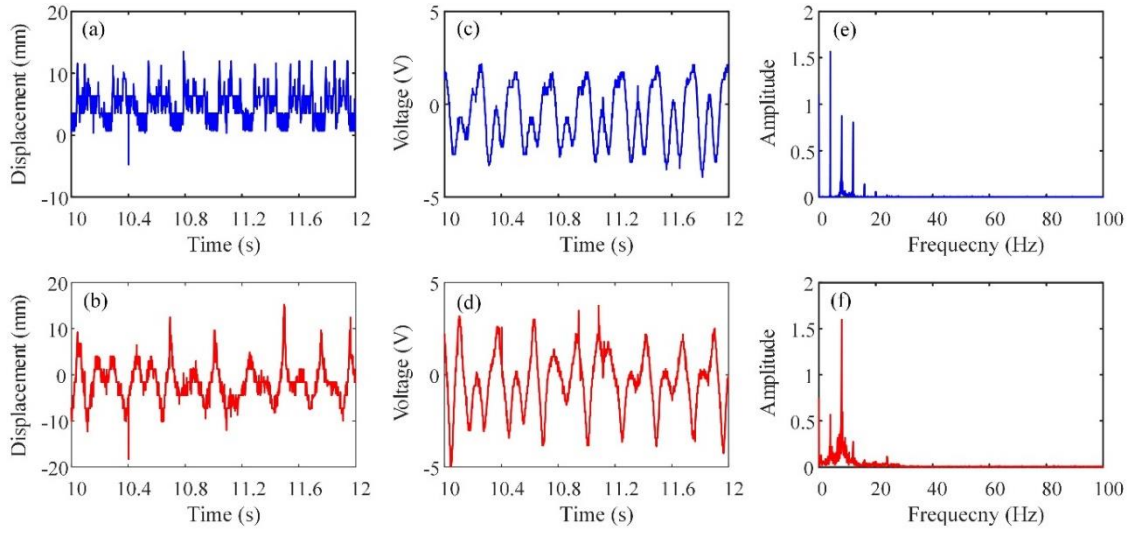


Figure 4.9 Measured displacement, output voltage and power spectrum of the bi-stable PEH (blue) and the tri-stable PEH (red) at the rotational speed of 240 rpm.

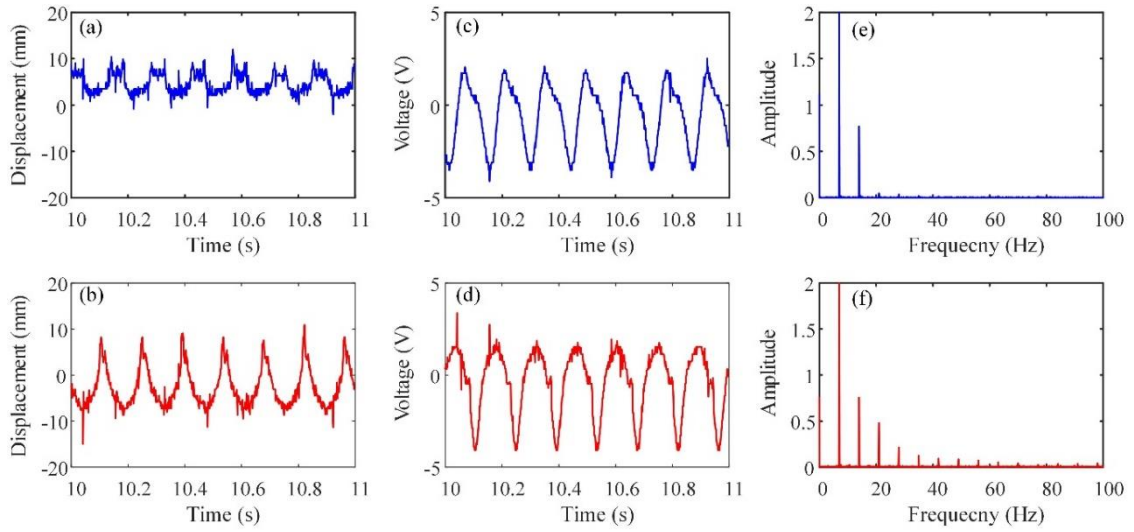


Figure 4.10 Measured displacement, output voltage and power spectrum of the bi-stable PEH (blue) and the tri-stable PEH (red) at the rotational speed of 430 rpm.

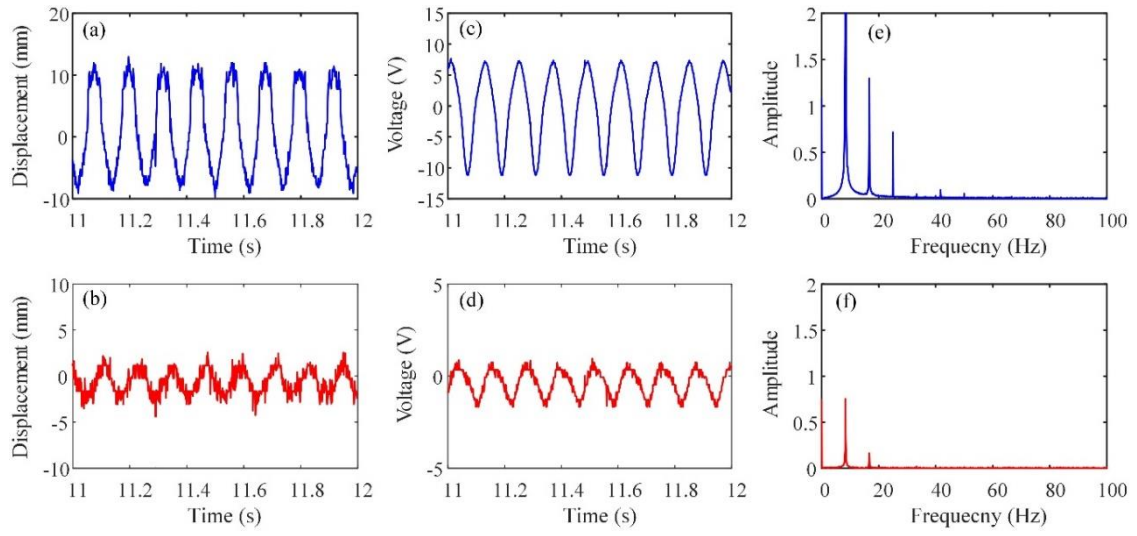


Figure 4.11 Measured displacement, output voltage and power spectrum of the bi-stable PEH (blue) and the tri-stable PEH (red) at the rotational speed of 520 rpm.

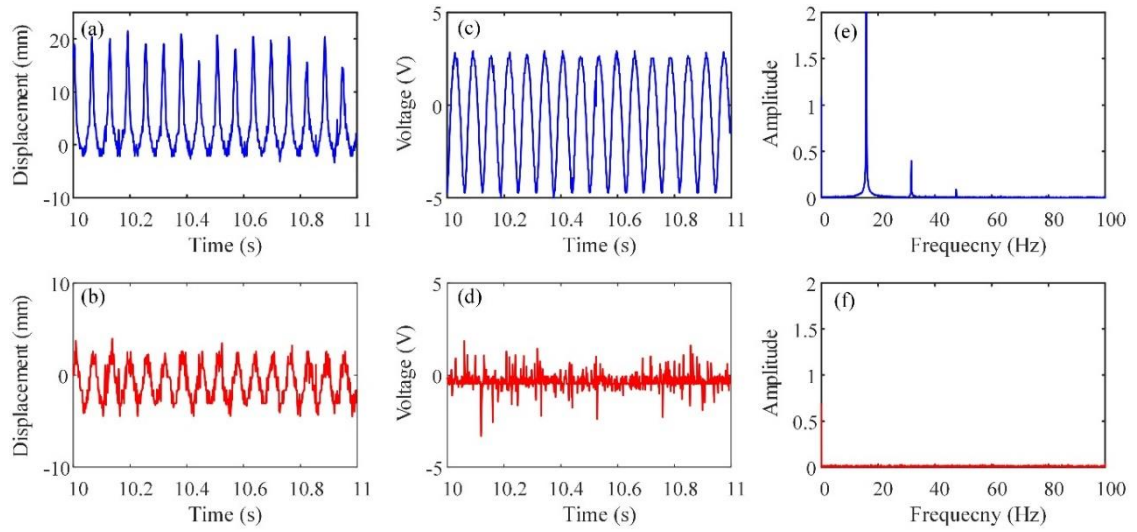


Figure 4.12 Measured displacement, output voltage and power spectrum of the bi-stable PEH (blue) and the tri-stable PEH (red) at the rotational speed of 950 rpm.

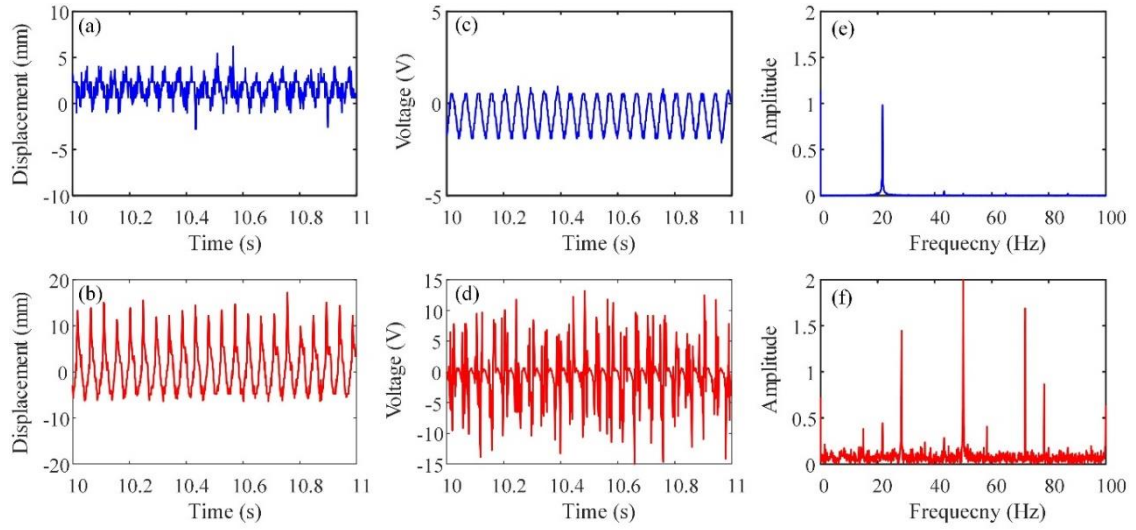


Figure 4.13 Measured displacement, output voltage and power spectrum of the bi-stable PEH (blue) and the tri-stable PEH (red) at the rotational speed of 1300 rpm.

4.4 Optimal Design for the Self-tuning Effect

In this Chapter, the effect of system parameters, including the rotational radius r , beam length L and tip mass M , on the self-tuning effect has been analysed. According to the numerical results, we can find that the perfect match region of self-tuning effect is sensitive to the system parameters. For the further optimal design, the effect of the beam thickness will be analysed in this section.

Firstly, when $L = 80$ mm, $r = 40$ mm and $M = 7.5$ g, the beam thickness, of $t_b = 0.16$ mm, $t_b = 0.18$ mm, $t_b = 0.20$ mm, $t_b = 0.22$ mm and $t_b = 0.24$ mm, has been respectively conducted to calculate the resonance frequency versus the rotational frequency 0 - 30 Hz (0 - 1800 rpm). Figure 4.14 shows the perfect match regions of self-tuning effect for different beam thicknesses. With the increase of the beam thickness, the equivalent stiffness of the beam will be increased simultaneously, thereby the corresponding perfect match occurs at 17 Hz (960 rpm) of $t_b = 0.16$ mm, 18.8 Hz (1128 rpm) of $t_b = 0.18$ mm, 21 Hz (1260 rpm) of $t_b = 0.20$ mm, 24 Hz (1440 rpm) of $t_b = 0.22$ mm and 26.2 Hz (1572 rpm) of $t_b = 0.24$ mm. Thus, in some situations, due to the limitation of dimensions of PEH, the effect way is to change the beam thickness to achieve the perfect match region of self-tuning effect.

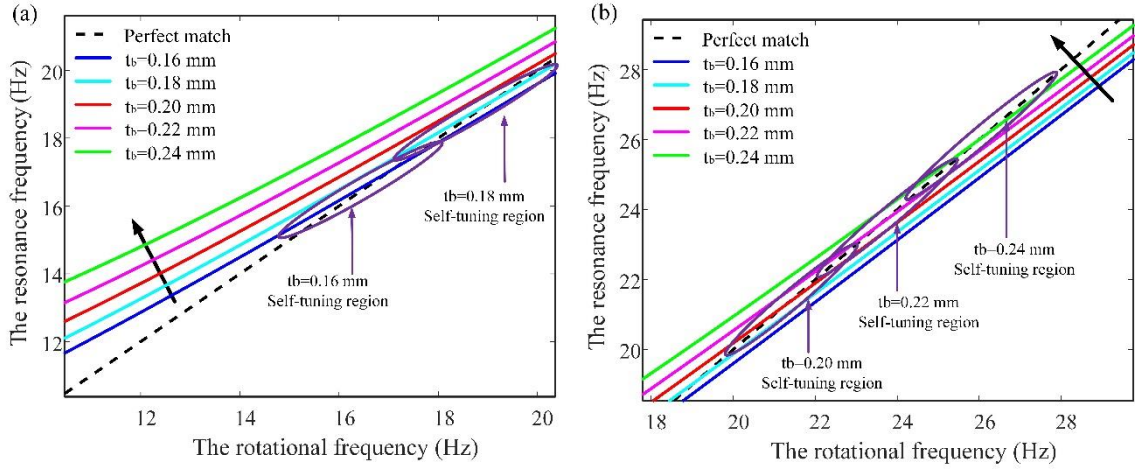


Figure 4.14 Calculated resonance frequency versus rotational frequency for different beam thickness, $t_b = 0.16$ mm, $t_b = 0.18$ mm, $t_b = 0.20$ mm, $t_b = 0.22$ mm and $t_b = 0.24$ mm respectively when $L = 80$ mm, $r = 40$ mm and $M = 7.5$ g.

In next parts, we assume the beam thickness $t_b = 0.18$ mm to further investigate the perfect match region for rotational radius r , beam length L and tip mass M , and corresponding results are shown in Figure 4.15, Figure 4.16 and Figure 4.17, respectively. As observed in Figure 4.15, the perfect match region of $r = 45$ mm is wider than that of others. From the results of Figure 4.16, the perfect match region of $L = 95$ mm is wider than others. From the results of Figure 4.17, the perfect match region of $M = 8.1$ g is wider than that of others.

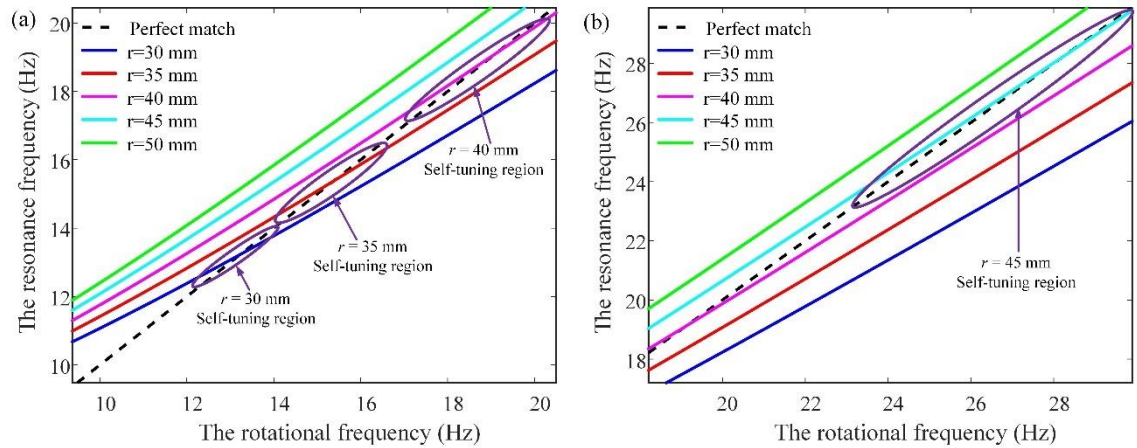


Figure 4.15 Calculated resonance frequency versus rotational frequency for different rotational radii, $r = 30$ mm, $r = 35$ mm, $r = 40$ mm, $r = 45$ mm and $r = 50$ mm respectively when $L = 80$ mm, $t_b = 0.18$ mm and $M = 7.5$ g.

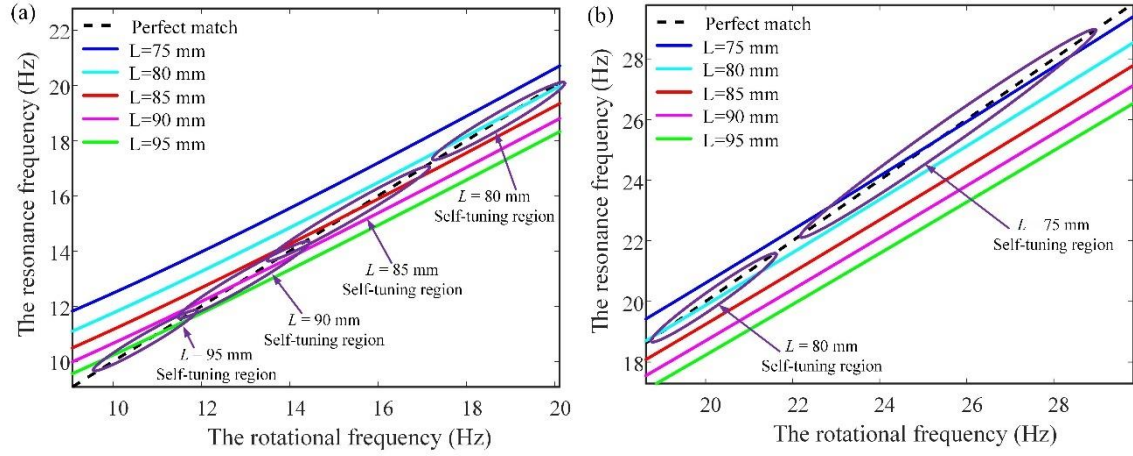


Figure 4.16 Calculated resonance frequency versus rotational frequency for different beam lengths, $L = 75$ mm, $L = 80$ mm, $L = 85$ mm, $L = 90$ mm and $L = 95$ mm respectively when $L = 80$ mm, $t_b = 0.18$ mm and $M = 7.5$ g.

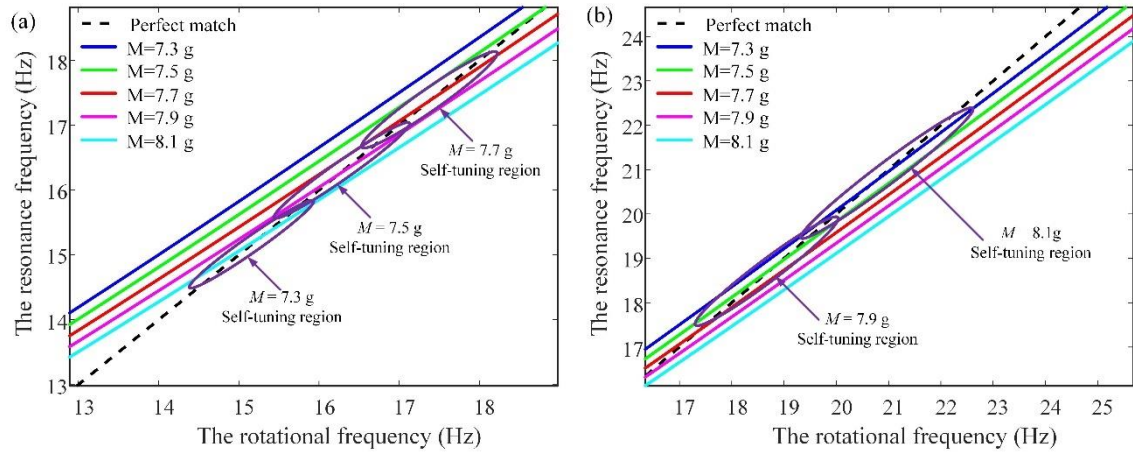


Figure 4.17 Calculated resonance frequency versus rotational frequency for different tip masses, $M = 7.3$ g, $M = 7.5$ g, $M = 7.7$ g, $M = 7.9$ g and $M = 8.1$ g respectively when $L = 80$ mm, $t_b = 0.18$ mm and $L = 80$ mm.

Based on the analyses in Figure 4.15, Figure 4.16 and Figure 4.17, the optimal parameters of the PEH are listed in Table 4.3. Figure 4.18(a) shows the relationship between the rotational frequency and resonance frequency. Figure 4.18(b) is the local amplification of Figure 4.18(a), and it is found that the rotational frequency can approximately track the equivalent resonance frequency over a wide frequency range 15 Hz – 45 Hz (900 rpm – 2700 rpm). Compared with the results of Figure 4.2, the perfect match region has been broadened largely after the optimal design.

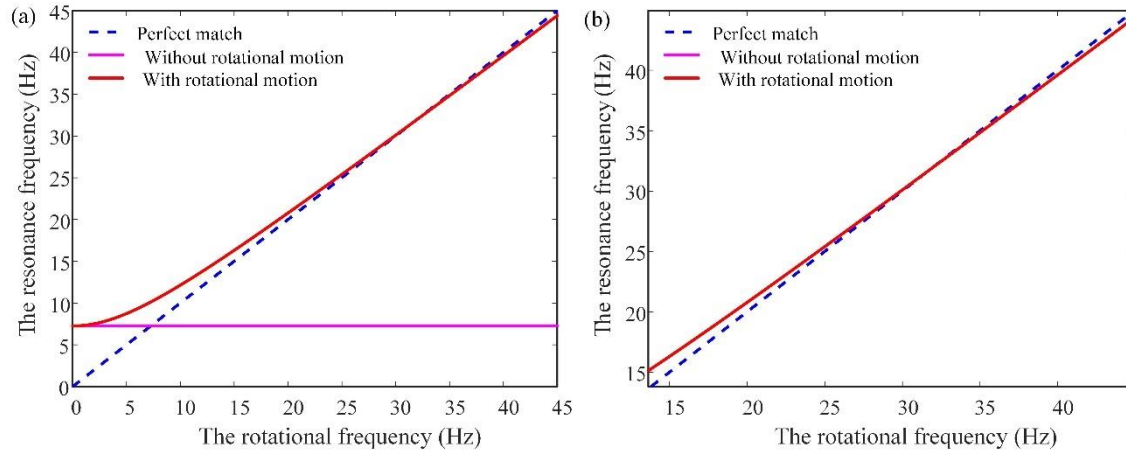


Figure 4.18 (a) The relationship between the rotational frequency and the equivalent resonance frequency of the optimal PEH; (b) the local amplification of Figure 4.18(a).

Table 4.3. The optimal parameter values

Symbol	r (mm)	L (mm)	b (mm)	t_b (mm)	M (g)	m_b (g)
Value	45	87	12	0.18	8.1	1.6

4.5 Discussion

Based on our previous study in Ref. [107], when the rotational speed is increased to a certain value (440 rpm), the centrifugal force acting on the tip mass of different PEHs will reduce deformation of piezoelectric beams, and this phenomenon is called the centrifugal stiffening effect. However, in experiments of Chapter 4, the bi-stable and tri-stable PEHs achieve the high output voltage in the ranges of 440 -720 rpm and 990 -1300 rpm respectively as shown in Figure 4.7. These should be the influence of self-tuning effect. By this method, the effective energy harvesting bandwidth can be broadened for the energy harvesting from the high-speed rotating machine. Furthermore, optimizing the self-tuning PEH with the wide frequency bandwidth and high performance has been investigated, and the experimental validations will be conducted in future research.

The passively self-tuning effect via the centrifugal stiffening effect is an effective way to broaden frequency bandwidth for enhancement of energy harvesting performance. Because the centrifugal stiffening effect occurs under high rotational speed, the potential application of passively potential application is the high-speed rotational machine. We can use the self-tuning PEH to provide the power supply for the wireless sensor, which are utilized for structural health monitoring.

4.6 Summary

In this chapter, according to the centrifugal stiffening effect, a self-tuning PEH in rotational motion is realized. According to the derived theoretical model, the effect of the parameters on the self-tuning effect, including the rotational radius, the length of piezoelectric beam and the tip mass, has been theoretically analyzed. The bi-stable and tri-stable PEHs with different rotational radiuses are adopted in experiments to validate the theoretical analyses. From the above studies, the following conclusions can be obtained:

- (1) The passively self-tuning effect can be achieved in rotational motion by the centrifugal force acting on the tip mass of a PEH.
- (2) The rotational radius has a great effect on the self-tuning rotational speed range which results in different energy harvesting performance, thus, this provides theoretical guidance for the optimization design of a PEH in rotational motion.
- (3) In the low rotational speed range (60 – 300 rpm), the tri-stable PEH shows better energy harvesting performance than the bi-stable one due to the advantage of lower potential barriers.

In summary, the centrifugal force acting on the tip mass of a PEH is a promising way to achieve a passively self-tuning PEH. Additionally, combining with the advantage of multi-stable characteristics, a passively self-tuning method is effective way to widen the operational frequency bandwidth.

Chapter 5

Low-frequency Energy Harvesting by Centrifugal Softening Effect

5. Low-frequency Energy Harvesting by Centrifugal Softening Effect

Although various PEHs in rotational motion have been proposed, there are few studies for energy harvesting when rotational speed is less than 120 rpm (2 Hz). Thus, it is still a great challenge to realize the self-powered wireless sensors in low-frequency rotational motion. To overcome this issue, inspired by the centrifugal stiffening effect, the centrifugal softening effect achieved by inverting the direction of centrifugal force is investigated so that the energy harvesting in low-frequency rotational motion can be enhanced.

5.1 Operating Principle

As shown in Figure 5.1, a nonlinear PEH is inversely installed in rotational motion, such as the blade of a wind turbine, to convert the low-frequency rotational energy into the electric energy for powering the wireless sensor nodes. Thus, a self-powered sensor can be achieved to monitor the structural health of the wind turbine. Two uni-morph piezoelectric patches are covered at fixed end of cantilever beam, and all of them are called piezoelectric beam. The nonlinear PEH is composed of a piezoelectric beam with a tip mass (magnet A) at the free end, and two external magnets are fixed on the frame. Note that all these magnets are permanent magnets. The whole PEH system is mounted on the blade of a wind turbine that rotates with its central axis in horizontal at a related rotational speed.

From Figure 5.1, we can notice that the centrifugal force caused by the rotational motion can be respectively divided into the axial direction and transverse direction. Namely, the axial component of centrifugal force can soften the piezoelectric beam, and the transverse component of the centrifugal force can enforce the piezoelectric beam vibration to enhance its energy harvesting performance in low-frequency rotational motion. In order to investigate the dynamic mechanism of this configuration, the corresponding theoretical model should be derived firstly.

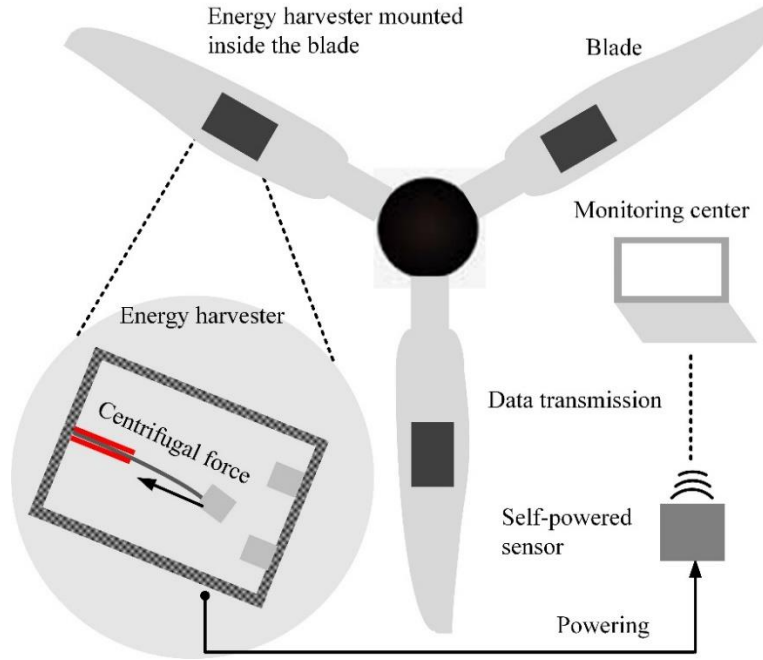


Figure 5.1 The schematic diagram of nonlinear PEH inversely installed in the blade of wind turbine.

5.2 Theoretical Modelling

Similarly, we mainly focus on the transverse displacement of the piezoelectric beam, which is time-varying due to the rotational motion. Therefore, the related theoretical model will also be derived in a rotational coordinate system, which is the same as that in Chapter 2. As shown in Figure 5.2, $X^*Y^*Z^*$ is a rotational coordinate system, XYZ is a fixed (Newtonian) coordinate system. Both of them are defined as the reference and inertial frame, respectively. It should be noted that Z axis is parallel to Z^* axis all the time as shown in Figure 5.2. r denotes the rotational radius, namely the distance from the rotational center to the tip mass. $\theta = \int_0^t \omega dt$, defined as the angle subtended by X axis and X^* axis as shown in Figure 5.2, is the angular displacement of the hub. Furthermore, L is the length of the cantilever beam. $w(x, t)$ and $u(x, t)$ are the transverse displacement and axial deformation associated with the distance x and the time t of the piezoelectric beam. R is assumed to be the position P_0 of an infinitesimal segment on the beam in the rotational coordinate system.

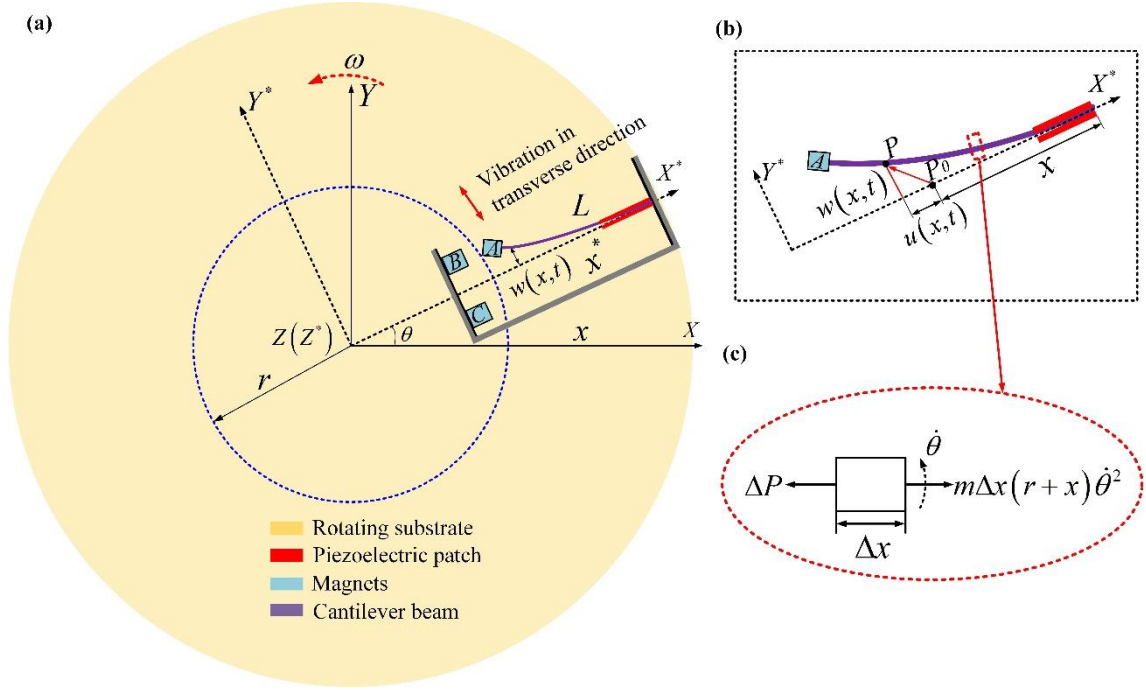


Figure 5.2 (a) The schematic diagram of an inverse nonlinear PEH in a rotational coordinate system; (b) the piezoelectric beam description of deformation with the consideration of axial deformation; (c) a differential beam element of the piezoelectric beam in rotational motion.

5.2.1 Kinetic Energy Description

Based on Figure 5.2, the following relationship can be obtained based on the geometrical configuration:

$$\mathbf{R} = [L + r - x - u(x, t)] \mathbf{i}^* + w(x, t) \mathbf{j}^* \quad (5.1)$$

where \mathbf{i}^* , \mathbf{j}^* and \mathbf{k}^* are the unit vectors of the rotational coordinate system along X^* , Y^* and Z^* axis, respectively. The axial deformation includes the pure axial deformation $u_a(x, t)$ and the deformation Δx associated with the foreshortening quantity due to the pure transverse deformation $w(x, t)$. For simplify, $u(x, t) = u_a(x, t) - \Delta x$ is defined in subsequent derivations.

Therefore, ignoring the high order small quantities, the corresponding velocity can be expressed as:

$$\dot{\mathbf{R}} = \left(\frac{d\mathbf{R}}{dt} \right)_R + \dot{\theta} \mathbf{k}^* \times \mathbf{R} = -w(x, t) \dot{\theta} \mathbf{i}^* + [\dot{w}(x, t) + (L + r - x - u(x, t)) \dot{\theta}] \mathbf{j}^* \quad (5.2)$$

where the overdot is the derivative with respect to time. Thus, the whole kinetic energy of the inverse PEH can be expressed as:

$$T = \frac{1}{2} m \int_0^L \dot{R}_1^2 dx + \frac{1}{2} M \dot{R}_A^2 + \frac{1}{2} J_A \dot{w}'(L, t)^2 \quad (5.3)$$

where M and J_A are the mass and inertia moment of tip mass (magnet A), respectively. m is the mass of piezoelectric beam per unit length. When $0 \leq x < l_p$, $m = \rho_b A_b + 2\rho_p A_p$. And as $l_p < x \leq L$, $m = \rho_b A_b$. A_b and ρ_b are the cross-sectional area and the material density of the cantilever beam, respectively. l_p , A_p and ρ_p are the length, the cross-sectional area and the material density of piezoelectric patches, respectively.

Thus, the velocity of piezoelectric beam and tip mass can be respectively expressed as:

$$\dot{R}_1^2 = \dot{\theta}^2 w^2(x, t) + [\dot{w}(x, t) + (L + r - x - u(x, t))\dot{\theta}]^2 \quad (5.4)$$

$$\dot{R}_A^2 = \dot{\theta}^2 w^2(L, t) + [\dot{w}(L, t) + (r - u(L, t))\dot{\theta}]^2 \quad (5.5)$$

For the tip mass, $x = L$, thus, the tip displacement and axial deformation are represented as $w(L, t)$ and $u(L, t)$, respectively. Substituting Eqs. (5.4) and (5.5) into Eq. (5.3), the whole kinetic energy of the harvester can be rewritten as:

$$T = \frac{1}{2} m \int_0^L \dot{\theta}^2 w^2(x, t) + [\dot{w}(x, t) + (L + r - x)\dot{\theta}]^2 dx + \frac{1}{2} J_A \dot{w}'(L, t)^2 + \frac{1}{2} M \left\{ \dot{\theta}^2 w^2(L, t) + [\dot{w}(L, t) + r\dot{\theta}]^2 \right\} \quad (5.6)$$

Note that for simplicity the axial motion has been neglected in the kinetic energy description. However, the axial deformation will be considered in the potential energy caused by the centrifugal force.

5.2.2 Potential Energy Description

For the nonlinear harvester system, the total potential energy is a sum of the elastic energy U_e of the piezoelectric beam, magnetic potential energy U_m , gravitational potential energy U_g and centrifugal potential energy U_c . Thus, it can be expressed as:

$$U = U_e + U_g + U_c + U_m \quad (5.7)$$

where $U_e = \frac{1}{2} EI \int_0^L [w''(x, t)]^2 dx$, $U_m = \oint F_m dx$, and $(\bullet)''$ refers to $\frac{\partial}{\partial x^2}$. F_m is the nonlinear magnetic force in the magnets configuration. Furthermore, U_g can be expressed as [96,98,99]:

$$U_g = mg \int_0^L [(L+r-x) \sin \theta + w(x,t) \cos \theta] dx + Mg [r \sin \theta + w(L,t) \cos \theta] \quad (5.8)$$

Next, the potential energy caused by the centrifugal force f_{cl} is given by [99]:

$$U_c = \frac{1}{2} \int_L^0 f_{cl} w'(x,t)^2 dx \quad (5.9)$$

where the centrifugal force f_r can be calculated as:

$$f_{cl} = m \int_0^{L-x} [\dot{\theta}^2 (L+r-x)] dx + Mr \dot{\theta}^2 \quad (5.10)$$

Thus, substituting Eq. (5.10) into Eq. (5.9), the centrifugal potential energy can be obtained:

$$U_c = \frac{1}{2} \int_L^0 \left[mr \dot{\theta}^2 (L-x) + \frac{1}{2} m \dot{\theta}^2 (L^2 - x^2) + Mr \dot{\theta}^2 \right] w'(x,t)^2 dx \quad (5.11)$$

where EI is the bending rigidity of the piezoelectric beam, and g is the gravitational constant ($9.8 \text{ m} \cdot \text{s}^{-2}$). Additionally, the internal electrical energy in the piezoelectric path is calculated, as follows [73]:

$$W_e = \int_0^{l_p} \mathcal{G}_{p1} v(t) w''(x,t) dx + \frac{1}{2} C_p v(t)^2 \quad (5.12)$$

where \mathcal{G}_{p1} is the electromechanical coupling coefficient, and C_p is the capacitance of the piezoelectric patch, $v(t)$ is the generated output voltage.

5.2.3 Governing Equation

The transverse displacement $w(x,t)$ can be written as:

$$w(x,t) = \sum_{i=1}^n \phi_i(x) q_i(t) \quad (5.13)$$

where $q_i(t)$ is the time dependent generalized temporal coordinate. $\phi_i(x)$ is the mode shape function of piezoelectric beam that satisfy the boundary conditions. The inverse nonlinear PEH is used for low-frequency rotational motion, additionally, the tip mass (magnet A) is larger than that of piezoelectric beam. Therefore, the single-mode approximation is enough. Taking into consideration of the geometric change caused by the installation of two piezoelectric patches at the fixed end, thus, at the break $x=l_p$, a discontinuous system is proposed to define the orthogonal basis function $\phi(x)$, which is expressed as:

$$\phi(x) = \begin{cases} \phi_1(x), & 0 \leq x < l_p \\ \phi_2(x), & l_p \leq x \leq L \end{cases} \quad (5.14)$$

Based on the above kinetic energy and potential energy of inverse nonlinear PEH, the related Lagrange function can be defined as:

$$L(w, v) = T - U + W_e \quad (5.15)$$

Similarly, by utilizing Lagrange function, the electromechanical equations of inverse PEH can be obtained as:

$$M_e \ddot{q}(t) + C \dot{q}(t) + (K_e - K_{c1} \dot{\theta}^2) q(t) + \chi_1 \ddot{\theta} - \mathcal{G}_p v(t) + F_m = -\Gamma_1 g \cos \theta \quad (5.16a)$$

$$C_p \dot{v}(t) + v(t) R_l^{-1} + \mathcal{G}_p \dot{q}(t) = 0 \quad (5.16b)$$

where M_e is the equivalent mass. C is the mechanical damping coefficient. K_e is the equivalent stiffness of the piezoelectric beam. Additionally, $\dot{\theta}$ and $\ddot{\theta}$ are the angular velocity and angular acceleration of the rotational motion, respectively. K_{c1} is the coefficient of the coupling term $\dot{\theta}^2 q(t)$. χ_1 is the coefficient of the angular acceleration. $\Gamma_1 g$ is the equivalent excitation from the gravity of the tip mass due to the rotational motion. F_m is the magnetic force along the direction of the tip displacement. R_l is the load resistance. Furthermore, the details of the above coefficients are given as:

$$M_e = m \int_0^L \phi(x)^2 dx + M \phi(L)^2 + \frac{1}{2} J_A \phi'(x)^2 \Big|_{x=L} \quad (5.17a)$$

$$K_e = EI \int_0^L \phi''(x)^2 dx \quad (5.17b)$$

$$K_{c1} = m \left(r \int_0^L (L-x) \phi'(x)^2 dx + \frac{1}{2} \int_0^L (L^2 - x^2) \phi'(x)^2 dx + \int_0^L \phi(x)^2 dx \right) + M \left[r \int_0^L \phi'(x)^2 dx + \phi(L)^2 \right] \quad (5.17c)$$

$$\chi_1 = Mr \phi(L) + m \int_0^L \phi(x) (L+r-x) dx \quad (5.17d)$$

$$\Gamma_1 = m \int_0^L \phi(x) dx + M \phi(L) \quad (5.17e)$$

$$\mathcal{G}_p = \mathcal{G}_{p1} \int_0^{l_p} \phi''(x) dx \quad (5.17f)$$

$$C = c \int_0^L \phi(x) dx \quad (5.17g)$$

Compared with the theoretical model of the forward nonlinear PEH proposed in Chapter 2, the

differences in the theoretical model of Eqs. (5.16a) and (5.16b) are the K_{c1} , χ_1 and Γ_1 coefficients.

5.3 Theoretical Analyses

The theoretical analyses and numerical simulations will be conducted in the section. All of them are conducted by MATLAB software. Defining the space vector of Eqs. (5.16a) and (5.16b) as:

$$\begin{bmatrix} y_1 & y_2 & y_3 \end{bmatrix}^T = \begin{bmatrix} q(t) & \dot{q}(t) & v(t) \end{bmatrix}^T \quad (5.18)$$

Thus, the governing Eqs. (5.18a) and (2.52b) of the nonlinear PEH in rotational motion can be rewritten as:

$$\dot{y}_1 = y_2 \quad (5.19a)$$

$$\dot{y}_2 = -\frac{1}{M_e} \left[Cy_2 + (K_e - K_{c1}\dot{\theta}^2)y_1 + F_m + \chi_1\ddot{\theta} - g_p y_3 + \Gamma_1 g \cos \theta \right] \quad (5.19b)$$

$$\dot{y}_3 = -\frac{1}{C_p} \left(\frac{1}{R_l} y_3 + g_p y_2 \right) \quad (5.19b)$$

Note that all parameters, adopted in the numerical simulations are the same as those of the experiments. The parameters are listed in Table 5.1.

Table 5.1 Parameter used in the numerical simulations

Parameter	Value	Unit
M_e	0.0096	Kg
C	0.005	N.s/m
K_e	16.4	N /m
K_{c1}	0.0136	
g_p	1.387e-4	
Γ_1	0.0094	
C_p	2.3e-7	
R_l	1000000	Ω

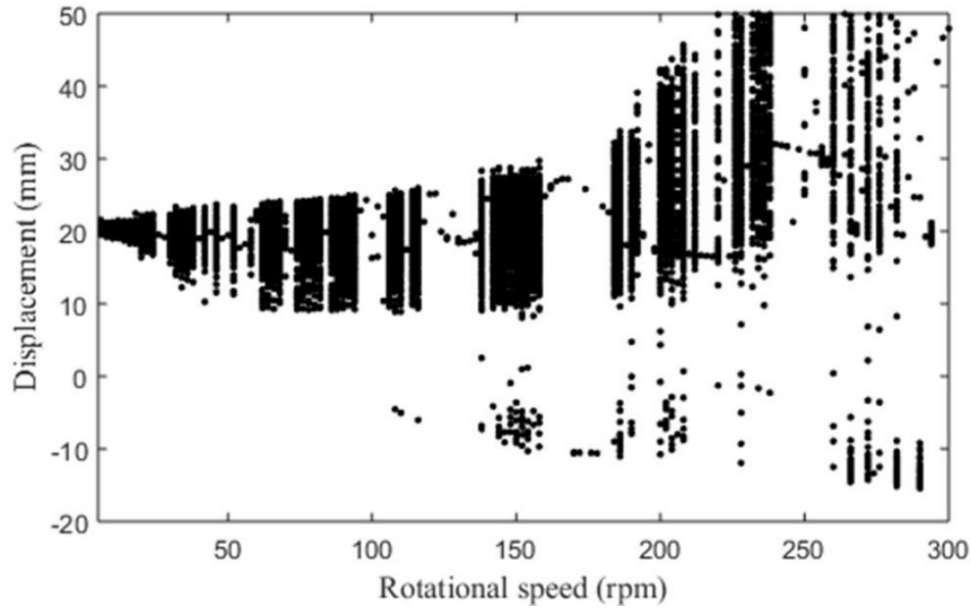


Figure 5.3 Bifurcation diagrams for an inverse nonlinear PEH versus various rotational speeds by the theoretical models.

In order to investigate the dynamic performance of an inverse nonlinear PEH, the bifurcation diagram of rotational speed 5 - 300 rpm is shown in Figure 5.3. It can be noticed that in low-rotational speed 5 - 105 rpm, the centrifugal force leads to the chaotic oscillation with peak tip displacement 22 mm, which results in the high output voltage. When the rotational speed is 160 -180 rpm, the inverse PEH experiences the inter-well oscillation. As the rotational speed is further increased to 180 rpm, the centrifugal force leads to a large deformation of the piezoelectrical beam. Although in this situation the output voltage is high, the large deformation may make the piezoelectric beam broken for the proposed parameters. However, if we add the thickness of piezoelectric beam, the Regin II is also beneficial for energy harvesting. Thus, depending on the system parameters, the inverse PEH is suitable for the low-frequency rotational motion.

With the aim to illustrate the dynamic performance and output voltage of the inverse PEH, the numerical results, of rotational speed 60 rpm, 90 rpm and 110 rpm, are shown in Figure 5.4. When the rotational speed is 60 rpm or 90 rpm, the inverse PEH undergoes the chaotic oscillations, and the peak output voltage can reach 10 V. As the rotational speed is 110 rpm, the inverse PEH exhibits the quasi-oscillations.

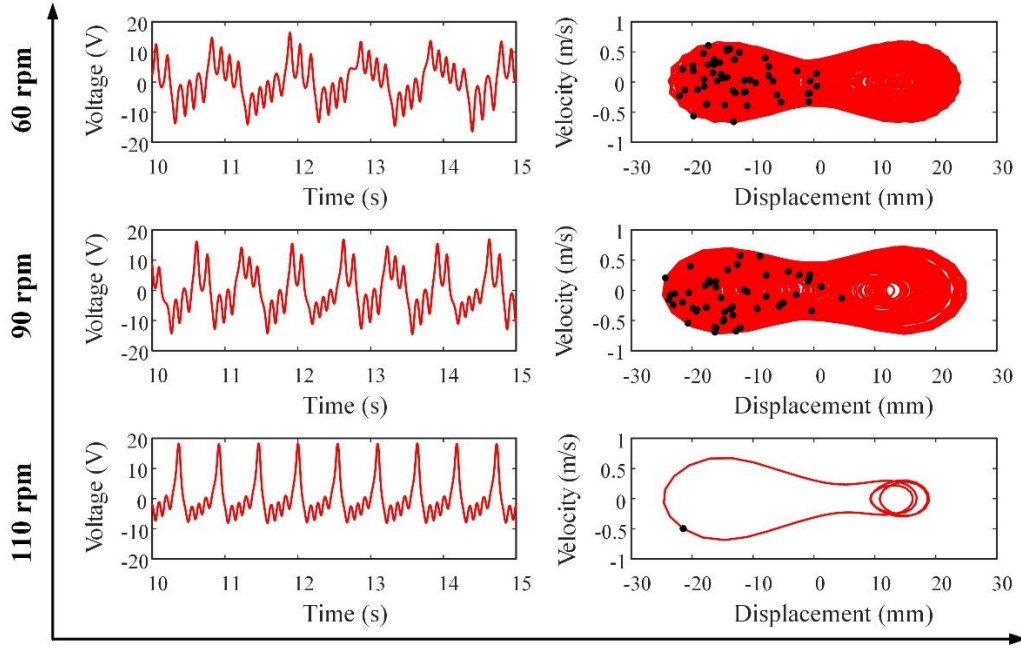


Figure 5.4 The numerical results of an inverse PEH in rational motion under the rotational speeds 60 rpm, 90 rom and 110 rpm.

5.4 Experimental Validation

5.4.1 Experimental Setup

In this section, in order to validate the enhancement of energy harvesting via the centrifugal softening effect, the corresponding experiments are carried out under various constant rotational speeds. The same nonlinear PEH is adopted in the experiments with forward and inverse installation methods, which can lead to the centrifugal stiffening and softening effects respectively, due to the opposite directions of centrifugal force.

It should be mentioned that the experimental setup as shown in Figure 5.5 is the same as previous on in Chapter 4, and the difference is the nonlinear PEHs. Note that all the magnets adopted in experiments are NdFeB cylinder magnets. The tip mass (magnet A) has the dimension of $D12 \times 7.1 \text{ mm}^3$ (D represents the diameter) is installed at the free end of the piezoelectric beam, and two external magnets with the same dimension of $D12 \times 7.1 \text{ mm}^3$ are fixed on the frame. Each piezoelectric patch (K2512U1, THRIVE, JAPAN) has a dimension of $25 \times 12 \times 0.13 \text{ mm}^3$. In the experiments, the same nonlinear PEH is adopted for the forward configuration and inverse configuration. Thus, we can make a comparison to validate the influence of centrifugal force direction on the energy harvesting performance. The parameters of the nonlinear are $h_1=20 \text{ mm}$, $h_2=10 \text{ mm}$ and $d=15 \text{ mm}$. The parameters in the experiments are listed in Table 5.2.

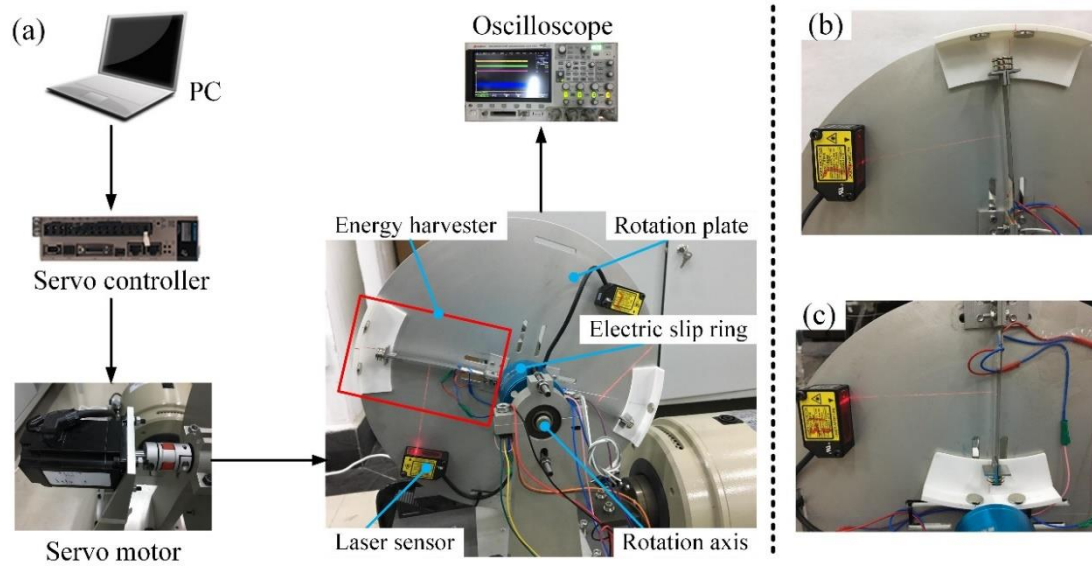


Figure 5.5 (a) The experiment setup for experiments in rotational motion; (b) the forward nonlinear PEH, namely the centrifugal force is along with the outside of radial direction; (c) the inverse nonlinear PEH, namely the centrifugal force is along with the inside of radial direction

Table 5.2. The parameters used in the experimental validation

Parameters	Symbol	Value
Cantilever beam		
Length \times Width \times Thickness	$L \times b \times t_b$	$95 \times 12 \times 0.20 \text{ mm}^3$
Young's modulus	E_b	210 Gpa
Density	ρ_b	7765 Kg/m^3
Damping ratio	C	0.005
Piezoelectric patch		
Length \times Width \times Thickness	$l_p \times b_p \times t_p$	$25 \times 12 \times 0.13 \text{ mm}^3$
Young's modulus	E_p	66 Gpa
Density	ρ_p	7800 Kg/ m^3
Coupling coefficient	d_{31}	$-320 \times 10^{-12} \text{ C/N}$
Permittivity constant	ϵ_{33}	$4000 \epsilon_0$
Permittivity of free space	ϵ_0	$8.854 \times 10^{-12} \text{ F/m}$
Permanent magnets		
Density	$\rho_A \quad \rho_B \quad \rho_C$	7500 Kg/ m^3
Magnet's residual flux density	B_r	1.2 T
Permeability of free space	μ_0	$4\pi \times 10^{-7}$
Load resistance	R_l	1 $\text{M}\Omega$

5.4.2 Experimental Results

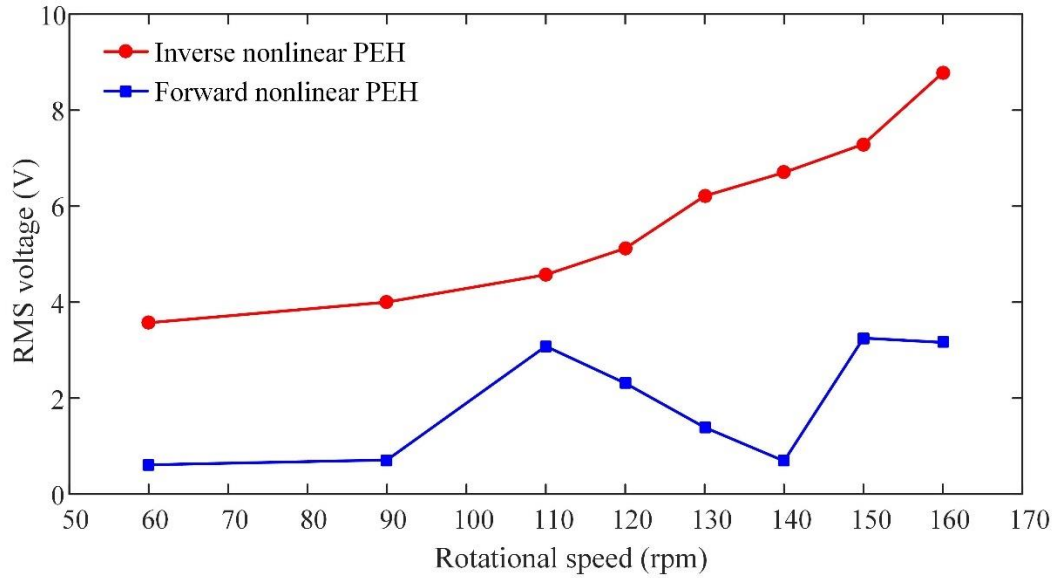


Figure 5.6 The experimental results RMS voltages of the inverse (red line) and forward nonlinear PEHs (blue line) under various rotational speeds.

In order to make a comparison of the energy harvesting performance between the inverse and forward nonlinear PEHs, the RMS voltages of inverse and forward nonlinear PEHs under various rotational speeds are illustrated in Figure 5.6. It is worth mentioning that both them are presented by the red line and blue line, respectively. As observed from Figure 5.6, in low-frequency rotational motion, the inverse nonlinear PEH shows better performance than the forward one, and the RMS voltage is more than 4 V. On the contrary, the forward nonlinear PEH undergoes the intra-well oscillations, leading to the low output voltage. With the aim to show further details of their energy harvesting performance, the experimental of 60 rpm, 90 rpm and 110 rpm are selected and shown in Figure 5.7, Figure 5.8 and Figure 5.9, respectively.

When the rotational speed is 60 rpm (1Hz), the inverse nonlinear PEH experiences the chaotic oscillations, and corresponding peak-peak voltage can reach almost 15 V as shown in Figure 5.7 (a). On the contrary, the forward PEH appears the intra-well oscillation around one stable position as shown in Figure 5.7 (d), consequently, the corresponding peak-peak output voltage is as low as 2 V. As the rotational speed is increased to 90 rpm (1.5 Hz), their experimental results are illustrated in Figure 5.8. For the inverse nonlinear PEH, it still undergoes the quasi-periodic oscillation, however, the forward nonlinear PEH maintains the same state of rotational speed 60 rpm. Furthermore, under rotational speed 110 rpm (1.83 Hz), the forward PEH exhibits the chaotic

oscillation with some snap-through phenomena, thus, the peak-peak output voltage is remarkably increased as high as 10 V as shown in Figure 5.9.

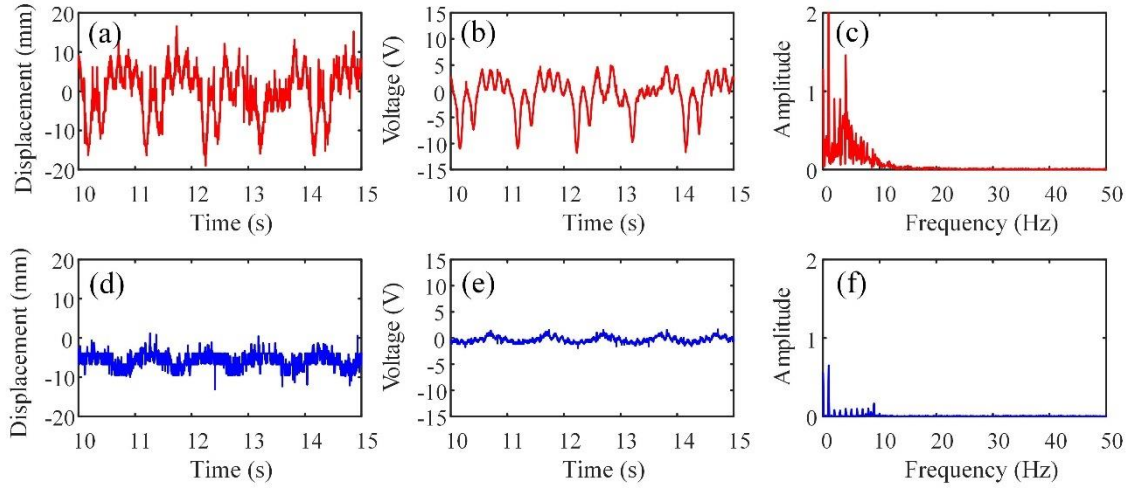


Figure 5.7 The experimental results of the inverse (red line) and forward nonlinear harvester (blue line) under the rotational speed 60 rpm.

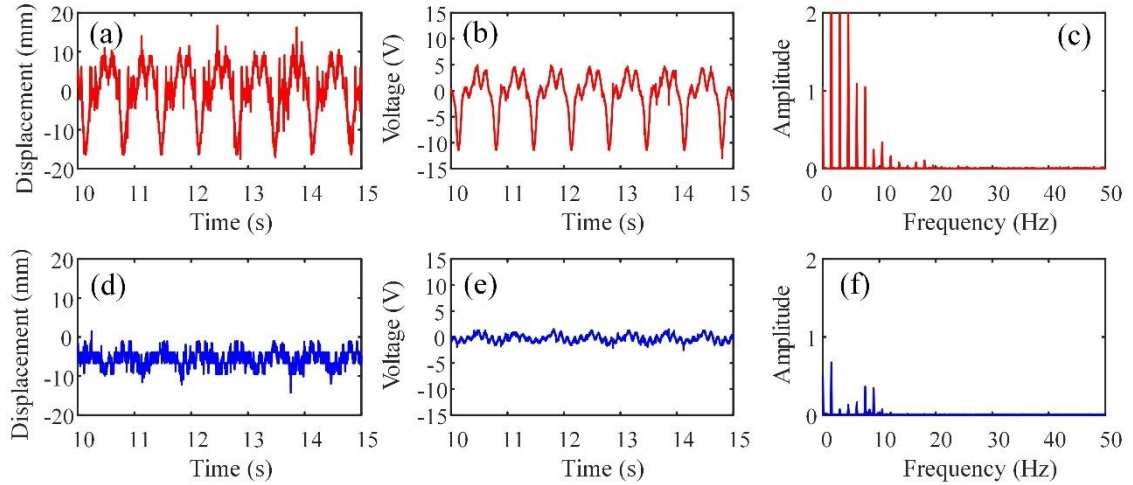


Figure 5.8 The experimental results of the inverse (red line) and forward nonlinear harvester (blue line) under the rotational speed 90 rpm.

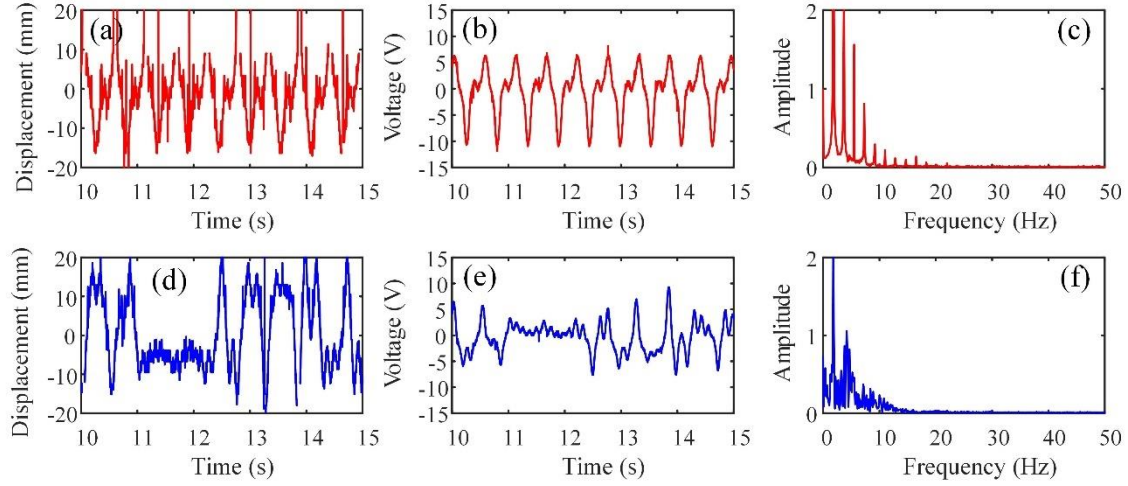


Figure 5.9 The experimental results of the inverse (red line) and forward nonlinear harvester (blue line) under the rotational speed 110 rpm.

5.5 Discussion

5.5.1 Further Improvement

In the above experiments, the centrifugal softening effect of an inverse nonlinear PEH has been experimentally investigated and its outstanding performance in low-frequency rotational motion has been demonstrated. According to the experimental results, it can be noticed that the piezoelectric beam undergoes the large deflection caused by the centrifugal softening effect. Although it is beneficial for the output power, it will also result in the machinal failure of the piezoelectric beam. To solve this issue, the further improvement is needed to complete this inverse configuration.

As shown in Figure 5.10, a pair of pre-load blocking beams will be added to the two sides to confine the deflection of piezoelectric beam. Additionally, the impact force of the tip mass can enforce the blocking beams to oscillate between two stable positions, thus, inducing the large-amplitude oscillation. In summary, after adding a pair of pre-load blocking beams, the redesigned inverse nonlinear PEH can not only protect the piezoelectric beam from the failure caused by the large deflection, but also enhance the output voltage due to the addition of two blocking beams. Next, after completing the mechanical part of inverse nonlinear PEH, the corresponding circuit management system is needed to provide the DC power supply for the wireless sensors. Lastly, a self-powered sensor will be realized, with our proposed mechanical harvester and attached circuit, to monitor the structural health of the blade of a wind turbine as shown in Figure 5.10(b).

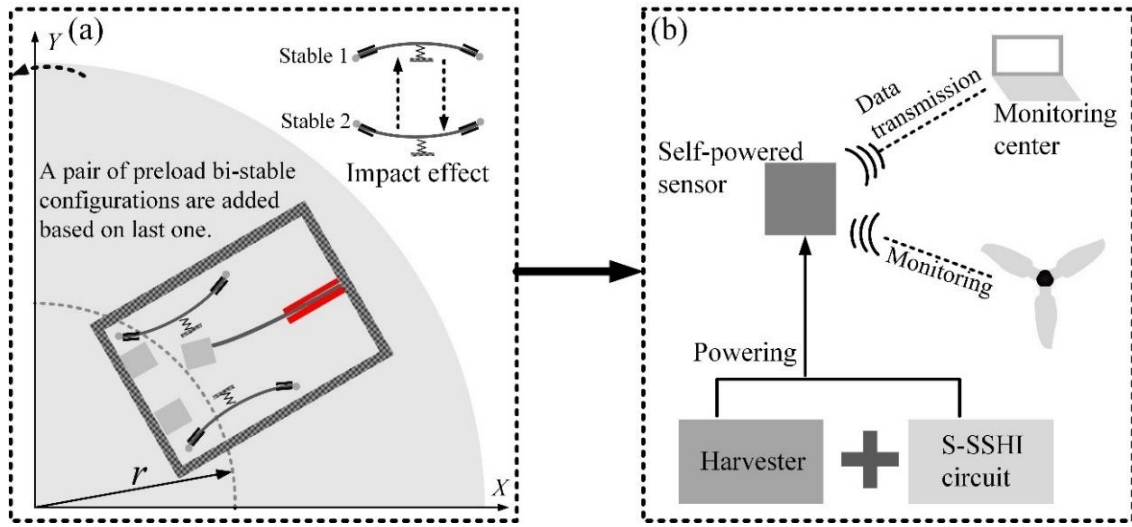


Figure 5.10 The schematic diagram of further improvement of an inverse PEH configuration in rotational motion.

5.5.2 Potential Application

As the published data in year 2018, the global wind energy capacity installation reaches 597 GW. All wind turbine installed by end of 2018 can cover close to 6 % of the global electricity demand [118]. How to make sure the normal work of wind turbine is important. Thus, recently many wireless sensors are widely used to reduce the potential damages, which may result in power loss, high maintenance costs and so on. The component health monitoring for wind turbine as shown in Figure 5.11 includes the drive train vibration, drive train torque, gearboxes vibration and individual gear bearing and health, blade flutter, tower dynamics and vibration, and so on.

Now the power supply of these wireless sensors are the batteries, consequently, due to the limited lifespan, the regular replacement of batteries is needed. The energy harvesting method from the low-frequency rotational motion is a promising way to provide the power supply for these wireless sensors. Such as for the blade flutter monitoring with the G-LINK-200 type wireless sensor, whose power supply is 3.6 V LiSOCL2 batteries [120]. Thus, from the experimental results, of an inverse PEH in rotational motion resulting in the centrifugal softening effect, in Figure 5.6, the RMS voltage of rotational speed 60 - 160 rpm is more than 4V, thus, the generated voltage is enough to provide the power supply for one wireless sensor. In future work, the more experiments under various low-frequency will be conducted to further validate the energy harvesting performance.

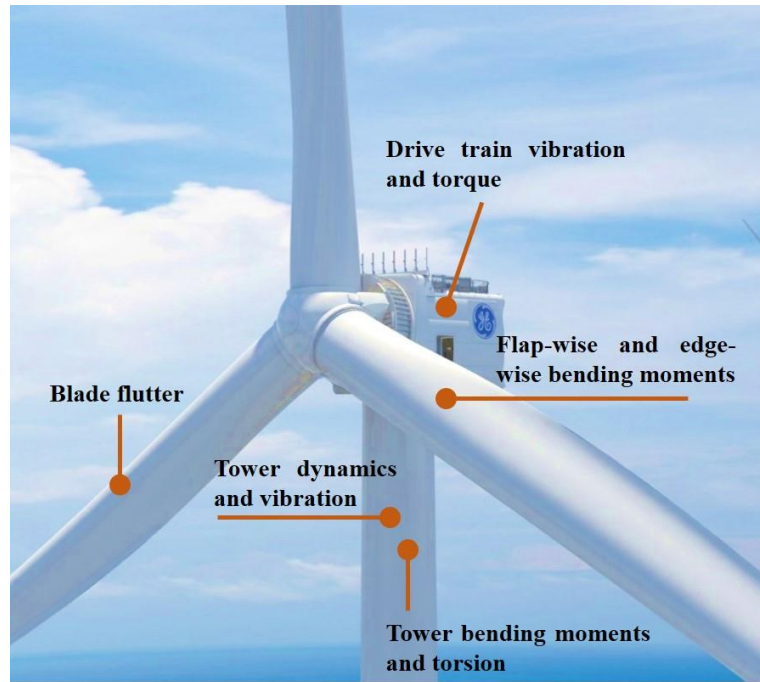


Figure 5.11 Component health monitoring for wind turbine [119].

5.6 Summary

In summary, this chapter explores an inverse PEH for energy harvesting in low-frequency rotational motion. The related theoretical model has been derived in a rotational coordinate system according to Lagrange equation. The corresponding experiments between the inverse and forward PEHs are conducted to make comparisons of their energy harvesting performance. Thus, the following conclusions can be obtained:

- (1) The centrifugal softening effect is an effective way for energy harvesting in low-frequency rotational motion.
- (2) The derived theoretical model can reveal the centrifugal softening effect by the K_{cl} coefficient.
- (3) For the low-frequency rotational motion, the proposed inverse PEH is superior to the forward one for rotational energy harvesting.

In future work, the research will focus on optimizing the parameter of the inverse PEH based on the centrifugal softening effect to redesign the PEH, so that it can provide a sustainable power source for wireless sensor nodes. Lastly, a self-powered wireless sensor is realized for the structural health monitoring of the blade of a wind turbine.

Chapter 6

Further Research and Discussion

6. Further Research and Discussion

In previous Chapters (Chapter 2- Chapter 5), the author investigated the nonlinear PEHs with forward and inverse configurations in rotational motion, which respectively correspond to the centrifugal stiffening and softening effects via the centrifugal force to tune the dynamic performance of piezoelectric beam to enhance the energy harvesting performance, addition to this, the influence of the potential barrier and time-varying potential energy of multi-stable PEH on energy harvesting performance are also explored.

For the forward PEH configuration, the different nonlinear PEHs, including the bi-stable, symmetric tri-stable, asymmetric tri-stable and quad-stable characteristics with different potential barriers, have been theoretically analysed and experimentally validated. Furthermore, the centrifugal stiffening effect has been validated in experiments. Based on this interesting phenomenon, a passively self-tuning PEH is achieved. For the inverse PEH configuration, it is suitable for the energy harvesting in low-frequency rotational motion via the centrifugal softening effect, and the potential application is to achieve a self-powered wireless sensor used for the structural health monitoring.

According to the experimental results, the efficiency and operational frequency range of energy harvesting has been improved and enhanced. As the above contents, the author investigates the energy harvesting performance of a PEH using centrifugal force and lower potential barriers. For the potential applications, the further research should be conducted.

6.1 Rotational Motion with Translational Motion

As illustrated in above Chapters, all the nonlinear PEHs are modelled and tested in rotational motion. We all know that it is difficult to provide the power source in rotational motion because of the difficulties of wire connection. Tire Pressure Monitoring System (TPMS) is an essential part for derive safety. The traditional method is to use the battery to provide power supply for these wireless sensors, but it should be replaced them in regular time. A promising way is the energy harvesting method. A potential application of the nonlinear PEH is to provide the power source for the TPMS. As shown in Figure 6.1, a vehicle is running on the road, the rotational motion and translation motion are both existing. In this situation, it is necessary to consider the effect of translational motion on the dynamic performance of the nonlinear PEH. In this section, the theoretical model with the consideration of translational motion will be derive, and then the

real-vehicle test on the road also will be conducted.

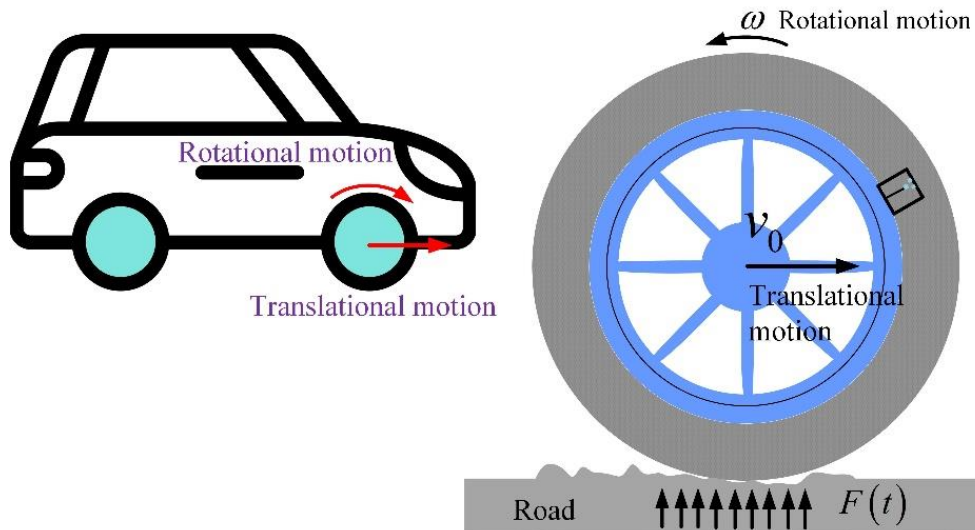


Figure 6.1 The schematic diagram of a vehicle running on the road. The nonlinear PEH in rotational motion with translational motion.

6.2 Theoretical Modelling with Translational Motion

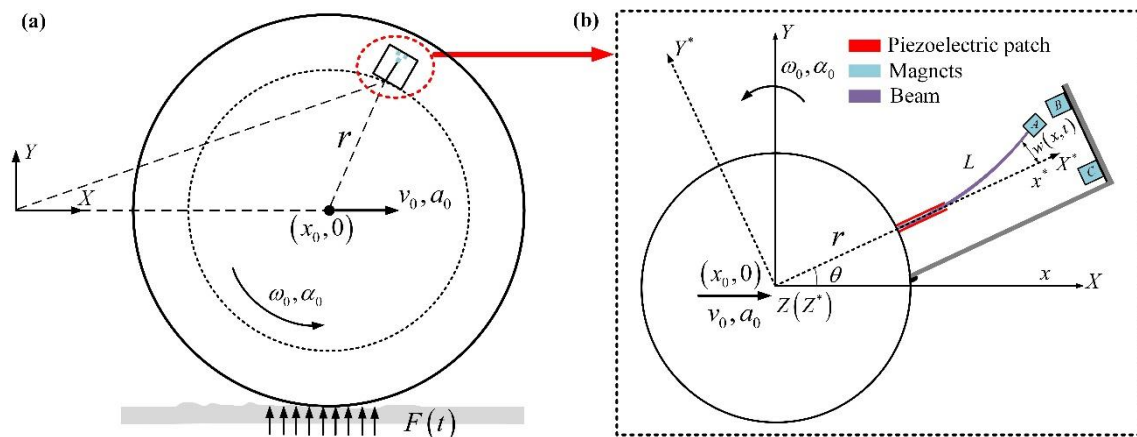


Figure 6.2 (a) The schematic diagram of a nonlinear PEH in rotational motion with the translational motion; (b) modelling in a rotational coordinate system with a translational speed v_0 .

Similarly, we mainly focus on the transverse displacement of the piezoelectric beam, which is always changing due to rotational motion. Thus, the related theoretical model will also be derived

in a rotational model with a translation motion. In Figure 6.2(a), ω_0 and α_0 are the rotational velocity and acceleration, respectively. v_0 and a_0 are the translational speed and acceleration, respectively. As shown in Figure 6.2(b), $X^*Y^*Z^*$ is the rotational coordinate system, XYZ is the fixed coordinate system. Both are defined as the reference and inertial frames, respectively. Note that Z axis is parallel to Z^* axis all the times, whose position is defined at $(x_0, 0)$. $\theta = \int_0^t \omega_0 dt$, defined as the angle subtended by X axis and X^* axis, is the angular displacement of the rotational hub. Additionally, L is the length of the piezoelectric beam. $w(x, t)$ is the transverse displacement associated with the distance x and the time t of the piezoelectric beam. R is assumed to be the position P_0 of an infinitesimal segment on the beam in the rotational coordinate system.

Kinetical Energy

According to Figure 6.2, the geometrical relationship can be calculated as follows:

$$\mathbf{R} = (x + r + x_0 \cos \theta) \mathbf{i}^* + [w(x, t) + x_0 \sin \theta] \mathbf{j}^* \quad (6.1)$$

while \mathbf{i}^* , \mathbf{j}^* and \mathbf{k}^* are the unit vectors of the rotating coordinate system along X^* , Y^* and Z^* axis, respectively. Therefore, the velocity of an infinitesimal segment of the system in rotational motion is:

$$\dot{\mathbf{R}} = \left(\frac{d\mathbf{R}}{dt} \right)_R + \dot{\theta} \mathbf{k}^* \times \mathbf{R} = [v_0 \cos \theta - \dot{\theta} w(x, t)] \mathbf{i}^* + [\dot{w}(x, t) + (x + r) \dot{\theta} + v_0 \sin \theta] \mathbf{j}^* \quad (6.2)$$

where the overdot is the derivative with respect to time. Based on Eq. (6.2), the velocity of piezoelectric beam and tip mass (magnet A) are respectively written as:

$$\dot{\mathbf{R}}_1^2 = [v_0 \cos \theta - \dot{\theta} w(x, t)]^2 + [\dot{w}(x, t) + (x + r) \dot{\theta} + v_0 \sin \theta]^2 \quad (6.3)$$

$$\dot{\mathbf{R}}_A^2 = [v_0 \cos \theta - \dot{\theta} w(L, t)]^2 + [\dot{w}(L, t) + (L + r) \dot{\theta} + v_0 \sin \theta]^2 \quad (6.4)$$

Thus, the whole kinetic energy of a nonlinear PEH ca be expressed as:

$$T = \frac{1}{2} m \int_0^L \dot{\mathbf{R}}_1^2 dx + \frac{1}{2} M \dot{\mathbf{R}}_A^2 + \frac{1}{2} J_A \dot{w}(L, t) \quad (6.5)$$

where M and J_A are the mass and inertia moment of tip mass (magnet A), respectively. m is the mass of the piezoelectric beam per unit length. For the tip mass, $x = L$, thus, the tip displacement is represented as $w(L, t)$. When $0 \leq x < l_p$, $m = \rho_b A_b + 2\rho_p A_p$, and $l_p < x \leq L$,

$m = \rho_b A_b$. A_b and ρ_b are the cross-sectional area and material density of the cantilever beam, respectively. l_p , A_p and ρ_p are the length, cross-sectional area and material density of the piezoelectric patches, respectively.

Note that the potential energy description and tip displacement separation are same as the section 2.3.2 and 2.3.3, respectively. The details will not be presented in this part. Lastly, according to Lagrange equations, the theoretical model of a nonlinear PEH in rotational motion with a translational motion can be obtained as:

$$M_e \ddot{q}(t) + C \dot{q}(t) + (K_e + K_{c2} \dot{\theta}^2) q(t) + \chi_2 \ddot{\theta} - \mathcal{G}_p v(t) + F_m = -\Gamma_2 \left[(g + \dot{\theta} v_0) \cos \theta + a_0 \sin \theta \right] + F(t) \cos \theta \quad (6.6)$$

$$C_p \dot{v}(t) + R_l^{-1} v(t) + \mathcal{G}_p \dot{q}(t) = 0 \quad (6.7)$$

where M_e is the equivalent mass. C is the mechanical damping coefficient. K_e is the equivalent stiffness of the piezoelectric beam. Additionally, $\dot{\theta}$ and $\ddot{\theta}$ are the angular velocity and angular acceleration of the rotational motion, respectively. v_0 and a_0 are the translational velocity (running speed) and acceleration, respectively. K_{c2} is the coefficient of the coupling term $\dot{\theta}^2 q(t)$. χ_2 is the coefficient of the angular acceleration. F_m is the magnetic force along the transverse direction. $F(t)$ is the external excitation from the interaction between the uneven road and vehicle wheel. R_l is the load resistance.

As observed from Eq. (6.6), it can be noticed that the rotational coefficients (θ , $\dot{\theta}$ and $\ddot{\theta}$) and the translational coefficients (v_0 and a_0) are all coupled in the theoretical model, which completes the theoretical models in previous studies. Importantly, there is a relationship between the rotational velocity $\dot{\theta}$ and the translational velocity v_0 , and also a relationship between rotational acceleration $\ddot{\theta}$ and the translational acceleration a_0 , respectively. Namely, $v_0 = r_{out} \dot{\theta}$ and $a_0 = r_{out} \ddot{\theta}$. Where r_{out} is the outer diameter of vehicle wheel. Thus, the governing equation of Eqs. (6.6) and (6.7) can be rewritten as:

$$M_e \ddot{q}(t) + C \dot{q}(t) + (K_e + K_{c2} \dot{\theta}^2) q(t) + \chi_2 \ddot{\theta} - \mathcal{G}_p v(t) + F_m = -\Gamma_2 \left[(g + \dot{\theta}^2 r_{out}) \cos \theta + \ddot{\theta} r_{out} \sin \theta \right] + F(t) \cos \theta \quad (6.8)$$

$$C_p \dot{v}(t) + R_l^{-1} v(t) + \mathcal{G}_p \dot{q}(t) = 0 \quad (6.9)$$

Based on that, the outer diameter of vehicle wheel has a great effect on the equivalent exciting force. Furthermore, the details of the above coefficients are given as:

$$M_e = m \int_0^L \phi(x)^2 dx + M \quad (6.10a)$$

$$K_e = EI \int_0^L \phi''(x)^2 dx \quad (6.10b)$$

$$K_{e2} = m \left(r \int_0^L (L-x) \phi'(x)^2 dx + \frac{1}{2} \int_0^L (L^2 - x^2) \phi'(x)^2 dx - \int_0^L \phi^2(x) dx \right) + M \left[(L+r) \int_0^L \phi'(x)^2 dx - \int_0^L \phi(x) dx \right] \quad (6.10c)$$

$$\chi_2 = M(L+r) + m \int_0^L (L^2 - x^2) \phi'(x)^2 dx + \dot{\theta} r_{out} \cos \theta \left(m \int_0^L \phi(x) dx + M \right) \quad (6.10d)$$

$$\mathcal{G}_p = \mathcal{G}_{p1} \int_0^{l_p} \phi''(x) dx \quad (6.10e)$$

$$\Gamma_2 = M + m \int_0^L \phi(x) dx \quad (6.10f)$$

$$C = c \int_0^L \phi(x) dx \quad (6.10g)$$

6.3 Scenario for Experimental Validation

6.3.1 Real-vehicle Experimental Validation on Road

The theoretical model with consideration of the translational motion has been derived in last section. Next, it is necessary to conduct the real-vehicle experiments on the road to test the energy harvesting performance of a nonlinear PEH, which is installed on a vehicle wheel. The experiments will be carried out as follows:

- (1) Firstly, the real-vehicle test will be conducted at following constant rotational speed: 5 Km/h, 10 Km/h, 15 Km/h, 20 Km/h, 25 Km/h, 30 Km/h, 35 Km/h and 40 Km/h. At the same time, a wireless acceleration sensor is installed on the front suspension of the vehicle to measure the external excitation from the road, which will be used in numerical simulation.
- (2) Secondly, the rotational radius r in the rotational vehicle wheel resulting in the change of centrifugal force will be adjusted to validate their corresponding energy harvesting performance.
- (3) Considering the potential application is for the power supply of TPMS, the inconstant rotational speed, including the acceleration process and deceleration process, will be conducted in the experiments.

After the accomplishments of the real-vehicle experiments, the experimental results will be utilized to validate the derived theoretical model in this chapter. In addition to this, based on the derived theoretical model, the influence of the translational motion will be further investigated.

6.3.2 Circuit Management System for Energy harvester

After completing the experimental validation of the proposed PEH in wheel rim of a real-vehicle, for the potential application of TPMS, the corresponding circuit management system (EMC) should be designed to manage the generated electric energy by the PEH. First of all, the AC-DC converted circuit of the EMC is needed to provide the DC power supply for the TPMS. In previous studies, most of the circuit system of the PEH mainly focused on the linear system due to the difficulty of the management of the energy branches of the nonlinear system. As a result, for the proposed PEH in wheel vehicle, the nonlinear characteristics will be adequately considered in the circuit to deal with its energy management.

Next, the experimental validations will be conducted to investigate the output voltage of the PEH under various oscillation types, including intra-well, chaotic and inter-well oscillations. Lastly, a self-powered wireless sensor will be realized, with our proposed PEH and EMC, for TPMS used in the tire pressure monitoring.

6.3.3 Potential Application

Considering the potential application is the TPMS of a vehicle, where the translational motion is existing, the completed theoretical model has been derived. Although some experiments are not conducted to validate the theoretical model, it also makes a promotion for the piezoelectric energy harvesting in rotational motion with the translational motion. In this situation, the potential application is for the power supply for TPMS.

US legislation has made TPMS on all vehicles manufactured after 2008. Keeping tires at the perfect pressure is not only beneficial for the driving safety, but also for the fuel economy. From the data source of Strategy Analytics in Jan 2018, the TPMS will represent more than 29% of the total pressure sensor market by 2023 [121].

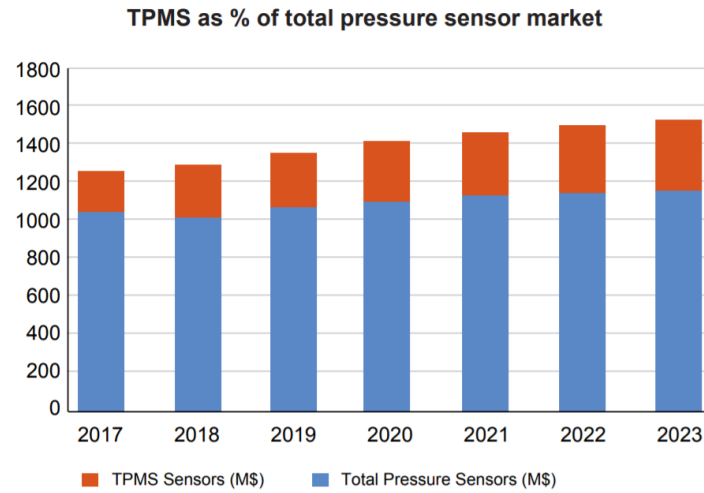


Figure 6.3 TPMS will represent more than 29 % of the total pressure sensor market by 2023 [121]. (Data source: Strategy Analytics, Jan 2018)

The most practical and cost-effective method of extracting the data from a rotating tire is to use a wireless sensor for wireless signal and wireless communication. Now the power supply is typically supplied with a battery contained in of most commercial TPMS, because it is difficult for the cable power supply in the rotational vehicle wheel. The disadvantage of battery is the limited lifespan. To enhance the lifespan of TPMS, the energy harvesting method is a promising way to provide the sustainable power supply for the TPMS.

According to data of type FXTH87 TPMS, which integrates an 8-bit microcontroller (MCU), pressure sensor, XZ-axis or Z-axis accelerometer and PF transmitter, the power supply should be more than 2.1 V [122]. As observed from the experimental results in Chapter 4 where we measure the energy harvesting performance of a nonlinear PEH in rotational motion without the translational motion, the RMS voltage of the bi-stable PEH meets the requirement when the rotational speed is from 60 -1000 rpm due to the self-tuning effect. When this bi-stable PEH is used in vehicle wheel, the further experimental investigation should be performed by a real-vehicle, as the translational motion has influence on the energy harvesting performance.

6.4 Discussion

The potential applications of centrifugal stiffening effect, centrifugal softening effect, and rotational motion with translational motion are respectively summarized in section 4.5, section 5.5.2 and section 6.3.3.

(1) the potential application of a passively self-tuning PEH is to provide the power supply for

wireless sensors in high-speed rotational machine.

(2) the potential application of centrifugal softening effect is the low-frequency rotational motion, such as the wind turbine.

(3) the potential application of theoretical model with consideration of translational motion is the TPMS.

Although the potential applications of three situations are illustrated according to the requirement of power supply of related wireless sensors, the optimal designs are needed for the further commercial applications, which can be applied to provide the power supply for wireless sensors.

6.4.1 Optimal Design for Centrifugal Stiffening Effect

The energy harvesting performance of different PEHs in rotational motion have been investigated in Chapter 3. The experimental RMS voltages of the quad-stable under various rotational speeds are illustrated in Figure 6.4. It can be observed that in Region I (60 – 420 rpm), the proposed PEH shows excellent energy harvesting performance. However, in Region II (440 – 960 rpm) due to the centrifugal stiffening effect the energy harvesting performance decreases dramatically. How to broaden the frequency bandwidth in Region II has become a vital issue.

The passively self-tuning effect via centrifugal stiffening effect for enhancing energy harvesting performance has been experimentally in Chapter 4. Figure 6.5 presents the experimental RMS voltage of a bi-stable PEH via self-tuning effect under various rotational speeds. It can be found that in Region II (440 – 740 rpm) of Figure 6.5, the self-tuning effect has a great enhancement for the energy harvesting performance.

For the quad-stable PEH in Figure 6.4, the related parameters are shown in Figure 6.6 (a). For the self-tuning bi-stable PEH in Figure 6.5, the related parameters are shown in Figure 6.6(b). If the advantages of the quad-stable PEH and the self-tuning effect are both combined, achieve wide bandwidth (Region I in Figure 6.4 and Region II in Figure 6.5) nonlinear PEH can be achieved. Therefore, based on the previous quad-stable PEH, the optimal design of a novel PEH is to adjust the length of piezoelectric beam as 80 mm, in Region II of Figure 6.4, the self-tuning effect via the centrifugal stiffening effect can be achieved. Consequently, the excellent energy harvesting performance of novel PEH can be achieved in wide frequency range. The further experiments will be conducted to validate this optimal design.

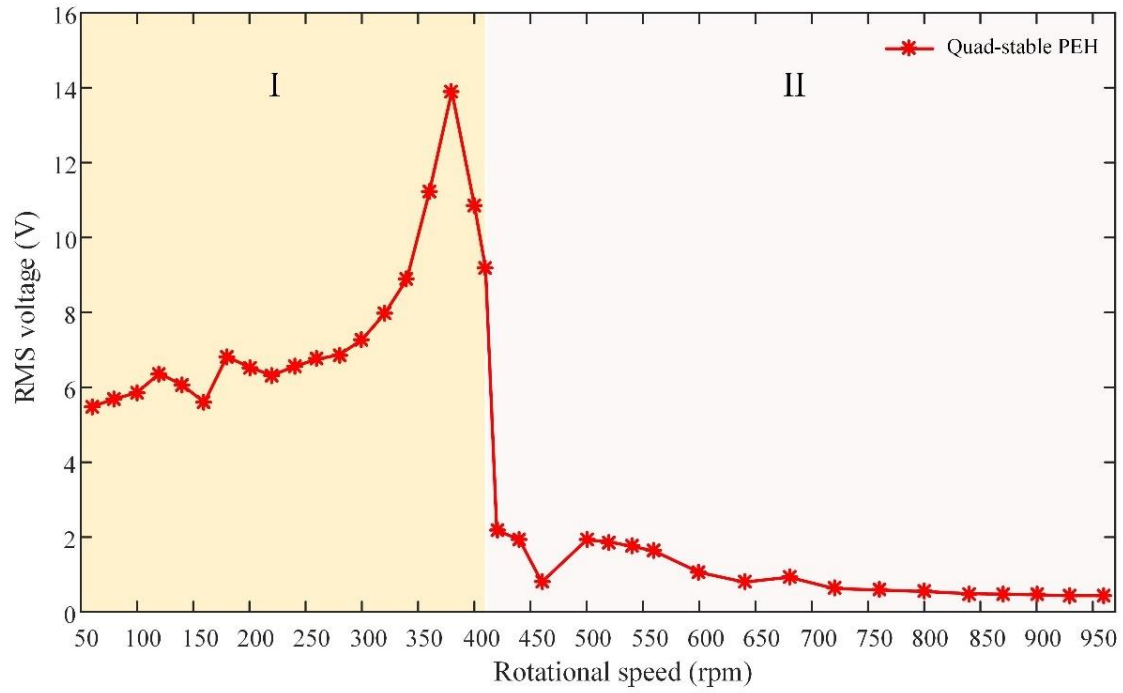


Figure 6.4 The experimental RMS voltage of the quad-stable PEH under various rotational speeds from 60 - 960 rpm.

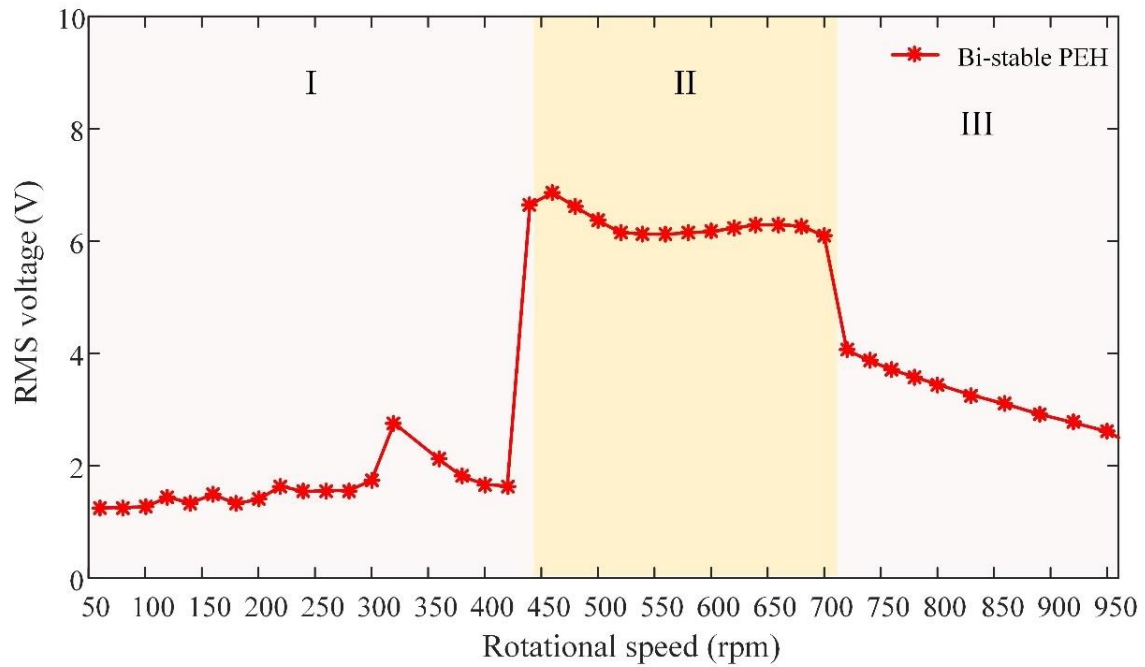


Figure 6.5 The experimental RMS voltage of a bi-stable PEH via self-tuning effect under various rotational speeds from 60 - 1060 rpm.

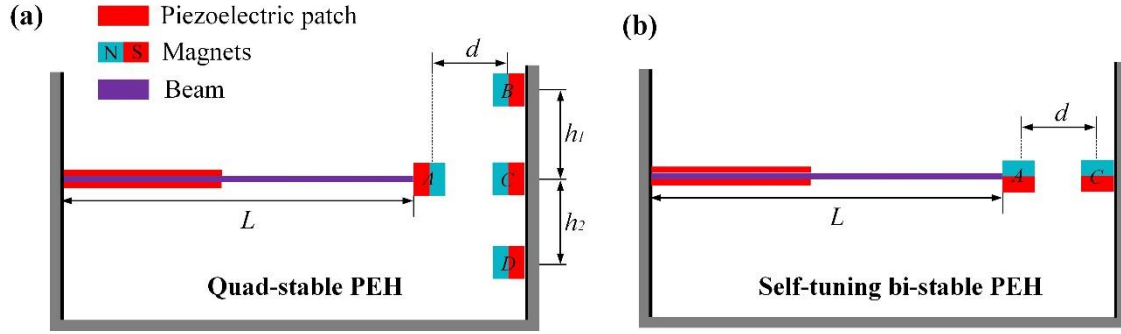


Figure 6.6 (a) The configuration of quad-stable PEH, $d=15$ mm, $h_1=h_2=20$ mm, $L=95$ mm; (b) the configuration of the self-tuning bi-stable PEH, $d=13$ mm, $L=80$ mm.

More external magnets can be added to further decrease the potential barrier, resulting in the multi-stable (five stable positions or more) which is beneficial for the energy harvesting performance. From Figure 6.7(a), the potential barrier of quad-stable PEH is so low that the inter-well oscillations can be easily achieved. If it is used in rotational motion, the corresponding time-varying potential well is shown in Figure 6.7 (b), from which it can be noticed that the rotational motion can enforce the piezoelectric beam to achieve inter-well oscillations due to the influence of gravity component of tip mass. If we add one more magnet to achieve quin-stable PEH, the corresponding potential barrier can be further reduced, but at the same time the whole mass will be increased. Thus, considering the practical application, the quad-stable PEH is appreciable for the energy harvesting in rotational motion. We can take full advantages of the time-varying potential energy resulting from the gravity component of tip mass and low potential barrier of quad-stable PEH. Thereby, the multi-stable (five stable positions or more) with lower potential barriers is not necessary for energy harvesting in rotational motion. However, in the future research work it is an interesting research topic for energy harvesting in rectilinear-based vibration energy harvesting.

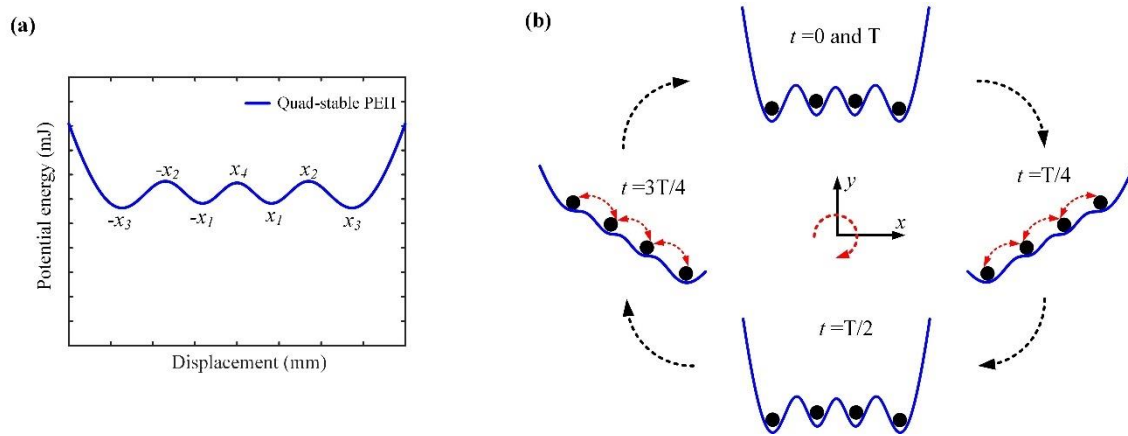


Figure 6.7 (a) The related potential energy of quad-stable PEH; (b) the related time-varying potential energy of quad-stable PEH in rotational motion.

6.4.2 Optimal Design for Centrifugal Softening Effect

In Chapter 5, an inverse PEH via the centrifugal softening effect has been explored for energy harvesting from low-frequency rotational motion. Based on the theoretical analyses as shown in Figure 5.3, when the rotational speed is more than 180 rpm, the deformation of the piezoelectric beam is more than 30 mm. Although large deformation is beneficial for the output voltage, it also may lead to the failure of piezoelectric patch. Thus, for the optimal design of the PEH, the stopper will be added to the two sides to confine the deflection of piezoelectric beam as shown in Figure 6.8. The further details can refer to section 5.5.1. The purpose of this section is to come up the optimal design for an inverse PEH in rotational motion. The further details of the parameters will be confirmed after the experimental validation.

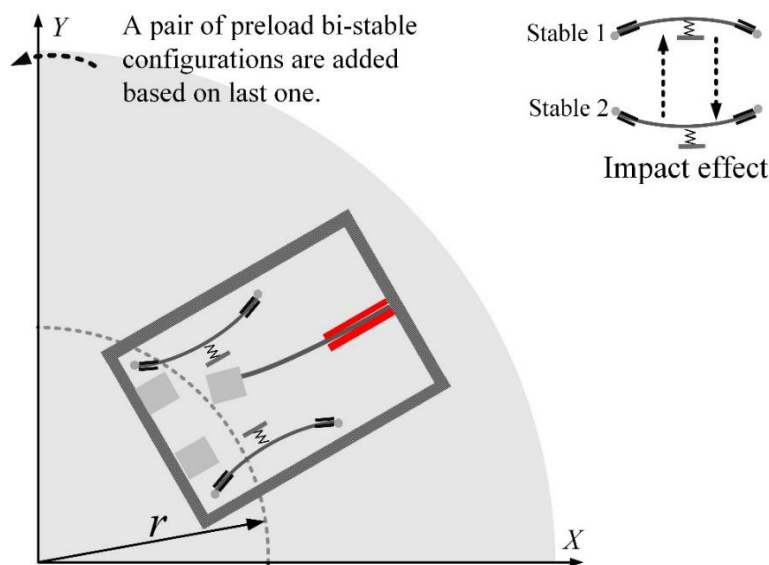


Figure 6.8 The further improvement for the inverse PEH in rotational motion.

6.5 Summary

In this dissertation, the author mainly focuses on applying the centrifugal force to enhance the energy harvesting performance in rotational motion, then be aimed to provide the sustainable power supply for the wireless sensors. Firstly, a theoretical model which considers the effect of rotational motion has been derived in a rotational coordinate system to complete previous studies. Based on that model, the centrifugal stiffening effect and softening effect are achieved. In the experiments, the energy harvesting performances of corresponding effect are verified. Thus, most important contribution of this dissertation is to provide the theoretical guidance for the optimization design PEH in different rotational motions, such as rotational machine (centrifugal stiffening effect), low-frequency wind turbine (centrifugal softening effect), and vehicle wheel (with translation motion).

In addition to these, according to power supply requirement of corresponding wireless sensor, the possibilities in the potential applications and related optimal designs have been analysed.

Chapter 7

Conclusions

7 Summary and Conclusion

Energy harvesting is one of the key technologies to implement intelligent and self-powered sensors, which provide significant merits and opportunities for the development and applications of the Internet of Things (IoT). Contributing to this attractive topic and promising method, this doctoral dissertation focused on nonlinear phenomena, including the bi-stable, symmetric tri-stable, asymmetrical stable and quad-stable characteristics, and the centrifugal stiffening and softening effects caused by the centrifugal force in rotational motion. It is worth highlighting that the centrifugal force caused by the rotation motion will change the stiffness of piezoelectric beam, then influence the dynamic performance of the nonlinear PEH in rotational motion, additionally, the different magnetic configuration can lead to different potential barrier and nonlinearity.

In Chapter 2, a theoretical model of nonlinear PEH in rotational motion has been originally proposed by modelling in a rotational coordinate system. Then based on the dipole-dipole method the magnetic forces of repulsive configuration in radial direction and attractive configuration in normal direction are respectively calculated. Furthermore, the theoretical comparisons, between the theoretical model with and without the consideration of rotational motion, are carried out. The numerical results demonstrate great differences especially at high rotational speeds. Namely, the predictions by the theoretical model without the consideration of rotational motion demonstrate that the nonlinear PEH undergoes the chaotic oscillations. On the contrary, the predictions by the proposed theoretical model show that the nonlinear PEH experiences the intra-well oscillations around the position $w(L, t) = 0$. Additionally, one term including the square of rotational speed in the theoretical model can predict and explain this phenomenon (centrifugal stiffening effect), which has been validated in the experiments. In a word, the proposed theoretical model is suitable for all cantilever-type PEH in rotational motion.

In Chapter 3, with the aim to achieve high output voltage, the various magnetically coupled nonlinear PEHs, including the bi-stable, symmetric tri-stable, asymmetric tris-table and quad-stable PEHs, have been theoretically and experimental investigated, respectively. The difference among these PEHs is the nonlinearity caused by the external magnets. By reducing their potential barriers, the large-amplitude inter-well oscillations can be trigger easier. Additionally, the gravity component of tip mass can be regarded as a periodic exciting force for the vibration of the piezoelectric beam, and it also leads to the time-vary potential energy. Based on the proposed theoretical model in Charter 2, the corresponding theoretical models of the bi-stable, symmetric tri-stable, asymmetric tris-table and quad-stable PEHs are respectively rewritten and expressed.

Utilizing the perturbation method, their governing equations have been solved to obtain the theoretical solutions. Lastly, the corresponding experiments are conducted to present the dynamic performances and output voltages under various constant rotational speed.

In Chapter 4, a passively self-tuning nonlinear PEH in rotational motion has been achieved. According to the proposed theoretical model, it is found that the centrifugal stiffening effect changes the resonance frequency of beam, namely, the resonance frequency of the piezoelectric beam is increasing of the increase of the rotational motion. When the parameters of nonlinear PEH are designed in appropriate values, the rotational frequency can track the resonance frequency over a wide frequency range. According to the derived theoretical model, the effect of the parameters, including the rotational radius, the length of piezoelectric beam and the tip mass, have been theoretically analysed. The experimental results demonstrate that the centrifugal force is a good way to achieve a passively self-tuning nonlinear PEH to broaden the effective frequency range.

In Chapter 5, an inverse nonlinear PEH for energy harvesting in low-frequency rotational motion has been proposed and investigated. The related theoretical model has been derived. The component of centrifugal force in axial direction softens the piezoelectric beam due to the compressional movement, and the other one in transverse direction forces the piezoelectric beam to vibrate. The corresponding experiments between the inverse and forward PEHs are conducted, the results demonstrate that in low-frequency rotational motion, the proposed inverse PEH is superior to the forward one, and the centrifugal softening effect is an effective way for energy harvesting enhancement in low-frequency motion.

In Chapter 6, it is comprehensively discussed that the further research based on this doctoral research is extended. As for the potential application of TPMS of vehicle wheel, where the translational motion is existing when the vehicle is running on the road. Considering this factor, the corresponding theoretical model has been established in a rotational motion with the translational motion. According to Eq. (6.8), the translational speed and translation acceleration have a great influence on the dynamic performance of nonlinear PEH. The next step is real-vehicle test on the road to validate this proposed theoretical model. In order to realize the application, the circuit management system should be designed to manage the captured electric energy for powering wireless sensor. Lastly a self-powered wireless sensor can be achieved for structural health monitoring. In addition to this, the optimal design for centrifugal stiffing effect, self-tuning effect and centrifugal softening effect are discussed and addressed.

All in all, the logical line of this doctoral dissertation is as shown in Figure 7.1.

(1) The theoretical model of the nonlinear PEH in rotational motion is derived, and it is also the

basement of the following three parts including the forward configuration, inverse configuration and rotational motion with the translational motion, which corresponds to three potential applications of rotational machine, wind turbine and vehicle wheel, respectively.

(2) Based on that, the nonlinear characteristics of bi-stable, symmetric tri-stable and asymmetric tri-stable and quad-stable PEHs are respectively explored, and it refers to the term F_m in the electromechanical equations.

(3) The proposed theoretical model predicts the centrifugal stiffening effect of PEHs, which has been successfully validated in our experiment. Thus, according to the centrifugal stiffening effect, it can be noticed that the resonance frequency of piezoelectric beam is increasing with the increase of rotational motion. Lastly, the passively self-tuning effect of bi-stable and tri-stable PEHs are achieved in experiments.

(4) Next, inspired by the centrifugal stiffening effect, a nonlinear PEHs is inversely installed, the energy harvesting performance is significantly enhanced in low-frequency rotational motion via the centrifugal softening effect.

(5) Considering the potential application is the Tire Pressure Monitoring System (TPMS), the translational motion is considered to complete the theoretical model.

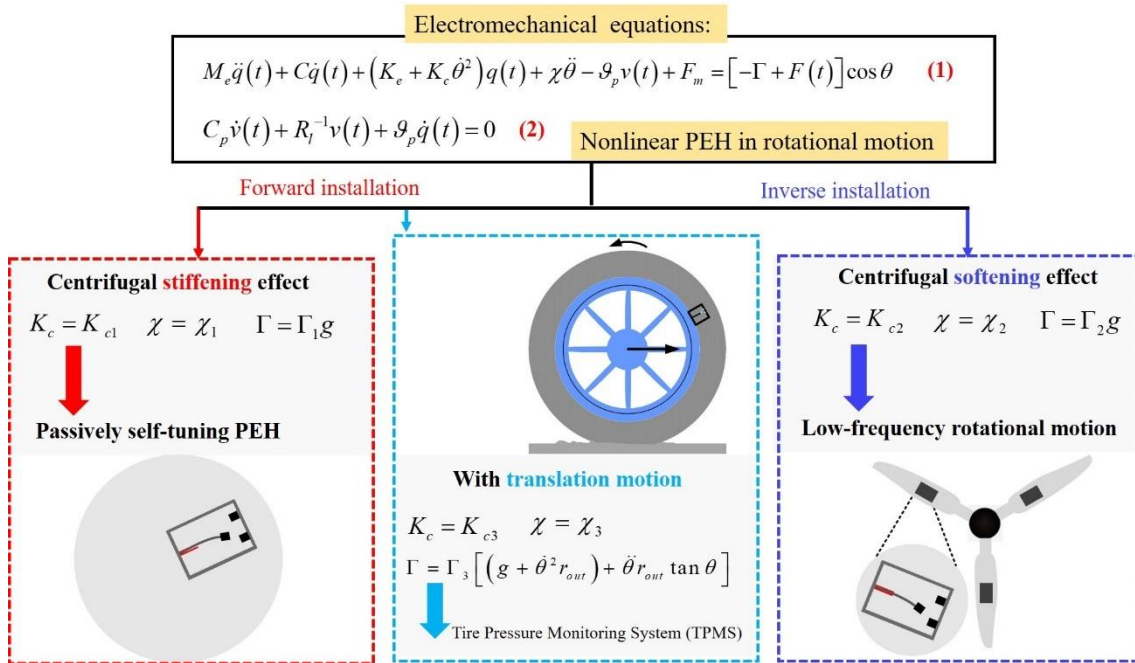


Figure 7.1 The logical line of the doctoral dissertation and the potential application.

In summary, the conclusions of this doctoral dissertation are highlighted as follows:

- (1) As for the nonlinear PEH in rotational motion, the effect of rotational motion should be considered in their theoretical model. The derived theoretical model considering the effect of centrifugal force is suitable for all cantilever-type PEHs in rotational motion. (**Chapter 2**)
- (2) The magnetically coupled multi-stable PEH with lower potential barrier is a good way to widen the effective frequency range in rotational motion. (**Chapter 3**)
- (3) The centrifugal stiffening effect can be used to achieve a passively self-tuning nonlinear harvester for energy harvesting enhancement in rotational motion. (**Chapter 4**)
- (4) The centrifugal softening effect of an inverse nonlinear PEH can be used to enhance energy harvesting performance in low-frequency rotational motion. (**Chapter 5**)

Additionally, the detailed structure flow of this dissertation is shown in Figure 7.2.

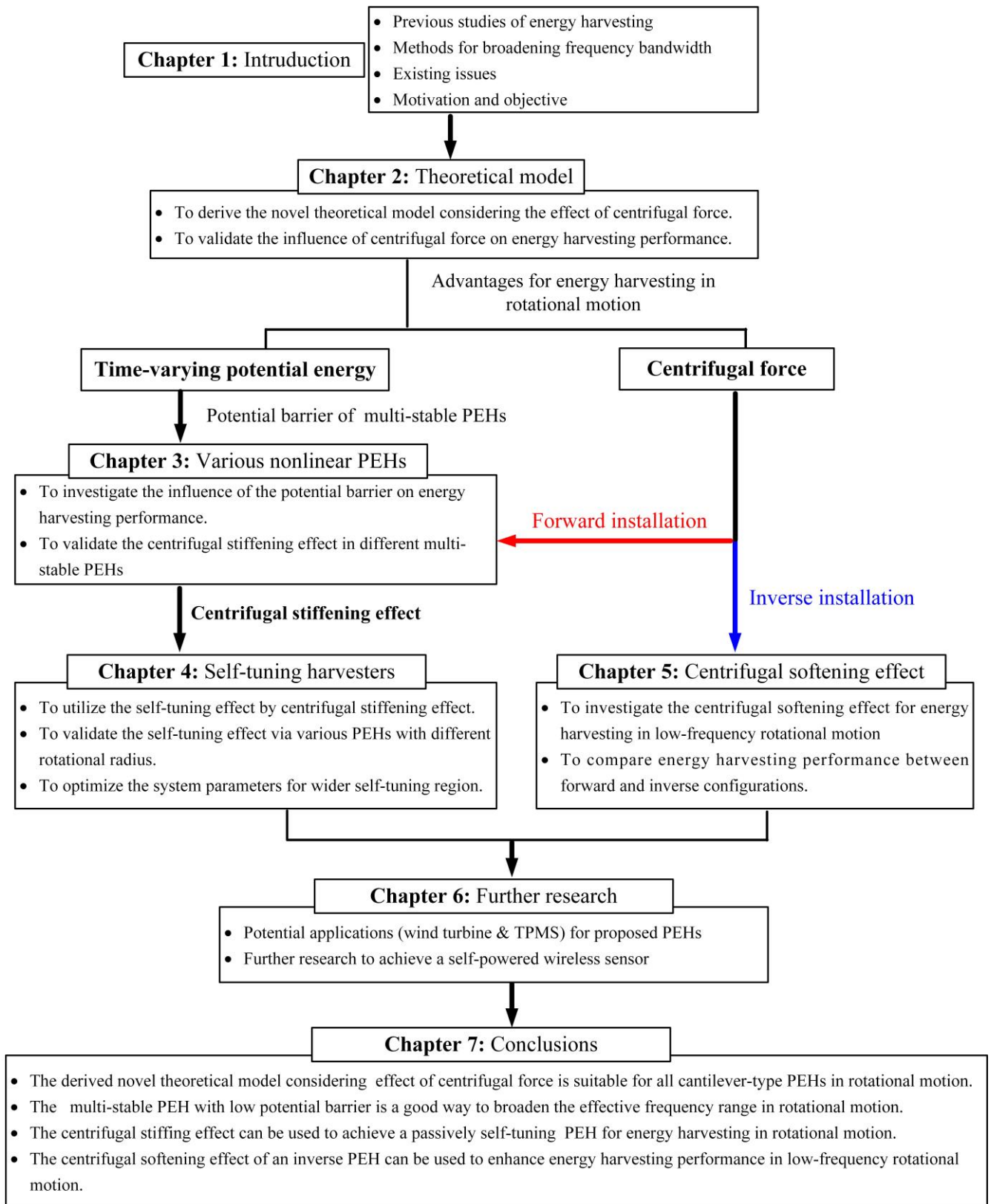


Figure 7.2 The detailed structure flow of this dissertation.

References

- [1] Yang, Z., Zhou, S., Zu, J., and Inman, D. (2018). High-performance piezoelectric energy harvesters and their applications. *Joule*, 2(4), 642-697.
- [2] Liu, H., Zhong, J., Lee, C., Lee, S. W., and Lin, L. (2018). A comprehensive review on piezoelectric energy harvesting technology: Materials, mechanisms, and applications. *Applied Physics Reviews*, 5(4), 041306.
- [3] Zou, H. X., Zhao, L. C., Gao, Q. H., Zuo, L., Liu, F. R., Tan, T., and Zhang, W. M. (2019). Mechanical modulations for enhancing energy harvesting: Principles, methods and applications. *Applied Energy*, 255, 113871.
- [4] Wei, C., and Jing, X. (2017). A comprehensive review on vibration energy harvesting: Modelling and realization. *Renewable and Sustainable Energy Reviews*, 74, 1-18.
- [5] Shaikh, F. K., and Zeadally, S. (2016). Energy harvesting in wireless sensor networks: A comprehensive review. *Renewable and Sustainable Energy Reviews*, 55, 1041-1054.
- [6] http://www.sensornets.org/Documents/Previous_Invited_Speakers/2018/SENSORNETS2018_Reindl.pdf
- [7] <https://perpetuum.com/news/>
- [8] Wang, P., Pan, L., Wang, J., Xu, M., Dai, G., Zou, H., ... and Wang, Z. L. (2018). An Ultra-Low-Friction Triboelectric–Electromagnetic Hybrid Nanogenerator for Rotation Energy Harvesting and Self-Powered Wind Speed Sensor. *ACS nano*, 12(9), 9433-9440
- [9] Liu, H., Hou, C., Lin, J., Li, Y., Shi, Q., Chen, T., ...and Lee, C. (2018). A non-resonant rotational electromagnetic energy harvester for low-frequency and irregular human motion. *Applied Physics Letters*, 113(20), 203901.
- [10] Li, Z., Zuo, L., Luhrs, G., Lin, L., and Qin, Y. X. (2012). Electromagnetic energy-harvesting shock absorbers: design, modeling, and road tests. *IEEE Transactions on vehicular technology*, 62(3), 1065-1074.
- [11] Nakano, K., Suda, Y., and Nakadai, S. (2003). Self-powered active vibration control using a single electric actuator. *Journal of Sound and Vibration*, 260(2), 213-235.
- [12] Suzuki, Y. (2011). Recent progress in MEMS electret generator for energy harvesting. *IEEE Transactions on Electrical and Electronic Engineering*, 6(2), 101-111.
- [13] Zhang, Y., Wang, T., Luo, A., Hu, Y., Li, X., and Wang, F. (2018). Micro electrostatic energy harvester with both broad bandwidth and high normalized power density. *Applied energy*,

212, 362-371.

- [14] Yang, Z., Tang, L., Tao, K., and Aw, K. C. (2019). Modelling and Validation of Electret-Based Vibration Energy Harvesters in View of Charge Migration. *International Journal of Precision Engineering and Manufacturing-Green Technology*, 1-11.
- [15] Zhang, D., Shi, J., Si, Y., and Li, T. (2019). Multi-grating triboelectric nanogenerator for harvesting low-frequency ocean wave energy. *Nano Energy*, 61, 132-140.
- [16] Wu, W., Cao, X., Zou, J., Ma, Y., Wu, X., Sun, C., ... and Zhang, L. (2019). Triboelectric nanogenerator boosts smart green tires. *Advanced Functional Materials*, 29(41), 1806331.
- [17] Wu, Y., Hu, Y., Huang, Z., Lee, C., and Wang, F. (2018). Electret-material enhanced triboelectric energy harvesting from air flow for self-powered wireless temperature sensor network. *Sensors and Actuators A: Physical*, 271, 364-372.
- [18] Meng, X., Cheng, Q., Jiang, X., Fang, Z., Chen, X., Li, S., ... and Wang, Z. L. (2018). Triboelectric nanogenerator as a highly sensitive self-powered sensor for driver behavior monitoring. *Nano Energy*, 51, 721-727.
- [19] Wang, J., Tang, L., Zhao, L., and Zhang, Z. (2019). Efficiency investigation on energy harvesting from airflows in HVAC system based on galloping of isosceles triangle sectioned bluff bodies. *Energy*, 172, 1066-1078.
- [20] Wang, J., Zhou, S., Zhang, Z., & Yurchenko, D. (2019). High-performance piezoelectric wind energy harvester with Y-shaped attachments. *Energy conversion and management*, 181, 645-652.
- [21] Zhang, Y., Nakano, K., Zheng, R., and Cartmell, M. P. (2016, September). Adjustable Nonlinear Mechanism System for Wideband Energy Harvesting in Rotational Circumstances. *In Journal of Physics: Conference Series* (Vol. 744, No. 1, p. 012079). IOP Publishing.
- [22] Zhou, S., Cao, J., Erturk, A., and Lin, J. (2013). Enhanced broadband piezoelectric energy harvesting using rotatable magnets. *Applied Physics Letters*, 102(17), 173901.
- [23] Lan, C., and Qin, W. (2017). Enhancing ability of harvesting energy from random vibration by decreasing the potential barrier of bistable harvester. *Mechanical Systems and Signal Processing*, 85, 71-81.
- [24] Tang, L., Yang, Y., and Soh, C. K. (2010). Toward broadband vibration-based energy harvesting. *Journal of intelligent material systems and structures*, 21(18), 1867-1897.
- [25] Zhao, L. C., Zou, H. X., Yan, G., Liu, F. R., Tan, T., Wei, K. X., and Zhang, W. M. (2019). Magnetic coupling and flextensional amplification mechanisms for high-robustness ambient wind energy harvesting. *Energy Conversion and Management*, 201, 112166.

- [26] Wang, J., Zhou, S., Zhang, Z., and Yurchenko, D. (2019). High-performance piezoelectric wind energy harvester with Y-shaped attachments. *Energy conversion and management*, 181, 645-652.
- [27] https://en.wikipedia.org/wiki/Triboelectric_effect
- [28] Hu, W., Zhang, C., and Wang, Z. L. (2018). Recent progress in piezotronics and tribotronics. *Nanotechnology*, 30(4), 042001.
- [29] Yang, H., Wang, M., Deng, M., Guo, H., Zhang, W., Yang, H., ... and Wang, Z. (2019). A full-packaged rolling triboelectric-electromagnetic hybrid nanogenerator for energy harvesting and building up self-powered wireless systems. *Nano energy*, 56, 300-306.
- [30] Pan, S., and Zhang, Z. (2019). Fundamental theories and basic principles of triboelectric effect: A review. *Friction*, 7(1), 2-17.
- [31] Erturk, A., Hoffmann, J., and Inman, D. J. (2009). A piezomagnetoelastic structure for broadband vibration energy harvesting. *Applied Physics Letters*, 94(25), 254102.
- [32] Stanton, S. C., Erturk, A., Mann, B. P., and Inman, D. J. (2010). Nonlinear piezoelectricity in electroelastic energy harvesters: modeling and experimental identification. *Journal of Applied Physics*, 108(7), 074903.
- [33] Erturk, A., and Inman, D. J. (2008). Issues in mathematical modeling of piezoelectric energy harvesters. *Smart Materials and Structures*, 17(6), 065016.
- [34] Erturk, A., and Inman, D. J. (2008). A distributed parameter electromechanical model for cantilevered piezoelectric energy harvesters. *Journal of vibration and acoustics*, 130(4), 041002.
- [35] Erturk, A., and Inman, D. J. (2009). An experimentally validated bimorph cantilever model for piezoelectric energy harvesting from base excitations. *Smart materials and structures*, 18(2), 025009.
- [36] Hosseini, R., Hamed, M., Golparvar, H., and Zargar, O. (2019). Analytical and Experimental Investigation into Increasing Operating Bandwidth of Piezoelectric Energy Harvesters. *AUT Journal of Mechanical Engineering*, 3(1), 113-122.
- [37] Zayed, A. A., Assal, S. F., Nakano, K., Kaizuka, T., El-Bab, F., and Ahmed, M. R. (2019). Design procedure and experimental verification of a broadband quad-stable 2-DOF vibration energy harvester. *Sensors*, 19(13), 2893.
- [38] Haitao, L., Weiyang, Q., Chunbo, L., Wangzheng, D., and Zhiyong, Z. (2015). Dynamics and coherence resonance of tri-stable energy harvesting system. *Smart Materials and Structures*, 25(1), 015001.

- [39] Dhote, S., Yang, Z., and Zu, J. (2018). Modeling and experimental parametric study of a tri-leg compliant orthoplanar spring based multi-mode piezoelectric energy harvester. *Mechanical Systems and Signal Processing*, 98, 268-280.
- [40] Abdelkefi, A., Barsallo, N., Tang, L., Yang, Y., and Hajj, M. R. (2014). Modeling, validation, and performance of low-frequency piezoelectric energy harvesters. *Journal of Intelligent Material Systems and Structures*, 25(12), 1429-1444.
- [41] Upadrashta, D., and Yang, Y. (2018). Trident-shaped multimodal piezoelectric energy harvester. *Journal of Aerospace Engineering*, 31(5), 04018070.
- [42] Xiong, L., Tang, L., and Mace, B. R. (2018). A comprehensive study of 2: 1 internal-resonance-based piezoelectric vibration energy harvesting. *Nonlinear Dynamics*, 91(3), 1817-1834.
- [43] Fang, S., Fu, X., and Liao, W. H. (2019). Asymmetric plucking bistable energy harvester: Modeling and experimental validation. *Journal of Sound and Vibration*, 459, 114852.
- [44] Fang, S., Fu, X., Du, X., and Liao, W. H. (2019). A music-box-like extended rotational plucking energy harvester with multiple piezoelectric cantilevers. *Applied Physics Letters*, 114(23), 233902
- [45] Khameneifar, F., Moallem, M., and Arzanpour, S. (2011). Modeling and analysis of a piezoelectric energy scavenger for rotary motion applications. *Journal of vibration and acoustics*, 133(1), 011005.
- [46] Khameneifar, F., Arzanpour, S., and Moallem, M. (2012). A piezoelectric energy harvester for rotary motion applications: Design and experiments. *IEEE/ASME Transactions on Mechatronics*, 18(5), 1527-1534.
- [47] Zhang, Y., Cao, J., Zhu, H., and Lei, Y. (2019). Design, modeling and experimental verification of circular Halbach electromagnetic energy harvesting from bearing motion. *Energy conversion and management*, 180, 811-821.
- [48] Guan, M., and Liao, W. H. (2016). Design and analysis of a piezoelectric energy harvester for rotational motion system. *Energy Conversion and Management*, 111, 239-244.
- [49] Febbo, M., Machado, S. P., Gatti, C. D., and Ramirez, J. M. (2017). An out-of-plane rotational energy harvesting system for low frequency environments. *Energy conversion and management*, 152, 166-175.
- [50] Nezami, S., Jung, H., and Lee, S. (2019). Design of a disk-swing driven piezoelectric energy harvester for slow rotary system application. *Smart Materials and Structures*, 28(7), 074001.
- [51] Sadeqi, S., Arzanpour, S., and Hajikolaie, K. H. (2014). Broadening the frequency

- bandwidth of a tire-embedded piezoelectric-based energy harvesting system using coupled linear resonating structure. *IEEE/ASME transactions on mechatronics*, 20(5), 2085-2094.
- [52] Zhang, Y., Zheng, R., Nakano, K., and Cartmell, M. P. (2018). Stabilising high energy orbit oscillations by the utilisation of centrifugal effects for rotating-tyre-induced energy harvesting. *Applied Physics Letters*, 112(14), 143901.
- [53] Zhang, Y., Zheng, R., Shimono, K., Kaizuka, T., and Nakano, K. (2016). Effectiveness testing of a piezoelectric energy harvester for an automobile wheel using stochastic resonance. *Sensors*, 16(10), 1727.
- [54] Xiao, Z., Yang, T. Q., Dong, Y., and Wang, X. C. (2014). Energy harvester array using piezoelectric circular diaphragm for broadband vibration. *Applied Physics Letters*, 104(22), 223904.
- [55] Upadrashta, D., and Yang, Y. (2016). Nonlinear piezomagnetoelastic harvester array for broadband energy harvesting. *Journal of Applied Physics*, 120(5), 054504.
- [56] Zhou, S., Yan, B., and Inman, D. (2018). A novel nonlinear piezoelectric energy harvesting system based on linear-element coupling: design, modeling and dynamic analysis. *Sensors*, 18(5), 1492.
- [57] Xie, Z., Xiong, J., Zhang, D., Wang, T., Shao, Y., and Huang, W. (2018). Design and Experimental Investigation of a Piezoelectric Rotation Energy Harvester Using Bistable and Frequency Up-Conversion Mechanisms. *Applied Sciences*, 8(9), 1418.
- [58] Zou, H. X., Zhang, W. M., Li, W. B., Gao, Q. H., Wei, K. X., Peng, Z. K., and Meng, G. (2017). Design, modeling and experimental investigation of a magnetically coupled flextensional rotation energy harvester. *Smart Materials and Structures*, 26(11), 115023.
- [59] Fang, S., Fu, X., and Liao, W. H. (2019). Modeling and experimental validation on the interference of mechanical plucking energy harvesting. *Mechanical Systems and Signal Processing*, 134, 106317.
- [60] Ferrari, M., Ferrari, V., Guizzetti, M., Andò, B., Baglio, S., and Trigona, C. (2010). Improved energy harvesting from wideband vibrations by nonlinear piezoelectric converters. *Sensors and Actuators A: Physical*, 162(2), 425-431.
- [61] Ferrari, M., Bau, M., Guizzetti, M., and Ferrari, V. (2011). A single-magnet nonlinear piezoelectric converter for enhanced energy harvesting from random vibrations. *Sensors and Actuators A: Physical*, 172(1), 287-292.
- [62] Wang, H., and Tang, L. (2017). Modeling and experiment of bistable two-degree-of-freedom energy harvester with magnetic coupling. *Mechanical Systems and Signal Processing*, 86, 29-39.

- [63] Deng, H., Du, Y., Wang, Z., Ye, J., Zhang, J., Ma, M., and Zhong, X. (2019). Poly-stable energy harvesting based on synergetic multistable vibration. *Communications Physics*, 2(1), 21.
- [64] Daqaq, M. F., Masana, R., Erturk, A., and Dane Quinn, D. (2014). On the role of nonlinearities in vibratory energy harvesting: a critical review and discussion. *Applied Mechanics Reviews*, 66(4).
- [65] Wang, W., Cao, J., Bowen, C. R., Zhang, Y., and Lin, J. (2018). Nonlinear dynamics and performance enhancement of asymmetric potential bistable energy harvesters. *Nonlinear Dynamics*, 94(2), 1183-1194.
- [66] Gu, L., and Livermore, C. (2010). Passive self-tuning energy harvester for extracting energy from rotational motion. *Applied Physics Letters*, 97(8), 081904.
- [67] Gu, L., and Livermore, C. (2011). Compact passively self-tuning energy harvesting for rotating applications. *Smart materials and structures*, 21(1), 015002.
- [68] Liu, T., and Livemore, C. (2012). Passively tuning harvesting beam length to achieve very high harvesting bandwidth in rotating applications. *Proceedings of PowerMEMS 2012*, 492-495.
- [69] Fan, K., Tan, Q., Zhang, Y., Liu, S., Cai, M., and Zhu, Y. (2018). A monostable piezoelectric energy harvester for broadband low-level excitations. *Applied Physics Letters*, 112(12), 123901.
- [70] Kumar, A., Ali, S. F., and Arockiarajan, A. (2018). Exploring the benefits of an asymmetric monostable potential function in broadband vibration energy harvesting. *Applied Physics Letters*, 112(23), 233901.
- [71] Cottone, F., Vocca, H., and Gammaitoni, L. (2009). Nonlinear energy harvesting. *Physical Review Letters*, 102(8), 080601.
- [72] Stanton, S. C., McGehee, C. C., and Mann, B. P. (2010). Nonlinear dynamics for broadband energy harvesting: Investigation of a bistable piezoelectric inertial generator. *Physica D: Nonlinear Phenomena*, 239(10), 640-653.
- [73] Erturk, A., and Inman, D. J. (2011). Broadband piezoelectric power generation on high-energy orbits of the bistable Duffing oscillator with electromechanical coupling. *Journal of Sound and Vibration*, 330(10), 2339-2353.
- [74] Litak, G., Friswell, M. I., and Adhikari, S. (2010). Magnetopiezoelectric energy harvesting driven by random excitations. *Applied Physics Letters*, 96(21), 214103.
- [75] Zheng, R., Nakano, K., Hu, H., Su, D., and Cartmell, M. P. (2014). An application of

stochastic resonance for energy harvesting in a bistable vibrating system. *Journal of Sound and Vibration*, 333(12), 2568-2587.

- [76] Zhou, S., Cao, J., Inman, D. J., Lin, J., Liu, S., and Wang, Z. (2014). Broadband tristable energy harvester: modeling and experiment verification. *Applied Energy*, 133, 33-39.
- [77] Cao, J., Zhou, S., Wang, W., and Lin, J. (2015). Influence of potential well depth on nonlinear tristable energy harvesting. *Applied Physics Letters*, 106(17), 173903.
- [78] Zhu, P., Ren, X., Qin, W., Yang, Y., and Zhou, Z. (2017). Theoretical and experimental studies on the characteristics of a tri-stable piezoelectric harvester. *Archive of Applied Mechanics*, 87(9), 1541-1554.
- [79] Leng, Y., Tan, D., Liu, J., Zhang, Y., and Fan, S. (2017). Magnetic force analysis and performance of a tri-stable piezoelectric energy harvester under random excitation. *Journal of Sound and Vibration*, 406, 146-160.
- [80] Kim, P., Son, D., and Seok, J. (2016). Triple-well potential with a uniform depth: Advantageous aspects in designing a multi-stable energy harvester. *Applied Physics Letters*, 108(24), 243902.
- [81] Panyam, M., and Daqaq, M. F. (2017). Characterizing the effective bandwidth of tri-stable energy harvesters. *Journal of Sound and Vibration*, 386, 336-358.
- [82] Zhou, Z., Qin, W., and Zhu, P. (2016). Improve efficiency of harvesting random energy by snap-through in a quad-stable harvester. *Sensors and Actuators A: Physical*, 243, 151-158.
- [83] Zhou, Z., Qin, W., and Zhu, P. (2017). A broadband quad-stable energy harvester and its advantages over bi-stable harvester: simulation and experiment verification. *Mechanical Systems and Signal Processing*, 84, 158-168.
- [84] Zhou, Z., Qin, W., Yang, Y., and Zhu, P. (2017). Improving efficiency of energy harvesting by a novel penta-stable configuration. *Sensors and Actuators A: Physical*, 265, 297-305.
- [85] Li, M., Wen, Y., Li, P., Yang, J., and Dai, X. (2011). A rotation energy harvester employing cantilever beam and magnetostrictive/piezoelectric laminate transducer. *Sensors and Actuators A: Physical*, 166(1), 102-110.
- [86] Li, M., Wen, Y., Li, P., and Yang, J. (2013). A resonance frequency self-tunable rotation energy harvester based on magnetoelectric transducer. *Sensors and Actuators A: Physical*, 194, 16-24.
- [87] Yu-Jen, W., Tsung-Yi, C., and Jui-Hsin, Y. (2017). Design and kinetic analysis of piezoelectric energy harvesters with self-adjusting resonance frequency. *Smart Materials and Structures*, 26(9), 095037.

- [88] Hsu, J. C., Tseng, C. T., and Chen, Y. S. (2014). Analysis and experiment of self-frequency-tuning piezoelectric energy harvesters for rotational motion. *Smart Materials and Structures*, 23(7), 075013.
- [89] Challa, V. R., Prasad, M. G., and Fisher, F. T. (2011). Towards an autonomous self-tuning vibration energy harvesting device for wireless sensor network applications. *Smart Materials and Structures*, 20(2), 025004.
- [90] Niri, E. D., and Salamone, S. (2012). A passively tunable mechanism for a dual bimorph energy harvester with variable tip stiffness and axial load. *Smart Materials and Structures*, 21(12), 125025.
- [91] Kozinsky, I. (2009). Study of passive self-tuning resonator for broadband power harvesting. *Proc. Power MEMS* (Washington, DC, Dec.), 388-9.
- [92] Zou, H. X., Zhang, W. M., Li, W. B., Wei, K. X., Gao, Q. H., Peng, Z. K., and Meng, G. (2017). Design and experimental investigation of a magnetically coupled vibration energy harvester using two inverted piezoelectric cantilever beams for rotational motion. *Energy Conversion and Management*, 148, 1391-1398.
- [93] Zhao, S., and Erturk, A. (2012). Electroelastic modeling and experimental validations of piezoelectric energy harvesting from broadband random vibrations of cantilevered bimorphs. *Smart Materials and Structures*, 22(1), 015002.
- [94] Kumar, K. A., Ali, S. F., and Arockiarajan, A. (2017). Magneto-elastic oscillator: Modeling and analysis with nonlinear magnetic interaction. *Journal of Sound and Vibration*, 393, 265-284.
- [95] Yoo, H. H., and Shin, S. H. (1998). Vibration analysis of rotating cantilever beams. *Journal of Sound and vibration*, 212(5), 807-828.
- [96] Guo, B., Chen, Z., Cheng, C., and Yang, Y. (2015). Characteristics of a nonlinear rotating piezoelectric energy harvester under variable rotating speeds. *International Journal of Applied Electromagnetics and Mechanics*, 47(2), 411-423.
- [97] Yigit, A., Scott, R. A., and Ulsoy, A. G. (1988). Flexural motion of a radially rotating beam attached to a rigid body. *Journal of Sound and Vibration*, 121(2), 201-210.
- [98] Shahruz, S. M., and Sundararajan, V. (2008). Design of energy scavengers mounted on rotating shafts. arXiv preprint arXiv:0809.2766.
- [99] Lee, H. P. (1994). Effect of gravity on the stability of a rotating cantilever beam in a vertical plane. *Computers & structures*, 53(2), 351-355.
- [100] Abdelkefi, A., and Barsallo, N. (2016). Nonlinear analysis and power improvement of

- broadband low-frequency piezomagnetoelastic energy harvesters. *Nonlinear Dynamics*, 83(1-2), 41-56.
- [101] Abdelkefi, A., and Barsallo, N. (2014). Comparative modeling of low-frequency piezomagnetoelastic energy harvesters. *Journal of Intelligent Material Systems and Structures*, 25(14), 1771-1785.
- [102] Abdelkefi, A., Hajj, M. R., and Nayfeh, A. H. (2012). Piezoelectric energy harvesting from transverse galloping of bluff bodies. *Smart Materials and Structures*, 22(1), 015014.
- [103] Abdelkefi, A., Yan, Z., and Hajj, M. R. (2013). Modeling and nonlinear analysis of piezoelectric energy harvesting from transverse galloping. *Smart materials and Structures*, 22(2), 025016.
- [104] Zou, H. X., Zhang, W. M., Li, W. B., Wei, K. X., Hu, K. M., Peng, Z. K., and Meng, G. (2018). Magnetically coupled flextensional transducer for wideband vibration energy harvesting: design, modeling and experiments. *Journal of Sound and Vibration*, 416, 55-79.
- [105] Zhao, L. C., Zou, H. X., Yan, G., Zhang, W. M., Peng, Z. K., and Meng, G. (2018). Arbitrary-directional broadband vibration energy harvesting using magnetically coupled flextensional transducers. *Smart Materials and Structures*, 27(9), 095010.
- [106] Tan, D., Leng, Y. G., and Gao, Y. J. (2015). Magnetic force of piezoelectric cantilever energy harvesters with external magnetic field. *The European Physical Journal Special Topics*, 224(14-15), 2839-2853.
- [107] Mei, X., Zhou, S., Yang, Z., Kaizuka, T., and Nakano, K. (2019). The benefits of an asymmetric tri-stable energy harvester in low-frequency rotational motion. *Applied Physics Express*, 12(5), 057002.
- [108] Zhou, S., Cao, J., Inman, D. J., Lin, J., and Li, D. (2016). Harmonic balance analysis of nonlinear tristable energy harvesters for performance enhancement. *Journal of Sound and Vibration*, 373, 223-235.
- [109] Zhou, S., and Zuo, L. (2018). Nonlinear dynamic analysis of asymmetric tristable energy harvesters for enhanced energy harvesting. *Communications in Nonlinear Science and Numerical Simulation*, 61, 271-284.
- [110] Yang, T., Liu, J., and Cao, Q. (2018). Response analysis of the archetypal smooth and discontinuous oscillator for vibration energy harvesting. *Physica A: Statistical Mechanics and its Applications*, 507, 358-373.
- [111] Panyam, M., and Daqaq, M. F. (2017). Characterizing the effective bandwidth of tri-stable energy harvesters. *Journal of Sound and Vibration*, 386, 336-358.

- [112] Panyam, M., Masana, R., and Daqaq, M. F. (2014). On approximating the effective bandwidth of bi-stable energy harvesters. *International Journal of Non-Linear Mechanics*, 67, 153-163.
- [113] Panyam, M., and Daqaq, M. F. (2016). A comparative performance analysis of electrically optimized nonlinear energy harvesters. *Journal of Intelligent Material Systems and Structures*, 27(4), 537-548.
- [114] Stanton, S. C., Mann, B. P., and Owens, B. A. (2012). Melnikov theoretic methods for characterizing the dynamics of the bistable piezoelectric inertial generator in complex spectral environments. *Physica D: Nonlinear Phenomena*, 241(6), 711-720.
- [115] Huang, D., Zhou, S., and Litak, G. (2019). Theoretical analysis of multi-stable energy harvesters with high-order stiffness terms. *Communications in Nonlinear Science and Numerical Simulation*, 69, 270-286.
- [116] Schmidt, G., and Tondl, A. (1986). Non-linear vibrations (Vol. 66). *Cambridge: Cambridge university press*.
- [117] Abdelmoula, H., Zimmerman, S., and Abdelkefi, A. (2017). Accurate modeling, comparative analysis, and performance enhancement of broadband piezoelectric energy harvesters with single and dual magnetic forces. *International Journal of Non-Linear Mechanics*, 95, 355-363.
- [118] <https://wwindea.org/blog/2019/02/25/wind-power-capacity-worldwide-reaches-600-gw-539-gw-added-in-2018/>
- [119] https://lordfulfillment.com/pdf/44/PB8260_WindTurbineMonitor_AppNote.pdf
- [120] <https://www.microstrain.com/wireless/G-Link-200>
- [121] <https://www.nxp.com/docs/en/white-paper/TPMSWP.pdf>
- [122] <https://www.nxp.com/docs/en/product-selector-guide/FXTH87A4FS.pdf>